# STUDIES ON ATMOSPHERIC CORROSION PROCESSES IN AA2024

BY

ANDREW DU PLESSIS

A thesis submitted to the University of Birmingham for the degree of

DOCTOR OF PHILOSOPHY

SCHOOL OF METALLURGY AND MATERIALS

COLLEGE OF ENGINEERING AND PHYSICAL SCIENCES

UNIVERSITY OF BIRMINGHAM

SEPTEMBER 2014

# ACKNOWLEDGEMENTS

I would like to thank my supervisors, Professor Alison J. Davenport and Dr. Yu Lung Chiu for their help and guidance during my period of study.

I would also like to thank Rachel du Plessis for her support and encouragement through the last several years, and Dr. Mike Jenkins for his invaluable advice whenever I have put him on the spot.

I would like to thank all of those in the corrosion group who have been there as a sounding board for ideas and have offered criticism/witticism both constructive and otherwise (you know who you are)!!

Also thanks to all of those in the School of Metallurgy and Materials and there are many of them (to many to name individually) who have helped out over the years in a variety of ways. Also my gratitude to the staff at the TOMCAT beamline at SLS, notably Dr. Peter Modregger and Dr. Marco Stampanoni, and Dr. Mark Basham and Profesor Trevor Raymont from Diamond Light Source for their input during tomography work.

Finally thanks to my parents for their encouragement over a growing number of years, as I appreciate that I am starting to get older these days.

Thanks also to those of you who take the time to read some or all of the following pages and not just dooming this thesis to the confines of a library shelf. I hope that my work is of some use to you or at the very least provides you with some amount of amusement.

# ABSTRACT

Atmospheric corrosion of aluminium alloy AA2024 was investigated using in situ synchrotron micro-tomography, which allows visualisation in a non-destructive manner in real time. The effect of atmospheric variables such as salt type, humidity, exposure time and salt deposition density on the corrosion rate was investigated. It was found that corrosion fissures grow along grain boundaries parallel to the rolling direction of the alloy, reaching a limiting depth, and then spread laterally. The volume of corrosion increases with salt density and relative humidity. Salt type has a limited effect on the volume of corrosion in microtomography measurements where the droplet is constrained at the top of a pin, but in parallel lab-based experiments on plate surfaces, it was found that NaCl and simulated ocean water droplets spread laterally, leading to increased corrosion owing to an increase cathodic area, whereas pure $MgCl_2$ and $CaCl_2$ droplets do not spread. Preliminary microtomography work on cycling the relative humidity showed transient increases in localised corrosion during wetting and drying phases, often associated with rapid growth of part of a localised corrosion site, or initiation of new sites.

# ACRONYMS

| | |
|---|---|
| **µm** | Micron |
| **AAxxxx** | Aluminium Alloy (series designation) |
| **ASTM** | American Society for Testing and Materials |
| **CAT** | Computer Aided Tomography |
| **CBM** | Condition Based Maintenance |
| **CDD** | Chloride Deposition Density |
| **$Cl^-$** | Chloride |
| **DRH** | Deliquescent Relative Humidity |
| **EDX** | Energy Dispersive X-Ray |
| **ERH** | Efflorescent Relative Humidity |
| **FIB** | Focussed Ion Beam |
| **GDP** | Gross Domestic Product |
| **GPB** | Gunier Preston Badayatsky |
| **IGC** | Inter Granular Corrosion |
| **L** | Longitudinal |
| **LT** | Long Transverse |
| **M** | Molar |
| **nm** | Nano-meters |
| **$OH^-$** | Hydroxide |
| **OM** | Optical Microscopy |

| | |
|---|---|
| **PFZ** | Precipitate Free Zone |
| **PHM** | Prognostic Health Management |
| **RH** | Relative Humidity |
| **SCC** | Stress Corrosion Cracking |
| **SEM** | Scanning Electron Microscopy |
| **SSSS** | Supersaturated solid state solution |
| **ST** | Short Transverse |
| **TEL** | Thin Electrolyte Layer |
| **TOW** | Time of Wetness |
| **µCT** | X-Ray Micro Tomography |

# 1 INTRODUCTION

Airframes are generally made from high strength aluminium alloys, which are susceptible to corrosion owing to the presence of copper-containing intermetallic phases in their microstructure. This necessitates the implementation of maintenance programs to combat the structural risks introduced by corrosion damage. These often require the removal of an aircraft from active service for a period of several months, and are thus expensive. It is therefore desirable to increase the maintenance intervals as much as possible while maintaining structural integrity. In order to achieve this, models are under development to predict the extent of corrosion based on the environment to which the aircraft has been exposed [1, 2]. This form of maintenance is referred to as Condition-Based Maintenance (CBM).

Aluminium alloy AA2024 (AlCuMg) is commonly employed in the wings and fuselage of aircraft, owing to its excellent strength and fatigue resistance. Its corrosion behaviour has been extensively studied in full immersion conditions [3-5]. However, surprisingly little work has been performed under the atmospheric corrosion conditions to which aircraft are commonly exposed. In this project, atmospheric corrosion of AA2024 was investigated using X-ray micro-tomography for in situ characterisation of corrosion damage. This method allows time-dependent characterisation of corrosion sites with micron-scale resolution, including the effect of alloy microstructure on corrosion morphology. This gives information both on the growth of corrosion sites under steady state conditions, and also allows investigation of the effect of fluctuations in relative humidity that are commonly encountered in

service. The effect of different salt types was examined, including simulated ocean water, and the constituent salts NaCl, $MgCl_2$ and $CaCl_2$, as well as factors such as the salt density and relative humidity. Tomographic measurements are made of corrosion under droplets at the tip of metal pins. The results are compared with the findings from lab-based measurements on metal plates, where droplets can spread laterally across the metal surface.

# 2 LITERATURE REVIEW

## 2.1 Aircraft Health Management

Maintenance of aircraft is carried out throughout their service life on a pre-scheduled basis. This requires removal of aircraft from operational service for a prolonged period of time, for inspection and undertaking necessary maintenance programmes. This result is the loss of an aircraft from service with an associated financial cost, which is a particular problem since the current fleet of both commercial and military aircraft are ageing. Maintenance and inspection of aircraft is made necessary owing to the degradation of their material components. Typically this takes the form of fatigue cracks or corrosion damage which results in the formation of preferential sites for fatigue cracking [6-9].

Removal of aircraft for material inspection on a “find and fix” basis is referred to as condition-based maintenance (CBM), where damage is assessed and repaired at regular pre-determined intervals. Models have been developed to predict the optimum intervals to be employed in a traditional CBM strategy [8, 10, 11]. In a move to make this process more efficient, development of prognostic health management (PHM) is being carried out [1, 2, 12-14]. Whereby “live” data accumulation from sensors attached to aircraft in service is used to perform accelerated “ahead of life” testing, which helps to better predict optimum maintenance intervals.

Sensors on aircraft and in the field provide information such as time of wetness (TOW) of a metal surface, temperature and accumulation of salts. Data is used to

design accelerated tests for fatigue, corrosion, fractures and failure of protective coatings. Combining this data it is possible to predict based on where aircraft have been operational, optimum intervals for maintenance [13, 14].

PHM is desirable for aircraft management, however, in addition to the data from sensors, it requires detailed data relating to the propagation of corrosion fissures or fatigue cracks which promote premature failure. This is at present relatively limited, hence the aim of this project is to provide underpinning information on the mechanisms and rates of corrosion to aid the development of PHM models.

## 2.2 Aluminium Alloy AA2024

### 2.2.1 Introduction

Aluminium is the most abundant metallic element on earth and is an essential material for use in a variety of applications [15, 16]. Specifically considering the 2xxx series alloys (wrought), the major alloying system is that of Al-Cu-Mg, used due to its ability to greatly improve the mechanical properties of the base metal. Initially this family of alloys was referred to as “duraluminium”. Over time, the major applications for 2xxx series alloys (especially 2024) shifted to become almost completely based in the aerospace industry [15, 17].

Aluminium alloy 2024 (AA2024) is employed in the aerospace industry due to its excellent strength to weight ratio, which is comparable to that seen for steels [6, 9, 16, 18]. Other benefits of aluminium alloys include their ability to perform at low temperatures, as well as their increased machinability. However, there are certain drawbacks to the use of aluminium alloys in the aerospace industry, such as their increased susceptibility to fatigue, a falloff in mechanical properties following

prolonged use at elevated temperatures, cost compared to other materials and their susceptibility to corrosion when exposed to the atmosphere [6, 9, 16, 18].

The nominal composition of AA 2024 is given in Table 2.1.

**Table 2.1 - Nominal Composition AA2024 [19, 20]**

| Element | Wt % | Element | Wt% |
|---|---|---|---|
| Al | 90.7-94.7 | Mn | 0.3-0.9 |
| Cr | Max 0.1 | Si | Max 0.5 |
| Cu | 3.8-4.9 | Ti | 0.15 |
| Fe | Max 0.5 | Zn | Max 0.25 |
| Mg | 1.2-1.8 | | |

Addition of alloying elements according to the specification in Table 2.1 leads to an improvement in mechanical properties of the parent material through thermomechanical processing [21]. Addition of alloying elements takes place following refinement of aluminium oxide into aluminium. Elements are added whilst metal is in its molten state, prior to being cast into billets and thermomechanically processed into plate form. Application of heat treatment at relatively high temperatures dissolves the alloying elements into a solid solution state, prior to application of rapid quenching to form a supersaturated solid solution. Typically for aerospace grade AA2024 tempers (T3 or T351), solution heat treatment of the alloy takes place at ~500 – 550 °C. Following quenching, the metal is allowed to age

naturally at room temperature; for T351 the addition of a cold working procedure ("stretching") follows the quench [15, 16, 22] .

### 2.2.2 Development of the Microstructure of AA2024

The microstructure of AA2024 contains three types of intermetallic particles: constituent particles, dispersoid particles and strengthening precipitates [16, 23, 24]. The constituent particles form during solidification of the alloy, and the major types are S-phase ($Al_2CuMg$) or based on the composition $Al_6(Fe,Mn,Cu)$. S-phase particles tend to be regular and spherical in shape, whilst $Al_6(Fe,Mn,Cu)$ particles tend to be larger in size with little regularity to their shape. θ-phase ($Al_2Cu$) particles have also been observed. These particles often fragment during the rolling process, forming "stringers" parallel to the rolling direction. Particles based on $Al_6(Fe,Mn,Cu)$ have a range of compositions [21, 24, 25].

Dispersoid particles are typically submicron size particles generally reported as being in the region of 0.05-0.5μm, and often contain transition metals in their composition. Examples of transition metal compositions [26] are: $Al_{20}Mn_3Cu_2$ and $Al_{12}Mg_2Cr$. Dispersoid particles play an important role during recrystallisation and grain growth, during the heat treatment phase of alloy production, by helping to maintain the position of original grain boundaries [16, 27-30]. They further play an important role in the development of microstructure, as they can lead to nucleation of dislocations within the matrix, which serve as sites for continued precipitation reactions [26, 27].

The nanometre-scale strengthening precipitates develop during ageing of supersaturated solid solution formed by solution treatment and quenching. They are typically <0.1μm in size and result from the accumulation of Cu and Mg atoms into

localised concentrations within the grains. This helps to reduce susceptibility to plastic deformation, by blocking the movement of dislocations [16, 24, 31, 32].
It has been well established that precipitation hardening sequence resulting in the formation of the traditionally observed microstructure in AA2024 proceeds according to the following mechanism [15, 16, 25, 33-36]:

$$SSSS \rightarrow Solute\ Clusters \rightarrow GPB + Solute\ Clusters$$
$$\rightarrow GPB + Solute\ Clusters + S\ Phase \rightarrow GPB + S\ Phase \rightarrow S\ Phase$$

Where: SSSS (supersaturated solid state solution), GPB (Guinier-Preston-Bagayatsky) and S-Phase (Secondary Phase)

Localised concentrations of alloying elements along grain boundaries can lead to the formation of a precipitate-free-zone (PFZ) in the matrix adjacent to both the grain boundary and the particles which have precipitated from solution [4, 16, 37-39]. These regions are often depleted in copper compared to the grain boundaries and particles which results in the establishment of an electrochemical gradient discussed in Section 2.3.6.

## 2.3 Corrosion of AA2024

### 2.3.1 Introduction

Aluminium is a thermodynamicaly “reactive” metal, but often has good corrosion resistance owing to the formation of a passive oxide film, typically $Al_2O_3$, which provides a barrier to the environment. The thickness of the film varies from ~1-5 nm when formed naturally [16, 40]; it is possible to artificially thicken the film through the

use of techniques such as anodising. The film is formed in the presence of water according to Equation 2.3.1.

$$2Al(s) + 3H_2O(l) \rightarrow Al_2O_3(s) + 6H^+ + 6e^- \qquad \textbf{Equation 2.3.1}$$

The passive film is stable (resistant to dissolution) in neutral environments, but can dissolve in acidic or alkaline environments. The effect of pH and interfacial potential on the stability of the oxide, leading to regions where aluminium shows passivity, immunity and corrosion have been represented in diagrammatic form by Pourbaix [41] (Figure 2.1).

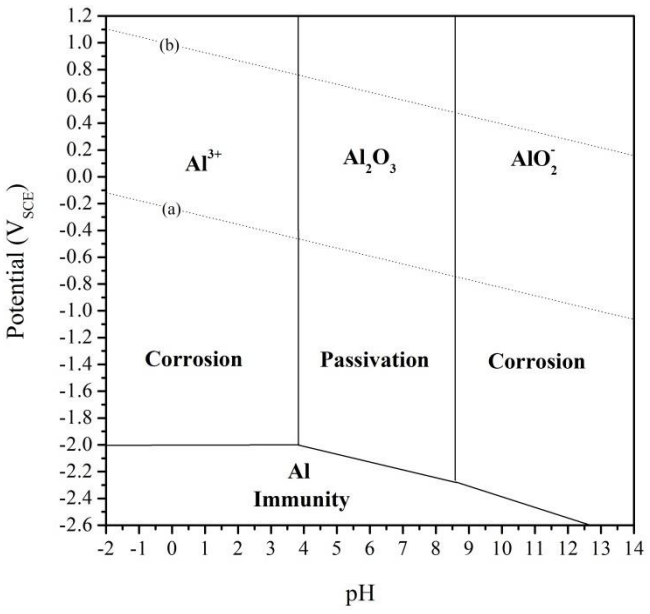


**Figure 2.1 - Pourbaix diagram showing theoretical conditions of corrosion, immunity and passivation of aluminium, at 25°C[41]**

Alumina is an insulator, so it inhibits the cathodic reaction at the aluminium surface, enhancing its resistance to corrosion [15, 32, 40, 42]. The range over which the film

is stable can vary depending on temperature, and other variables such as the presence of other chemical species.

Unlike many other metals, which corrode only in the presence of highly acidic environments, breakdown of passivity in aluminium can also occur in the presence of alkaline environments. This typically results in a more general attack of the surface. This ability to undergo corrosion under both acidic and alkaline regimes is referred to as being amphoteric [40, 43].

Under acidic conditions, the electrochemical dissolution of aluminium proceeds according to the reaction below [16, 43-46]:

$$Al \rightarrow Al^{3+} + 3e^{-} \qquad \textbf{Equation 2.3.2}$$

Hydrolysis of the aluminium ions, in the presence of water is the next process in a stepwise corrosion mechanism, leading to the formation of a more sustained localised acidic region[43]. Hydrolysis of aluminium ions proceeds according to the following reaction [32, 40, 47, 48]:

$$Al^{3+} + H_2O \rightarrow AlOH^{2+} + H^{+} \qquad \textbf{Equation 2.3.3}$$

The most common cathodic reaction for corrosion of aluminium alloys is oxygen reduction, which leads to a local increase in pH [32, 40, 47, 48]:

$$O_2 + 2H_2O + 4e^{-} \rightarrow 4OH^{-} \qquad \textbf{Equation 2.3.4}$$

The other common cathodic reaction for corrosion of aluminium is hydrogen evolution (Equation 2.3.6). This sometimes takes place within localised corrosion sites, leading to the formation of hydrogen bubbles, which can be characteristic of the presence of localised corrosion processes [32, 40, 47, 48].

$$2H^+ + 2e^- \rightarrow H_2$$ **Equation 2.3.5**

Pure aluminium is very resistant to corrosion due to the presence of an insulating passive film that blocks the cathodic reaction (typically oxygen reduction). In alloys such as AA2024 the addition of alloying elements leads to the formation of intermetallic particles with thinner (Figure 2.2) more conductive oxide layers results in the formation of preferential cathodes at which localised corrosion can initiate [16, 40, 47] [40, 49]. This effect was demonstrated by Missert [46], where copper islands equally spaced within an aluminium matrix were shown to be preferential locations for oxygen reduction.

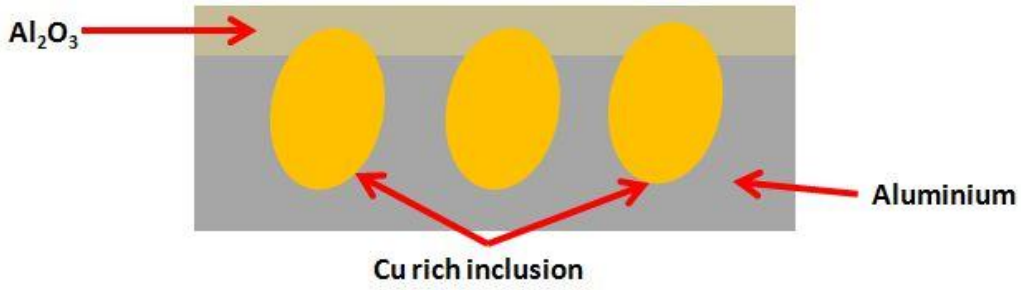


**Figure 2.2 - Distribution of Cu rich inclusions within aluminium matrix and associated thinner oxide film at the surface**

### 2.3.2 Alkaline Trenching

The localised increase in pH at intermetallic precipitates due to oxygen reduction, results in a localised region of alkalinity in their immediate vicinity [48, 50, 51]. This localised increase in pH leads to alkaline “grooving” or “trenching”, which is dissolution of the matrix around the cathodically active particles and is a rapidly occurring process. Furthermore, it has been shown that trenching attack occurred preferentially at S-Phase particles at low concentrations of $Cl^-$. However, with increasing concentration, trenching was also observed in the vicinity of Al-Cu-Mn-Fe

particles as well [50]. An example of an Al-Cu phase exhibiting trenching/grooving behaviour can be seen in Figure 2.3.

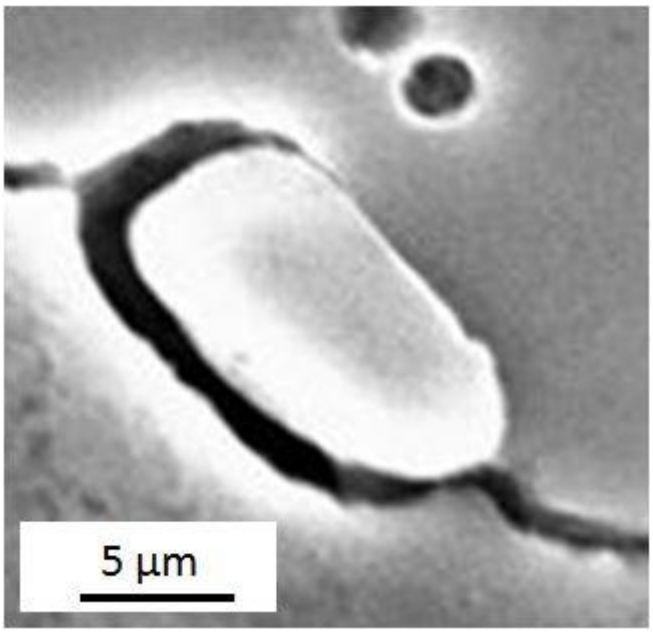


**Figure 2.3- Example of grooving around the edge of a Al-Cu intermetallic phase in AA2024 matrix, image taken during this work**

### 2.3.3 Localised Corrosion of AA2024

Pit initiation on AA2024 generally takes place in the vicinity of intermetallic particles [21, 28, 52-64], especially S-phase precipitates. Preliminary stages of localised corrosion have been attributed to dissolution of aluminium and magnesium from within the S-phase precipitates [21, 58, 65] leaving behind a copper-rich phase which is increasingly noble to the surrounding aluminium matrix.

In addition a number of studies consider the mechanism of passive film breakdown a key step in initiation of localised corrosion [66-74]. Whilst it is important to understand the mechanisms for anion transport through the passive film to the surface, when considering corrosion on AA2024, initiation takes place primarily at intermetallic

phases with thinner oxides, the role of oxide thickness and the role that the intermetallic particles plays is perhaps more important.

A number of reviews on pitting mechanisms for aluminium and other metals have been written over the past few decades, the most comprehensive of which are those by Foley [75], McCafferty [70], Frankel [76] and Szklarska-Smialowska [61].

### 2.3.4 Metastable Pitting

During the initial stages of pitting corrosion, metastable pitting (the formation of short lived shallow pits) is reported to take place [61, 65, 77]. Metastable pits initiate and repassivate rapidly during the early stages of localised corrosion on aluminium, providing none become sufficiently large or aggressive to allow for a transition to stable pitting to take place[61, 78]. Metastable pits are typically small and random in shape with diameters in the order of microns. Coupled with shallow depth they are often difficult to detect by means of surface inspection and are often referred to more often during electrochemical studies.

Stable pitting will take place once the environment in one of the metastable pits becomes sufficiently aggressive to prevent repassivation taking place. The criterion used for the transition from metastable to stable type pitting events is the critical pitting potential. Critical pitting potential ($E_{pit}$) refers the most negative potential above which a stable pit can form and grow [79]. It is highly dependent on the environmental factors to which the metal is exposed, for example chloride ion concentration and temperature, as well as the surface roughness [78, 80-82]. For pure aluminium the suggested criterion for transition from metastable to stable pitting

is in the region of $x.i \leq 10^{-2}$ A/cm$^2$, with x being pit depth, and i being pit current density [78, 83].

### 2.3.5 Stable Pitting

Following the establishment of a stable pit site, with the pit behaving as a net anode which draws current from available cathodic sites in its vicinity, sustained growth of this site takes place [16, 40, 51, 52, 61, 65, 70, 80, 84]. Within the pit, where conditions are aggressive, the acidity rises due to continued hydrolysis of aluminium, and migration of chloride ions in solution to the active front is observed in order to maintain charge balance [16, 40, 51, 52, 61, 65, 70, 80, 84]. The presence of chloride ions and an acidic environment both contribute to preventing the re-growth of the passive layer. This is a self-sustaining process whilst the pre-requisite conditions for localised corrosion are maintained, as such stable pitting is often referred to as being auto-catalytic in nature.

Whilst dissolution of the metal is favoured over repassivation, and the rate of transport of metal ions away from the pit remains below the rate of their production. It is possible for the pit bottom to become supersaturated by metal ions resulting in the presence of a salt layer, which is indicative of stable pit growth in an acidic environment [61, 85, 86].

At the surface of the metal around the pit site where a region of mild acidity is found, it has been observed that the metal remains entirely unattacked [87]. This indicates that the pH is at a value where the solubility of the passive film is low in these locations; this is shown in Figure 2.4, where the solubility of the passive film is reduced in the pH range 4-7. At the junction between this region and the net cathodic

region, the precipitation of corrosion product takes place [79, 88]. Precipitation of corrosion products takes place in this location due to migration of $Al^{3+}$ towards the cathodic (alkaline) regions in order to maintain charge balance in the presence of $OH^-$ evolved during oxygen reduction.

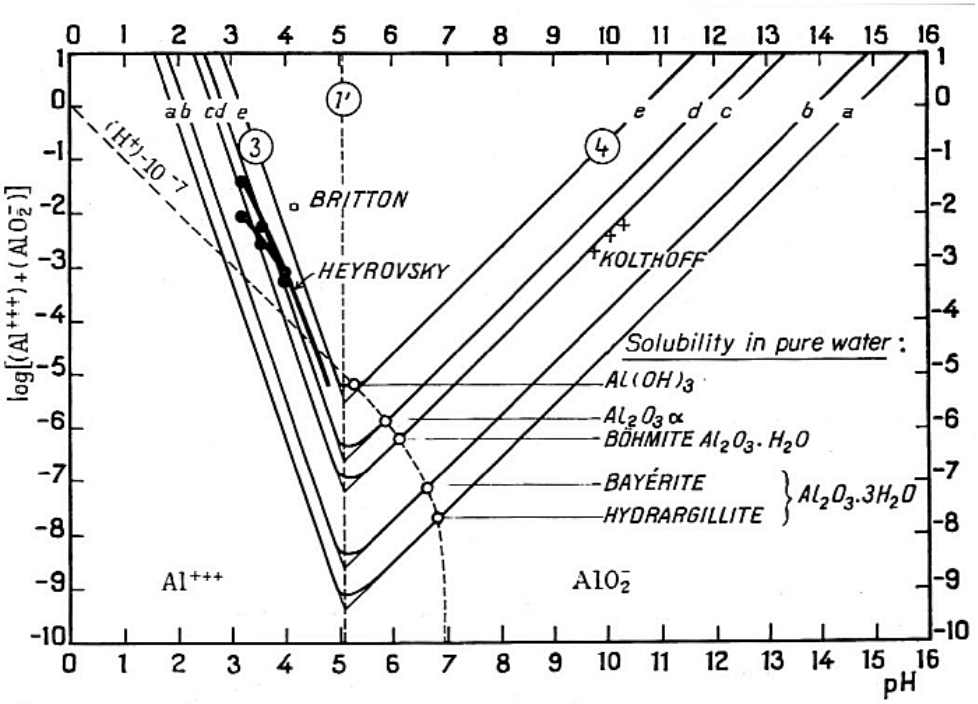


**Figure 2.4 – Influence of pH on the solubility of $Al_2O_3$ and its hydrates, at 25°C [41], p.174**

Growth of pits takes place along the most susceptible route, which in AA2024 is typically along grain boundaries into the interior of the metal (see below). Thus the transition from pitting to intergranular corrosion (IGC) in AA2024 often takes place rapidly and accounts for the complex geometry observed when considering localised corrosion of AA2024 [4, 5, 89-93].

Measurement of the pit growth rate has been undertaken in several studies, using techniques such electrochemical measurements (potentiostatic [77, 78]) or thin film penetration [89]) or it has been suggested that growth rate can be estimated via mass loss [94]. It is difficult to measure pit growth rates with great accuracy due to their complex and irregular geometry, with extension down susceptible grain boundaries taking place [5, 77, 95-97].

### 2.3.6 Intergranular Corrosion (IGC)

As has been outlined, in AA2024 there is significant overlap between pitting corrosion and IGC growth, as pits will often develop along grain boundaries and transition into IGC fissures [5, 16, 47, 98].

Intergranular corrosion (IGC), sometimes referred to as inter-crystalline corrosion, is a form of localised attack in zones adjacent to grain boundaries in susceptible alloys [16, 40, 48, 63, 99, 100]. IGC at aluminium surfaces is often difficult to detect as fissures often initiate at pit bottoms. IGC fissures can also initiate at surface defects or on surface breaking susceptible grain boundaries, and in these cases fissures are also difficult to detect as they are very fine.

2xxx series aluminium alloys are susceptible to IGC [63, 101] owing to the formation of copper-depleted zones adjacent to grain boundaries, during the ageing process [16, 40, 63]. Galvele[102] described formation of this copper-depleted region, which can be seen in Figure 2.5, as the most important pre-requisite for the occurrence of IGC in Al-Cu alloying systems.  Intergranular attack is particularly important as

fissures can penetrate several 100's of microns up to several mm into the bulk of the alloy, leading to an increased susceptibility to the onset of Stress Corrosion Cracking (SCC).

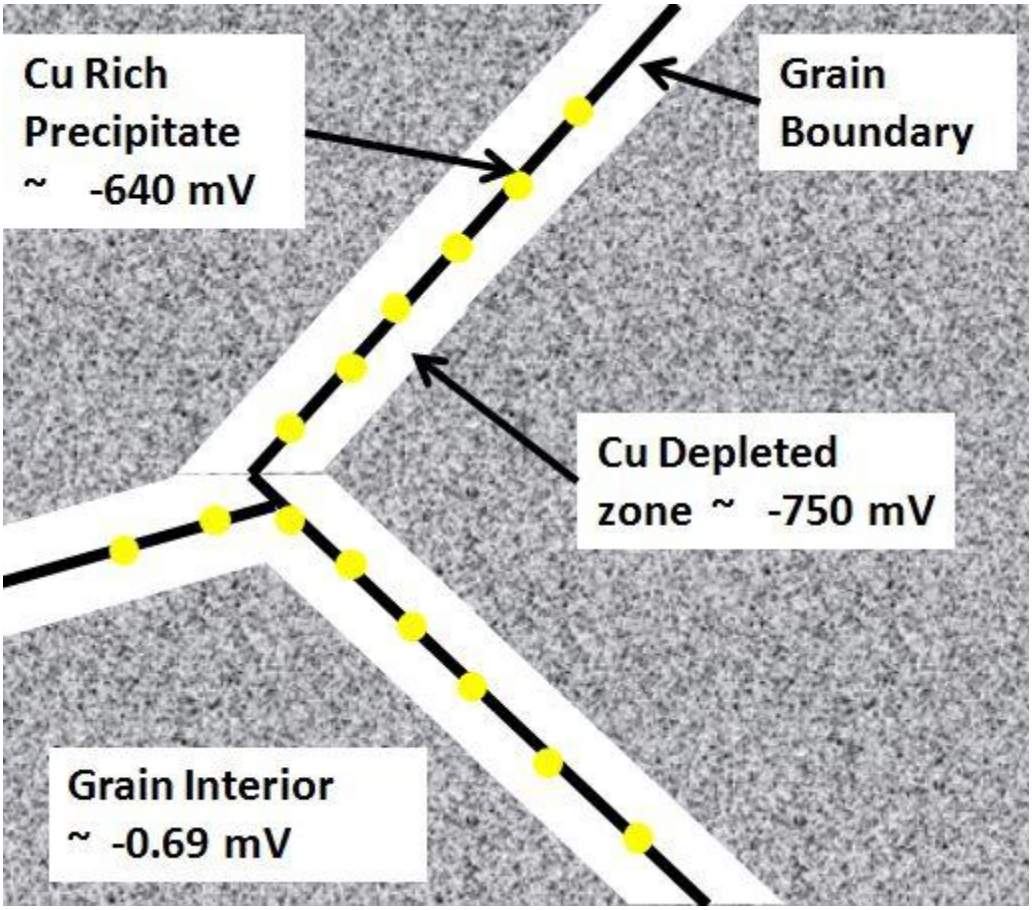


**Figure 2.5 - Grain boundary region, with formation of Cu depleted zone towards grain exterior, Cu rich precipitates along boundary, modified schematic [47, 102] and potentials taken from Vargel[47] and Guillaumin[4]**

In AA2024, precipitation of copper-rich phases takes place along grain boundaries in the alloy, Figure 2.5, with associated diffusion of copper out of solid solution. As a result, a copper-depleted zone forms adjacent to the grain boundaries, which has an

increased susceptibility to dissolution. During IGC it is this copper-depleted zone which becomes the net anode due to a lowered electrochemical potential when compared with the copper-rich matrix [16, 40]. The grain boundary precipitates can act as localised cathodes, contributing to the overall cathodic reactions taking place.

Both precipitation of copper-rich intermetallic phases along grain boundaries and the associated region of copper depletion result in the formation of zones which are more susceptible to localised corrosion. Diffusion of the copper out of solid solution increases aluminium's tendency to dissolution, as it leaves behind a less noble phase. The copper-rich phases which precipitate become net cathodes[4, 47, 102] with respect to the copper-depleted zone, which results in the copper-depleted zone becoming the net anodic region, and undergoing dissolution. The copper-depleted zone tends to be very narrow, typically on the nanometre scale.

IGC growth rates have been measured in AA2024 most commonly by using foil penetration [97] radiography [5, 91, 103-105], or more recently using X-ray microtomography (μCT) [92, 106-108]. Other techniques have also been employed to evaluate IGC, including FIB SEM [96, 109] and metallographic sectioning [93, 95] being the most relevant. Results indicated the IGC fissure propagation rates where highly dependent on metallographic orientation, and it was shown that the exposure in the ST (short transverse) orientation results in a slower growth rate than for either LT (long transverse) or L (longitudinal) [5, 92, 106]. Increased growth rate was attributed to elongation of grains in the LT and L orientation due to mechanical processing. Differential growth rates were observed for foil penetration and radiography [91], with foil penetration resulting in a greater depth of attack, which were related to sample type and differences in resolution of the techniques.

Metallographic sectioning was deemed time consuming but effective in exposing the extent of grain boundary attack [93, 95], and μCT provided a non-destructive method of evaluating IGC development [92, 106-108].

## 2.4 Atmospheric Corrosion of AA2024

### 2.4.1 Introduction

Atmospheric corrosion involves the corrosion of metals under droplets or thin layer electrolytes. Corrosion is often studied under conditions of full immersion, but atmospheric corrosion is less well studied despite its practical importance, particularly in corrosion of airframes. With a confined electrolyte, there is easier access of oxygen compared with full immersion conditions, since oxygen can diffuse more rapidly through thin electrolyte layers, and there is particularly easy access of oxygen at the three phase boundary between the metal, electrolyte and air at the edge of droplets. Furthermore, the concentration of the electrolyte is controlled by the relative humidity of the surrounding air. This can lead to the formation of more corrosive salt solutions that are more concentrated and more aggressive than, for example, seawater.

Atmospheric droplets form on a metal surface either through direct solution transfer, for example rain or sea spray from waves, or through deposition of solid salt particles, for example from marine aerosols. These are termed wet and dry deposition mechanisms. Often during dry deposition particulates are airborne and transported from locations quite remote from that where corrosion processes are observed. Gradients of the sphere of influence of aerosol sources on amount and type of salt have been extensively carried out [110-112]. Modelling of transportation

and deposition mechanisms involved in atmospheric corrosion processes has been carried out quite extensively, based on both predictive modelling, and through accumulation and analysis of sensor data [113-116].

Often particulate aerosols are considered as being primarily from marine sources. However, there are other sources of atmospheric aerosols from both industrial and agricultural sources such as industrial emissions, fertilisers, and spray from de-icing salts used on roads. These are generally categorised as rural, urban, industrial or marine [63, 117-120].

### 2.4.2 Solution Equilibrium with Environment

During atmospheric exposure, solution present on a surface has a specific equilibrium concentration which varies as a function of RH (relative humidity) [121-123]. The saturation concentration of solutions corresponds to a specific RH. The deliquescence relative humidity (DRH) corresponds to the point during wetting at which salt on a metal surface begins to take moisture up from water vapour in the environment to form a solution. During loss of moisture from a solution (efflorescence) there is a point at which solid salt starts to form is known as the efflorescence relative humidity (ERH).

The deliquescence process is shown in Figure 2.6, and the reported equilibrium RH values for saturated salt solutions commonly found in atmospheric droplets, along with their reported DRH and ERH values are shown in Table 2.2. Further the predicted equilibrium RH values based on thermodynamic predictions made using OLI software[124, 125] are shown.

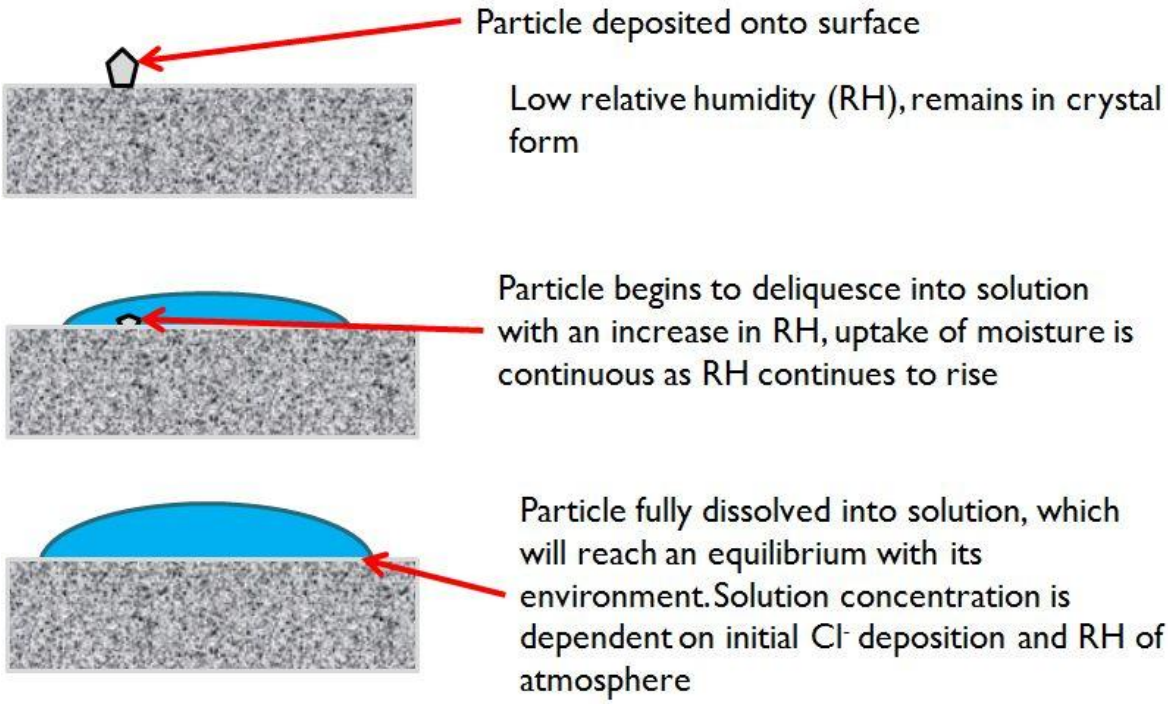


**Figure 2.6 - Deliquescence of an aerosol particle on metal surface**

**Table 2.2 DRH at 25°C of salts found under atmospheric corrosion conditions**

| Salt | Equilbrium RH of Saturated Solution | DRH (%) Reported | ERH (%) Reported | Equilibrium RH at precipitation point calculated OLI software[124, 125] |
|---|---|---|---|---|
| NaCl | 75.5-76% [122, 126-129] | 74-76 %[130, 131] | 41-50% [132] | 75.7% |
| $MgCl_2$ | 33-35% [122, 126-129] | 33-35 %[131, 133] | | 38.2% |
| $CaCl_2$ | 29.5-30% [128, 129, 134] | 29 %[135] | | 28% |

Tsutsumi [136] plotted the measured RH of water vapour phase in equilibrium with $MgCl_2$ solutions of a range of concentrations; this is shown in Figure 2.7. Wheeler [122] measured the equilibrium RH for some common salt solutions, and proposed that Equation 2.4.1 can be used to calculate the equilibrium RH for given salt solutions of known concentration. Calculation of the equilibrium concentration as a

function of RH, initial amount of chloride present and salt type is plotted in Section **Error! Reference source not found.**. A comparison between the values measured y Tsutsumi [136] and the predicted equilibrium RH for different salt types used during this study are plotted in Section **Error! Reference source not found.**., in Figure 4.4.

$$\boldsymbol{RH = \left(1 - \frac{xM}{\left(xM + \frac{1000}{18}(1 - yM)\right)}\right) * 100} \qquad \textbf{Equation 2.4.1}$$

Where M = molar concentration of salt, x = total number of ions in compound which dissociate into solution, and *y* can be calculated using the equation below:

$$\boldsymbol{y = \frac{(\frac{1}{\rho})M}{1000}} \qquad \textbf{Equation 2.4.2}$$

Where ρ = Density and M = Molecular Weight.

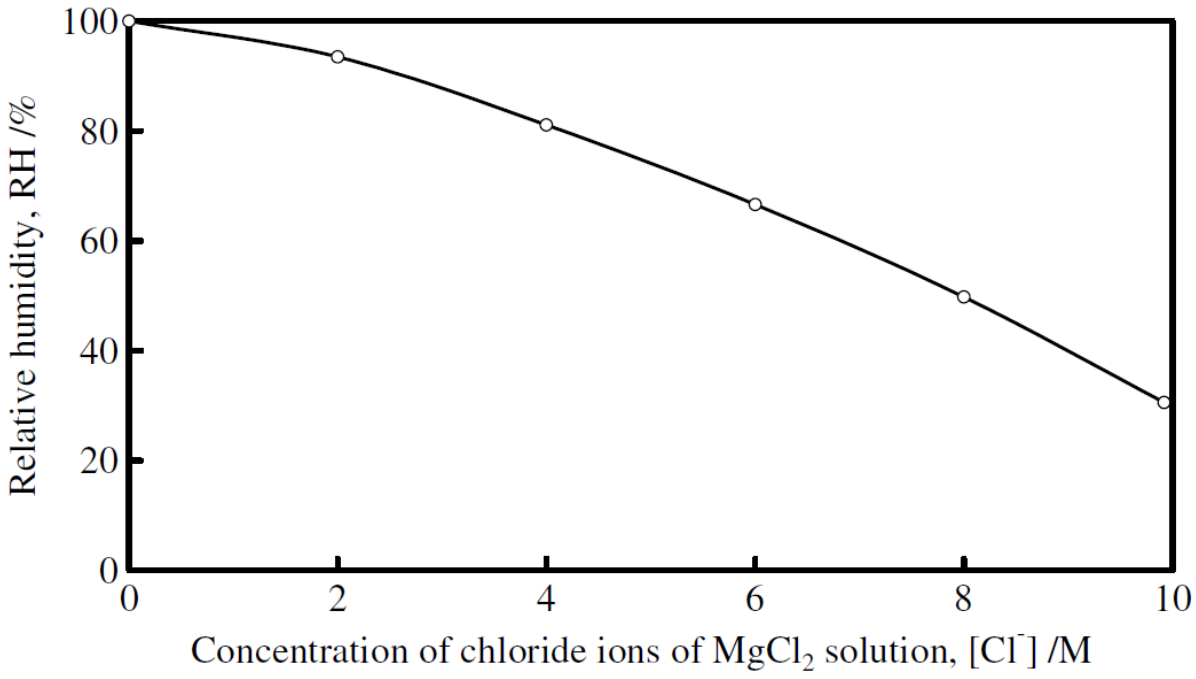


**Figure 2.7 - Equilibrium RH as a function of changing $MgCl_2$ solution concentrations as plotted by Tsutsumi [136]**

The importance of knowing the concentration of salt solution in equilibrium with a given RH is such that salt will take moisture up from the environment until the equilibrium point is reached. This governs the volume of atmospheric solution droplets and the solution layer thickness. The importance of solution layer thickness is that it determines how atmospheric corrosion is proceeds as the solution layer thickness affects both oxygen transport and resistance to ionic mobility within the solution.

Tomashov [137] and Leygraf [117, 138] have indicated the typical layer thickness under different conditions as follows: dry atmospheric corrosion <10 nm, moist atmospheric corrosion 10 nm – 1 µm, wet atmospheric corrosion 1 µm – 1 mm thickness, and full immersion >1 mm thickness.

The approximate equilibrium volume of the atmospheric droplet can be calculated by rearranging the formula used by Li [139], from the form seen in equation 2.4.3 to that of equation 2.4.4. From the volume, it is possible to predict the thickness of a solution layer for a fixed surface area, as the equilibrium concentration will be controlled by RH of the environment and as such the final solution volume will be the equilibrium volume.

$$\boldsymbol{C = C_o\left(\frac{V_o}{V}\right)} \qquad \textbf{Equation 2.4.3}$$

$$\boldsymbol{V = \frac{V_o}{\left(\frac{C}{C_o}\right)}} \qquad \textbf{Equation 2.4.4}$$

Where C is final solution concentration, $C_o$ is original solution concentration, $V_o$ is original volume of solution and V is final solution volume.

For a fixed amount of salt per unit area on a metal surface, the volume and height of a solution droplet or layer changes as a function of RH, in order to maintain its equilibrium concentration. A common measure of the amount of salt on a metal surface is the chloride deposition density (CDD), and considers the mass of chloride per unit area. Accordingly for a fixed RH changes in the initial CDD will alter the equilibrium volume/height of a droplet.

Changes in droplet height are important as they influence the ionic transport processes in solution. An increase in the droplet height will result in a reduction in the resistance of the solution in the droplet which promotes net ionic movement. Importantly the resistance between the cathode and the anode is lowered which increases the flow of ions allowing for an increase in the reaction rate, and a corresponding increase in the rate of corrosion [79, 88].

Further an increase in droplet height results in an increase in length of the oxygen diffusion path to the cathode. As such for a droplet of greater height it is the rate of transport of oxygen through the droplet which becomes the important factor in cathodic processes, which is assisted by the lowered resistance in solution.

Changes in droplet concentration due to changes in RH for a fixed CDD, are important as solution concentration affects the pH, viscosity and conductivity of a solution[121, 123, 140]. It has been suggested that typically the greater the concentration in solution the more conductive a solution becomes[121, 123], however this is not necessarily always the case, as a more concentrated solution is often more viscous. Viscosity is influenced similarly to the effect that it will increase with concentration [121, 123, 140, 141]. A more viscous solution (with a lowered water activity) leads to increased resistance between the electrodes which slows the overall reaction rate. With an increase in concentration associated with a decrease in RH it is likely that ionic mobility will begin to be inhibited. increase in concentration of solution also results in a more acidic solution [140].

### 2.4.3 Secondary Spreading

Secondary spreading refers to the formation of a thin layer of moisture or a concentrated zone of microdroplets, in the immediate periphery of an atmospheric droplet on a metallic surface. Formation of micro-droplets and a secondary spread region has been observed in a number of studies on steel [142-147], zinc [133, 147-150], magnesium [151] and aluminium [145, 152].

Formation of micro-droplets has been shown to be associated with establishment of a potential gradient from the centre of the main droplet towards its periphery [142-

144]. Development of this potential gradient is likely due to the tendency for droplets to form a cathodic region at their periphery (there is easy access of oxygen at the edge of a droplet), with the anode forming within the droplet. The cathodic region has an associated increase in pH (from generation of $OH^-$) as a result of oxygen reduction, which draws cations present in solution (e.g. $Na^+$) in order to maintain charge balance. This effect has been demonstrated on stainless steel [143] and AA7050 [152].

A schematic showing the formation of micro-droplets on a carbon steel sample and the migration of cations into the spread zone is shown in Figure 2.8 [142]. Over time, coalescence of individual droplets into an electrolyte layer tends to take place; this layer is referred to as a zone of secondary spreading. It has been shown by means of two connected steel electrodes that microdroplets would only form on the cathode [142].

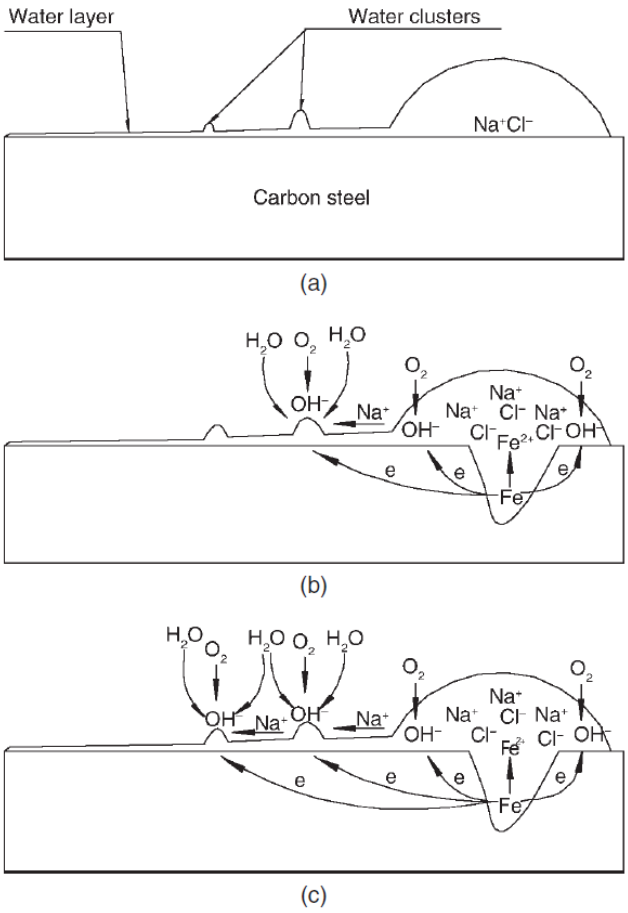


**Figure 2.8 – Development of secondary spreading (Zhang et al.[142]): (a) formation of a thin electrolyte layer and water clusters, (b) oxygen reduction and water molecule adsorption, (c) movement of cations from main droplet into peripheral region resulting in the formation of micro-droplets.**

Zhang [142], showed that NaCl and KCl exhibited secondary spreading behaviour on carbon steel, zinc and brass (but not on stainless steel), whilst $MgCl_2$ and $CaCl_2$ did not form spread zones on any metal. Cole [133] and King [96, 109] observed secondary spreading under saturated and unsaturated sea water on zinc and galvanised steel surfaces.

It has further been shown that rate of spreading is controlled in part by the exposure time [133, 142], with a more prolonged exposure leading to a larger secondary spreading zone. Cole[133] demonstrated that relative humidity played a role during exposure to ocean water solutions, with no spreading observed RH values of 53% or below, possibly this is due to a decrease in the amount of corrosion associated with lower RH.

In the case of studies where the formation of microdroplets has been observed [133, 142-144, 147], the time taken until the onset of micro-droplet growth is rapid, often within the first hour following deliquescence.

### 2.4.4 Influence of Salt Type on during Atmospheric Corrosion

Influence of salt type, both cation and anion, has been considered for some of the primary atmospheric constituent salts, such as NaCl, $MgCl_2$, $CaCl_2$, $Na_2SO_4$ and ocean water during droplet studies on AA2024[96, 109] and other metals [153-156]. However, some immersion studies [140, 157, 158] have made direct comparisons of the influence of cation type and findings are of interest to atmospheric study.

King [96, 109] examined the corrosion behaviour of AA2024 under ocean water solutions, using FIB SEM to study the development of localised IGC fissures along grain boundaries. Cole[133] also used ocean water solutions on steel and zinc, and further indicated that there were many similarities between their behaviour and that under NaCl solutions.

Prosek et al. [153] carried out atmospheric corrosion studies of carbon steel and zinc with chloride solutions containing Ca, Na and Mg as the cations. The accumulated

mass gain was used to assess the corrosion kinetics over time; the cations were rated according to their relative aggressiveness in the following order $Mg^{2+}<Ca^{2+}<Na^{+}$.

Beom [157], reported $CaCl_2$ to have a lower pH than that observed for NaCl, during immersion at 35$^{o}$C. This resulted in a lowered pitting potential on stainless steel surfaces. It was suggested that the lowered pH is due to the preferential tendency for hydrolysis of $CaCl_2$ when compared with NaCl or $MgCl_2$ [157, 158]. Similarly Ernst [140], reported a small reduction in critical pitting temperature on stainless steel during substitution of Ca for Na.

Composition of the ASTM standard for simulated ocean water can be seen in Table 2.3. The addition of the heavy metal constituents has been omitted.

**Table 2.3 - Composition of Substitute Ocean Water, ASTM Standard Practice for Preparation of Substitute Ocean Water[159]**

| Salt Compound | Concentration (g/L) |
|---|---|
| NaCl | 24.53 |
| $MgCl_2$ | 5.20 |
| $Na_2SO_4$ | 4.09 |
| $CaCl_2$ | 1.16 |
| $NaHCO_3$ | 0.695 |
| KBr | 0.201 |
| $H_3BO_3$ | 0.101 |
| $SrCl_2$ | 0.025 |
| NaF | 0.003 |

### 2.4.5 Wet-Dry Cycling

During exposure of in service components there is considerable fluctuation in the relative humidity. The fluctuating periods of high and low RH during wet-dry cycles means that when RH falls below the ERH of a salt drying of the surface will take place, but following a rise in RH surpassing the DRH, re-wetting of the metal surface

can take place. During dry periods when no solution is present on a surface, corrosion will not proceed. However, during wetting and drying, peaks in corrosion rate may be observed due to the presence of highly concentrated solutions. On pure Al surfaces under a thin electrolyte layer, the corrosion rate increased during early stages of surface wetting [160]. Similarly, on stainless steel surfaces, current was observed to abruptly increase during the early stages of drying before dropping to almost zero [157], during potentiostatic measurements under droplets.

Larignon [95] used repeated immersion testing to simulate cyclic exposure of AA2024 under NaCl solutions.. Further it was observed that during cyclic testing there was no significant increase in the observed maximum depth of localised attack, but there was an increase in the number of grain boundaries attacked, when compared to samples left constantly immersed.

### 2.4.6 Atmospheric Corrosion Studies on AA2024

Mechanisms of localised corrosion under atmospheric corrosion of AA2024 follow many of the same principals as under full immersion conditions. However, there are some differences with regard to initiation and propagation which take place under the highly concentrated solutions found during atmospheric exposure of AA2024.

Atmospheric corrosion work on AA2024 was initially focussed on analysis of exposed coupon samples: Sun [111] measured weight loss of clad AA2024 and bare AA2024 samples. It was determined that coastal samples experienced greater weight loss, for

both materials than urban samples. In addition increased levels of chloride were found on coastal samples.

Cheng [161] used EIS to measure the influence of electrolyte layer thickness on the oxygen reduction kinetics under thin electrolyte layers of 3% NaCl solution. The measured corrosion rate was greatest under a layer of thickness ~100 µm during early stages of exposure; after prolonged exposure a shift in maximum rate was observed with an increase in layer thicknesses up to ~170 µm. It suggested that for layers 100-200 µm in thickness, the rate determining step is the oxygen diffusion, but for layers 50-100 µm, the formation of a layer of aluminium hydroxide inhibits oxygen reduction sites at the metal surface.

Atmospheric droplet studies on AA2024 have been carried out in more recent years by King [96, 109] and Knight [92, 106, 162]. Knight [92, 106, 162] used µCT to study growth of localised corrosion fissures during atmospheric exposure of AA2024 pin samples in three dimensions. Time-dependent measurements were made on localised growth kinetics, and it was determined that IGC was most rapid in the L direction of the alloy. RH was shown to influence the development of localised corrosion under NaCl solution droplets, such that high RH increased the amount of corrosion.

King [96, 109] used FIB SEM to study corrosion of AA2024 under ocean water droplets. Subsurface attack of S-phase particles at the matrix/particle interface was observed along the propagating corrosion front. Furthermore, precipitation of a layer of aluminium hydroxide was observed both at the metallic surface and along the attacked grain boundaries.

### 2.4.7 Experimental Testing Methods in Atmospheric Corrosion

Atmospheric testing has been carried out using coupon exposure and lab-based experimental testing. A2024 coupons have been used to determine mechanisms operating during true atmospheric exposure conditions, in order to provide data to design accelerated lab based exposure tests [111, 163, 164].

Accelerated lab based exposure testing has been used to simulate atmospheric exposure. Several experimental methods have been employed to deposit droplets or thin electrolyte layers onto samples and to quantify localised corrosion. The most common method has been the placing of droplets onto a metallic surface by means of syringes or micro-pipettes [96, 136, 145, 151, 162, 165-167]. In these experiments, droplet volume, composition and concentration can be carefully controlled. Less accurate but also commonly employed has been salt spray testing [168], whereby large surfaces can be covered, however, less accuracy is possible in terms of controlling salt deposition densities and exact surface area coverage. More recently, modified inkjet printers have been used to control salt deposits on metal surfaces [169-171].

Quantification of atmospheric corrosion has been undertaken using different methods over the past few decades, and can be broken down into two categories, either mechanical/optical inspection or electrochemical testing. Traditionally mass loss or gain measurements were suggested as a good means of quantifying severity of localised attack. Microscopy both optical and SEM [96, 109, 169] have been used to observe localised corrosion behaviour. In addition, recently, µCT has been used to observe the development of localised attack [92, 106, 172]. Electrochemical methods

that have been used include impedance under thin electrolyte layers [161, 173-176], scanning Kelvin probe[146, 149], multi electrode arrays[150] and micro-capillaries.

## 2.5 Synchrotron Microtomography

### 2.5.1 Introduction

Tomography has its roots in medical applications but over the past couple of decades advances in technology have made it possible to make high resolution measurements in a variety of different application areas, including materials science. Measurements can be made using both lab-based and synchrotron X-ray sources.

### 2.5.2 Principles of Synchrotron X-Ray Microtomography (µCT)

Microtomography (µCT) requires a series of radiographs (x-ray images) to be taken of a sample at different rotation angles, which are reconstructed to create a 3-D model. Reconstruction of the radiographs is carried out using a mathematical algorithm. Data are obtained in a non-destructive manner which means that repeated measurements can be made on the same sample/object.

µCT using synchrotron radiation provides a similar resolution to that seen for lab based sources, e.g. sub-micron, but with the added benefit of a greatly reduced time for data collection. This is due to the extremely high flux of the X-ray beam which is generated, this means that the intensity of the X-rays produced are significantly greater than those possible from lab based sources[177]. A further advantage of synchrotron radiation is that either white or monochromatic beam can be generated, whereas lab based x-ray sources must use white beams.

The higher flux for synchrotron sources leads to a reduced acquisition time for a complete tomographic scan, so that it is possible to make time-dependent measurements at a rate which makes true in-situ experiments possible in an accurate manner [178]. In addition imaging at synchrotron facilities offers the possibility of enhanced phase contrast due to the improved tuneability of the x-rays[177, 178].

Radiation at third generation synchrotrons is typically generated in the following manner; electrons are injected into a linear accelerator (linac) via an electron gun. The linac accelerates the electrons through into a booster ring where they are further accelerated prior to insertion into the main storage ring of the synchrotron facility. Within the storage ring are a series of high powered bending magnets which help to focus the electron beam along its ideal orbit in order to achieve the ideal beam energy. However, there will naturally be fluctuations from both the ideal energy and orbit as they are focussed round the storage ring, it is these small fluctuation and the larger changes in direction of the beam around the ring which result in changes in the electro-magnetic field [179].

It is this radiation which is the source of x-rays used to make experimental measurements by users at the beamline end-stations. As the x-ray radiation in the form of photons escapes tangentially to the ring, beamlines are placed in an according arrangement around the storage ring. X-rays are focussed along the beamline to the experimental hutch, where the sample is located. A typical layout for a third generation synchrotron facility can be seen in Figure 2.9, the path which the synchrotron light follows is outlined, from electron injection through to the experimental hutch on a beamline.

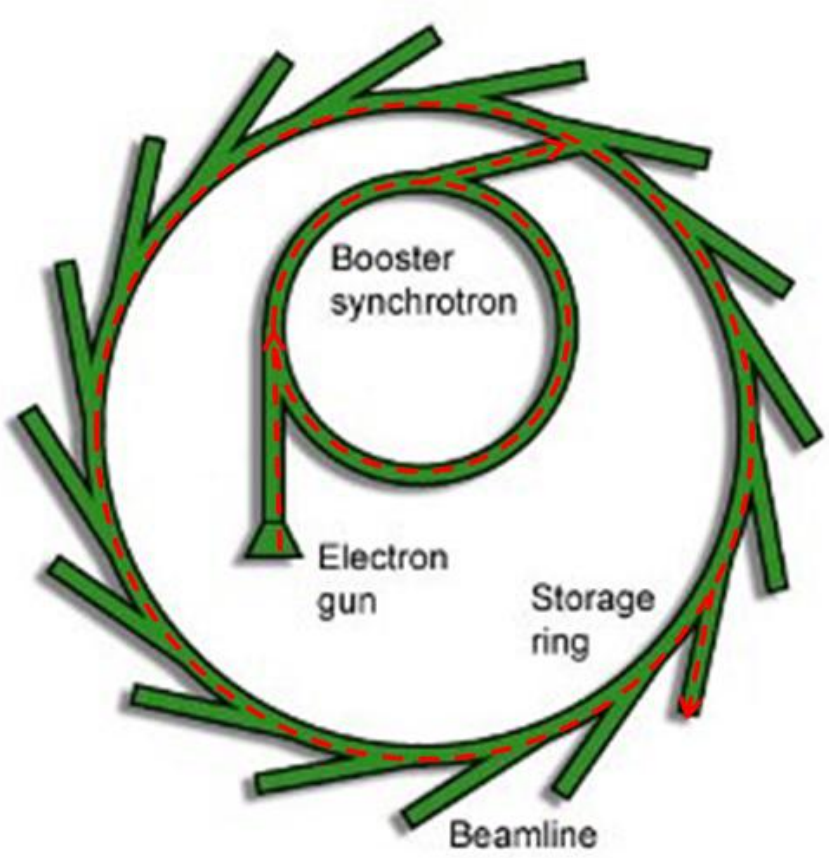


**Figure 2.9 - Typical layout of third generation synchrotron facility, with path of electrons from source to sample shown**

As the X-ray beam passes through the sample a certain intensity of the x-rays is attenuated, the level of which is determined by the density of the sample, with each material being attributed a specific absorption coefficient. The specific absorption coefficient of a material as a function of its thickness can be calculated using the *Beer-Lambert law* of attenuation, Equation 2.5.1. Where; $I_o$ is the initial X-ray intensity, $I$ is the final X-ray intensity following attenuation, $d$ is sample thickness, and $\mu$ is absorption coefficient of the material[180, 181].

$$\frac{I}{I_o} = \exp(-\mu d) \qquad \textbf{Equation 2.5.1}$$

A scintillator placed behind the sample collects the x-rays which have not been fully attenuated by the sample, and converts them into visible light. The image is magnified by an objective lens, and captured with a high speed CCD camera. The image is known as a radiograph, and example of is shown in Figure 2.10. In order to generate the 3-dimensional model of the sample, a series of radiographic projections are captured over rotation steps from $0^{o}$-$180^{o}$. Radiographs are reconstructed via methods such as a filtered-back projection algorithm or a gridding reconstruction algorithm [182]. Figure 2.11 illustrates how measurements are made at a beamline.

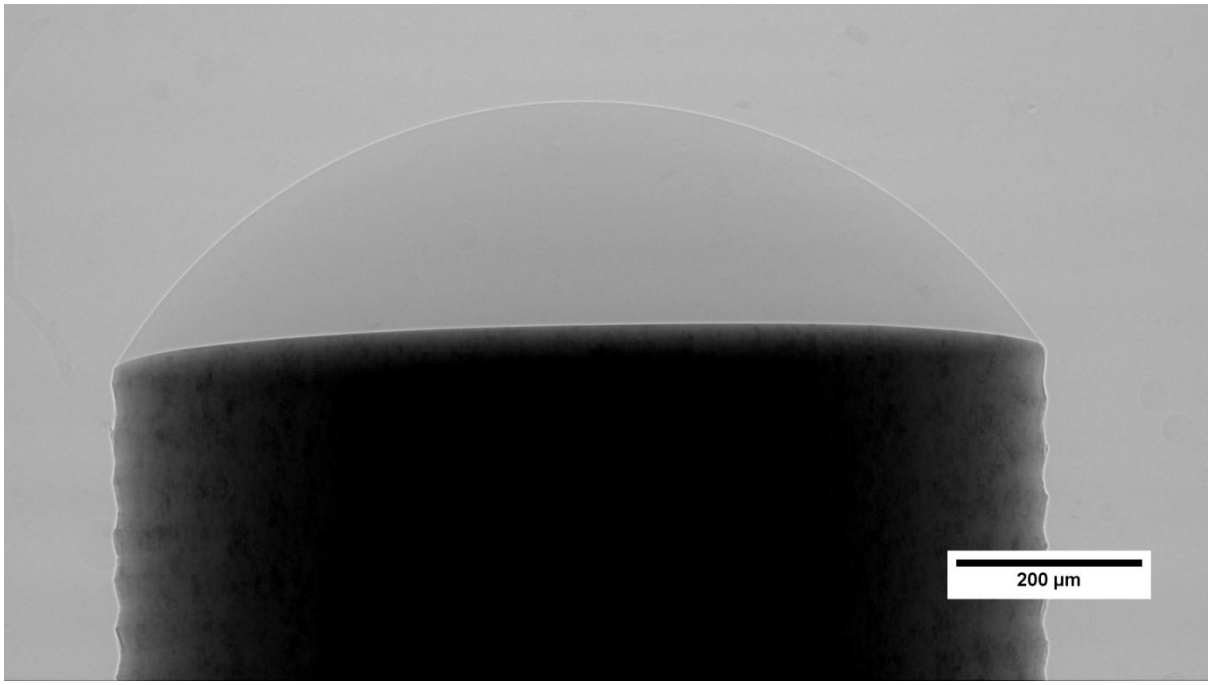


**Figure 2.10 - Radiograph obtained during synchrotron µCT measurements, showing a droplet on the surface of an AA2024 pin during atmospheric corrosion measurements**

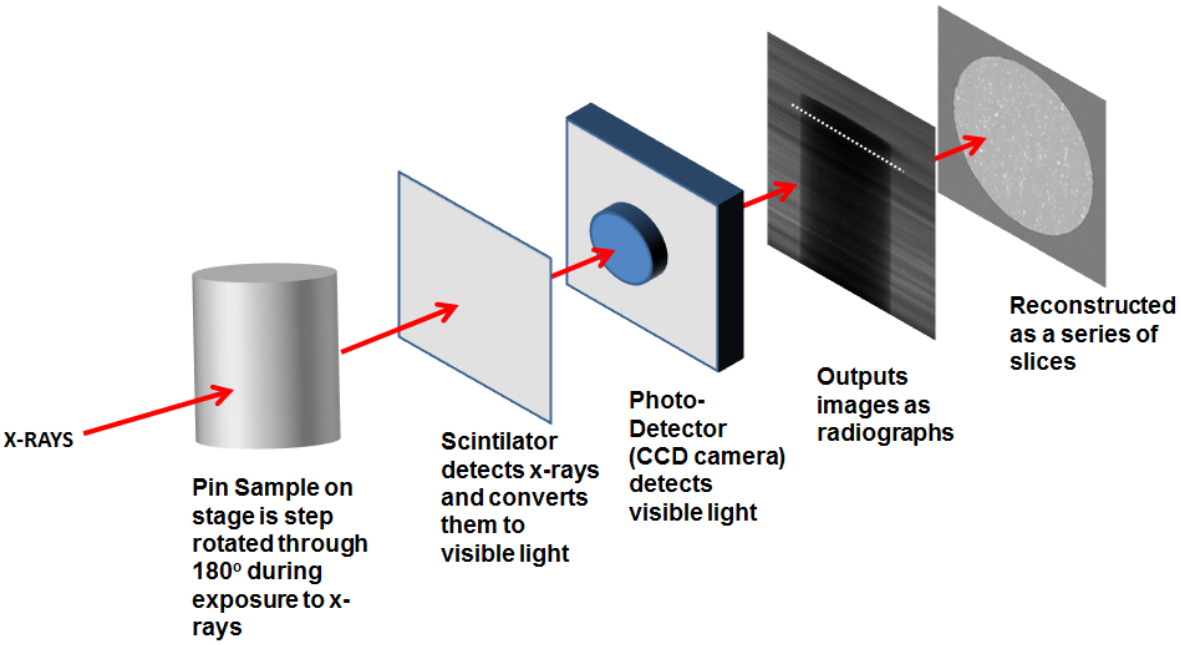


**Figure 2.11 – Schematic diagram illustrating data collection in synchrotron µCT**

### 2.5.3 Limitations of Synchrotron µCT

As with most experimental techniques there are certain limitations or drawbacks which must be considered during interpretation of results. In the case of synchrotron µCT the most common limitations of the technique which must be considered are; sample size and resolution limits, beam-hardening, ring artefacts and hydrolysis of solutions. Sample size and resolution are a limitation for some applications, as there is a trade of in the quality of the resolution attainable and the sample size which can be used, generally this is to the effect that the smaller the sample the better the resolution. This is further dependent on the density of specific materials as higher density materials require smaller sample sizes in order to achieve the maximum resolution limits.

### 2.5.4 Application in Corrosion Science

Owing to the possibilities offered for non-destructive evaluation of dynamic processes occurring internally in a sample in a real time (in-situ) manner, synchrotron µCT promotes itself as a very attractive technique in materials science. Generalised reviews of the applications of synchrotron µCT in the discipline of materials science research has been undertaken successively over the past couple of decades [183-188],with applications including 3D elemental mapping, stress mapping and most relevant to this work in-situ monitoring of the development of corrosion.

Micro-tomography has been used in corrosion studies for several different materials, and has proved successful in providing 3D information into the growth kinetics of corrosion attack for a number of materials. In-situ evolution of pitting on stainless steel (for alloys 304L and 316L) has been successfully observed[172, 189], as has the development of pitting corrosion and more generalised attack for magnesium alloy WE43[190]. In-situ work has also been carried out on aluminium alloys under immersion in NaCl solution [107, 108, 191], and using simulated atmospheric NaCl droplets [92].

Fox [108] employed µCT to study corrosion of FSW (friction stir welded) AA2024-T351, under immersion in 0.6 M NaCl solutions. It was shown that penetration was greater in the L and T directions than for the S direction. It is also suggested that development of IGC fissures could be divided into two stages, a rapid initial vertical

penetration of the metal, followed a by a widening of the fissures over time. Ghosh[191] similarly employed μCT to quantify IGC growth rates under stressed conditions. Quantitative growth rates were determined for IGC, and a suggestion of a limiting maximum depth attack in the L direction within the alloy is made.

### 2.5.5 In-Situ Atmospheric Corrosion Measurements

To date there has been relatively little work using x-ray micro-tomography or synchrotron x-ray micro-tomography to monitor the evolution of corrosion during atmospheric exposure of aluminium. Knight and co-workers have used both in-situ and ex-situ tomography to study the development of IGC within AA2024 over a prolonged period of time. In-situ work showed that it was possible to make time dependent measurements during simulated atmospheric corrosion[92], whilst ex-situ work endeavoured to provide more quantifiable results[106]. It was suggested that for AA2024 there is an effect of RH on the rate of corrosion, and that IGC would grow fastest in the longitudinal direction (perpendicular to the direction of rolling). In addition it is suggested that despite reaching a maximum fissure depth IGC fissures may continue to propagate along grain boundaries [92, 106].

Use of this technique in atmospheric corrosion research is of an added benefit as it is possible to monitor evolution of other relevant atmospheric interactions. For example changes in shape of droplets as a function of time, and the evolution of hydrogen during localised corrosion. Visualisation of droplets, hydrogen, metal and air simultaneously is possible due to the difference in x-ray attenuation associated with each material.

## 2.6 Summary

Much work has previously been undertaken on the localised corrosion of AA2024 under immersion conditions. Owing to its complex microstructure, development of localised corrosion takes place rapidly. Recently a shift towards studies of the influence of atmospheric variables such as RH, exposure time, temperature and salt type have begun to be explored using droplet studies. However, relatively little work has been undertaken under these atmospheric conditions to date on AA2024.

Atmospheric corrosion is dependent on environmental variables including; temperature, RH, salt type and exposure time. A gradual understanding of complex chemistry and processes involved is taking place on several metallic substrates.

That which has been carried out indicates mechanisms operating are similar to those observed for full immersion testing, with regards to localised attack of metal. However, a further understanding needs to be developed on localised corrosion behaviour on AA2024 surfaces exposed to atmospheric droplets, and the influence of CDD, salt type and exposure to wet-dry cycles on the corrosion rate. Further little work has considered the behaviour of droplets on AA2024 surfaces, including processes such as secondary spreading and its influence on corrosion rate. As such the development of in-situ techniques such as micro-tomography have enabled continual non-destructive evaluation of samples to be carried out.

Through a combination of in-situ μCT and lab based droplet measurements the aim of this project was to develop a better understanding of the influence of atmospheric exposure on the development of localised corrosion in AA2024.

# 3 EXPERIMENTAL METHODS

## 3.1 Material

AA2024-T351 10 mm plate was supplied by Aero Metallic; the composition is given in Table 3.1.

**Table 3.1 – Composition of AA2024 plate as supplied by Aero Metallic**

| Element | Wt % | Element | Wt% |
|---|---|---|---|
| Al | 90.7-94.7 | Mn | 0.3-0.9 |
| Cr | Max 0.1 | Si | Max 0.5 |
| Cu | 3.8-4.9 | Ti | 0.15 |
| Fe | Max 0.5 | Zn | Max 0.25 |
| Mg | 1.2-1.8 | | |

The nominal compositions of AA3004 and AA5083 are shown in Table 3.2. These metals were used as a control for the presence of magnesium during spreading experiments.

**Table 3.2 – Nominal composition of AA3004 and AA5083[16, 31, 192]**

| | |
|---|---|
| AA3004 | Al-97.8%, Mn-1.2%, Mg-1% |
| AA5083 | Mg 4-4.9%, Mn 0.4-1%, Si 0.4%, Fe 0.4%,Zn |

| | |
|---|---|
| | 0.25%, Ti 0.15%, Cu 0.1%, Cr 0.05-0.25%, Al-balance |

## 3.2 Sample Preparation

### 3.2.1 Laboratory Samples

Plate samples were cut to size for lab tests using a Buehler Isomet 4000, with silicon carbide cutting blades, to minimise the introduction of mechanical defects into the metal. Plates were cut into samples of dimensions length ~ 26 mm, width ~12 mm and height ~6.5 mm. For microstructural characterisation, samples were hot mounted in conductive Bakelite. Surface preparation was carried out by grinding using wet/dry discs, to a finish of 4000 grit, prior to a final polish down to 0.04 µm using a colloidal silica solution. Grinding was carried out using an oil based lubricant (DP-Brown, supplied by Struers), to avoid any potential influence of water on the sample surface. Following each stage of the grinding process surfaces were cleaned using methanol to remove any impurities and to degrease.

Samples for atmospheric corrosion experiments were primarily left un-mounted, and were either ground/polished to 4000 grit or 1µm, depending on the test conditions. Prior to application of droplets samples were left to passivate in sealed desiccators for a period of 1 hour.

### 3.2.2 µCT Samples

µCT samples (1 mm diameter pins) were machined by from plate samples; orientation with respect to the plate is shown in Figure 3.1 such that exposure surface was aligned perpendicular to the direction of rolling, L direction. Pin sample

dimensions are shown in Figure 3.2. Prior to exposure, samples were immersed in nitric acid (~70%, Fisher Scientic) for 2 minutes to thicken the surface oxide layer in order to prevent unwanted crevicing on the pin side. The exposure surface was then ground on wet/dry paper to a finish of 4000 grit, degreased in ethanol and allowed to passivate for 1 hour.

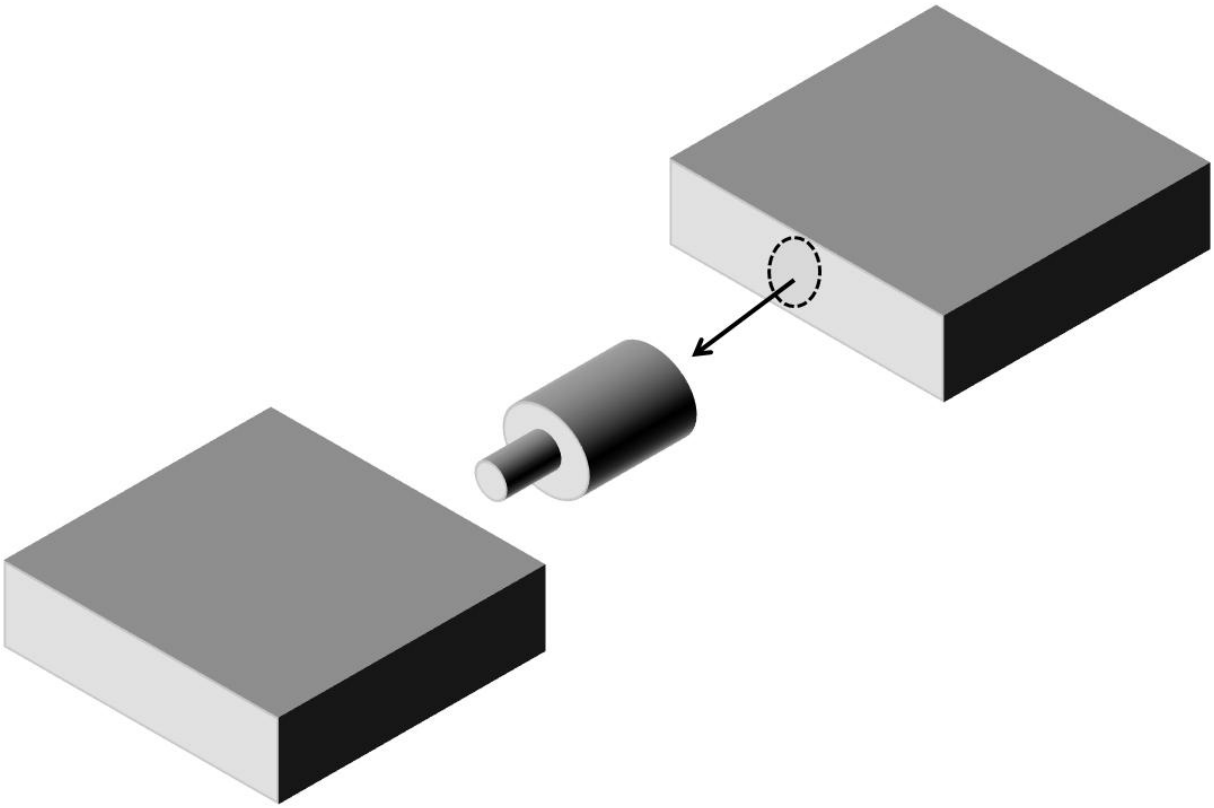

**Figure 3.1 – Orientation of pin sample with respect to plate from which it was cut**

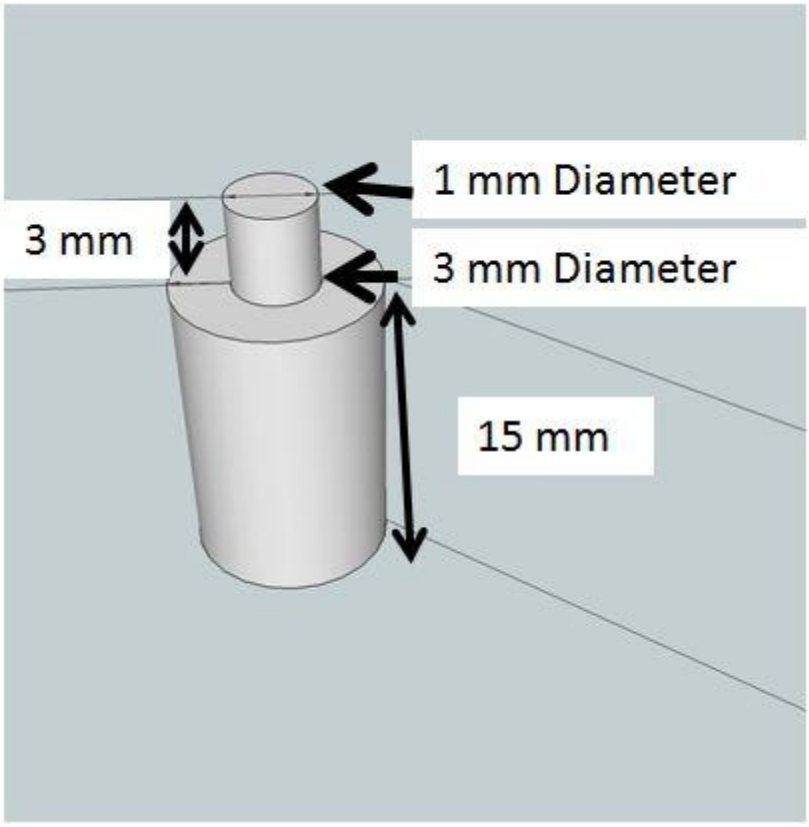


**Figure 3.2 - AA2024-T351 dimensions of pin samples for µCT experiments**

### 3.2.3 Preparation of Salt Solutions

Laboratory-grade salts were stored in an environment of ~0% RH, in the presence of silica gel, for a minimum period of 24 hours before being mixed with de-ionised water to produce solutions for experiments to ensure accurate weighing.

Substitute ocean water was prepared in accordance with ASTM standard D114-98, “Standard Practice for the Preparation of Substitute Ocean Water” [159]. The composition of substitute ocean water prepared according to this standard can be seen in Table 3.3.

**Table 3.3 - Composition of Substitute Ocean Water, ASTM Standard Practice for Preparation of Substitute Ocean Water[159]**

| Salt Compound | Concentration (g/L) |
|---|---|
| NaCl | 24.53 |
| $MgCl_2$ | 5.20 |
| $Na_2SO_4$ | 4.09 |
| $CaCl_2$ | 1.16 |
| $NaHCO_3$ | 0.695 |
| KBr | 0.201 |
| $H_3BO_3$ | 0.101 |
| $SrCl_2$ | 0.025 |

### 3.2.4 Droplet Deposition

Droplet deposition was carried out by means a Hamilton HPLC 7000 series micro-syringe, capable of dispensing solution droplets down to an accuracy of ~0.1 µl. Solution droplets were aspirated and dispensed using a cheney adaptor (Hamilton Company) to allow a fixed volume to be maintained. A schematic of droplets deposited onto a plate surface is shown in Figure 3.3, and onto a pin surface Figure 3.5.

**Figure 3.3 - Schematic of droplets deposited onto an AA2024 plate sample**

### 3.2.5 Maintenance of Relative Humidity

Maintenance of RH within simulated atmosphere was achieved by means of ASTM E104-02, “Standard Practice for Maintaining Constant Relative Humidity by Means of Aqueous Solution”[159]. Preparation was carried out by adding de-ionised water in small quantities to salt until a small quantity of free solution remained, quantities were dependent upon test chamber used. Saturated solutions used as part of this work are outlined in Table 3.4.

**Table 3.4 - Salt type and associated fixed environmental RH for saturated salt solutions, ASTM E104-02 [127]**

| RH (%) | Salt Type | Effective Temperature Range($^{o}$) |
|---|---|---|
| 12 | Lithium Chloride (LiCl) | 5 – 80 |
| 23 | Potassium Acetate ($CH_3COOK$) | 10 – 30 |
| 33 | Magnesium Chloride ($MgCl_2$) | 5 – 80 |
| 43 | Potassium Carbonate ($K_2CO_3$) | 5 – 30 |
| 59 | Sodium Bromide (NaBr) | 5 – 80 |
| 70 | Potassium Iodide (KI) | 5 – 80 |
| 75 | Sodium Chloride (NaCl) | 5 – 80 |
| 85 | Potassium Chloride (KCl) | 5 – 80 |
| 98 | Potassium Sulfate ($K_2SO_4$) | 5 – 50 |

Saturated salt solutions in Table 3.4 were tested for their accuracy compared to the given ASTM values in a laboratory environment, using OMEGA-USB2 data loggers and ThermaData humidity-Temperature Loggers, and were found to correspond closely to the given values. Data logger plots for the salt types used during this experiment can be found in Appendix 10.1.

### 3.2.6 Cell Design

Experimental cells for lab based exposure were constructed from modified cell culture bottles, with a resin moulded in, to allow saturated salt solution to be placed in two wells either side of raised sample. Top of the cell was sealed with a glass cover, to allow in-situ imaging to be carried out on the droplet, an example of the cell used can be seen in Figure 3.4. For larger numbers of plate samples exposed

simultaneously, sealed desiccators were employed using saturated salt solutions to maintain the RH of the simulated atmosphere.

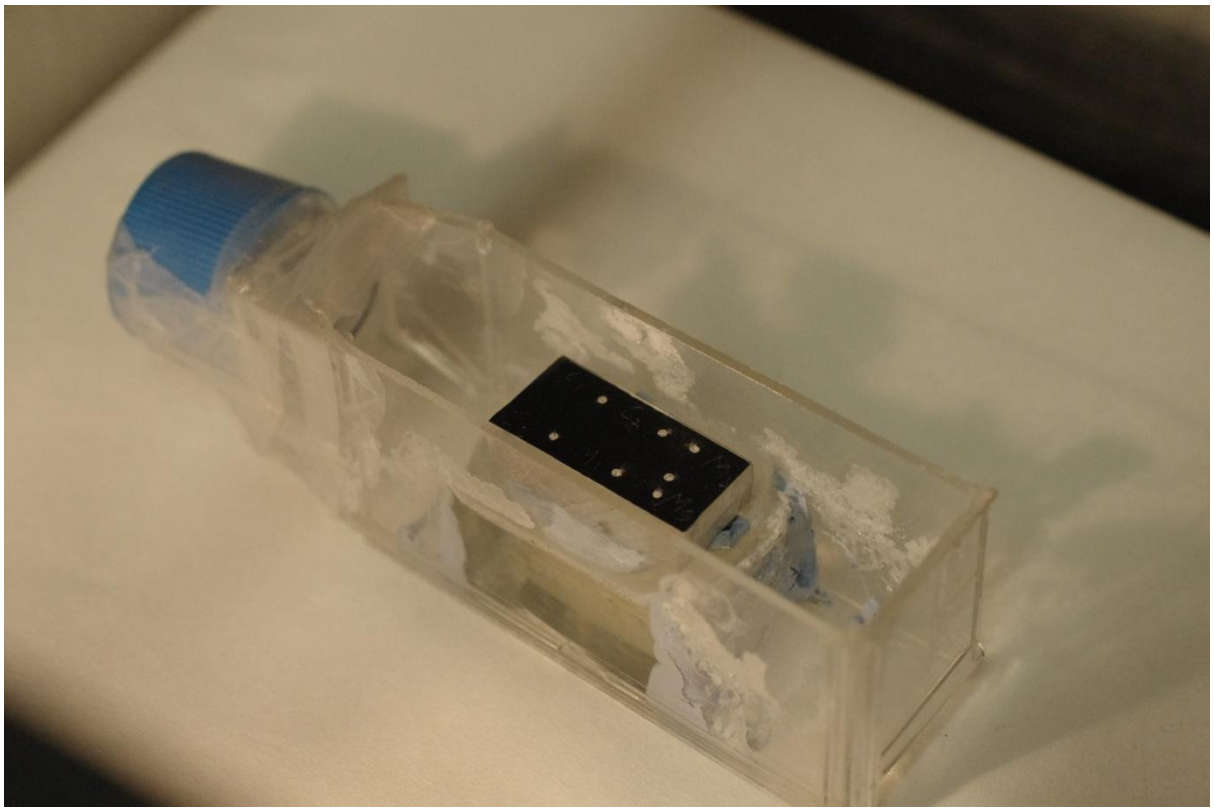

**Figure 3.4 - Atmospheric cell used during lab based exposures, with glass lid for in-situ imaging to be carried out**

Design of the experimental cell used for the micro-tomographic measurements, was based on a modified combination of those used by Connolly et al.[107], and Knight et al[92]. A schematic of the cell can be seen in Figure 3.5 and an image of the sealed cell is shown in Figure 3.6. A filter paper soaked in saturated salt, and containing solid crystallites was placed inside silicone tubing (versilic) with internal diameter of 3 mm, which was then placed over the outer diameter of the metal pin, and an aluminium stopper was placed in the end. For a known chloride density on the tip of the pin, the height of the droplet was an indication of the relative humidity within the

cell.  Tests showed that the droplet height, and thus relative humidity could be maintained for up to a week.

During wet-dry cycling, the tubing was replaced with one containing filter paper with a different saturated salt solution, or a tube containing dried silica gel spheres to achieve “0% RH” (probably ~3-5% RH as measured in larger cells into which humidity loggers could be placed.

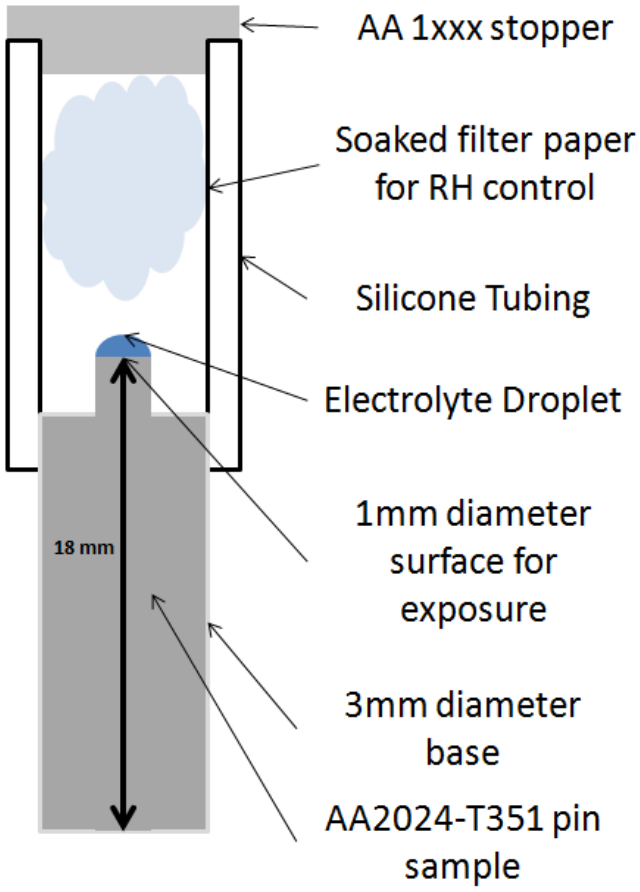


**Figure 3.5 - Atmospheric cell for micro-tomography measurements**

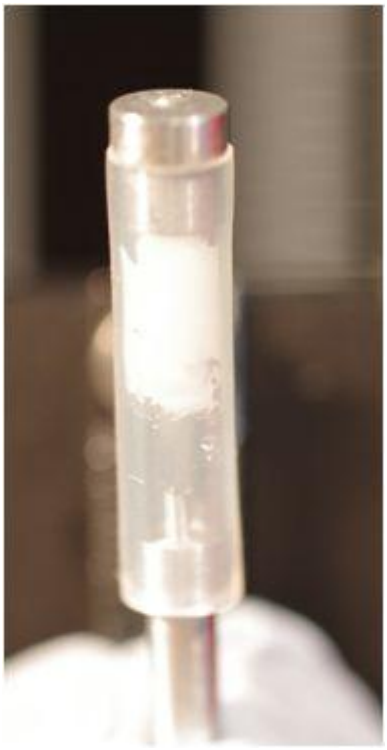

**Figure 3.6 - Sealed tomography cell prior to in-situ measurements**

### 3.2.7 Removal of Corrosion Product

Salt deposits were cleaned from sample surfaces by immersion in methanol in an ultrasonic bath, for a period of 2 minutes. Corrosion product was removed by means of immersion in nitric acid for ~2 minutes, according to ASTM Standard G46-96[193]. Any remaining products could be removed by fine polishing of 0.04 µm (procedure the same as for microstructural characterisation, using colloidal silica solution) for a period of 10 seconds.

## 3.3 Measurements

### 3.3.1 µCT Measurements

Synchrotron micro-tomography was carried out at the Swiss Light Source (SLS), on the dedicated tomography beamline TOMCAT [194]. An X-ray energy of 21.9 keV was selected by a double multi-layer monochromator. For image detection, the x-rays were converted to visible light by a 20 µm LuAg scintillator, and the corresponding image was magnified onto the detector by an optical system with 10x magnification. In combination with the physical pixel size of the employed detector (pco.2000, PCO AG, Kelheim, Germany) led to an effective pixel size of 0.74 µm for each projection or radiograph.

In total 1200 projections were acquired over $180^{o}$ rotation with an exposure time of 150 ms for each radiograph. Raw projections (radiographs) were collected as .tif image files. Raw projections were reconstructed using a gridding method [182], developed at TOMCAT.

### 3.3.2 Lab Based Measurements

A Leica DFC 420 light microscope was used to take optical images of lab samples during lab base droplet exposures. Microscope was fitted with objective lenses over the range 25x to 500x, with additional capability for a 2x insert for a maximum magnification of 1000x.

Scanning electron microscopy (SEM) was used to carry out visual inspection of samples and for elemental analysis by means of energy dispersive x-ray (EDX). SEM was carried out using a combination of four machines; imaging was carried out using

a Phillips XL-30, JOEL S4000, JOEL 6060 and JOEL 7000 machines. Elemental analysis was undertaken on Phillips XL-30, JOEL 6060 and JOEL 7000 machines fitted with Oxford Instruments EDX systems and INCA analysis software. Both imaging and EDX were undertaken using an accelerating voltage of 15.0 keV, using a working distance of 10 mm.

### 3.4 Calculation of Equilibrium Concentrations, Heights and Volumes

Calculation of the equilibrium concentration ($C_{eq}$) was made using an equation proposed by Wheeler[122]:

$$RH = \left(1 - \frac{xM}{\left(xM + \frac{1000}{18}(1 - yM)\right)}\right) * 100 \qquad \textbf{Equation 2.4.1}$$

Where M = molar concentration of salt, x = number of ions in solution, and *y* can be calculated using the equation below:

$$y = \frac{(\frac{1}{\rho})M}{1000} \qquad \textbf{Equation 2.4.2}$$

Where ρ = Density and M = Molecular Weight.

Following calculation of $C_{eq,}$ theoretical predictions of the equilibrium volume ($V_{eq}$) and equilibrium droplet height ($DH_{eq}$) were made. Calculation of theoretical $V_{eq}$ was made using the equation proposed by Li et al[139] rearranged to the form in equation 3.3.3. Initial droplet volume was fixed at 0.2 µl, and initial concentration was controlled depending on desired CDD.

$$V_{eq} = V_o(\frac{C_{eq}}{C_o}) \qquad \textbf{Equation 3.3.1}$$

Where $V_{eq}$ is the calculated theoretical equilibrium volume, $V_o$ is original volume, $C_{eq}$ is equilibrium molar concentration (M) and $C_o$ is original solution molar concentration (M). This method of calculating $V_{eq}$ was used during work on stainless steel by Mi [172], and was shown to be quite accurate when making a comparison against measured droplet $V_{eq}$.

Calculation of the predicted height was made using a combination of equation 3.3.4 and equation 3.3.5. The former used by Li et al[139] and the latter simply being the formula for an ellipse. During calculation of the maximum predicted height the following assumption were made, (1) droplet is modelled as a spherical cap or an ellipse, (2) for the pin samples used the surface area of the cap base is constant at 0.0025cm$^2$.

$$V = \frac{1}{6}\pi h_o(3r_o^2 + h_o^2) \qquad \textbf{Equation 3.3.4}$$

$$V = \frac{4}{3}\pi r^2 h \qquad \textbf{Equation 3.3.5}$$

Where: V is volume, h is height and $h_o$ is original height.

Droplet volume and height were measured experimentally and compared to the predicted values. Droplet heights were measured from radiographs like those in Figure 4.6 for tomography samples, or from optical images of droplets taken in-situ. Height was measured using FIJI image analysis software[195]. Volume was measured by two means for tomography samples. (1) a cumulative sum of subsequent surface areas for the whole height of the droplet, (2) through application of thresholding to the reconstructed data set and use of a voxel (3-D pixel) counting algorithm. Agreement between the two methods was observed to be good, and as

such the former method was applied to the measurement of optical images, as segmentation in 3-dimensions was not possible.

## 3.5 Data Analysis

### 3.5.1 Tomography Data

Analysis was carried out using a combination of software packages, primarily FIJI/ImageJ software[195] (freeware) and Avizo (VSG) were employed for data processing and measurement. Data were reconstructed in .DMP image format, specific to TOMCAT at SLS, as such conversion to .tif image format was carried out first, using the script written for FIJI, appendix 10.3. Script requires input of image file location, and desired brightness and contrast for the output reconstruction image file.

Converted reconstruction images were then able to be opened using FIJI for initial visualisation and analysis. To reduce memory intensive processes associated with the large data set size, unwanted regions were cropped and combined image stack was outputted as an Avizo mesh file.

Mesh files were loaded into Avizo and a box filter was applied to better separate greyscale values of individual pixel regions. Prior to quantification of data, segmentation or partitioning of image stacks was undertaken, to generate the quantifiable data groupings. During segmentation pixels are essentially “labelled” as wanted or unwanted according to their specific greyscale values. Greyscale values are dependent on the specific density of each material, higher density materials show up brighter, such as the copper rich intermetallic particles. Segmentation process of an IGC fissure in reconstructed dataset of AA2024 pin sample is shown in Figure 3.7.

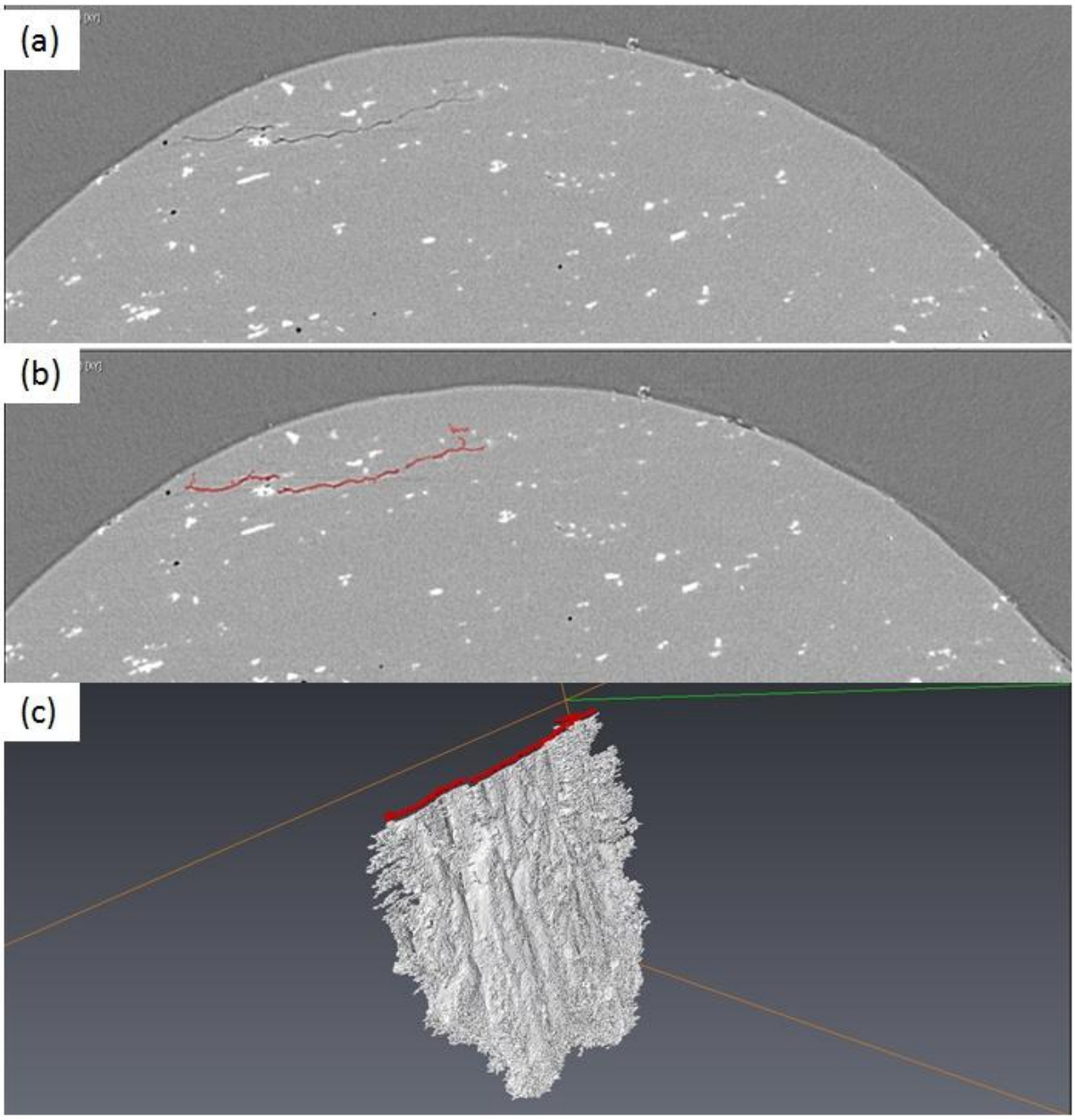


**Figure 3.7 - Segmentation of tomographic data set, (a) fissure is visible top left of the tomographic slice, (b) following "labelling" of the fissure as material interior, (c) labelled fissure section as it forms part of the completed segmentation of the fissure volume**

Following segmentation of datasets, the segmented regions were counted for the number of voxels (3-dimensional pixel) contained within the region. Effective pixel size for datasets was 0.74 µm, producing an effective voxel volume of 0.405 $\mu m^3$.

Voxel counting algorithm was contained within the material statistics module of Avizo software. In addition voxels were counted using a FIJI plugin file, to establish a test for consistency of the Avizo method. For analysis using the FIJI method over and under thresholding of the datasets was performed for a further method of consistency.

Fissure depth was measured using FIJI software vertically reconstructed sections were placed into a series of images. Point of maximum depth was initially determined by eye, then a line such as that shown in Figure 3.8, was marked on the dataset and comparisons of the vertical sections either side were made to ensure that the point of maximum depth had truly been obtained.

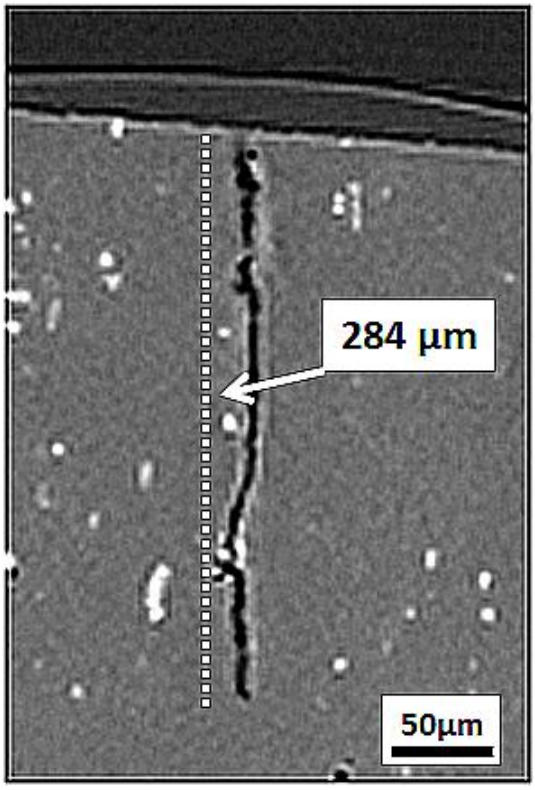


**Figure 3.8 – Example of depth measurement method used for analysis of tomography samples**

### 3.5.2 Lab Based Analysis

#### 3.5.2.1 Droplet Imaging

During lab based exposure sample surfaces were imaged immediately following application of droplets, and at the end of exposure period, or continually during in-situ time-lapse experiments. Surface area coverage of the droplet was measured using FIJI. Image of droplet on surface was thresholded, shown in Figure 3.9, prior to application of an area counting algorithm on FIJI software. Initial CDD was calculated, using image of droplet on deposition, and changes in droplet shape and surface area were measured. Simulated atmospheric exposure was carried out in one of the previously described cells. Initial CDD was calculated using the following equation:

$$Initial\ CDD\ (\frac{\mu g}{cm^2}) = \frac{V\ x\ [M] x\ (n\ x\ 35.45)\ x\ 10^6}{Droplet\ Area\ Measured\ (cm^2)}$$

Where V is volume in litres and M is molarity in mols.

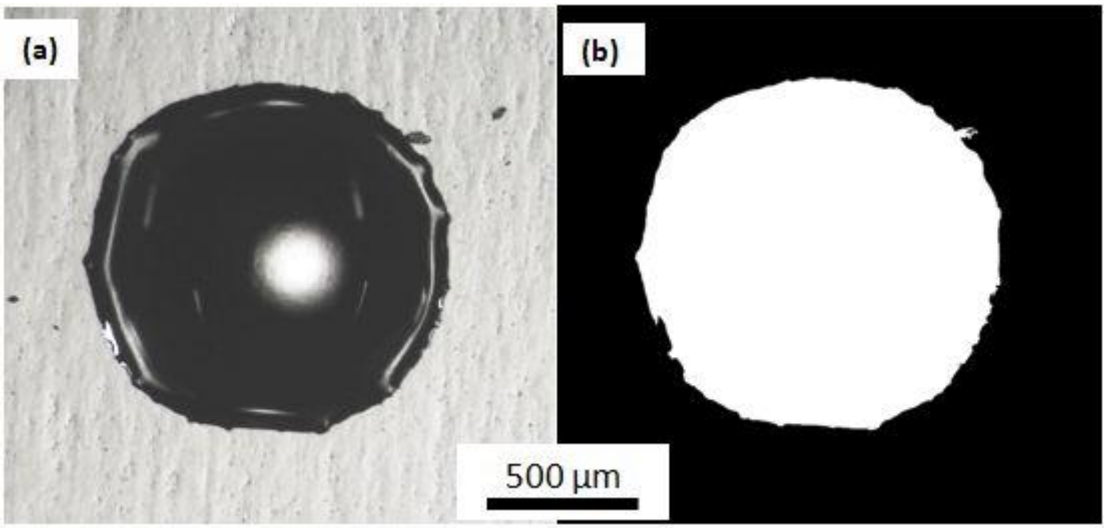


**Figure 3.9 - Droplet on deposition onto AA2024 plate surface (a), and following thresholding for calculation of CDD (b)**

Following the end of exposure time, droplets were dried in a desiccator with RH set at ~0%RH. EDX analysis was carried out on some dried deposits, to determine elemental distribution. Sample surface was again imaged by OM and SEM following removal of corrosion product, prior to sectioning. No observed weight loss occurred as a result of immersion in nitric acid, nor was any surface attack observed.

#### 3.5.2.2 Measurement of Localised Corrosion Depth

Two methods were used to measure maximum depth of localised corrosion in plate samples, firstly by cross sectional section of samples [193], and secondly by the method described here after, the latter was determined to be more accurate. Final depth measurements were made by measuring thickness of sample following removal of corrosion products by means of a micrometer (+/- 1 µm). A series of successive polishing steps were carried out on sample surface using a 1 µm polishing cloth, and a visual inspection and height measurements were made

following every ~10-15 seconds on the polishing wheel. This process was repeated until no further signs of localised corrosion were visible at the sample surface, giving the final measured depth for lab samples.

#### 3.5.2.3 Measurement of Secondary Spread Zones

Measurements on secondary spread regions were made using FIJI/Image J image analysis software. Optical microscope images from the end of exposure were loaded into FIJI/Image J and radius was measured from the centre point of the droplet at increments round the circumference to the outer edge of the spread zone, and an average was taken for each droplet. An example is shown in Figure 3.10.

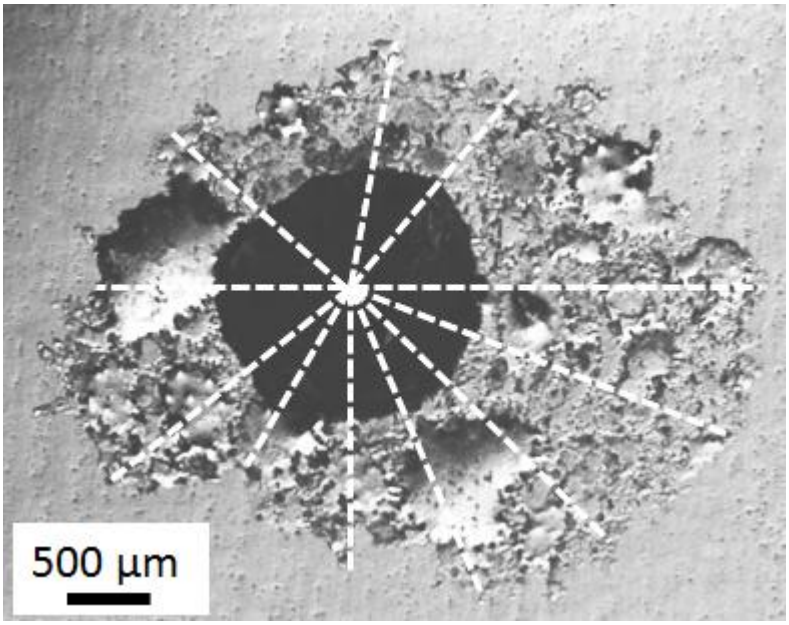


**Figure 3.10 – Measurements of spread region on AA2024 samples during atmospheric exposure**

#### 3.5.2.4 Localised Corrosion Measurements on Sample Surfaces

Following removal of corrosion product from sample surfaces by means of immersion in nitric acid, and a light polish of 0.04 µm to reveal localised corrosion damages at the surface. An example of a surface following removal of corrosion product (left) and following thresholding (right) is shown in Figure 3.11. Following thresholding application of an area calculating script was used on FIJI/Image J in order to count the number of pixels making up the localised corrosion sites. Pixel number was then scaled to provide surface area coverage in $mm^2$.

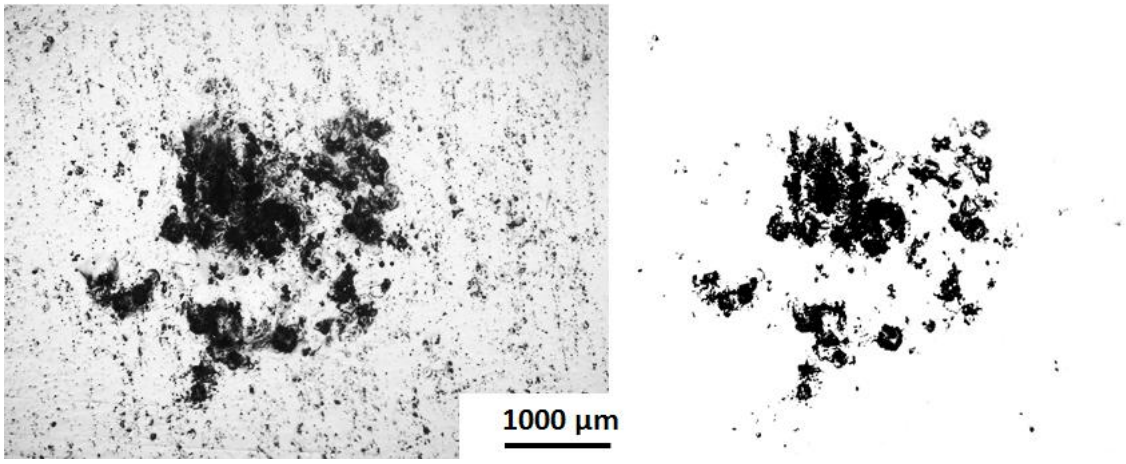


**Figure 3.11 – (left) shows a site of localised corrosion following removal of corrosion product and light polish of 0.04 µm, (right) shows site following image thresholding for surface area calculation**

# 4 STEADY STATE ATMOSPHERIC EXPOSURE

## 4.1 Introduction

Little work has focussed on the localised corrosion behaviour of AA2024 under realistic atmospheric droplet conditions, so the focus of this section is on developing an understanding of some of the key factors which play a role. Steady state exposure during this work refers to tests where one atmospheric variable (RH, CDD, salt type) or exposure time was altered, whilst fixing the other variable as a comparison. Core conditions against which comparisons were made was exposure to a droplet of NaCl solution of volume 0.2 µl, with a fixed initial CDD of ~500 µg/cm$^2$, for a period of 24 hours in an environment of ~85% RH. A combination of µCT and lab based methods have been used to quantify localised corrosion in AA2024 samples.

## 4.2 Results

### 4.2.1 Microstructure of AA2024

Micro-structural characterisation of the alloy was carried out to confirm the presence of the commonly reported precipitate phases in AA2024. Figure 4.1shows an SEM image of precipitate phases detected in the alloy, which were of basic composition $Al_6$(CuMnFeSi), $Al_2CuMg$ (S-Phase) or $Al_2Cu$ (θ-Phase), along with EDX traces identifying them. A magnified view of a θ-phase particle is shown in Figure 4.2, along with EDX maps showing elemental distribution.

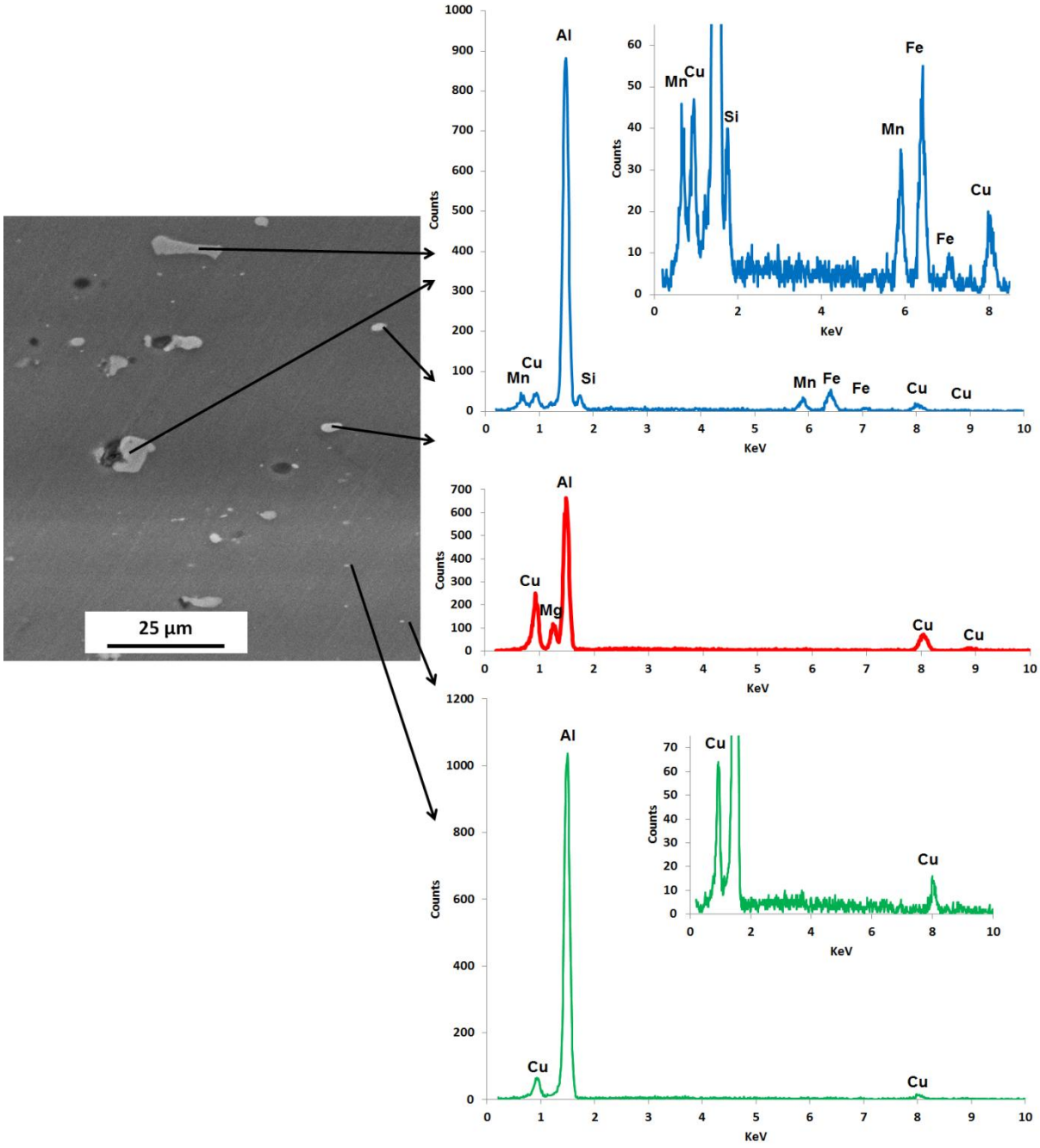


**Figure 4.1 - Typical intermetallic phases found in AA2024-T351 plate used during this work, with EDX traces showing their elemental composition, inset images show magnified trace of non Al peaks**

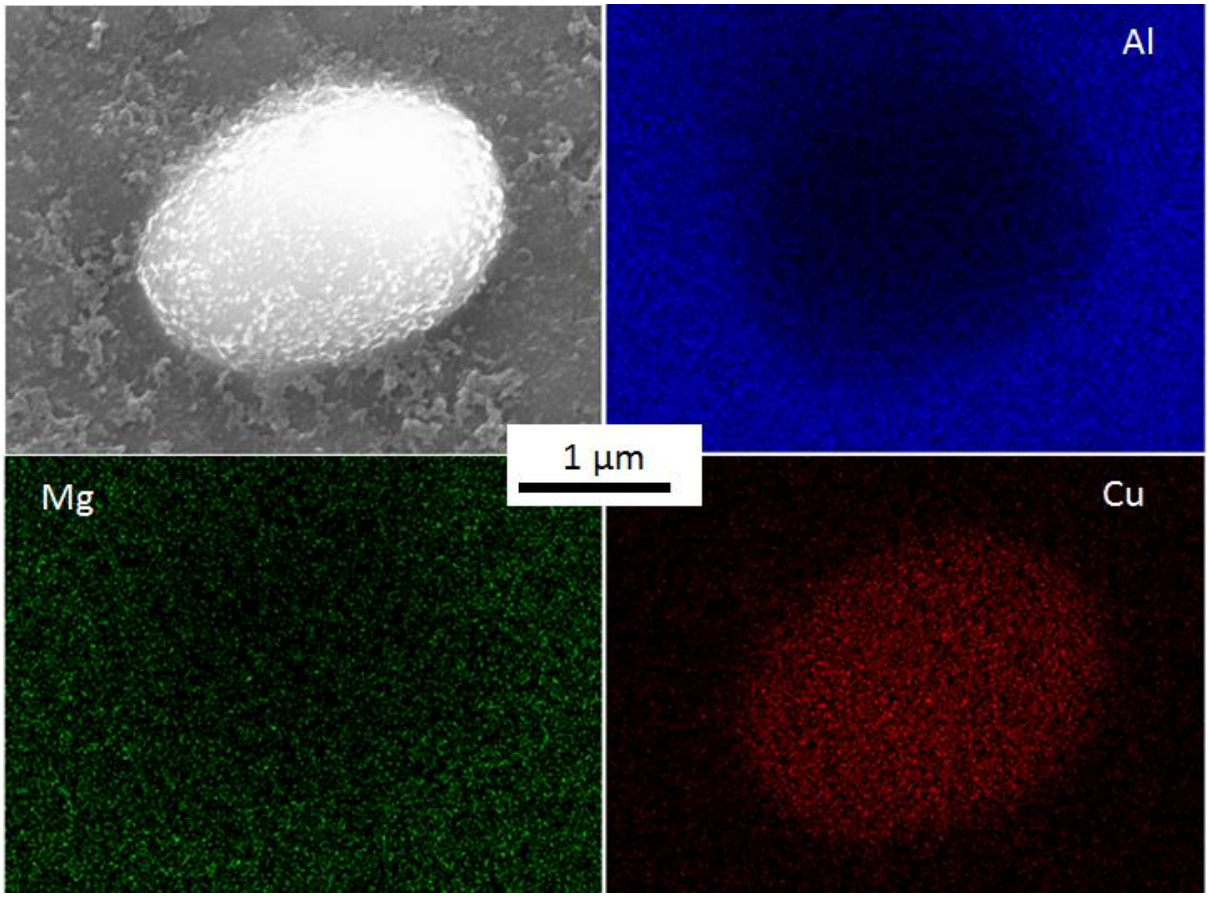


**Figure 4.2 – θ-Phase particle of composition $Al_2Cu$, found in AA2024, with EDX maps showing elemental distribution**

Figure 4.3 shows reconstructed sections of an AA2024 pin sample used during µCT measurements. The intermetallic precipitates, are visible as bright white phases. In the vertical reconstructed section strings of particles can be seen aligned to the rolling direction of the alloy, indicated by the arrow. The broken line indicates the location of the horizontal section shown in the bottom image. The magnified inset shows that the resolution achieved with the µCT measurements was good enough to distinguish individual precipitate phase particles.

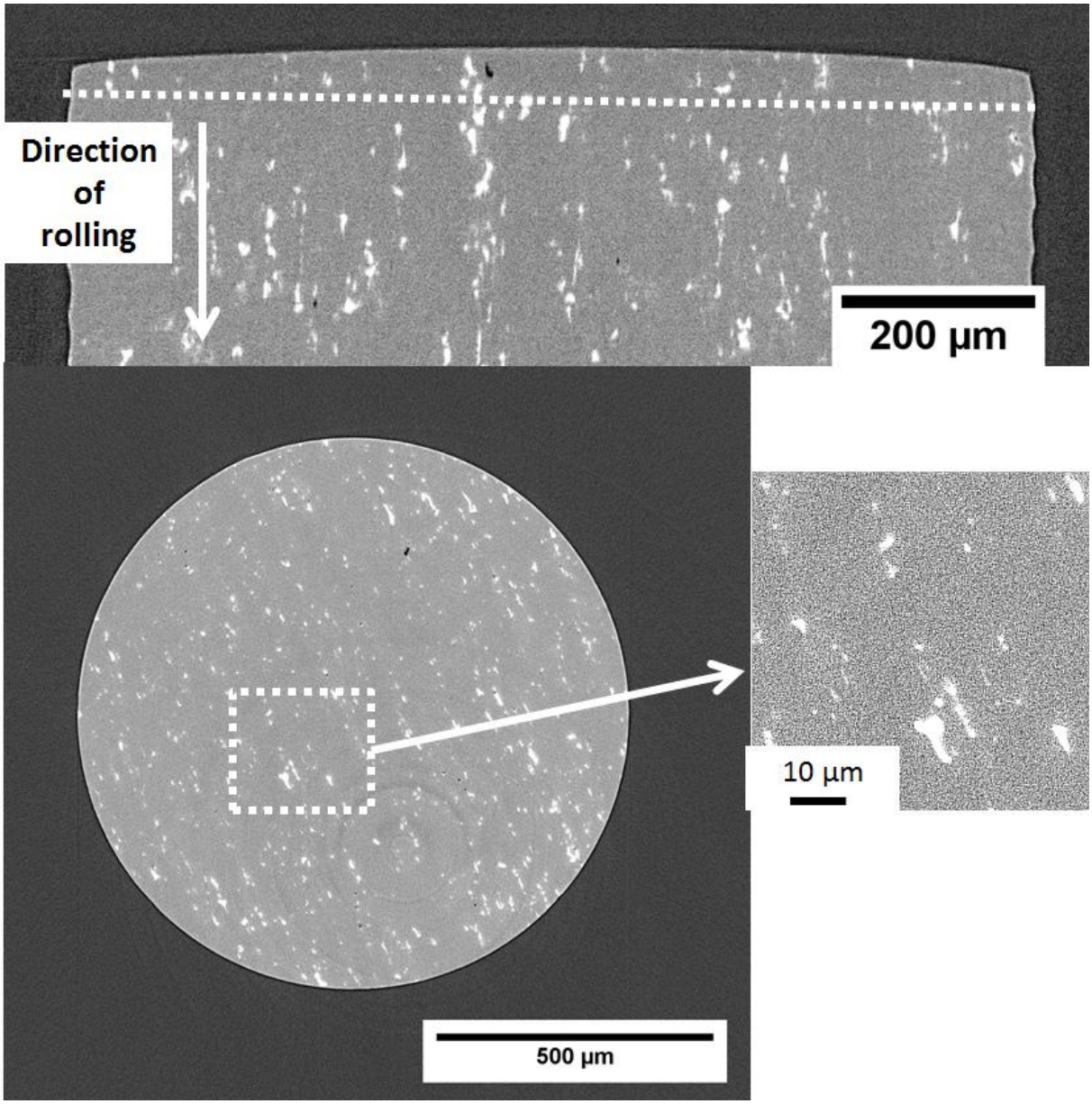


**Figure 4.3 - Microstructure of AA2024 following reconstruction of µCT data: the top image is vertical section through pin (arrow indicates rolling direction of rolling), the broken line indicates location of horizontal section shown below. A higher resolution image of the horizontal section is shown bottom right.**

### 4.2.2 Influence of the Environment of Droplet Behaviour

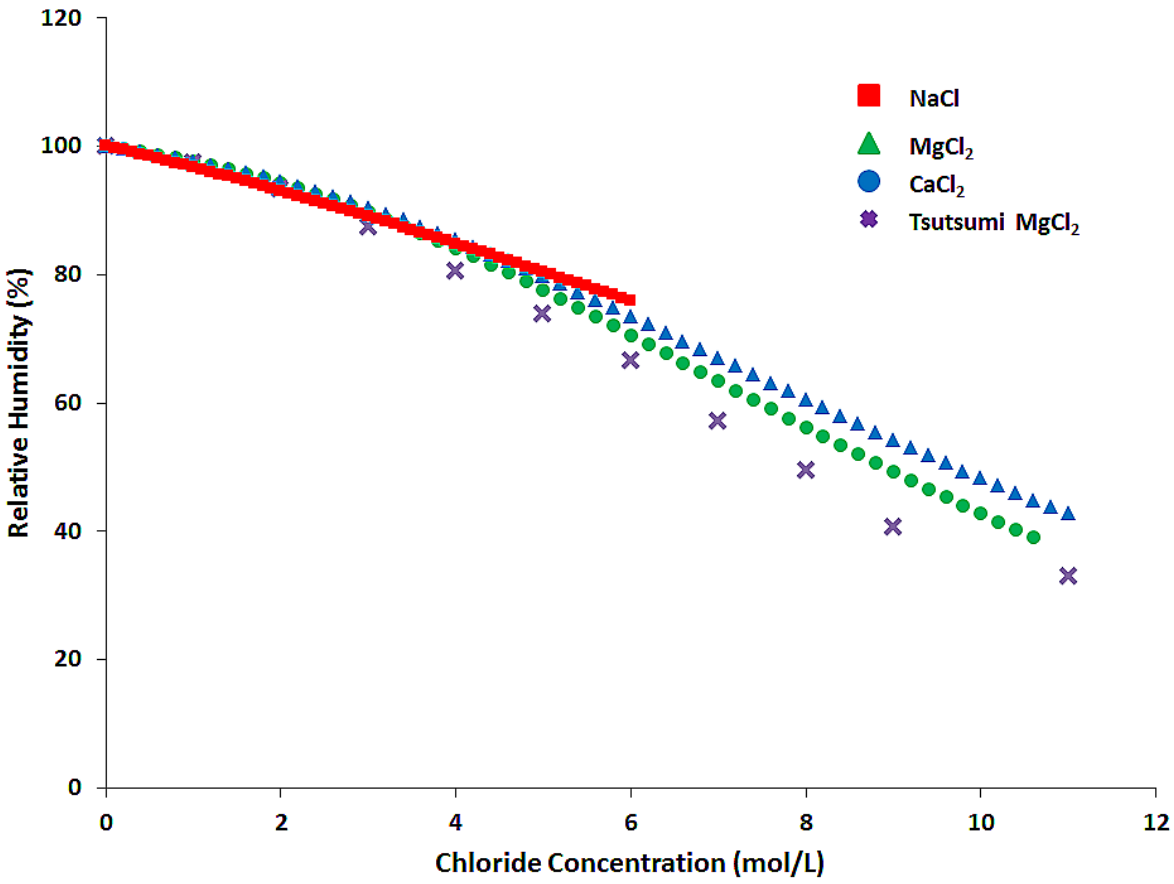


**Figure 4.4 – Relative humidity in equilibrium with salt solutions as a function of concentration of chloride ion for NaCl, $MgCl_2$ and $CaCl_2$ calculated using equation 5.3.1 proposed by Wheeler[122] and checked using OLI software, and data for $MgCl_2$ from Tsutsumi[136]**

Figure 4.4 shows the RH in equilibrium with NaCl, $MgCl_2$ and $CaCl_2$ as a function of chloride concentration calculated using equation 2.4.1, outlined by Wheeler[122], and checked using OLI software. As the $[Cl^-]$ increases, the RH decreases continually for all salt types. In addition plotted is the published equilibrium concentration for $MgCl_2$ solution as a function of RH, by Tsutsumi[136].

Figure 4.5 shows how an atmospheric droplet changes height and shape following deposition (initial concentration 0.5 M NaCl) when placed in a RH of 85% (equilibrium concentration ~3.9 M). After 12 hours, the droplet is considerably smaller, and is rough, probably owing to the formation of some corrosion products. Corrosion sites are not visible in the figure, but hydrogen bubbles can be seen, which are likely to have formed at a localised corrosion site.

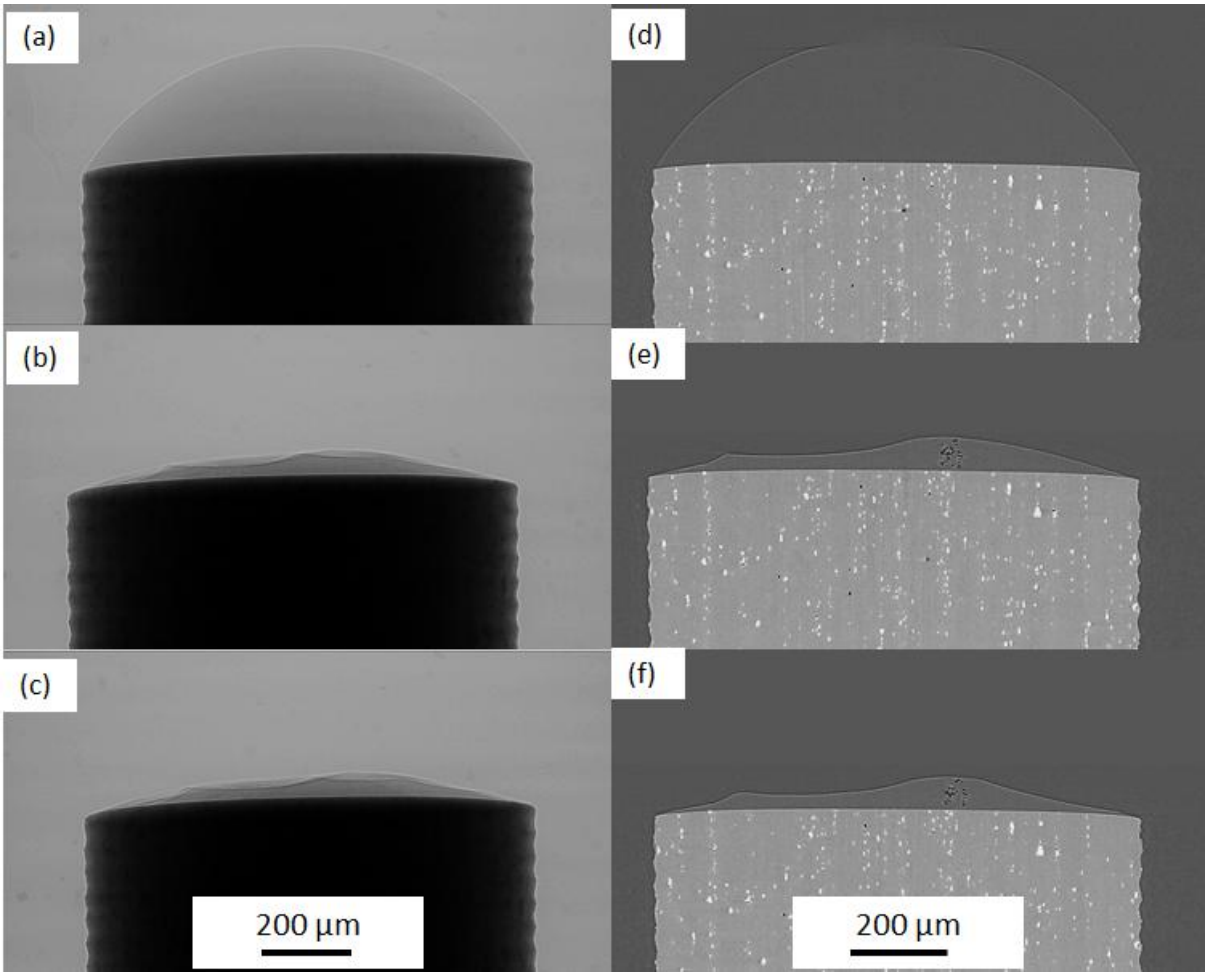


**Figure 4.5 - Radiographs ((a), (b), (c)) and vertical sections of tomograms ((d), (e), (f)) as a function of time ((a), (d), 5 mins, (b), (e) 12 hours and (c), (f) 24 hours), following deposition of a fresh droplet of NaCl solution (0.5 M) on an AA2024 sample, which was then exposed to 85% RH at 22 °C.**

Figure 4.6 shows radiographs of atmospheric droplets of NaCl solution initial volume of 0.2 µl, with three concentrations (different CDD's), following equilibration at 85% RH. It is evident that the higher the initial CDD the greater the droplet height and volume for the same solution concentration at equilibrium.

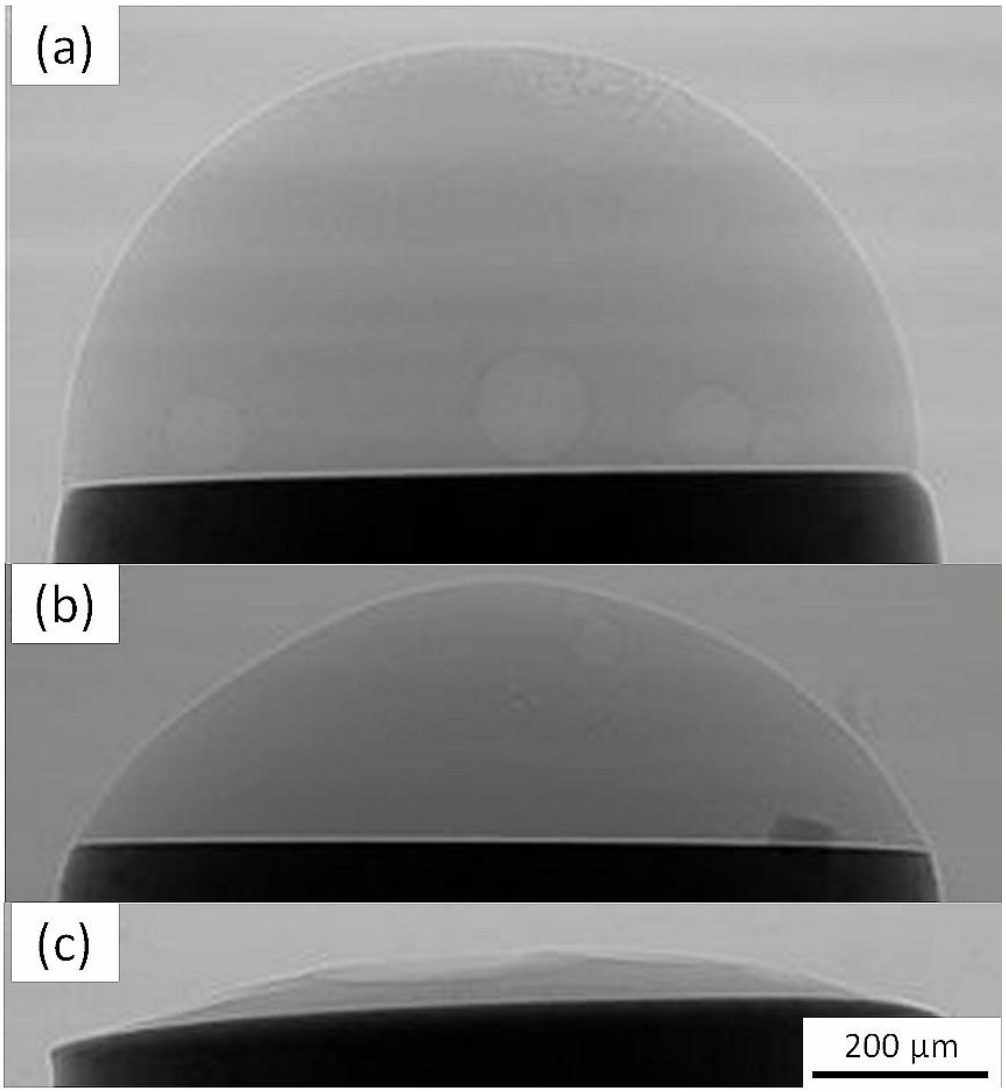


**Figure 4.6 - Effect of initial chloride deposition density on droplet height during simulated atmospheric exposure at 85% RH for NaCl solution droplets of initial volume 0.2 µl. Top to bottom ~4500 µg/cm$^2$, ~2250 µg/cm$^2$ and ~500 µg/cm$^2$**

Figure 4.7-1.10 show a comparison of the theoretically predicted droplet heights and volumes with measured values from both tomography and lab based measurements, as a function of initial CDD and RH. Method of calculation and measurement are described in Section 3.4.

It can be seen that as a function of initial CDD the predicted increase in droplet height (Figure 4.7) and volume (Figure 4.8) are linear for a fixed RH of 85% RH, further the agreement between the predicted and the measured values was good. When considering the influence of RH for a fixed initial CDD the increase predicted in droplet height (Figure 4.9) and volume (Figure 4.10) is non-linear and increases exponentially above ~80% RH. Time to attain equilibrium was typically 1-3 hours, µCT measurements used for equilibrium heights were made from the 12 hour time point scans. Lab based measurements were made on droplets following ~14-16 hours exposure.

Figure 4.11 demonstrates how droplet height varies for solutions of the same initial CDD (~500 µg/cm$^2$) when exposed to different RH environments, for $CaCl_2$ solutions. It is evident that as RH decreases both height and volume of the droplet decrease, as has been plotted in Figures 4.7-4.10. There is some variability in droplet height which can be attributed to either small variations in RH of the environment, or to the presence of corrosion products and precipitated solid salt phases. These account for the rippled appearance seen in some of the atmospheric droplets.

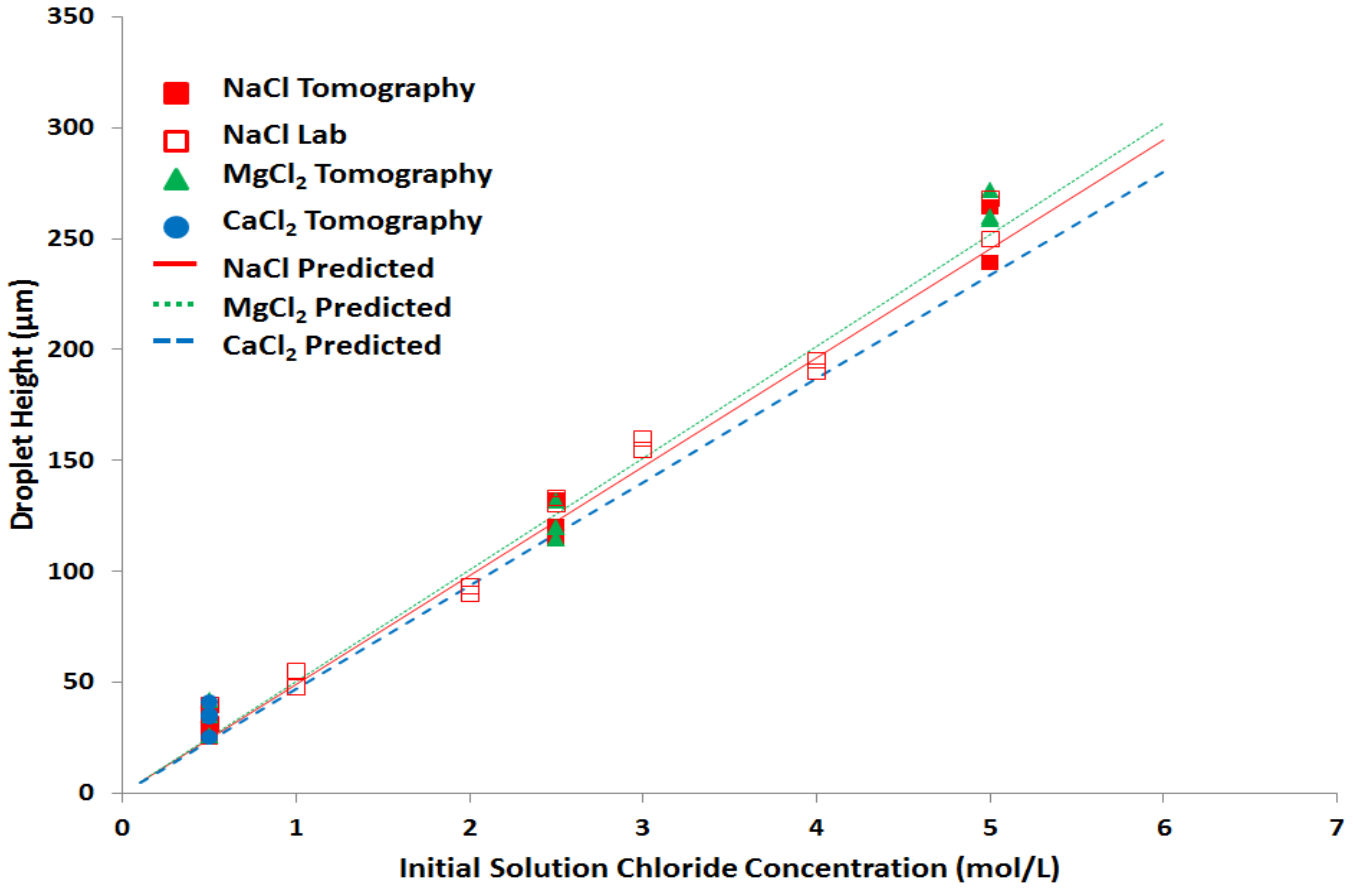


**Figure 4.7 - Measured and theoretically predicted droplet equilibrium heights as a function of initial molar chloride concentration, for 0.2 µl droplets of NaCl, $CaCl_2$ and $MgCl_2$ solutions, at a fixed RH of 85%**

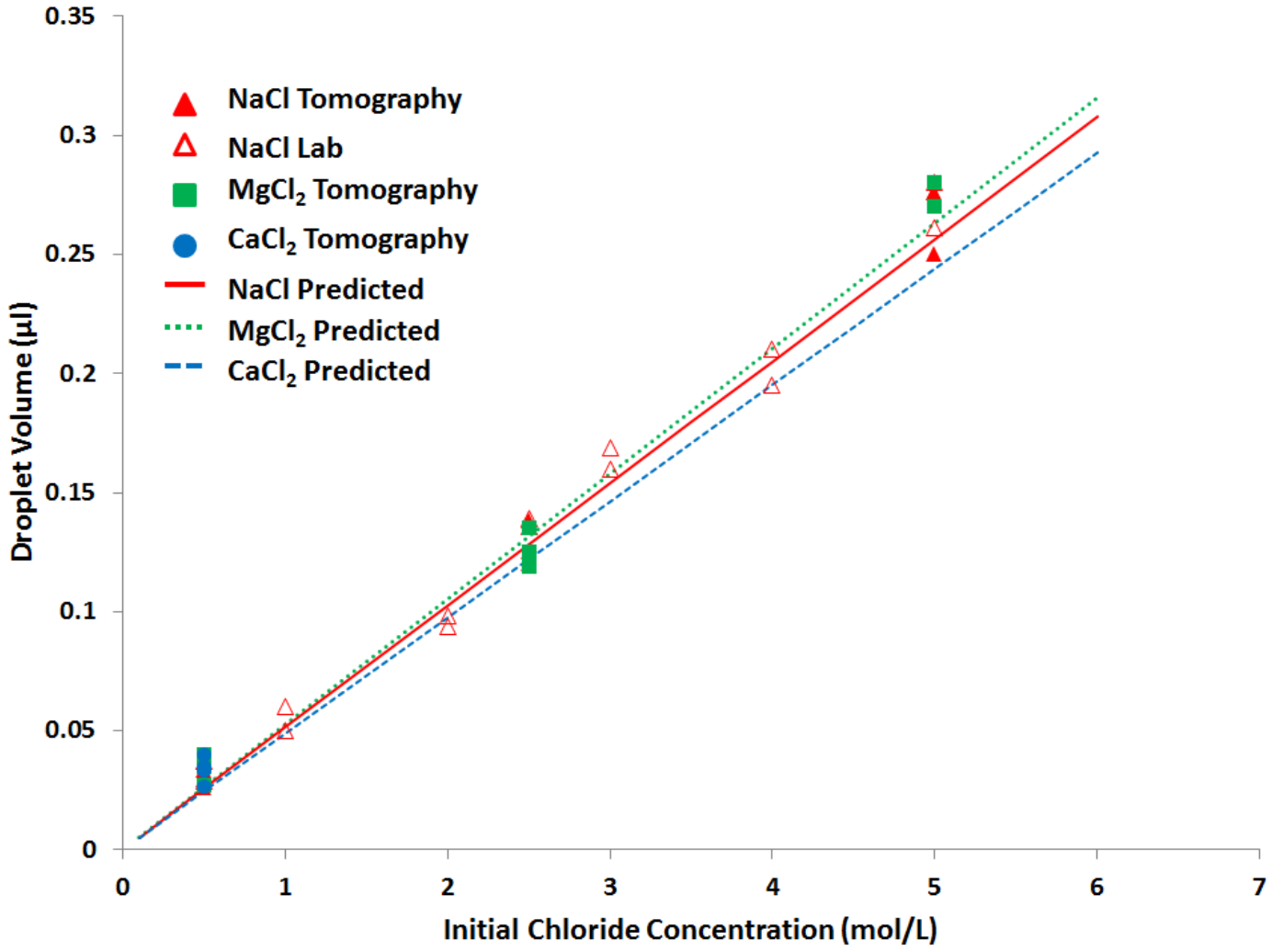


**Figure 4.8 - Measured and theoretically predicted droplet equilibrium volumes as a function of initial molar chloride concentration, for 0.2 µl droplets of NaCl, $CaCl_2$ and $MgCl_2$ solutions, at a fixed RH of 85%**

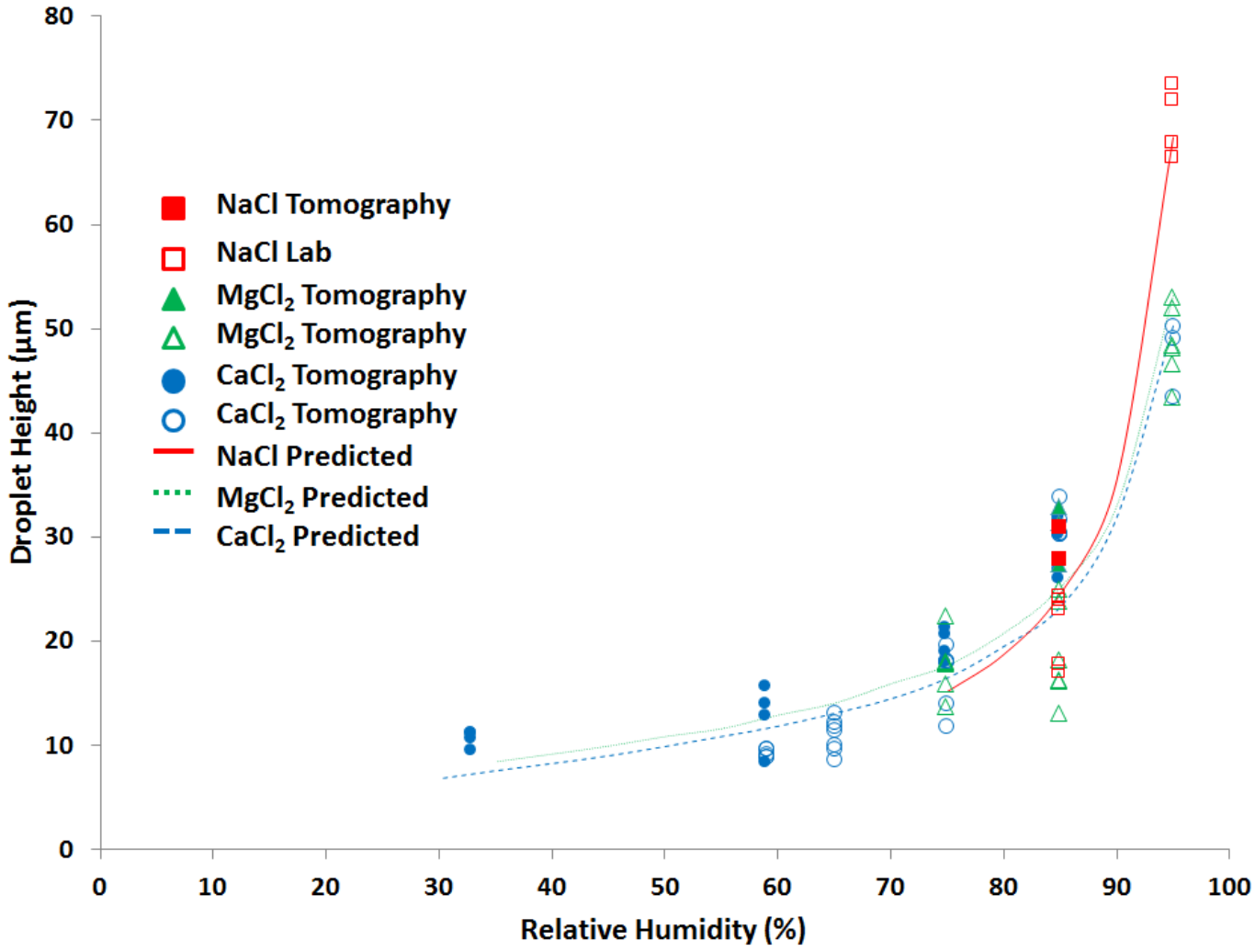


**Figure 4.9 - Predicted and measured droplet heights for 0.2 µl droplets of NaCl, $MgCl_2$ and $CaCl_2$ salt solutions as a function of RH, initial CDD fixed at 500 µg/cm$^2$**

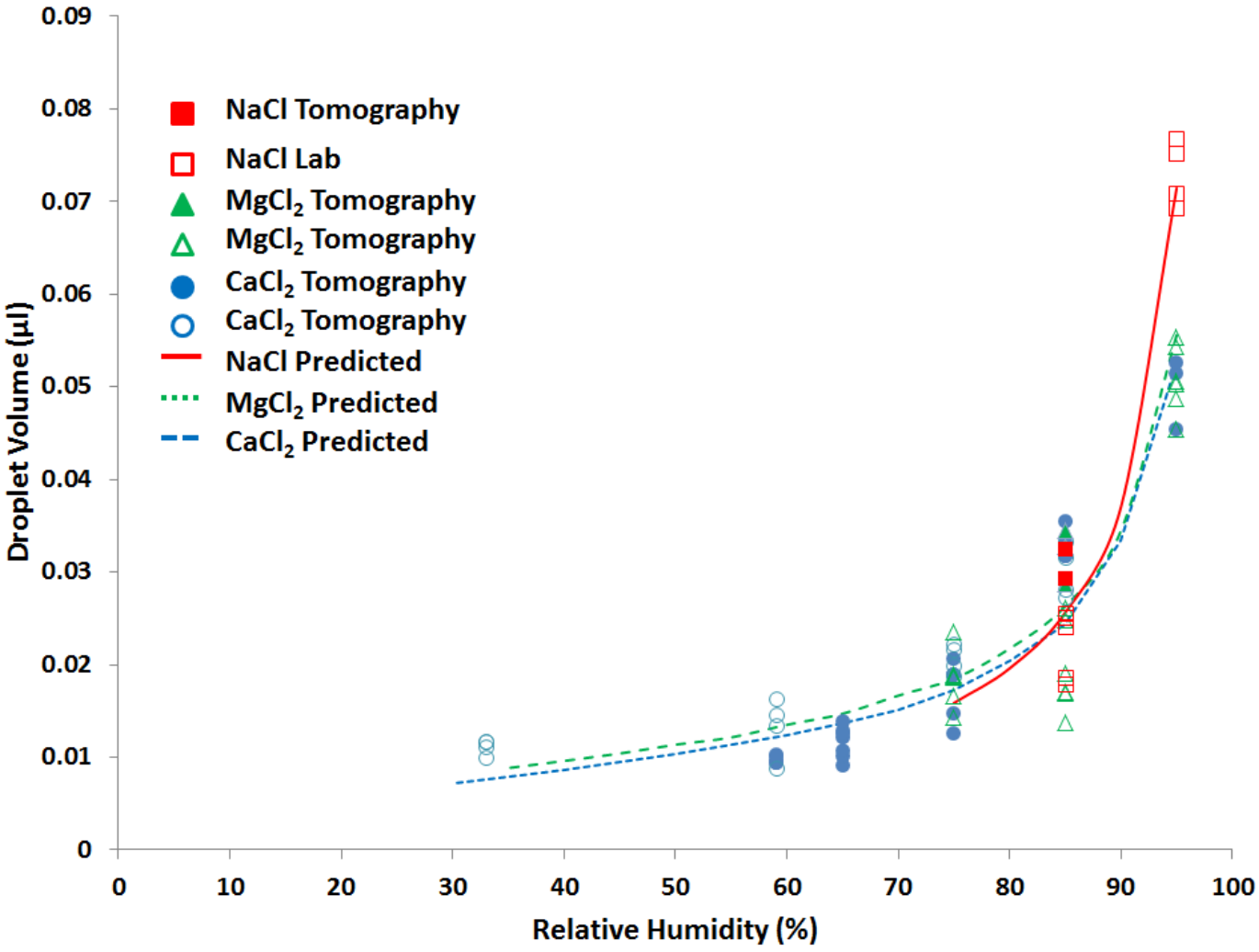


**Figure 4.10 - Predicted and measured droplet volumes for 0.2 µl droplets of NaCl, $MgCl_2$ and $CaCl_2$ salt solutions as a function of RH, initial CDD fixed at 500 µg/cm$^2$**

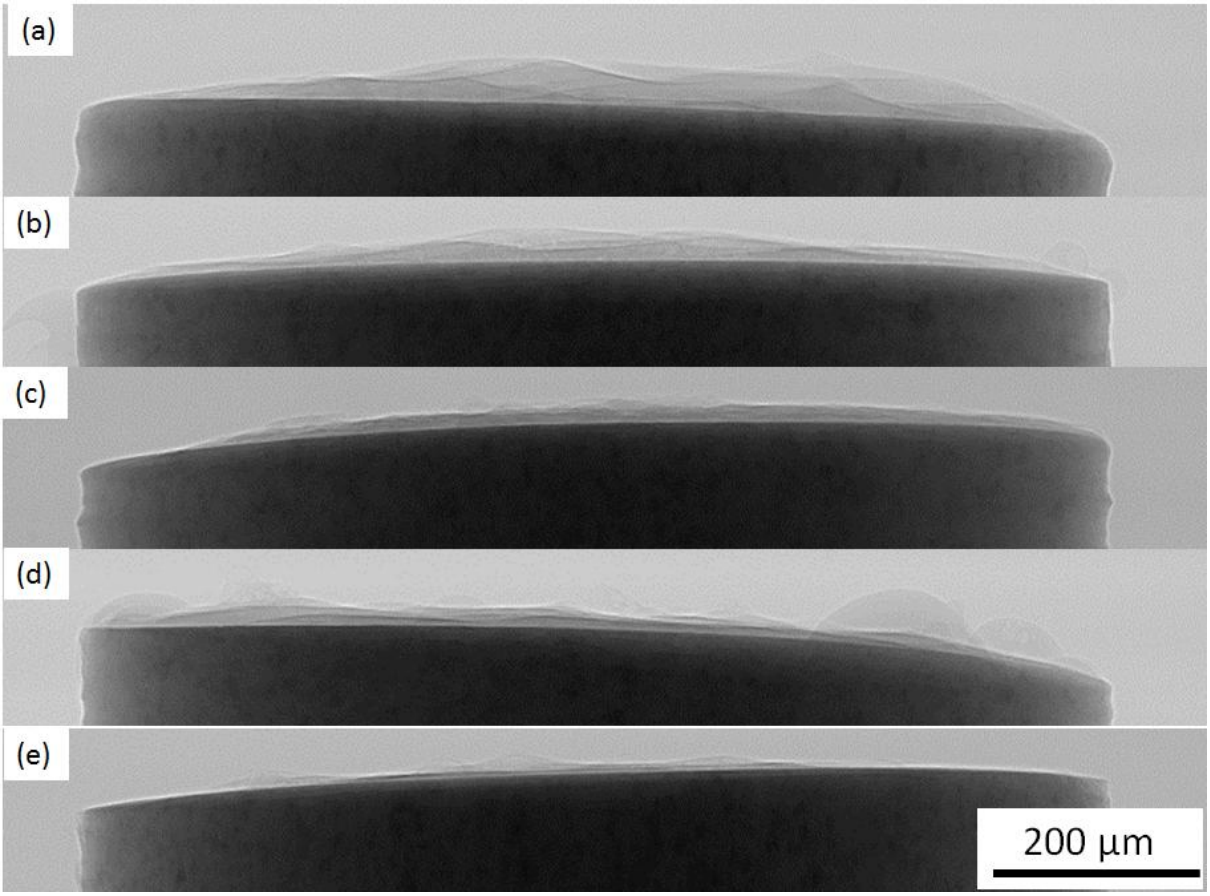


**Figure 4.11- Radiographs of varying droplet height as a function of exposure RH for $CaCl_2$ solution droplets initial CDD fixed at ~500 µg/cm$^2$, (a)85%, (b) 75%, (c) 59%, (d) 45% and (e) 33% RH**

### 4.2.3 Typical Morphology and Role of Microstructure in the Development of Localised Corrosion in AA2024 Samples During Atmospheric Exposure

Figure 4.12,Figure 4.13 Figure 4.14 show the typical morphology of IGC fissures observed during the localised corrosion of AA2024. Figure 4.12 shows a cropped view of pin sample with an IGC fissure extending form the surface to a depth of ~200 µm on the left, with a reconstructed 3-D rendering of a fissure on the right hand side. It is evident that the fissures grow both vertically and laterally and are quite complex in shape. It is important to note that there is range in the width of the fissures observed

from several microns down to 100-200 nm, SEM images of pin samples following mechanical sectioning show this very well in Figure 4.13.

The complex shape and an growth of fissures within the sample is shown on the left hand image in Figure 4.13 and in Figure 4.14. Both show how growth of fissures follows the grain boundary network both at the metal surface and within the interior.

Figure 4.15 and Figure 4.16 further demonstrate how microstructure of the alloy influences the development of localised corrosion; fissures can be seen initiating at (Figure 4.15) and following (Figure 4.16) strings of intermetallic particles through the depth of the metal. Initiation in the vicinity of intermetallic precipitates was observed in the majority of the μCT atmospheric measurements, as well as during lab based exposures. These strings were aligned to the direction of rolling of the alloy, and were often seen to be associated with the development of fissures during atmospheric exposure.

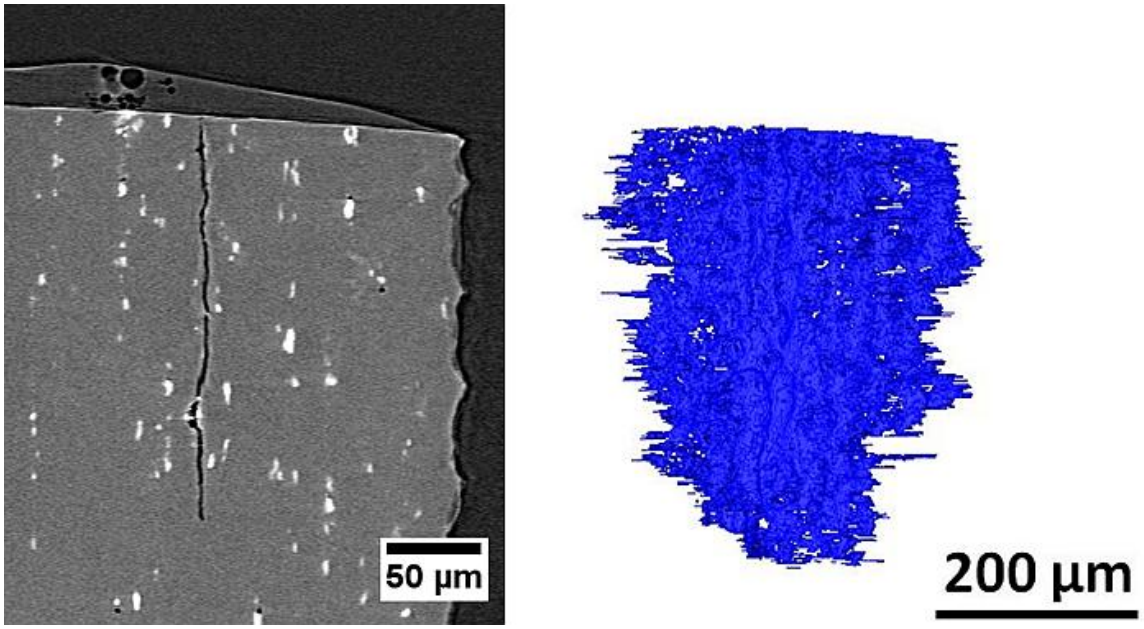


**Figure 4.12 – Left: portion of vertical section reconstruction showing typical development and morphology of IGC fissure through an AA2024 pin sample, following 24 hours at 85% RH with CDD of 500 µg/cm$^2$. Right: 3-D reconstruction of typical morphology of corroded fissure volume within an AA2024 pin sample following 24 hours at 85% RH with CDD of 500 µg/cm$^2$.**

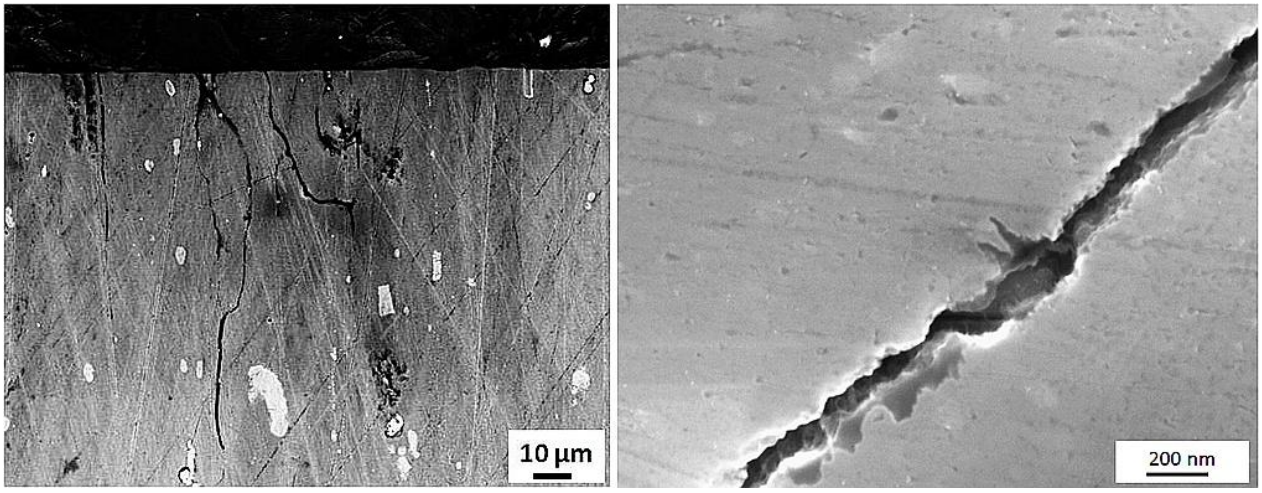


**Figure 4.13 – Left: SEM image showing vertical cross-section of AA2024 pin sample following mechanical sectioning, exposed to a NaCl droplet for 24 hours at 85% RH to droplet initial CDD 4500 µg/cm$^2$. Right: SEM image of the cross section of a narrow fissure in AA2024 sample, exposed to a NaCl droplet for 24 hours at 85% RH to droplet initial CDD 4500 µg/cm$^2$.**

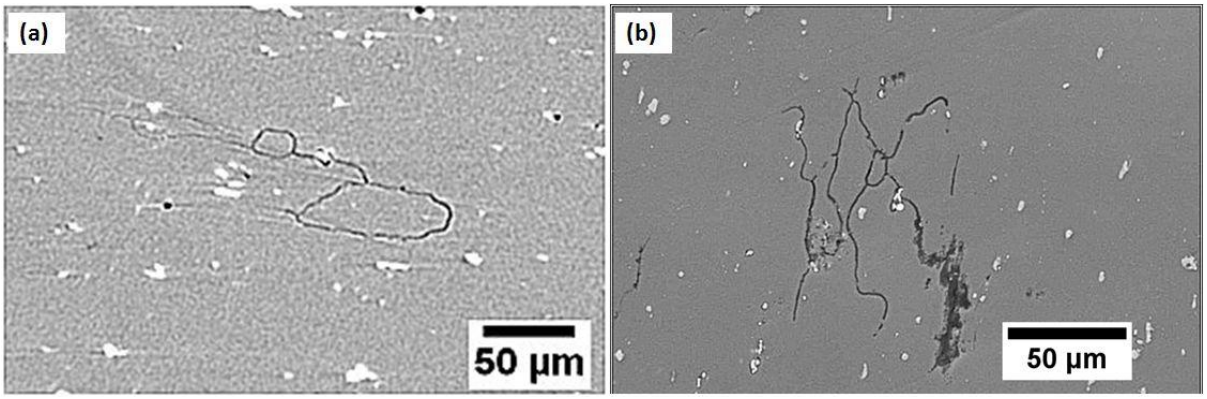


**Figure 4.14 - Grain boundary attack in AA2024 samples under atmospheric exposure to NaCl solutions (a) µCT horizontal reconstructed section, (b) SEM image of sample surface, both exposed to a NaCl droplet for 24 hours at 85% RH to droplet initial CDD 4500 µg/cm$^2$.**

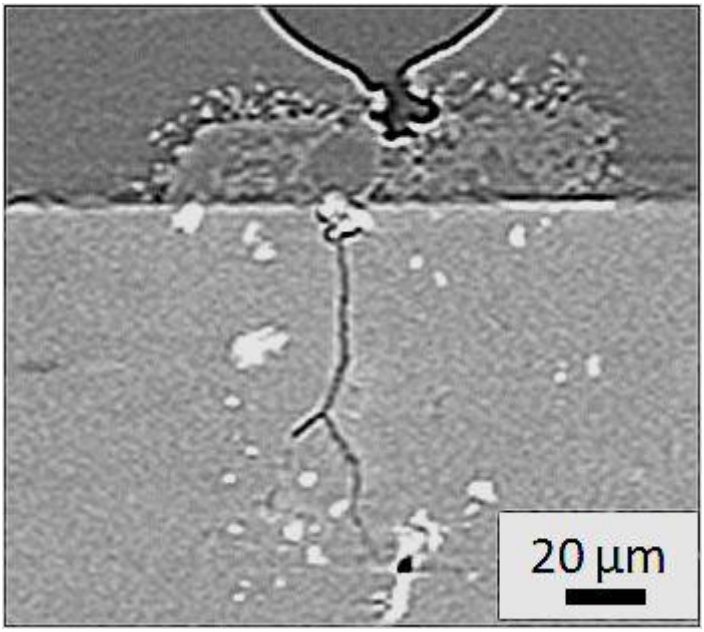


**Figure 4.15 - Growth of IGC fissure below intermetallic phase, formation of corrosion product visible at the mouth of the fissure beside particle, following 12 hours exposure at 85% RH under NaCl solution droplet, with initial CDD of 4500 µg/cm$^2$.**

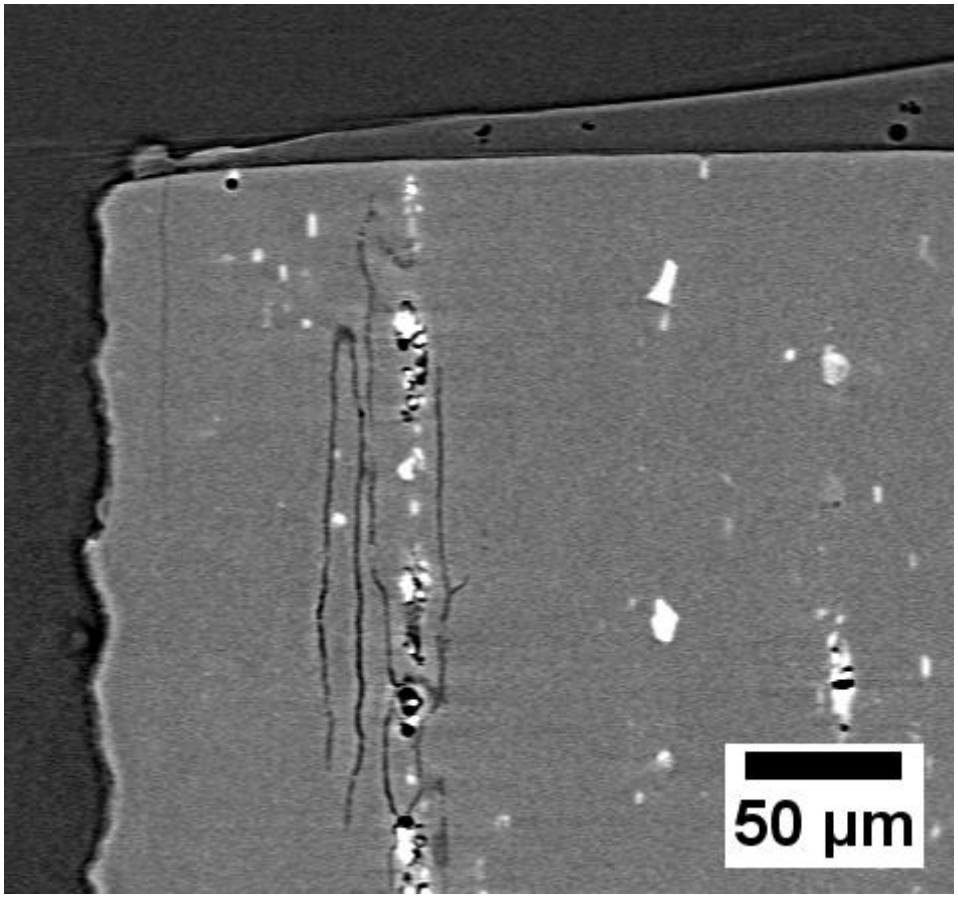


**Figure 4.16 - Development of IGC fissure in the vicinity of a string of intermetallic precipitates aligned to the direction of rolling through the bulk of AA2024 pin sample, during exposure to NaCl solution with initial CDD of ~500 µg/cm$^2$ exposed at 85% RH for 24 hours.**

### 4.2.4 Influence of Initial CDD on Development of Localised Corrosion in AA2024 Samples during Atmospheric Exposure

Figure 4.17 shows an example of the development of localised corrosion in an AA2024 pin exposed to the core condition for this work. Figure 4.17 (a) shows a near surface horizontal section with the fissure highlighted. The broken line indicates the location at which the vertical section (bottom left) is taken, which is the point of maximum fissure depth. On the bottom right a 3-D reconstruction of the fissure volume is shown, it can be seen that the fissure has extended both vertically and laterally from the metal surface.

Figure 4.18 shows the effect of increasing the initial chloride deposition density on the development of localised corrosion in an AA2024 pin sample following 24 hours exposure in an environment of 85% RH. It can be seen that as the initial CDD is increased there is an increase in the amount of localised attack, both at the sample surface (top image in each group) and in terms of the volume (3-D reconstruction in each group), quantified in Figure 4.18. The orientation of the fissure with respect to the sample surface is indicated by black square and circle markers. Vertical section reconstructions on the bottom left of each grouping shows the point of maximum depth for each of the fissures, the location is indicated on the surface section by a broken line.

It can be seen that as CDD is increased the increase in maximum depth of fissure observed is limited, and that there is an increase in the number of interconnected fissures which run parallel to one another throughout the grain boundary network.

Measured values for the maximum fissure depth as a function of changing initial CDD for exposure at 85% RH, is plotted in Figure 4.19. The plot shows data obtained during both tomography and lab based measurements (right hand plot shows and expanded view of CDD values <100 μg/cm$^2$). At lower levels of CDD (<1000 μg/cm$^2$), the maximum depth increases with CDD. However, above this value, the depth is approximately constant, ~230±30 μm. The lab-based measurements (determined with successive polishing) appear to be broadly consistent with the tomography measurements. However, the two tomography measurements made with $CaCl_2$ appear to show deeper attack.

The measured volume of localised corrosion in AA2024 pin samples from μCT measurements following 24 hours exposure at 85% RH is plotted in Figure 4.20. Data

are shown for multiple X-ray measurements (during a time-dependent sequence), single X-ray measurements at 24 hours, and “ex situ” measurements where the samples have been corroded in the lab, and dried out before exposure to X-rays. It generally appears that samples measured in situ for either single or multiple measurements show similar volumes, suggesting that there is no obvious effect of beam damage for multiple exposures. Where both “ex situ” and “in situ” measurements have been made, the “ex situ” ones appear to show higher volumes, suggesting that the drying process may itself induce corrosion. For the same conditions, NaCl, $MgCl_2$, and ocean water appear to show similar volumes, but the measurements with $CaCl_2$ showed higher volumes.

Measurements at CDDs of ≥1000 µg/cm$^2$ are substantially higher than those at 500 µg/cm$^2$, but above 1000 µg/cm$^2$, the results are somewhat scattered.

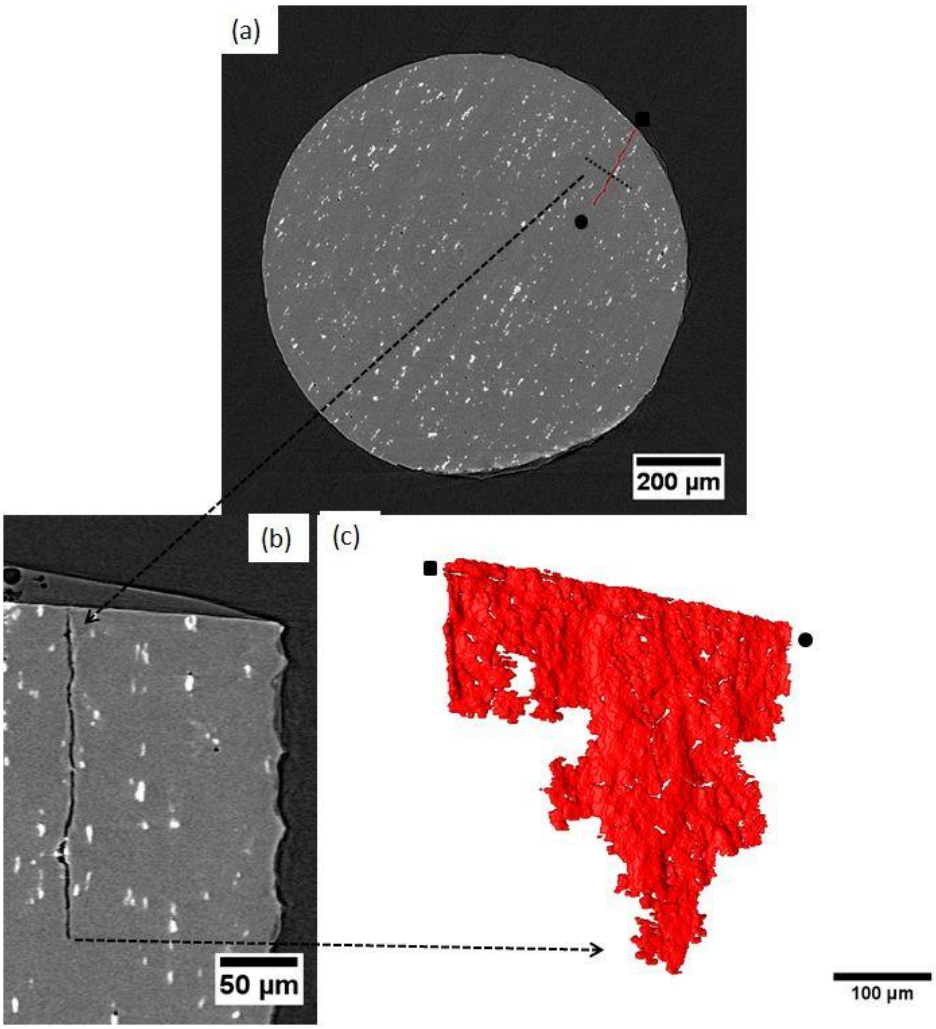


**Figure 4.17 - IGC fissure which developed within AA2024 pin sample following 24 hours exposure in simulated atmosphere of ~85% RH, with an initial CDD of ~500 µg/cm$^2$ (core condition), site highlighted on near surface section (a), point of maximum depth taken along broken line is shown in (b), 3-D reconstruction of the corroded fissure volume is shown in (c).**

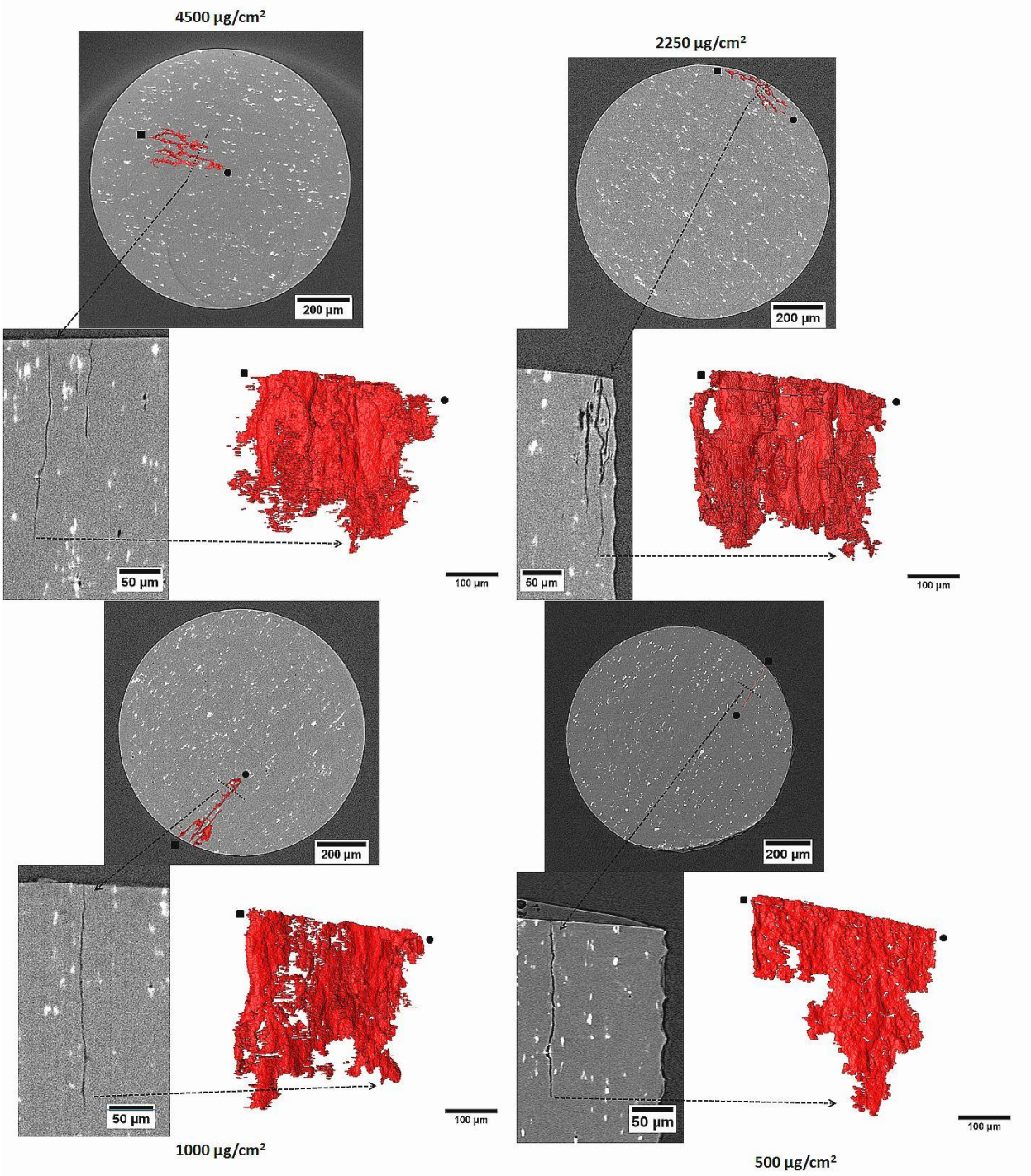


**Figure 4.18 - Effect of increasing initial CDD of NaCl solution droplets on observed growth of localised corrosion in AA2024 pin samples, for 24 hours exposure to 85% RH, top left: 4500 µg/cm$^2$, top right: 2250 µg/cm$^2$, bottom left: 1000 µg/cm$^2$, bottom right: 500 µg/cm$^2$. Near surface section with localised corrosion sites highlighted, points of maximum depth position indicated by broken line and 3-D reconstructed volumes are shown for each condition.**

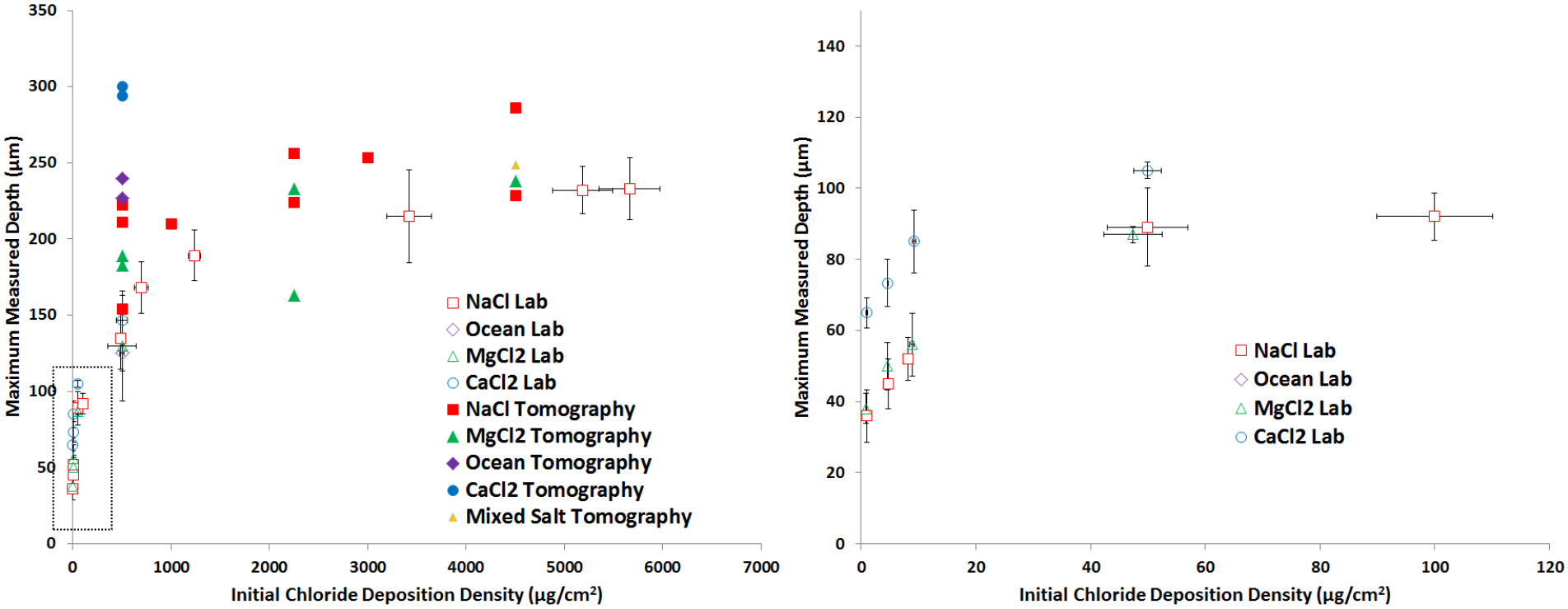


**Figure 4.19 - Maximum measured depth of corrosion as a function of initial CDD for µCT (pin sample) and lab based (plate sample) atmospheric exposures, exposure time fixed at 24 hours and RH 85% RH, right hand figure shows highlighted region for CDD values <100 µg/cm$^2$**

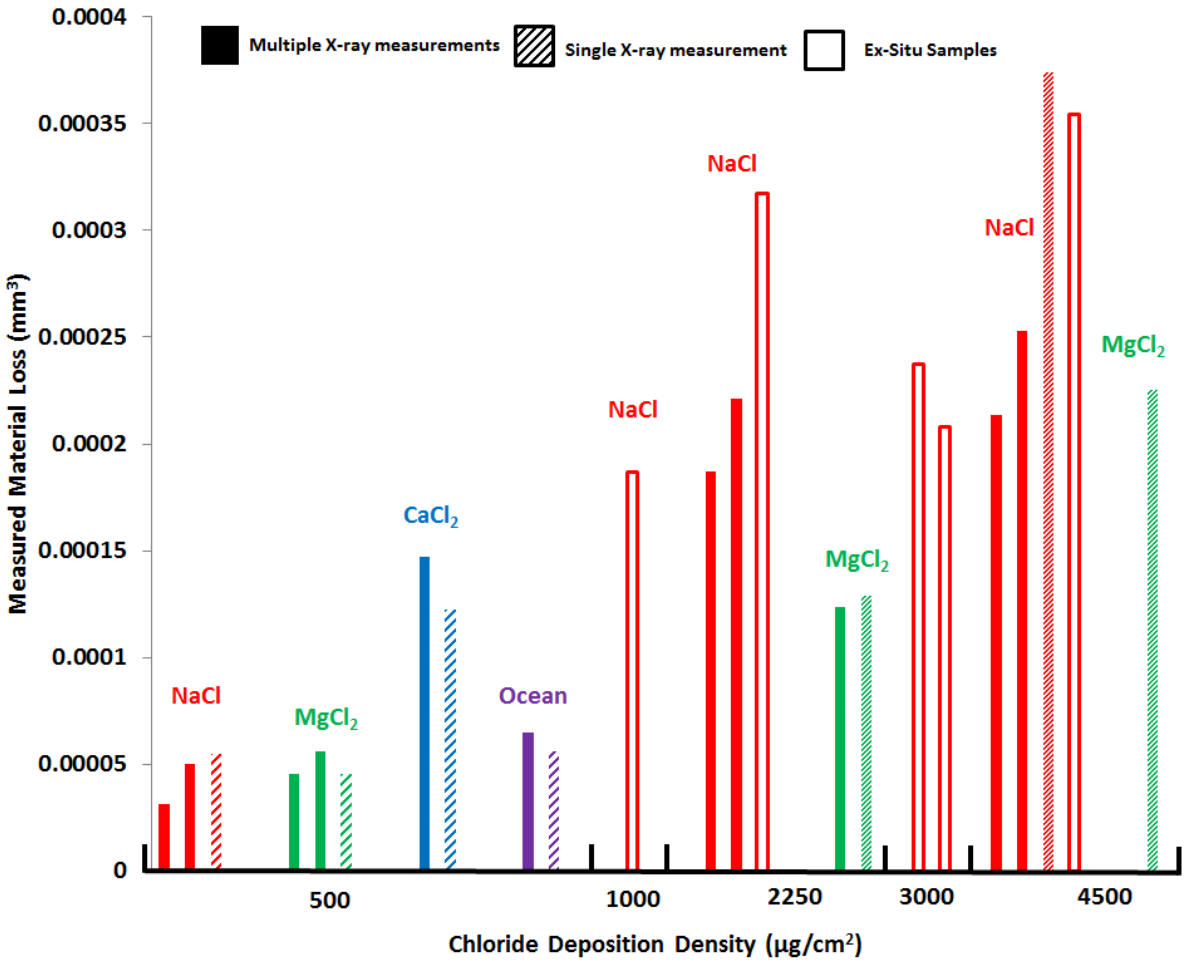


**Figure 4.20 - Measured volume of corrosion as a function of initial CDD for µCT measurements (24 hours at 85% RH). In-situ (solid bar), control (diagonal stripes) and ex-situ (solid outline) samples are plotted where appropriate. In-situ shows volume measurement at 24 hours, control shows volume based on single measurement at 24 hour time point and ex-situ shows volume for measurement of sample corroded for 24 hours in the lab and dried 1 hour at 0% RH.**

### 4.2.5 Determination of Threshold for Onset of Localised Corrosion inAA2024 Plate Samples during Atmospheric Exposure

Figure 4.21 and Figure 4.22 show observed localised corrosion for CDD values of 1 µg/cm$^2$ and 500 µg/cm$^2$ respectively, using SEM to observe surface damage following removal of corrosion product. Measurements were made in an effort to determine the threshold (for initial CDD) at which localised corrosion occurred in AA2024 plate samples under atmospheric droplets during 24 hour exposures at 85% RH. No specific value was obtained for a threshold, but it is possible to say that during this study the threshold was <1 µg/cm$^2$ for NaCl solution droplets with an initial volume of 0.2 µl. For samples with droplets of initial CDD 1 µg/cm$^2$, 12/12 showed signs of localised attack following removal of corrosion product from the surface.

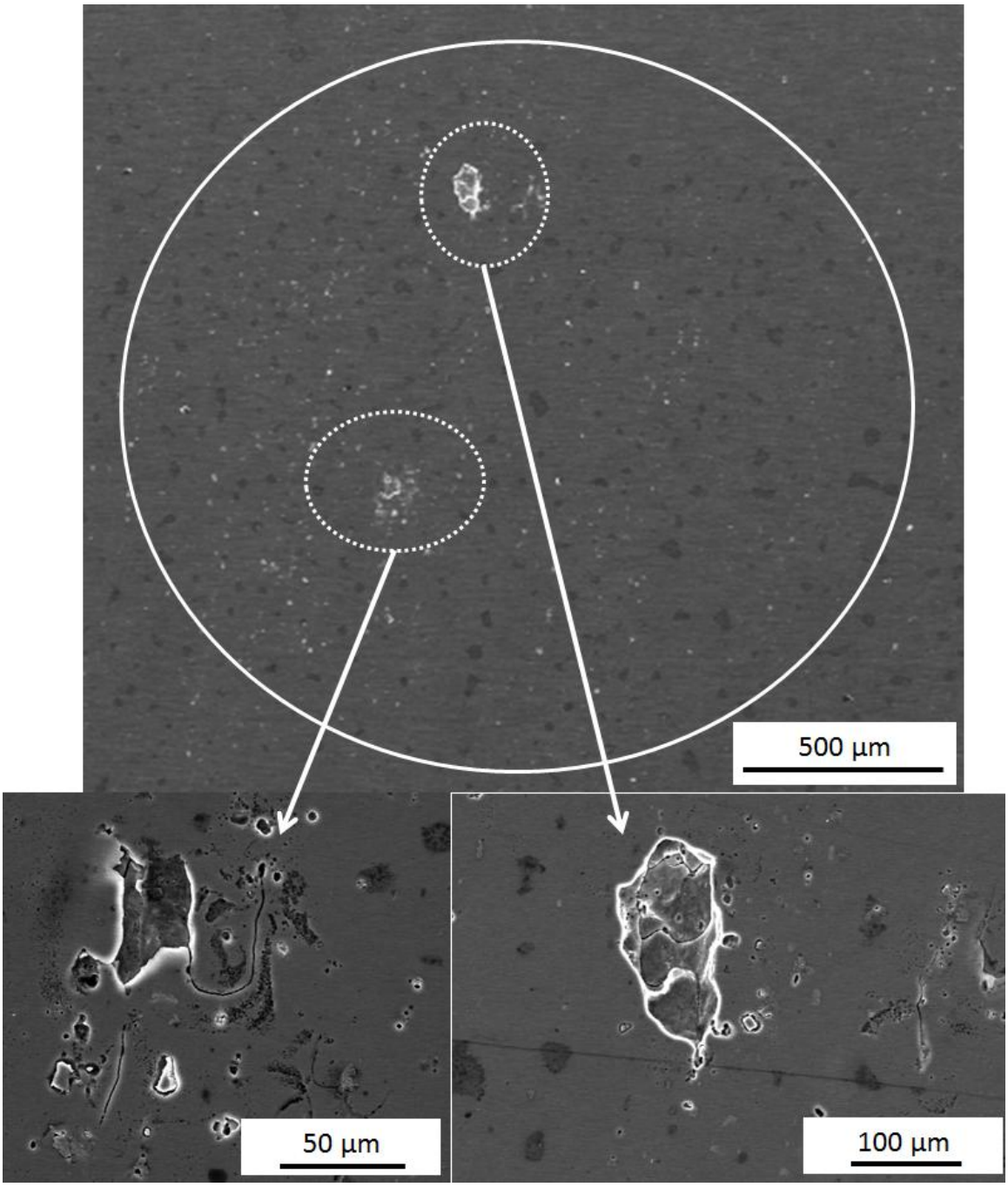


**Figure 4.21 - Secondary electron SEM images of localised corrosion on AA2024 plate sample, surface orientation in L direction. Following 24 hours exposure at ~85% RH, under initial CDD ~1 µg/cm$^2$, for NaCl solution droplets. Corrosion product removed by immersion in nitric acid for ~2 minutes, and 10 seconds polish at 0.04 µm.**

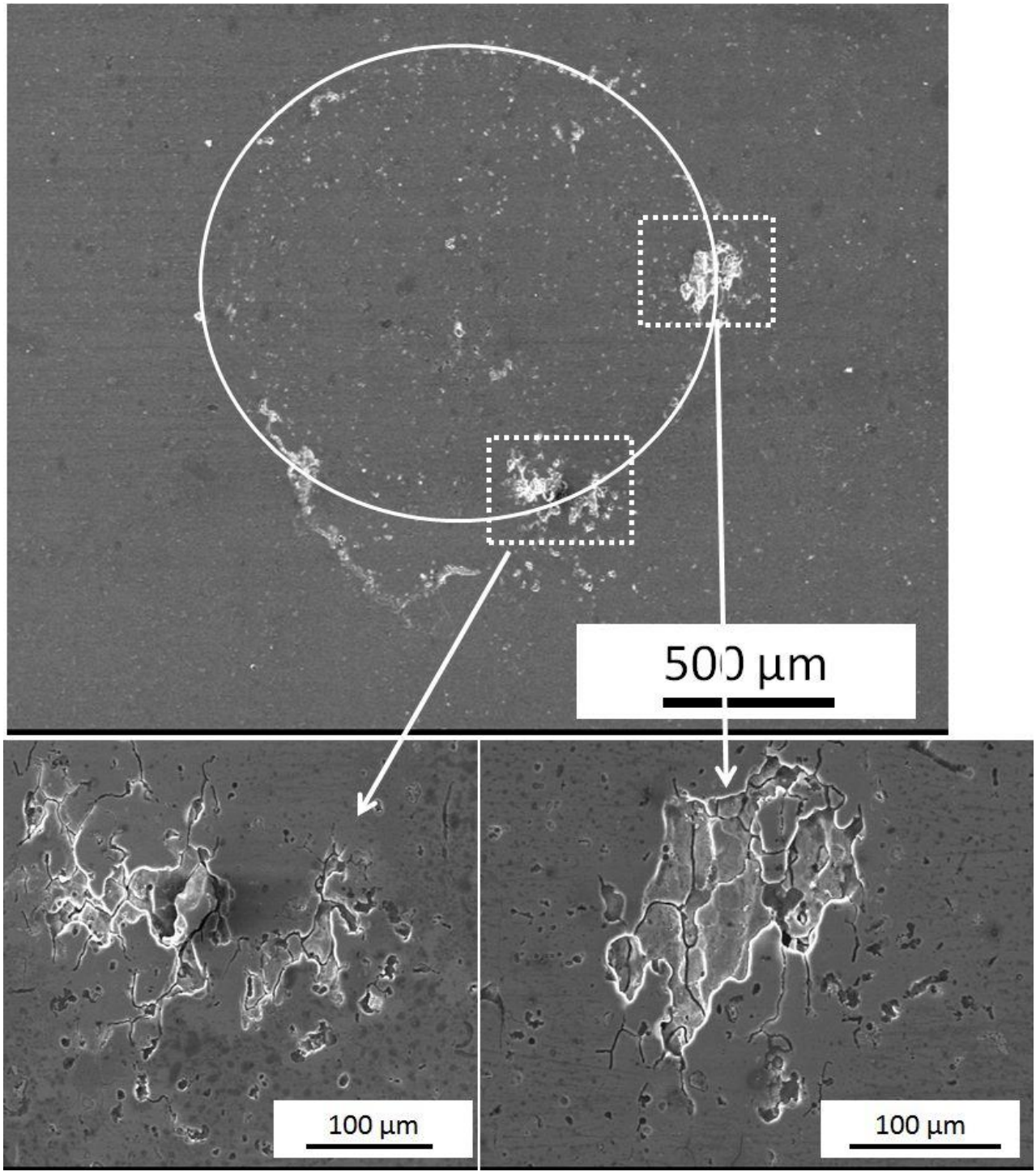


**Figure 4.22 - Secondary electron SEM images of localised corrosion on AA2024 plate sample, surface orientation in L direction. Following 24 hours exposure at ~85% RH, under initial CDD ~500 µg/cm$^2$, for NaCl solution droplets. Corrosion product removed by immersion in nitric acid for ~2 minutes, and 10 seconds polish at 0.04 µm.**

### 4.2.6 Time Dependent Measurements on the Development of Localised Corrosion in AA2024 Samples during Atmospheric Exposure as a Function of Initial CDD

Figure 4.23 the volume of corrosion as a function of time under NaCl droplets determined from in-situ µCT measurements. It can be see that for sample of a lower initial CDD, the corrosion rate remains relatively constant throughout the 24 hour exposure. For higher initial CDD values the corrosion rate increased significantly between ~20 and ~24 hours.

Visual examples of the time dependent development of localised corrosion in AA2024 pin samples can be found in Figure 4.24, Figure 4.25 and Figure 4.26. Figure 4.24 shows a vertical section of a samples exposed to NaCl solution with an initial CDD of ~500 µg/cm$^2$ at ~85% RH at 1,12 and 24 hours of exposure for AA2024 pin samples. The vertical sections are located at the point of maximum fissure depth at the end of exposure. No corrosion is visible after 1 hour. After 12 hours, two fissures can be seen in the 3D segmented image at the bottom of the figure, but only one is visible in the vertical section. After 24 hours, the largest fissure has increased both in depth and width (3D image), and multiple fissures can be seen in the vertical section, and the 3D image. Close inspection of the 3D image (not shown), indicates that the fissures are interconnected.

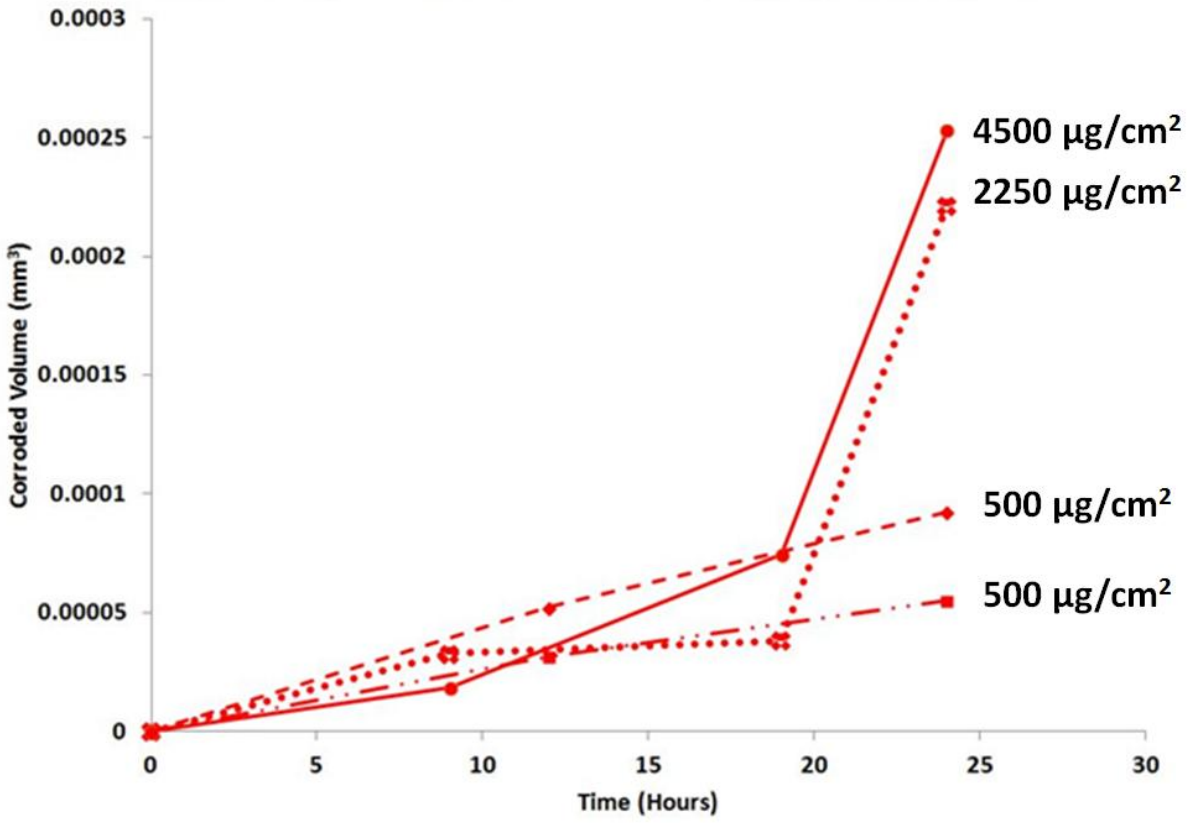


**Figure 4.23 - Measured volume of corrosion as a function of time for AA2024 pin samples exposed to NaCl solution droplets, all samples exposed for 24 hours at 85% RH, to different initial CDD's**

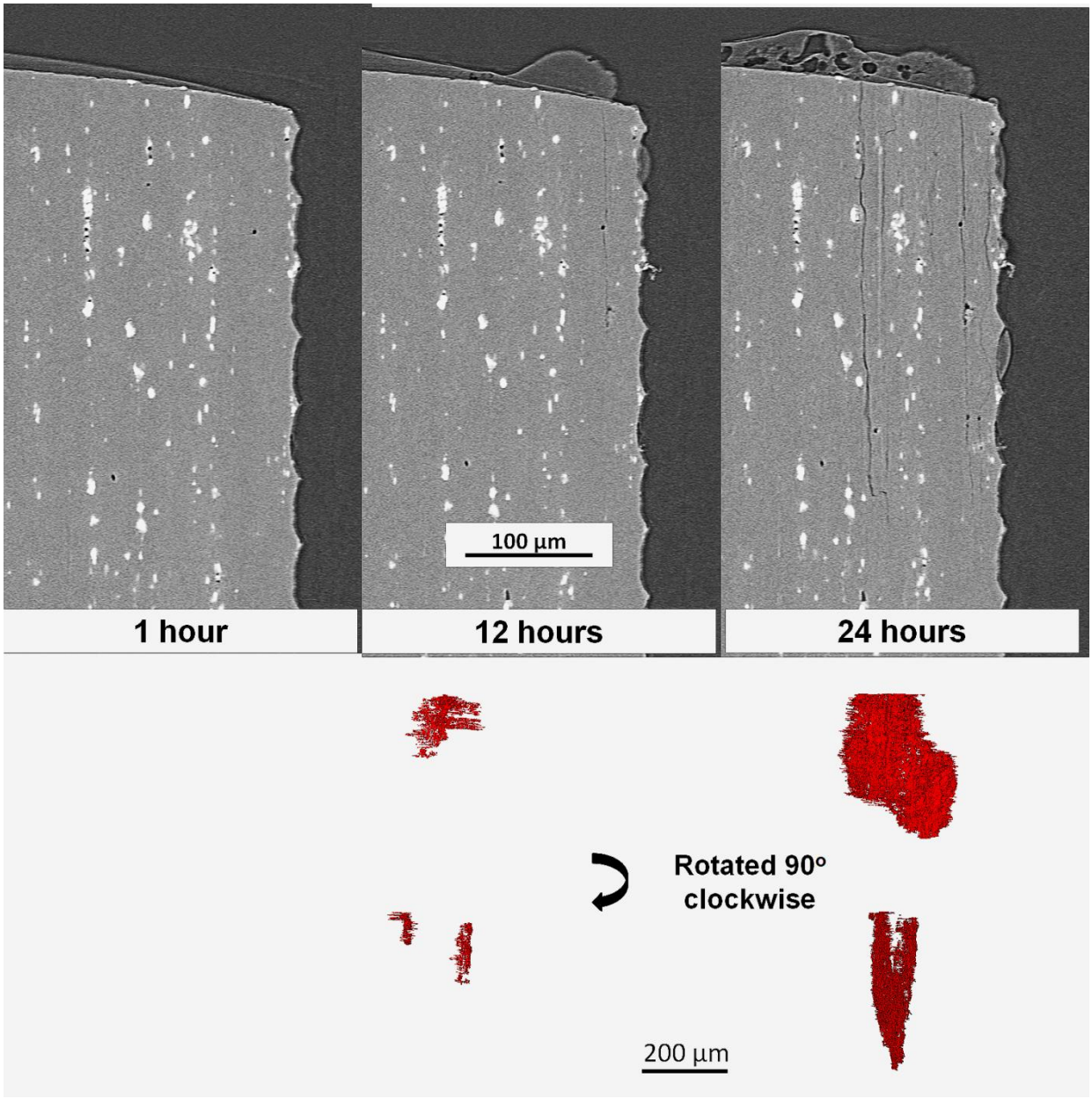


**Figure 4.24 - Vertical sections of tomograms of an AA2024 pin exposed to NaCl solution (CDD ~500 µg/cm$^2$) at 85% RH for the times indicated.. The lower images show the segmented localised corrosion fissures at 0$^o$ (perpendicular to the fissures) and 90$^o$ (parallel to the fissures) for 12 and 24 hours.**

Figure 4.25 shows the development of fissures in another sample exposed to the same conditions as Figure 4.24. At 12 hours, fine fissures are shown, which appear to be intergranular.  At 24 hours, the fissures appear to be wide and deeper, and a new fissure can be seen to the right. Figure 4.26 shows overlaid 3D segmented images of the corrosion volume at 12 hours (blue) and 24 hours (red). It can be seen how fissure growth has taken place both vertically through the pin and laterally through the grain boundary network.

Figure 1.27 plots the measured volume loss over time for MgCl2 samples exposed to different initial CDD values for a 24 hours exposure at 85% RH. As with NaCl samples an increase in the initial CDD resulted in an increase in the corrosion rate through the exposure period. In this case only the highest CDD used showed a large acceleration in corrosion rate during the latter stages of exposure.

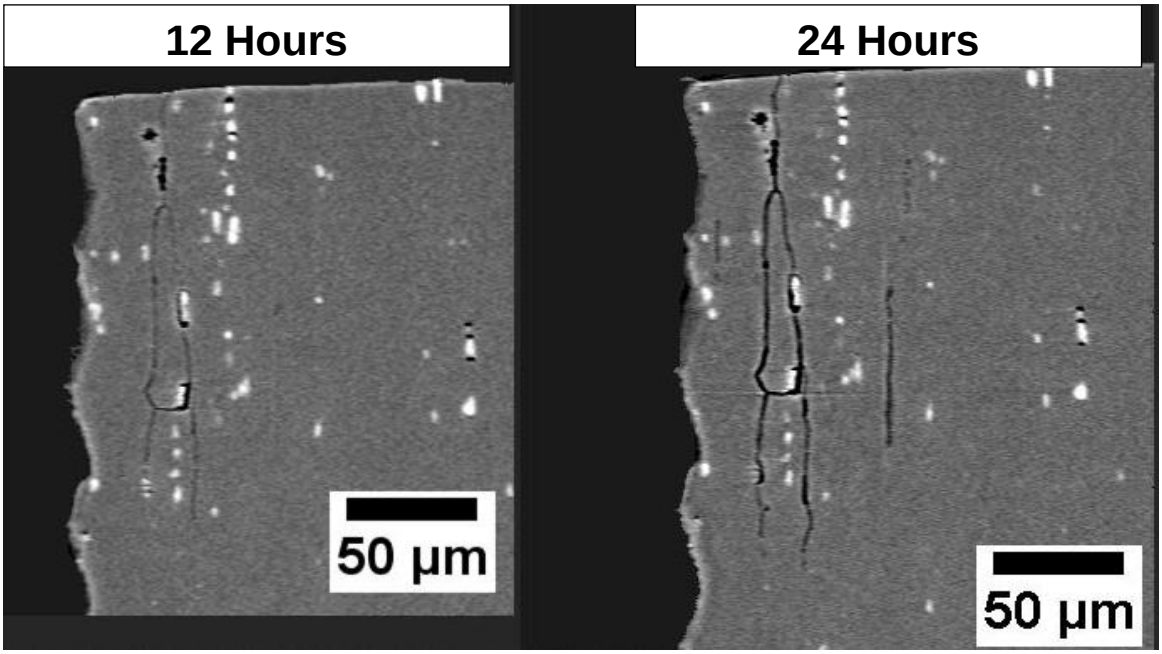


**Figure 4.25 - Vertical sections of tomograms of an AA2024 pin exposed to NaCl solution (CDD ~500 µg/cm$^2$) at 85% RH for the times indicated.**

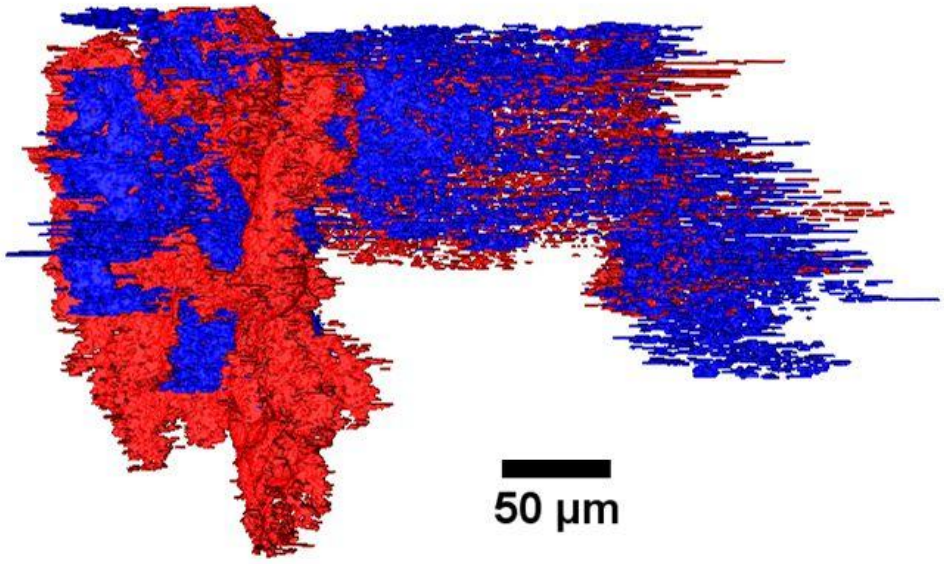


**Figure 4.26 - Fissure volume growth during in-situ measurements, during atmospheric exposure to NaCl solution, initial CDD ~500 µg/cm$^2$, (blue) 12 hours exposure and (red) 24 hours exposure**

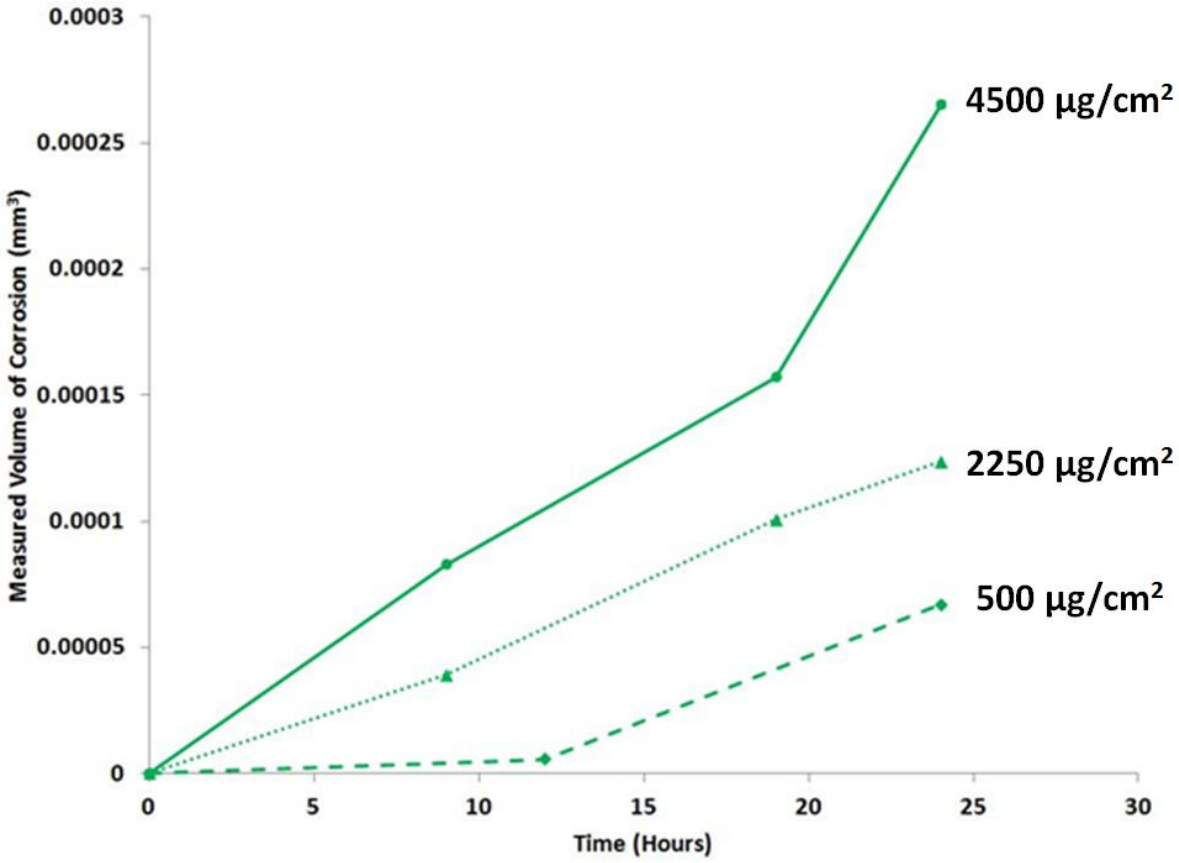


**Figure 4.27 - Measured volume of corrosion as a function of time for AA2024 pin samples exposed to $MgCl_2$ solution droplets, all samples exposed for 24 hours at 85% RH, to different initial CDD's**

### 4.2.7 Effect of Salt Type on the Development of Localised Corrosion in AA2024 Samples during Atmospheric Exposure

A direct comparison of the different salt types used for comparison is made in Figure 4.28, for core conditions, initial CDD of ~500 µg/cm$^2$ and exposure at 85% RH for 24 hours. For each salt type, the near surface section indicates the location of the fissure, the broken line shows point from which the vertical section showing maximum depth was taken. Both vertical sections and 3-D renderings of the volumes show that the morphology of attack observed for the different salt types was similar.

This is further evidenced by the SEM images in Figure 4.29, for the same exposure conditions. For all salt types morphology of attack at the plate surface was comparable.

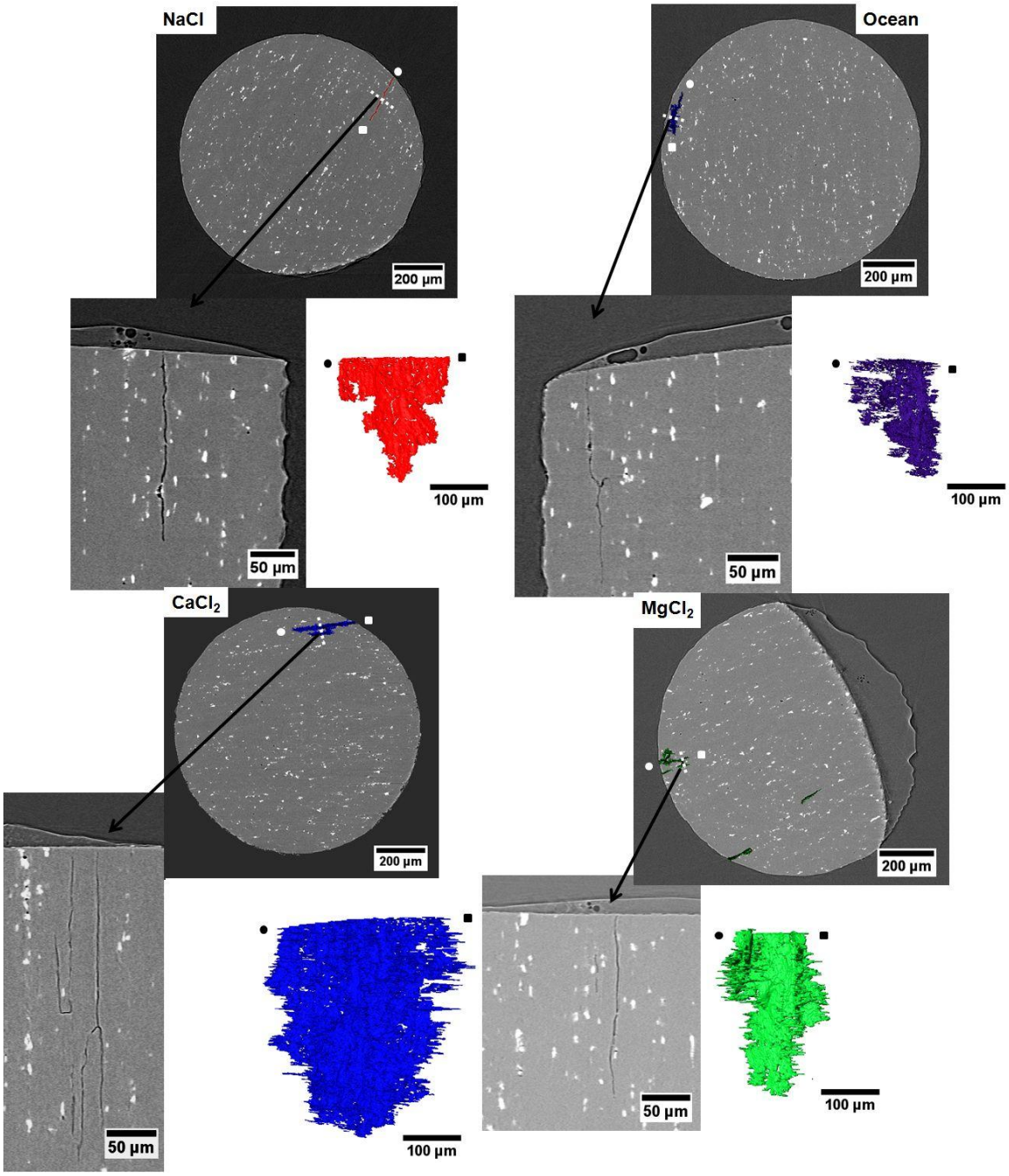


**Figure 4.28 - µCT measurements on the effect of cation type during simulated atmospheric exposure at ~85% RH, for all salts initial CDD was fixed at ~500 µg/cm$^2$. Near surface sections for each show highlighted fissure with broken line indicating where vertical section with maximum depth was located. Orientation of 3-D reconstructed volume is indicated by circle and dot markers.**

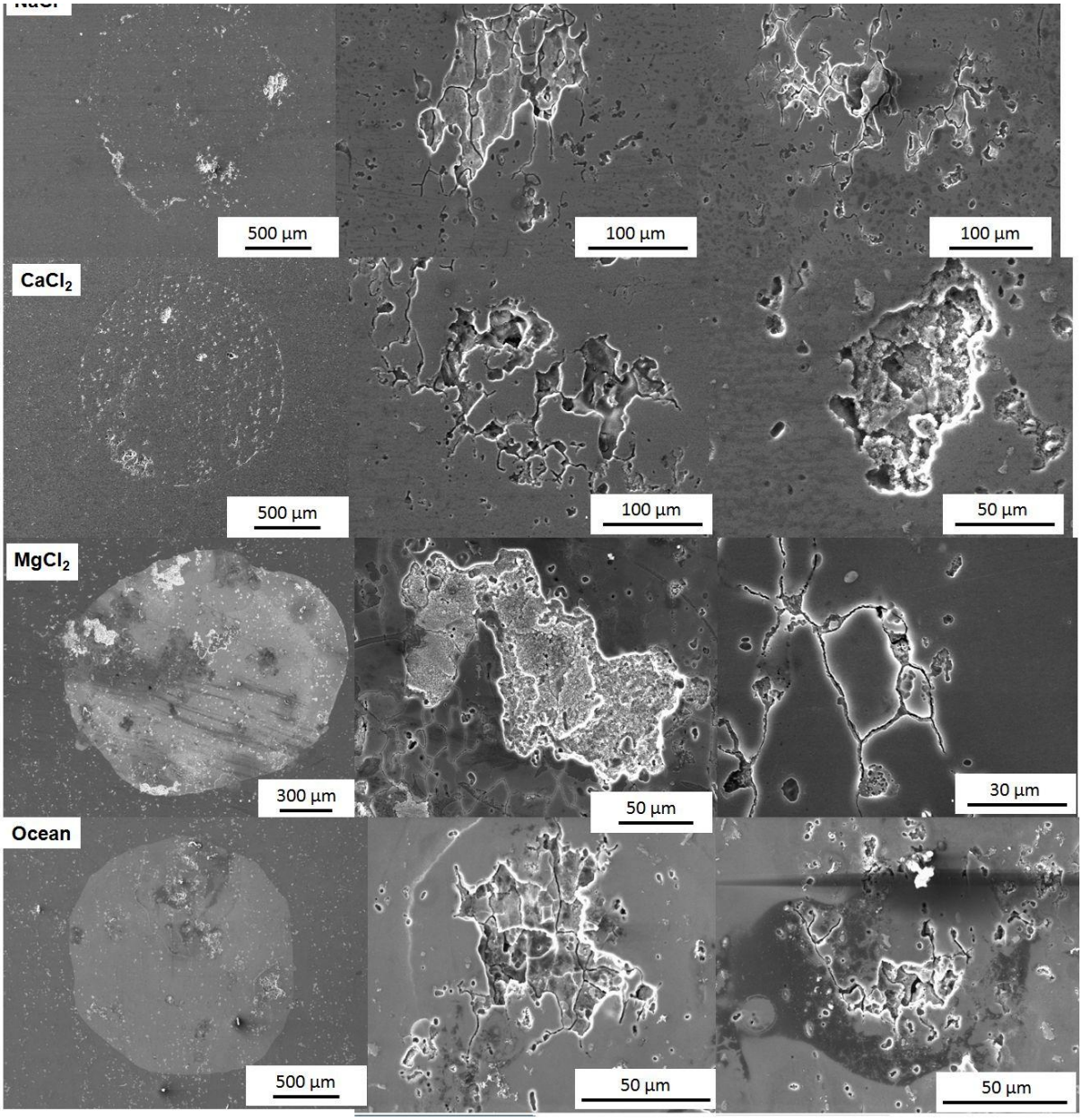


**Figure 4.29 - Secondary electron SEM images showing effect of cation type during simulated atmospheric exposure at ~85% RH, for all salts initial CDD was fixed at ~500 µg/cm$^2$**

Figure 4.30 plots the measured volume of corrosion over time for different salt types exposed at the core condition of 500 µg/cm$^2$ to an environment of 85% RH for a period of 24 hours. It can be seen that for typical development of fissures, the end

volume of damage was comparable for NaCl, $MgCl_2$ and simulated ocean water, but $CaCl_2$ experienced a greater corrosion rate and final amount of damage. It was observed that for $CaCl_2$ corrosion rate remained relatively constant or indeed showed a slight increase during the second half of the exposure period, whilst for other salt types the rate appeared to decrease slightly during the second half of the exposure period.

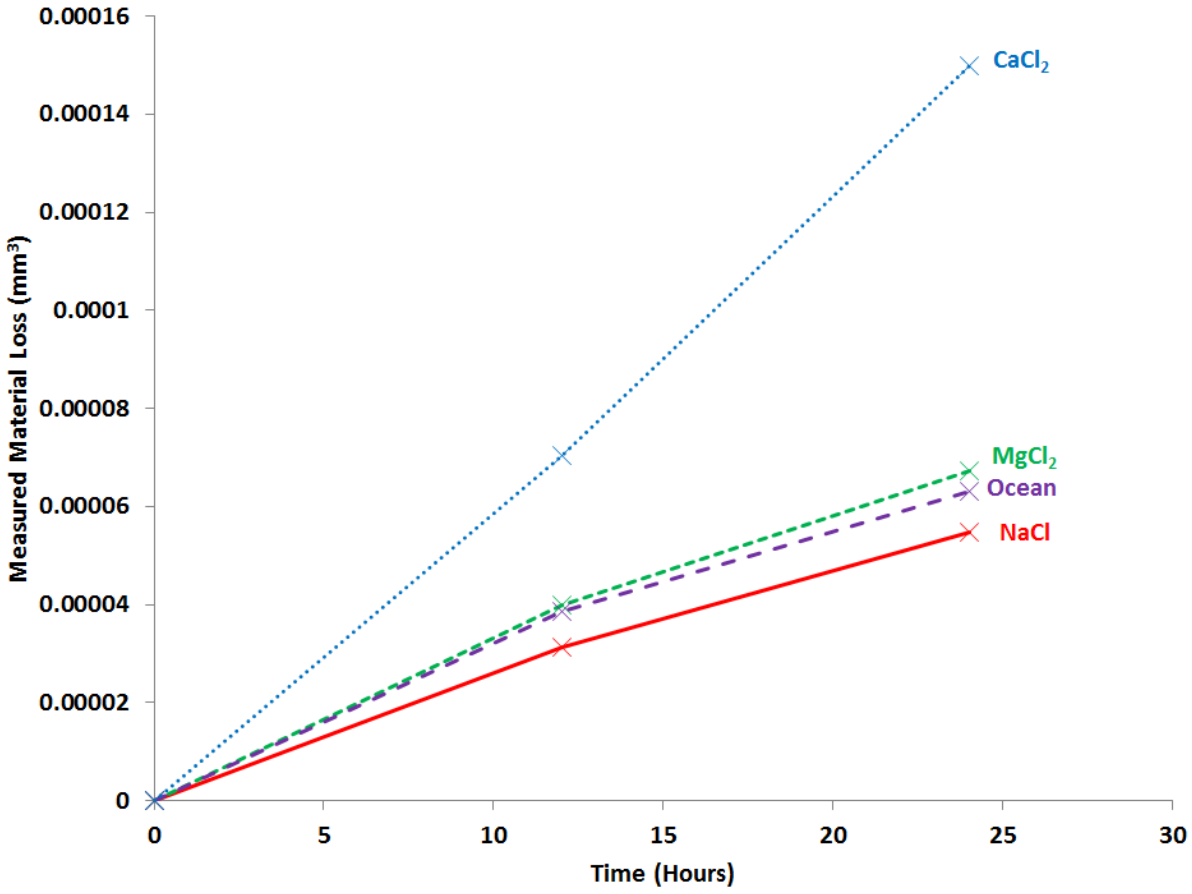


**Figure 4.30 - Measured volume of corrosion as a function of time for AA2024 pin samples exposed to solution droplets of differing salt type, samples exposed for 24 hours at 85% RH, to initial CDD of ~500 µg/cm$^2$**

### 4.2.8 Influence of Relative Humidity on the Development of Localised Corrosion in AA2024 Samples During Atmospheric Exposure

Influence of RH on the rate and development of localised corrosion in AA2024 samples is shown in Figure 4.31-Figure 4.37. Figure 4.31 plots the maximum measured depth of localised corrosion in AA2024 pin samples as a function of RH for a fixed initial CDD. It can be seen that there is a marked influence on the maximum depth of fissure to the effect that as RH increases the maximum fissure depth increases accordingly. The indication is that $CaCl_2$ results in a marginal increase in fissure depth as compared with the other salt types studied.

Figure 4.32 and Figure 4.33 show SEM images of AA2024 plate samples with NaCl solution droplets exposed to 75% and 85% RH respectively. It can be seen that localised corrosion was observed in both cases, for 59% RH which was the next RH considered no evidence of localised corrosion was observed for NaCl solutions.

Tomography measurements were made over a wider range of RH values for for $CaCl_2$ solution droplets on AA2024 pins, examples of typical reconstructions for the range of 33-85% RH are shown in Figure 4.34. From top left (85% RH) it is evident that as RH is decreased there is an associated decrease in the size both in terms of depth (vertical sections) and volume (3-D reconstruction) of the amount of localised attack. It is also interesting to note that as RH is reduced an increase in the number of sites is observed.

Figure 4.35 shows the same behaviour for samples exposed to $MgCl_2$ solution droplets over an RH range of 45-85% RH. Behaviour for $MgCl_2$ samples was the

same as that observed for the $CaCl_2$ ones, with higher RH's resulting in greater depth of fissure and greater final volume of corrosion. Similarly to the $CaCl_2$ samples as RH decreased there was an increase in the number of localised sites, although this effect was less pronounced than in the former.

Figure 4.36 shows the same series of images over the RH range 33-85% RH for samples exposed to solutions of substitute ocean water. Again as the RH of the environment is reduced the depth of localised corrosion as well as the measured volume of corrosion are in turn reduced. As RH is reduced towards DRH of NaCl which is the major component of the substitute ocean water there is an increase in the number of sites, but below this RH the number of sites begins to drop once more.

Measured volume of corrosion in AA2024 pin samples from µCT measurements made through a range of RH's from 33-85%, is plotted in Figure 4.37. From left to right as RH is increased the measured volume of corrosion increases for all salt types. For all RH values the greatest volume of measured material loss is observed for samples exposed to droplets of $CaCl_2$ solution. For other salt types measured material loss is comparable with some outliers, at the core exposure RH of 85%, NaCl, $MgCl_2$ and substitute ocean water exhibited a very similar volume loss.

In addition as a control against artificial acceleration in quantities of corrosion due to radiation induced beam damage, control samples were run ex-situ and measured only once. These samples showed comparable volumes of material loss to those which were measured multiple times, indicating that the influence of beam damage on the development of localised corrosion is limited.

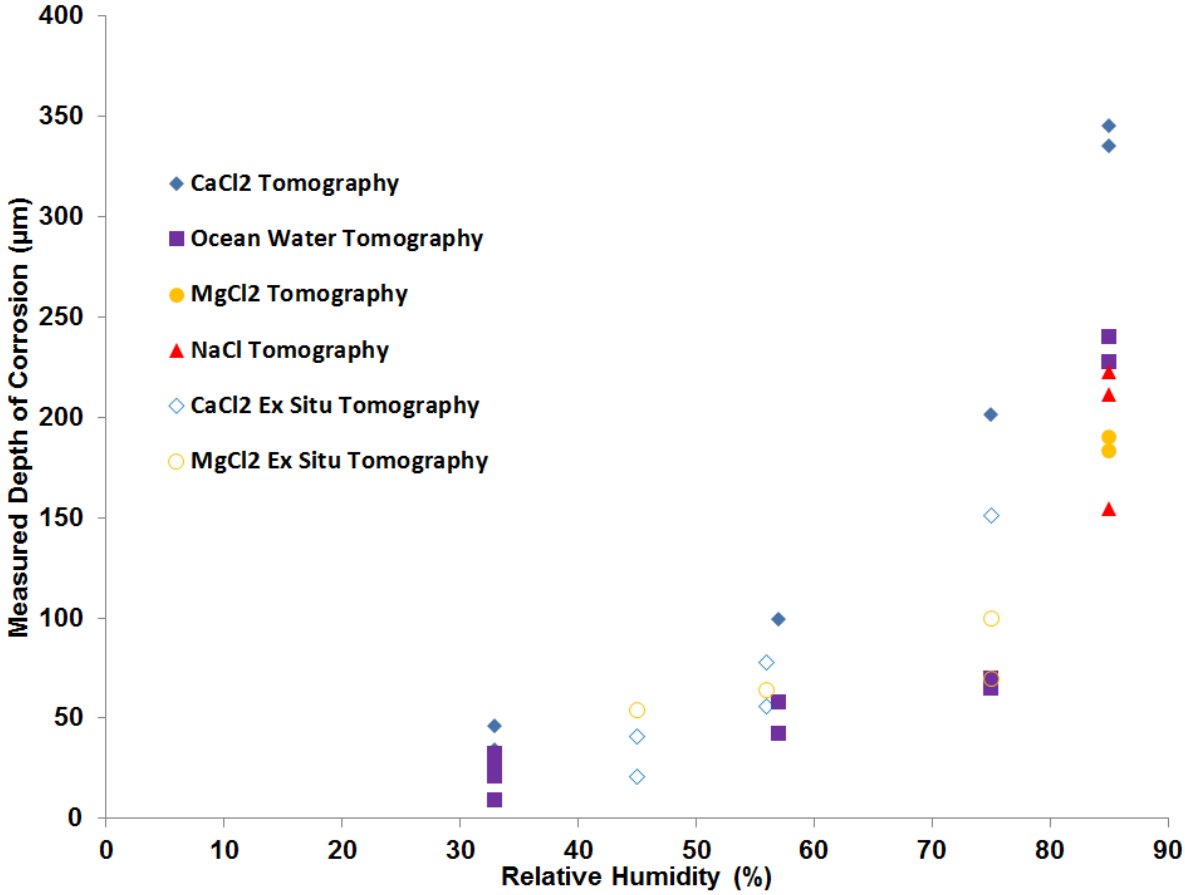


**Figure 4.31 - Maximum measured depth of localised corrosion following 24 hours exposure as a function of RH, for an initial CDD of ~500 µg/cm$^2$, for different salt types during µCT and lab based measurements**

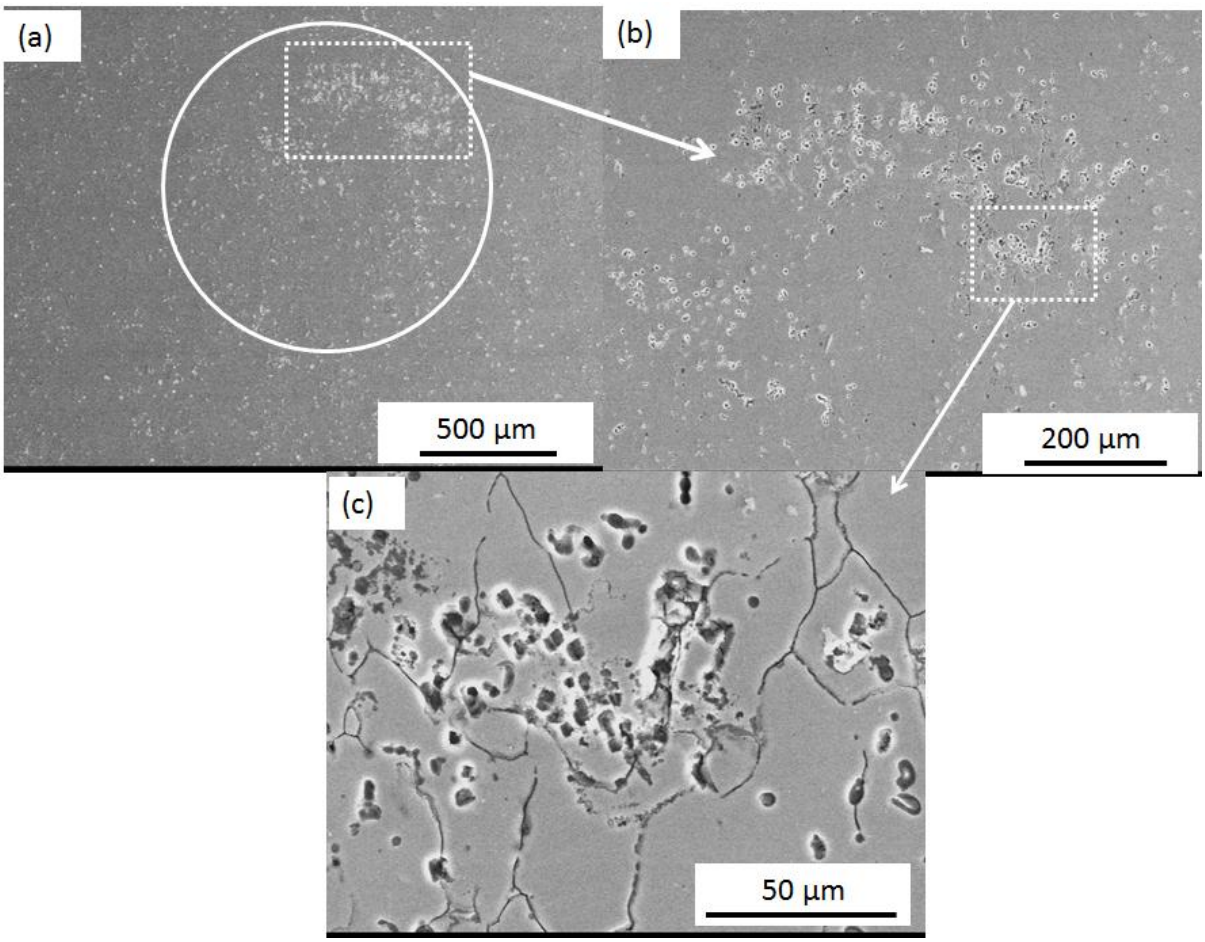


**Figure 4.32 - Secondary electron SEM images of localised corrosion on AA2024 surface following 24 hours exposure at ~75% RH, location of original droplet is shown by solid white circle, with rectangles indicating locations of insets**

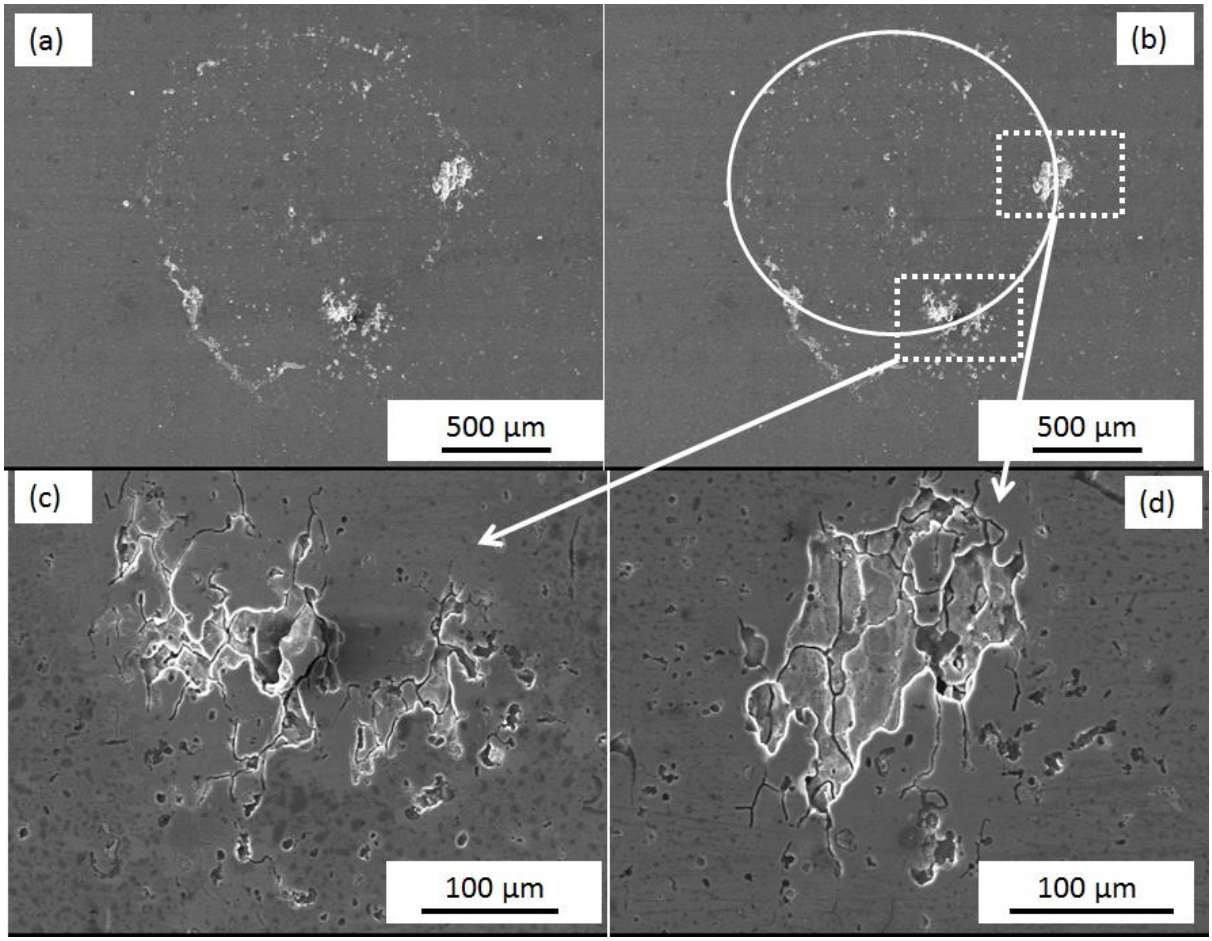


**Figure 4.33 - Secondary electron SEM images of localised corrosion on AA2024 surface following 24 hours exposure at ~85% RH, location of original droplet is shown by solid white circle, with rectangles indicating locations of insets**

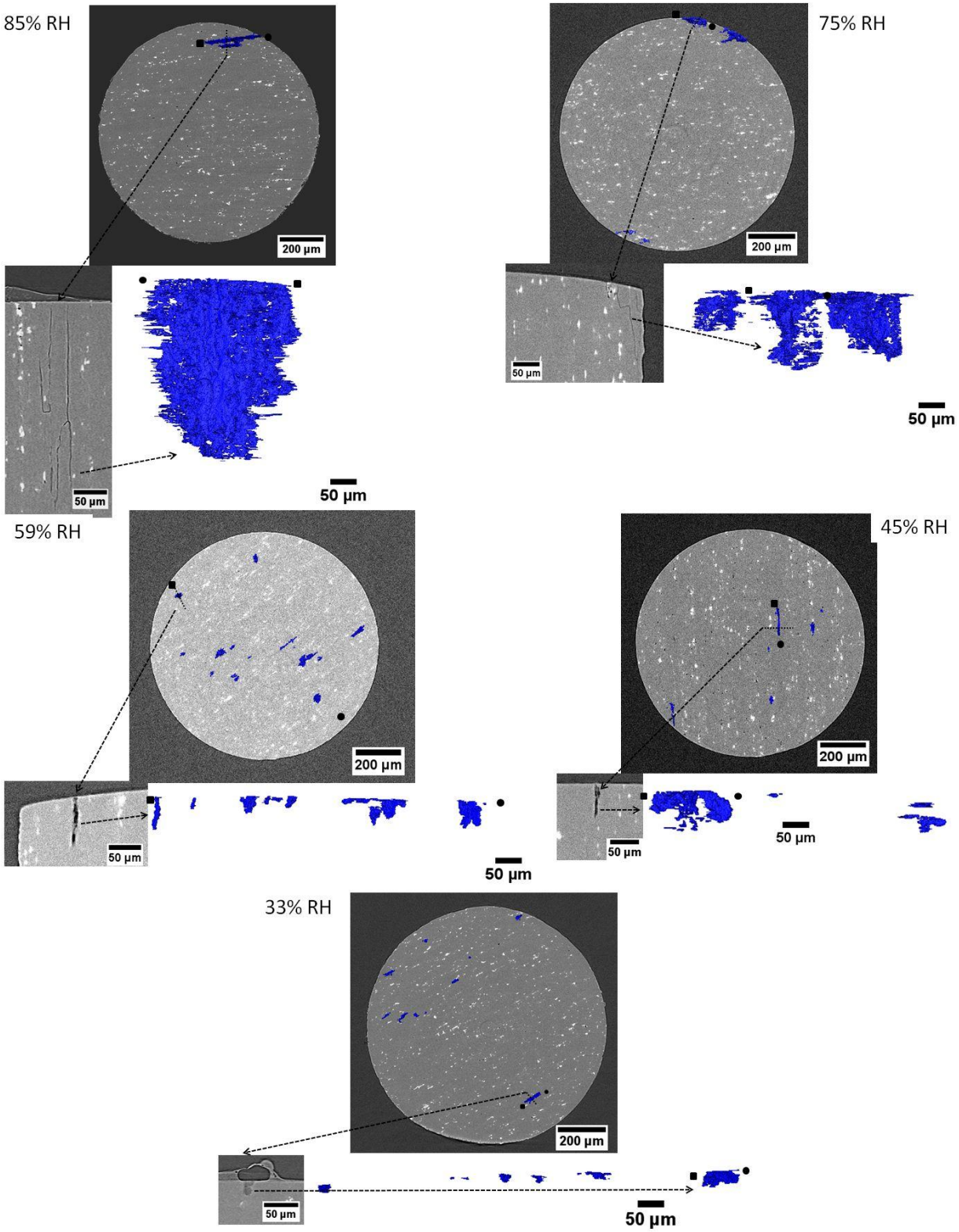
85% RH
200 µm
50 µm
50 µm
75% RH
200 µm
50 µm
50 µm
59% RH
200 µm
50 µm
50 µm
45% RH
200 µm
50 µm
50 µm
33% RH
200 µm
50 µm
50 µm

**Figure 4.34 - Tomographic sections from AA2024 pin samples, horizontal and vertical showing influence of exposure RH (33-85%) on development of localised corrosion under $CaCl_2$ solution droplets, CDD fixed at ~500 µg/cm$^2$**

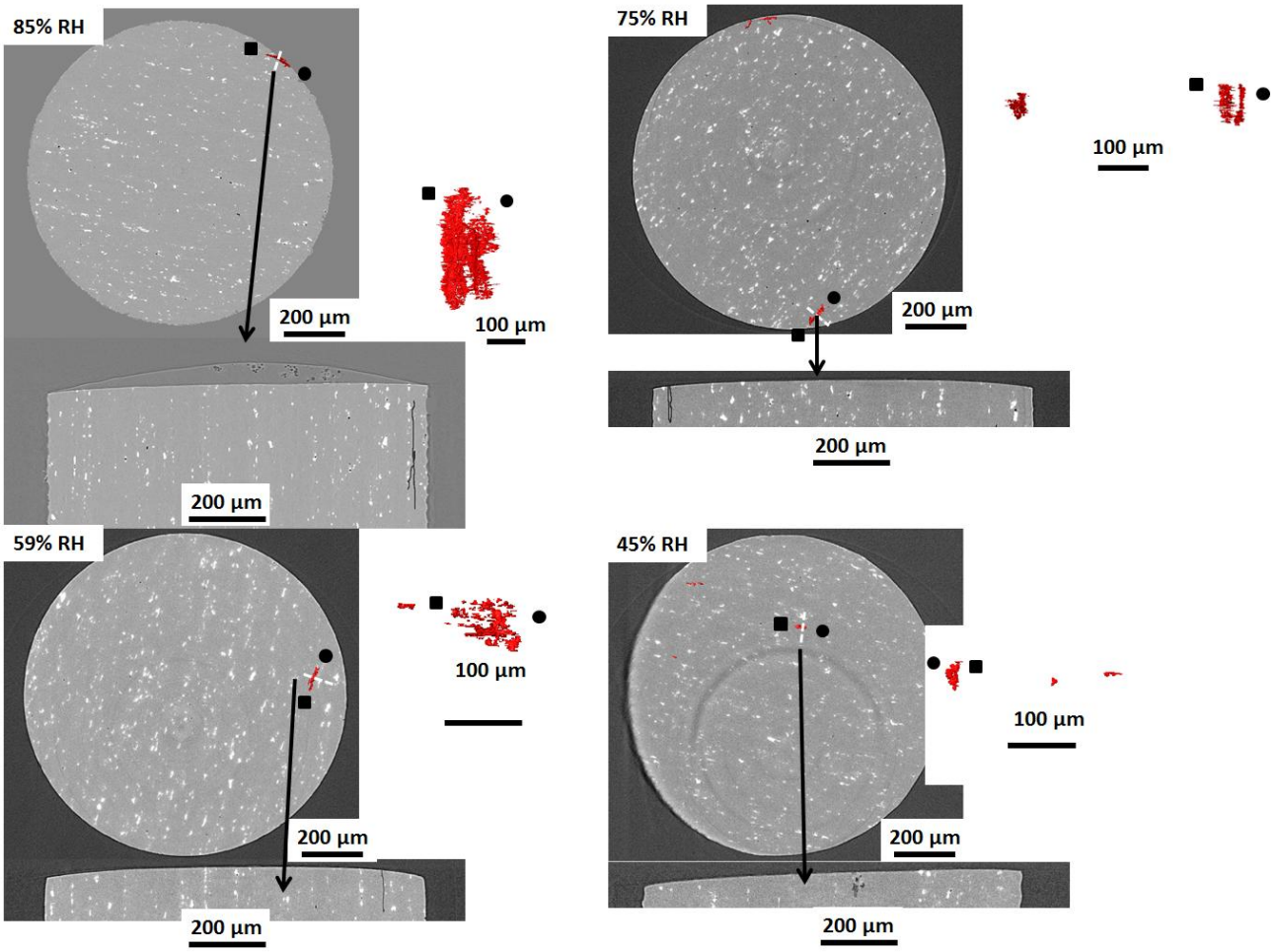


**Figure 4.35 - Tomographic sections from AA2024 pin samples, horizontal and vertical showing influence of exposure RH (45-85%) on development of localised corrosion under $MgCl_2$ solution droplets, CDD fixed at ~500 µg/cm$^2$**

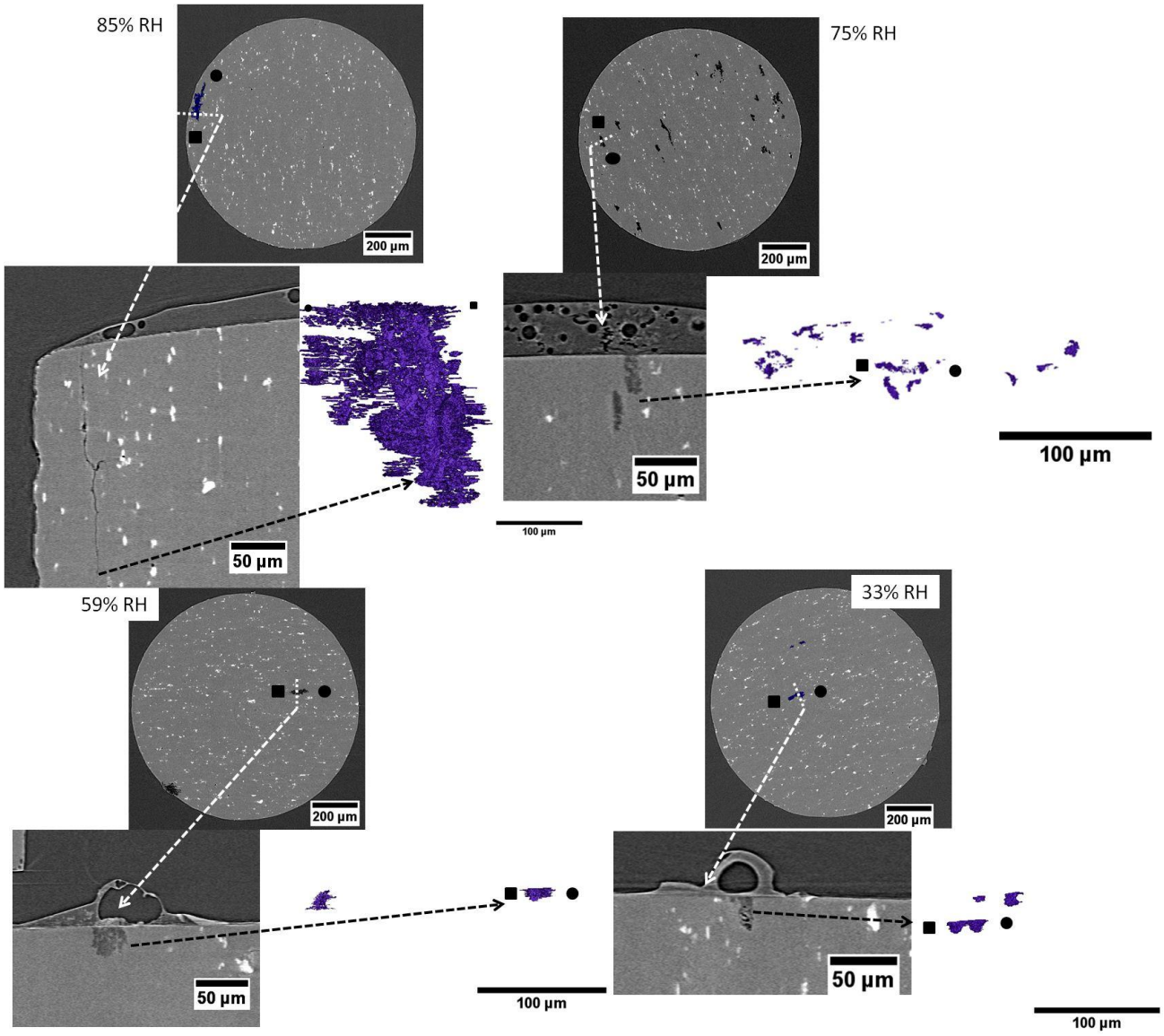


**Figure 4.36 - Tomographic sections from AA2024 pin samples, horizontal and vertical showing influence of exposure RH (33-85%) on development of localised corrosion under simulated ocean water solution droplets, CDD fixed at ~500 µg/cm$^2$**

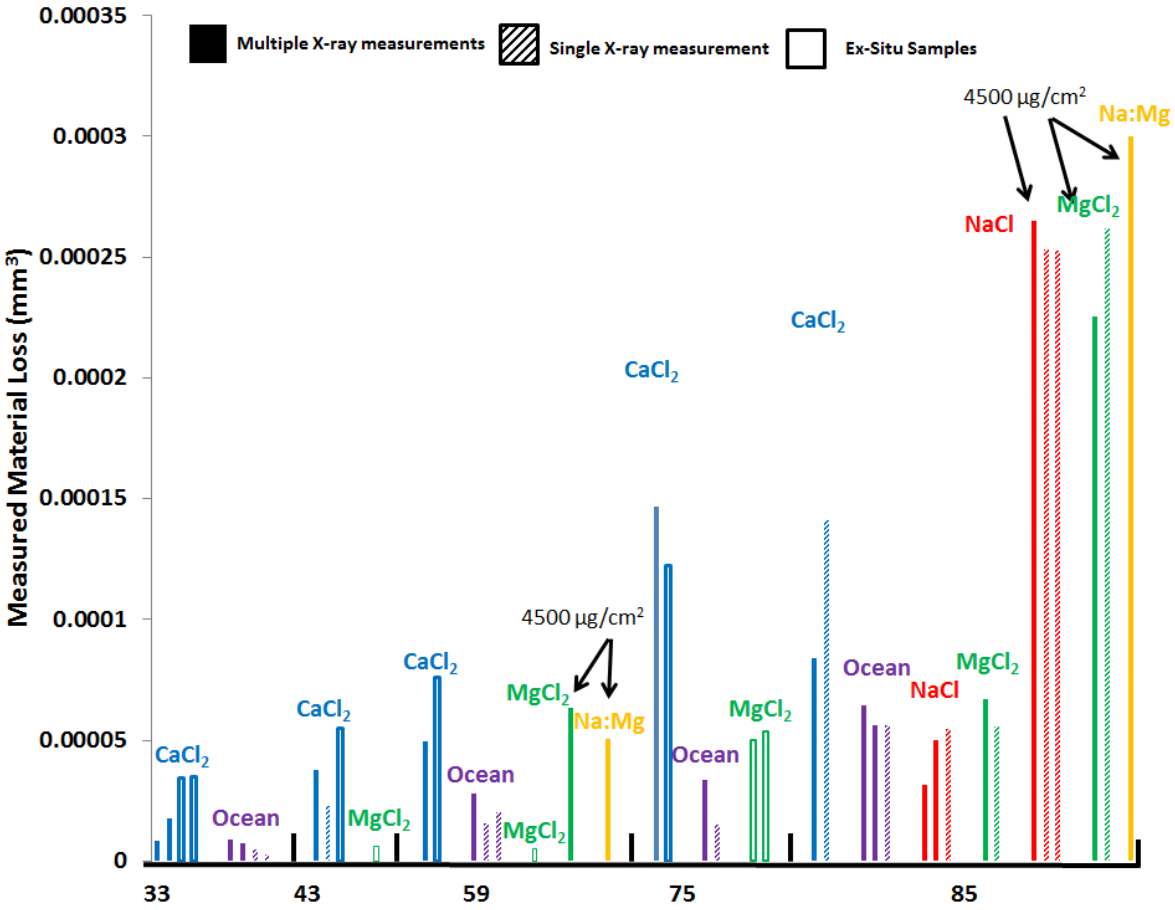


**Figure 4.37 - Measured volume of localised corrosion following 24 hours exposure as a function of RH, for an initial CDD of ~500 µg/cm$^2$**

### 4.2.9 Time Dependent Measurements on the Development of Localised Corrosion in AA2024 Samples during Atmospheric Exposure as a Function of Relative Humidity

Figure 4.38 plots the measured material loss in AA2024 pin samples during atmospheric exposure to $CaCl_2$ solutions at a CDD of 500 µg/cm$^2$ exposed to a range of RH's. For higher RH values the corrosion rate was significantly increased when compared to that seen for samples exposed at lower RH environments. In addition for lower RH exposures the corrosion rate remains at a fairly constant level

throughout exposure, whilst for higher RH values there is an increase during the second half of the exposure period.

Figure 4.39 shows the development of a fissure in during exposure to CaCl2 solution droplets, it can be seen that growth takes place vertically and laterally along the grain boundary network.

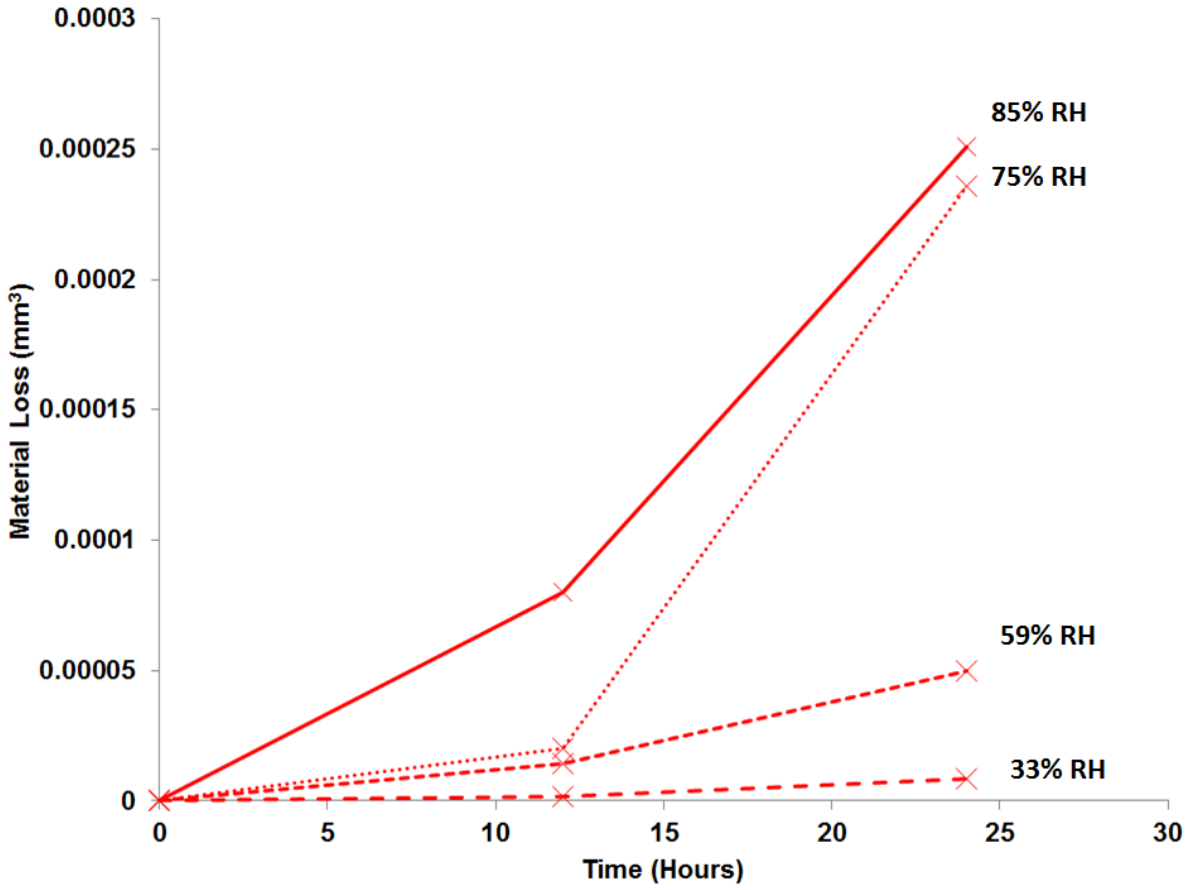


**Figure 4.38 - Measured volume of corrosion as a function of time for AA2024 pin samples exposed to $CaCl_2$ solution droplets, all samples exposed for 24 hours over a range of RH environments**

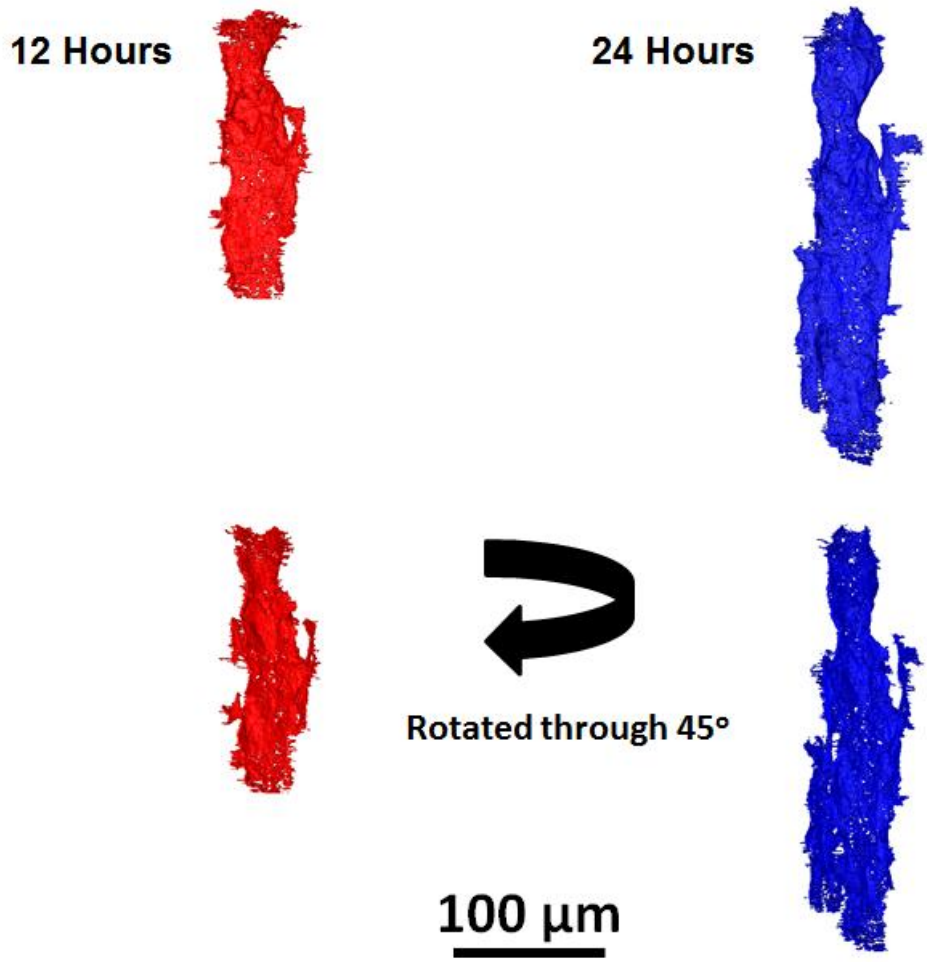


**Figure 4.39 - 3-dimensional reconstruction of fissure formed at 85% RH under a $CaCl_2$ solution of initial CDD ~500 µg/cm$^2$, left: following 12 hours exposure, right: following 24 hours. Sample is shown head on and through a 45$^o$ rotation.**

Figure 4.40 plots the measured material loss in AA2024 pin samples during atmospheric exposure to substitute ocean water solutions at a CDD of ~500 µg/cm$^2$ exposed to a range of RH's. For higher RH values the corrosion rate was significantly increased when compared to that seen for samples exposed at lower RH environments. In addition for lower RH exposures the corrosion rate does not increase as significantly as for higher RH exposures during the latter stages of the exposure period.

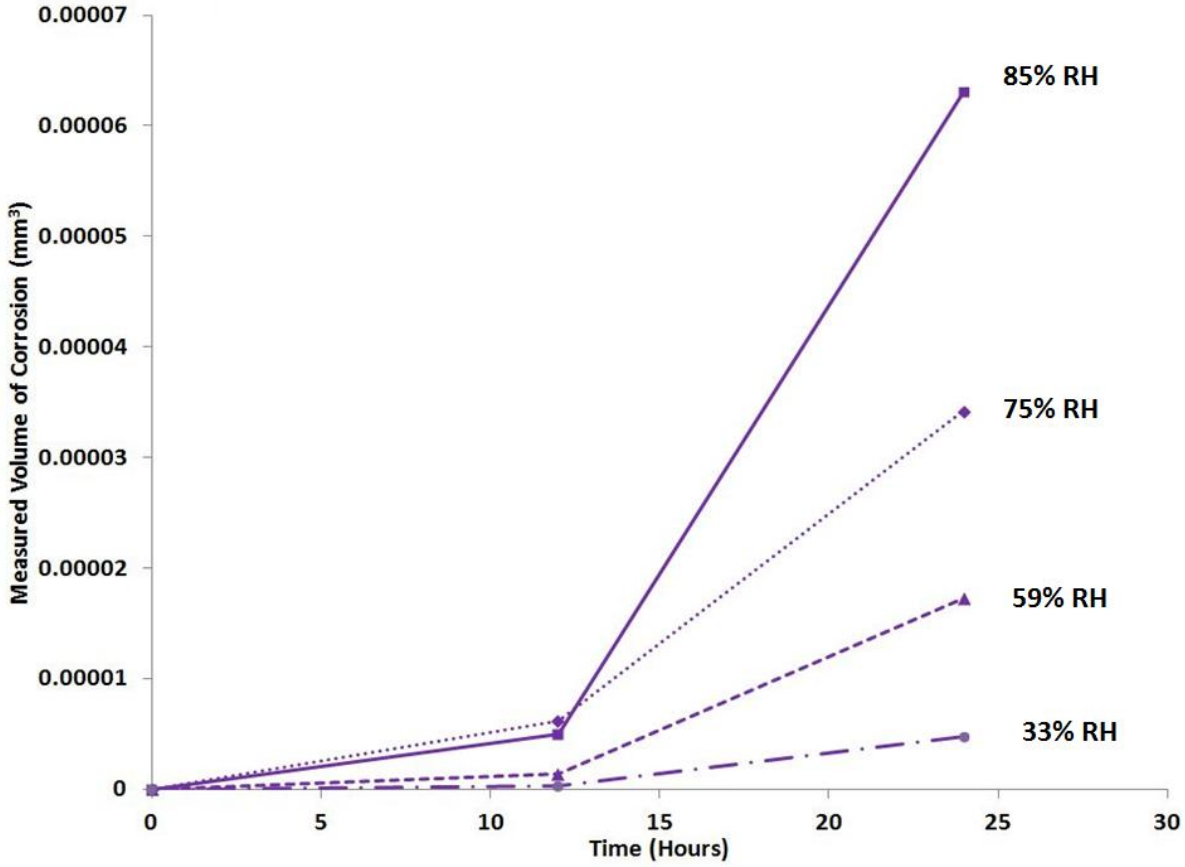


**Figure 4.40 - Measured volume of corrosion as a function of time for AA2024 pin samples exposed to simulated ocean water solution droplets, all samples exposed for 24 hours over a range of RH environments**

## 4.3 Discussion

### 4.3.1 Microstructural Influence on the Development of Localised Corrosion under Atmospheric Conditions

Microstructure of AA2024 is well known to be influential on the development of localised corrosion attack. As such basic characterisation of the important precipitate phases found in the alloy was carried out, the basic compositions identified were $Al_6(CuMnFeSi)$, $Al_2CuMg$ (S-phase) and $Al_2Cu$ (θ-phase). These are typically of the

agreed elemental composition from previous bodies of work [16, 23, 24, 196-201], in addition the size range of particles observed herein and the suggested shapes are similar to those suggested as being typical [16, 23, 24, 196-201]. Figure 4.1 and Figure 4.2 provide evidence of the primary particles identified during this work, showing the 3 main precipitate phases and maps of the elemental distribution in θ-phase particles respectively. Further example of the microstructure typically observed in the pin samples used during this work is shown in Figure 4.3, alignment of the precipitate phases within the pin along the direction of rolling of the alloy. In addition the magnified inset image demonstrates that the resolution of the µCT measurements was sufficient to distinguish clearly the precipitate phases >1 µm in size.

### 4.3.2 Environmental Influence on Droplet Behaviour

Influence of the exposure environment on the behaviour of atmospheric salt deposits and droplets has been covered to some extent in previous bodies of work [63, 112, 117, 130, 136, 138, 162, 202, 203]. However little work has focussed on the how the environment influences the behaviour of atmospheric droplets on metallic samples. Tsutsumi [136] measured the equilibrium concentration of $MgCl_2$ solutions as a function of RH, and values calculated herein based on an equation proposed by Wheeler [122] produced a good agreement. Once droplets reached equilibrium with their environment (Figure 4.5) volume was maintained, both initial CDD (Figure 4.6) and environment RH (Figure 4.11) affected the droplet size and shape.

It has been shown that it is possible to predict with some accuracy the equilibrium volume of solution, and as such the height of an atmospheric droplet at equilibrium,

by comparing calculated and measured values (Figure 4.7,Figure 4.8, Figure 4.9,Figure 4.10), for a fixed sample surface area. Droplet height and volume are important as they influence the properties of the electrolyte solution, such as solution concentration and solution resistance[121, 204], this is discussed further in the coming paragraphs. Development of localised corrosion measured using µCT, was seen to follow the traditionally reported attack of grain boundaries typical of AA2024, in regions of copper depletion [40, 47, 100, 102], a typical example of attack at grain boundaries is highlighted in Figure 4.14. Visualisation of localised corrosion in AA2024 using µCT has previously been carried in a number of bodies of work[92, 106-108], and both the reconstructed slices and volumes are comparable in morphology during this work (Figure 4.12). The limitations of the experimental technique are primarily related to the resolution achievable, and whilst sufficient to observe features to the order of 1 µm in size, some fissures observed in lab based samples were significantly smaller in scale to the order of 200 nm (Figure 4.13). Resolution limits account for some of the gaps which are seen in the 3-D reconstructions of fissures in this work; other gaps are the result of the presence of Cu rich phases around which localised attack has developed.

Further influence of microstructure on the development of localised was observed with fissures initiating at precipitate intermetallic phases, this is a well-documented process in AA2024 [5, 28, 90, 101] under immersion conditions. It is important to know that the mechanics of initiation and propagation of localised corrosion under atmospheric exposure conditions is similar to those under fully immersed conditions.

### 4.3.3 Influence of Initial CDD

As initial CDD was increased the measured volume of localised corrosion increased during atmospheric exposure of AA2024 samples. Up to a given CDD value the maximum depth of localised attack was observed to increase above this little increase in depth was observed. As has been shown growth of fissures within pin samples follows the pathway of the most susceptible grain boundary within the alloy. Growth takes place vertically down the pin samples along the direction of rolling initially, following this growth laterally along the grain boundary network takes place and fissures become more complex in nature Figure 4.18.

Lateral growth of fissures begins to take place once the length of the ionic migration pathway to the active front deeper in the sample is increased. Beyond a certain depth growth of fissure vertically reaches a limiting depth , which is reached more rapidly for higher initial CDD's, owing to the greater lateral growth which is observed. This suggestion of a limiting depth being attained in AA2024 has been reported previously [43, 92, 106, 108, 205], and Ghali has observed the lateral growth of fissures following attainment of limiting depth[43, 205], however it was not clear if lateral growth occurred prior to attainment of maximum depth. From the evidence herein, it can be seen that lateral growth begins to occur prior to the attainment of a limiting (maximum) depth. With regards to limiting depth in this work there was some discrepancy observed between the samples used in the lab and for µCT measurements. A difference in the rate of development of localised corrosion in AA2024 using different techniques has previously been observed [91]. This is likely accounted for by the greater number of sites seen in the lab samples owing to their

not being limited in terms of size, the result being that the time required to obtain the maximum depth is increased, or indeed the limiting depth is reduced.

Increased corrosion damage observed as a function of increasing initial CDD is linked to the behaviour of droplets on the sample surface. As has been discussed the higher the initial CDD for a fixed RH value the greater the droplet volume and height for the same concentration at equilibrium. Solution conductivity will remain unchanged whilst RH remains at a constant, as solution conductivity is typically proportional to concentration[121, 123, 204]. However, given a droplet of greater height and volume for a fixed concentration, the number of ions per unit area is reduced significantly, which results in a lowered solution resistance between the anode and the cathode, reducing the IR drop [63, 121, 204]. This also serves to facilitate and drive ionic migration within the droplet as a whole resulting in an overall increase in the rate of corrosion.

Time dependent measurements made on the development of localised corrosion fissures in AA2024 pin samples using µCT indicated that fissure growth under a droplet which remains wet will proceed in a continual manner. With the growth rate being dependent on the initial CDD for both $MgCl_2$ and NaCl solution droplets, to the effect that as initial CDD is increased the rate of corrosion measured increases. Growth of fissures took place both vertically and laterally as has been outlined previously, but over time existing fissures were also seen to widen. Higher CDD's tended to show acceleration in the measured corrosion rate whilst lower CDD's tended to remain at a more steady state. As has been outlined over the previous paragraphs, the lower CDD samples with smaller droplets on the surface experience a greater resistance in solution reducing the overall corrosion rate. Lowered solution

resistance allows for faster transport of ions through solution, which helps sustain the increase in corrosion rate observed in the higher CDD samples.

### 4.3.4 Influence of Salt Type

Influence of salt type was considered for NaCl, $MgCl_2$, $CaCl_2$ and substitute ocean water solution droplets. Evidence suggests that $CaCl_2$ solutions result in a slight increase in the corrosion rate in AA2024 samples, as measured volume loss and maximum measured depth was increased slightly when compared to other salt types. It has previously been determined that $CaCl_2$ solutions exhibit a lower pH [153, 157, 206], due to its preferential tendency to undergo hydrolysis [158]. pH values were measured for the solutions used herein using a pH meter and universal indicator, and in order of ascending pH $CaCl_2$ < $MgCl_2$ < Ocean water < NaCl. Slight lowering of pH may result in a shortened induction time to stable pit formation and a more aggressive solution which helps sustain a slightly elevated corrosion rate when compared with the other solutions used. Further work on the corrosion behaviour of AA2024 under solutions of $CaCl_2$ is required in order to provide a better understanding of the processes taking place, and provide confirmation of this hypothesis.

With regards to the morphology of the localised attack, in all cases behaviour was observed to similar (Figure 4.28 and Figure 4.29), this is in good agreement with observations made on studies of AA2024 under simulated ocean water[96, 109], and under NaCl [28, 51, 92, 106] solutions. This indicates that morphology of localised

corrosion in AA2024 appears to be dominated primarily by the microstructure of the alloy rather than the solutions to which it may be exposed.

### 4.3.5 Influence of Relative Humidity

In addition to the influence of initial CDD and salt type on the development of localised corrosion in AA2024 samples the effect of exposure to different RH environments for a fixed initial CDD was considered. It has previously been suggested that RH influences the corrosion rate during atmospheric exposure [92], and in this work it has been shown that RH significantly affects the corrosion rate of AA2024. RH influenced both the maximum depth of localised corrosion and the measured volume of corrosion, to the effect that for all salt types corrosion rate increased as a function of increasing RH.

This can be related again to the behaviour of the droplet on the surface of the sample, with samples showing the greatest amount of attack exposed to conditions where droplets are greater in volume and height. In this case however solution concentrations differ as a function of RH, with an increase in RH resulting in a lowering of the solution concentration. As such this might be the inverse of what is expected with whereby solutions of greater concentration result in more aggressive conditions.

It is known that as solution concentration rises the viscosity of the solution increases alongside [121, 141, 207, 208], which serves to raise the resistance within the atmospheric droplet. As such ionic flow between the cathode and anode is reduced; this lowers the corrosion rate under these exposure conditions. In addition a more

viscous solution slows the diffusion rate of oxygen through the droplet to the cathode, further reducing the corrosion rate.

It has been observed in this work that when RH is reduced the number of sites observed to initiate during µCT measurements was seen to increase (Figure 4.34, Figure 4.35 and Figure 4.36). It is reasonable to assume that the greater solution concentration will likely result in a shorter time to pit initiation, but will reduce the depth to which localised attack is able to penetrate as ionic migration is limited due to raised solution resistance. As such new pit sites will initiate at the surface in preference to continued growth of the existing site, resulting in sequential initiation and growth of new sites under these higher solution concentrations. Further investigation is being carried out into sequential pit initiation and growth at the University of Birmingham.

For all of the RH conditions studied $CaCl_2$ solution droplets resulted in a considerably increased rate of localised corrosion when compared with other salt types. For lower RH values this can be related to the fact that the DRH of $CaCl_2$ is lower than the other salt types, at ~23% RH. As such, an increase in exposure time for these samples results in an increase in the measured amount of corrosion. For higher RH values as has been previously discussed the increase seen for $CaCl_2$, is due to an increased depth and width of fissures possibly resulting from the lowered pH found for the $CaCl_2$ solutions used.

### 4.3.6 Limitations

Considering the possibilities for error with the measurements made during this work, beam damage was one of the primary concerns for which mitigation was required. To compensate control samples were used where a single measurement was made at the end point of exposure, these are plotted on summary plots Figure 4.20 and Figure 4.37. Little influence of artificial increase in the final volume of corrosion was observed, suggesting that for the short ~5 minute measurements made once every 12 hours x-ray exposure had little negative effect on the experiments. However, as mentioned previously there are associated resolution issues with the µCT techniques used, which result in small discontinuities in fissures, these can account for small differences in measured volume and therefore must be considered. In addition there is a certain amount of sample to sample variation in the measured depths and volumes for the µCT samples, which due to the limited time periods available for making measurements cannot be turned into more statistically robust datasets. However, the trends which emerge are consistent across both lab and µCT measurements which gives confidence in the findings.

## 4.4 Conclusions

1. During atmospheric exposure to NaCl and $MgCl_2$ solutions, an increase in the initial CDD results in an increase in the final measured amount of material loss.
2. For 24 hour simulated atmospheric exposures there appears to be a limiting depth of localised attack in the L direction which is reached. After this point

corrosion will expand laterally along susceptible grain boundaries, aligned parallel to the direction of rolling of the alloy.

3. No specific value for the threshold CDD for the occurrence of localised corrosion was determined, but corrosion was observed down to a CDD of ~1 µg/cm$^2$
4. There is an associated increase in the measured material loss with an increase in environmental RH for all salt types
5. Above ~59% RH there is a transition from pitting corrosion of limited depth and severity, to more sustained IGC like attack morphology for $MgCl_2$, $CaCl_2$ and simulated ocean water solutions.
6. Microstructure of AA2024 is influential on the localised corrosion behaviour; (a) localised corrosion sites are aligned to the direction of rolling of the alloy, (b)intermetallic precipitate phases provide initiation sites and when aligned in strings through the bulk of the sample can provide preferential pathways for localised attack,(c) fissure development will follow the most susceptible grain boundary pathway

# 5 SECONDARY SPREADING EFFECTS DURING ATMOSPHERIC CORROSION OF AA2024

## 5.1 Introduction

Formation of micro-droplets at the periphery of atmospheric droplets, and a zone of secondary spreading beyond has been observed on several metals previously[142, 143, 145, 147, 151, 209, 210]. Formation of microdroplets and secondary spread zones has been documented occur under natural atmospheric corrosion conditions[112]. Mechanisms of formation and spreading of micro-droplets have been outlined in Section 2.4.3. However, little consideration of spreading behaviour during the atmospheric corrosion of aluminium or AA2024 has been undertaken[145]. Micro-droplets are a precursor to the formation of a secondary spreading zone, the influence of salt type, CDD, RH and exposure time on the development and growth of this secondary spread zone is outlined in this chapter.

## 5.2 Results

### 5.2.1 Formation of Microdroplets

Figure 5.1 shows a droplet of NaCl on the surface of AA2024 plate over the course of 12 hours. Close examination of the droplet shows the appearance of corrosion sites in the lower part of the droplet, and at the edge, fine droplets start to appear. These can be seen at higher magnification in Figure 5.2, where initial formation was seen to take place within the first few hours of atmospheric exposure. Some microdroplets appear to be separate from the main droplet. Over time the initial micro-droplets

were observed to coalesce into a thin electrolyte layer of secondary spreading around the original droplet.

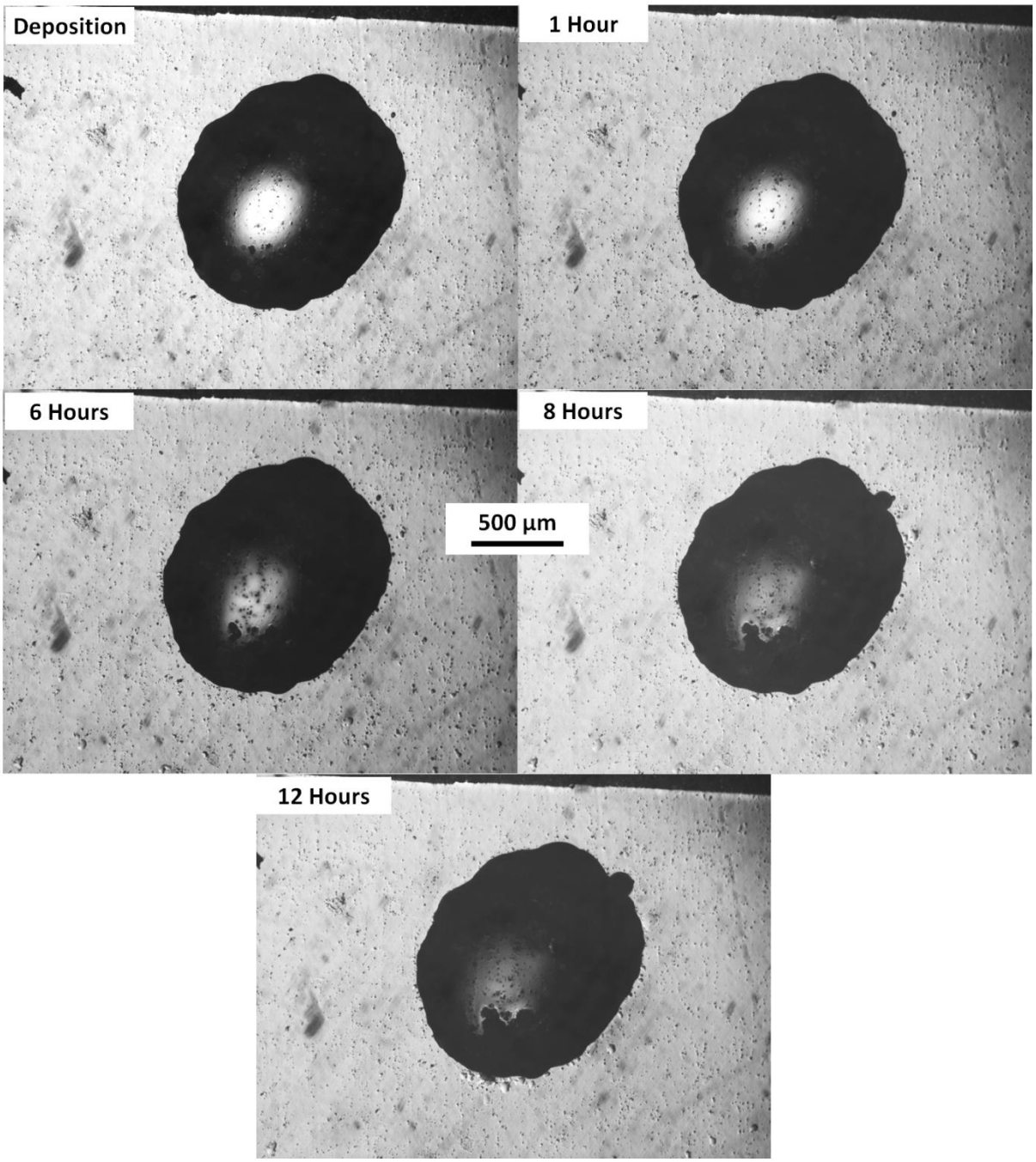


**Figure 5.1 – Optical images showing the formation of micro-droplets at the periphery of main droplet on AA2024 surface as a function of time, for NaCl droplet at ~85% RH for initial CDD of 500 µg/cm$^2$**

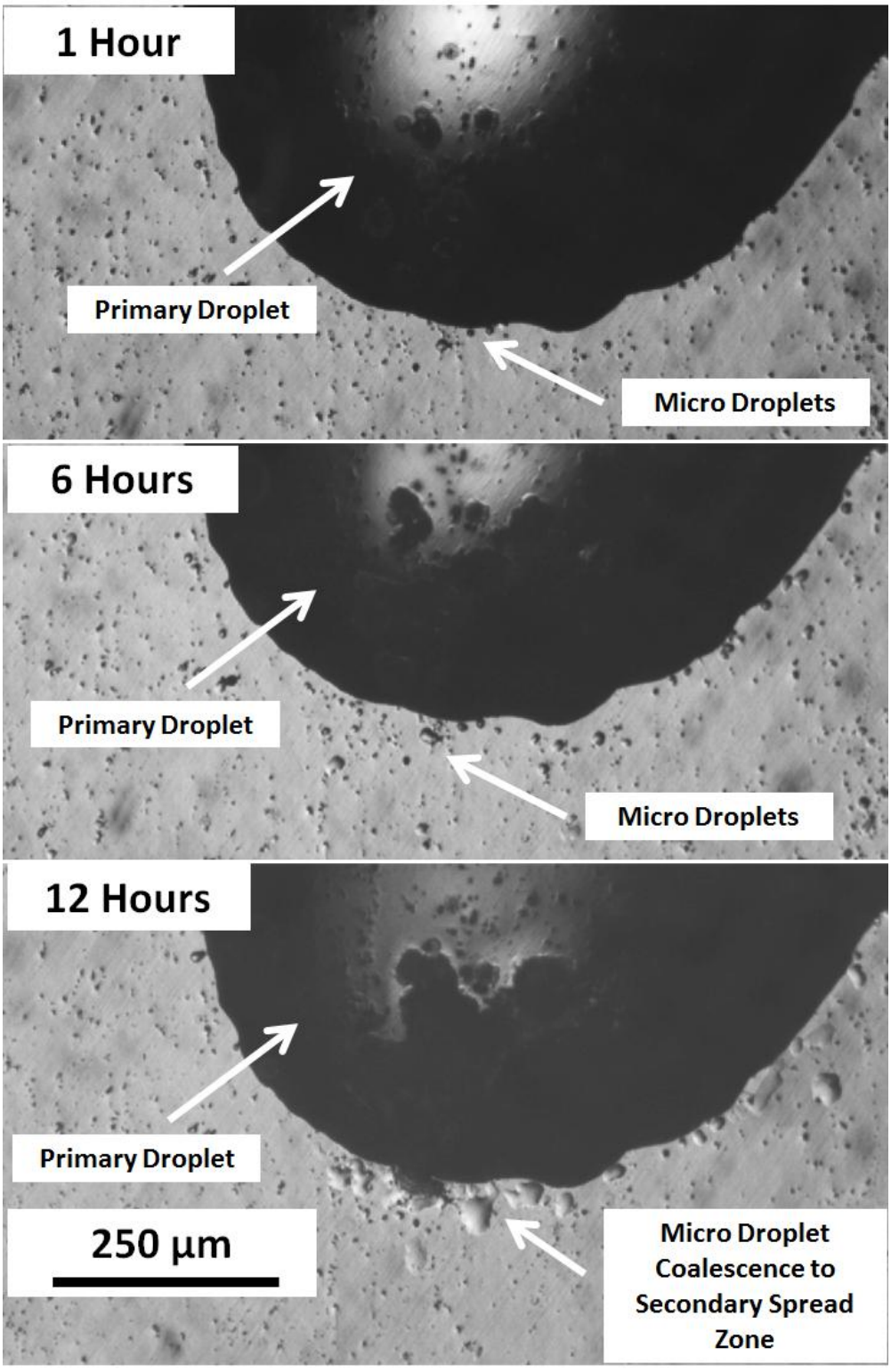


**Figure 5.2 – Magnified views of the periphery of the droplet shown in Figure 5.1 showing formation of micro-droplets on AA2024 at 1, 6 and 12 hours exposure at ~85% RH, under NaCl droplet with initial CDD ~500 µg/cm$^2$**

### 5.2.2 Influence of Salt Type on Spreading Behaviour

Solution composition was observed to influence the secondary spreading behaviour of droplets during atmospheric exposure on AA2024 surfaces, Figure 5.3. It can be seen that for 24 hour exposure at a constant RH of 85% and initial CDD of 500 $\mu g/cm^2$, droplets of NaCl and ocean water, whilst no spreading was observed for $MgCl_2$ and $CaCl_2$ solutions.

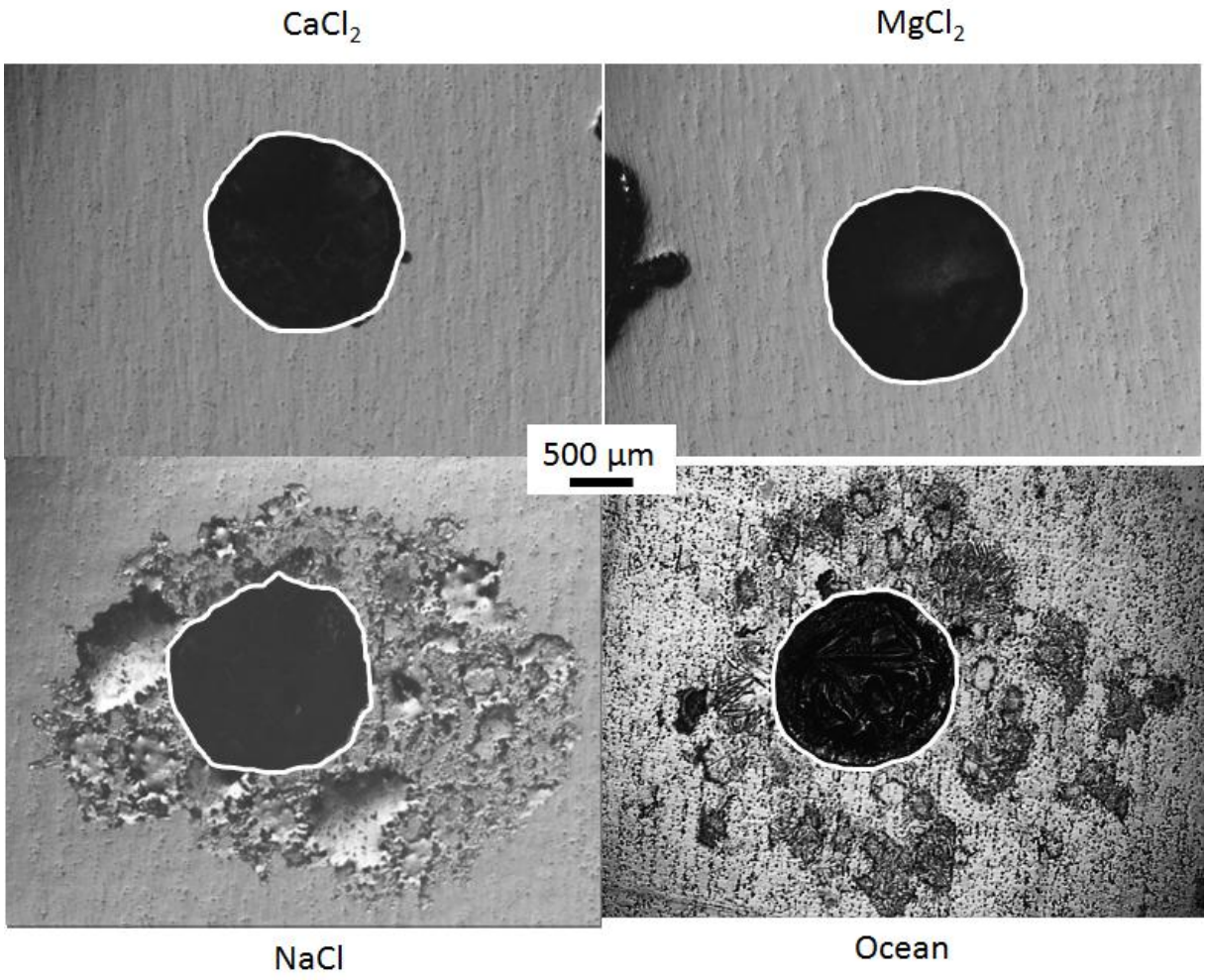


**Figure 5.3 – Optical images of salt droplets on AA2024 surfaces, showing the development of secondary spread zones during atmospheric exposure. Droplets exposed for 24 hours at 85% RH with an initial CDD of 500 µg/cm$^2$. The white circles show the original perimeter of the droplet.**

Mapping of the distribution of the key elements in dried salt deposits is shown in Figure 5.4 - Figure 5.7. The secondary electron image in the top left of each figure shows the dried salt deposit and EDX maps are shown for chlorine, oxygen and the major cation present. It can be seen that in all cases chlorine was restrained to the bounds of the original droplet, the same is true for magnesium (Figure 5.5) and calcium (Figure 5.6). However, in solutions where sodium was present (Figure 5.4

and Figure 5.7) migration of $Na^+$ to the periphery of the droplet and into the secondary spread region took place. In addition it can be seen that for $MgCl_2$ and $CaCl_2$ solutions the highest concentration of oxygen at the end of sample exposure was located within the bounds of the primary droplet. Whilst in the case of solutions containing sodium some oxygen was detected in the spread zone.

Figure 5.8 shows an EDX linscan across a dried NaCl salt deposit following 24 hours at 85% RH and drying in 0% RH. Linescan is indicated by the yellow line on the top image, from the sodium and chlorine lines below, it is further evident that migration of $Na^+$ outside the periphery of the primary droplet took place, whilst $Cl^-$ remained within the primary droplet.

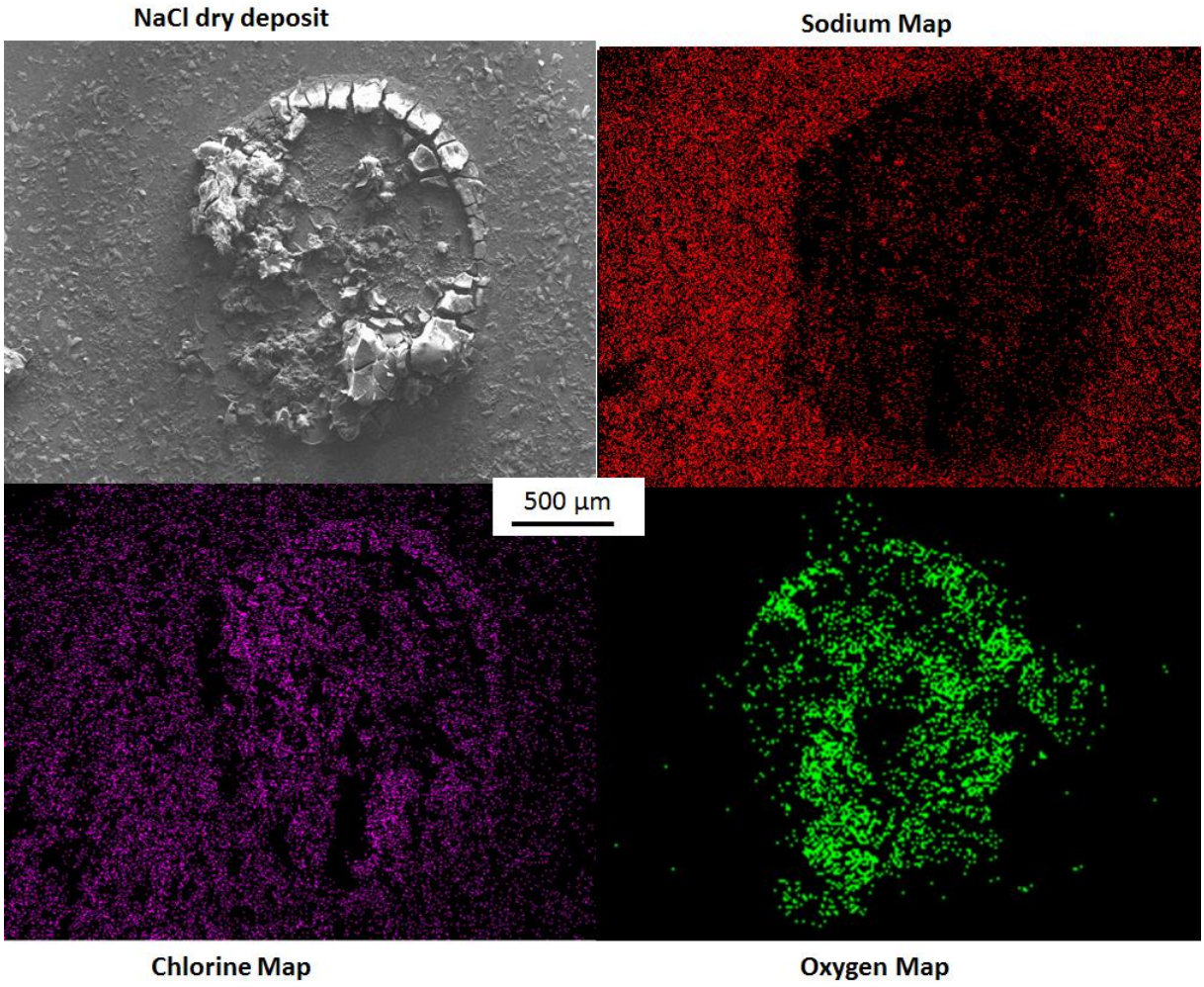


**Figure 5.4 – SEM image and EDX maps of Na, Cl, and O of AA2024 that has corroded under a droplet of NaCl for 24 hours at 85% RH, with an initial CDD of 500 µg/cm$^2$. and then been dried.**

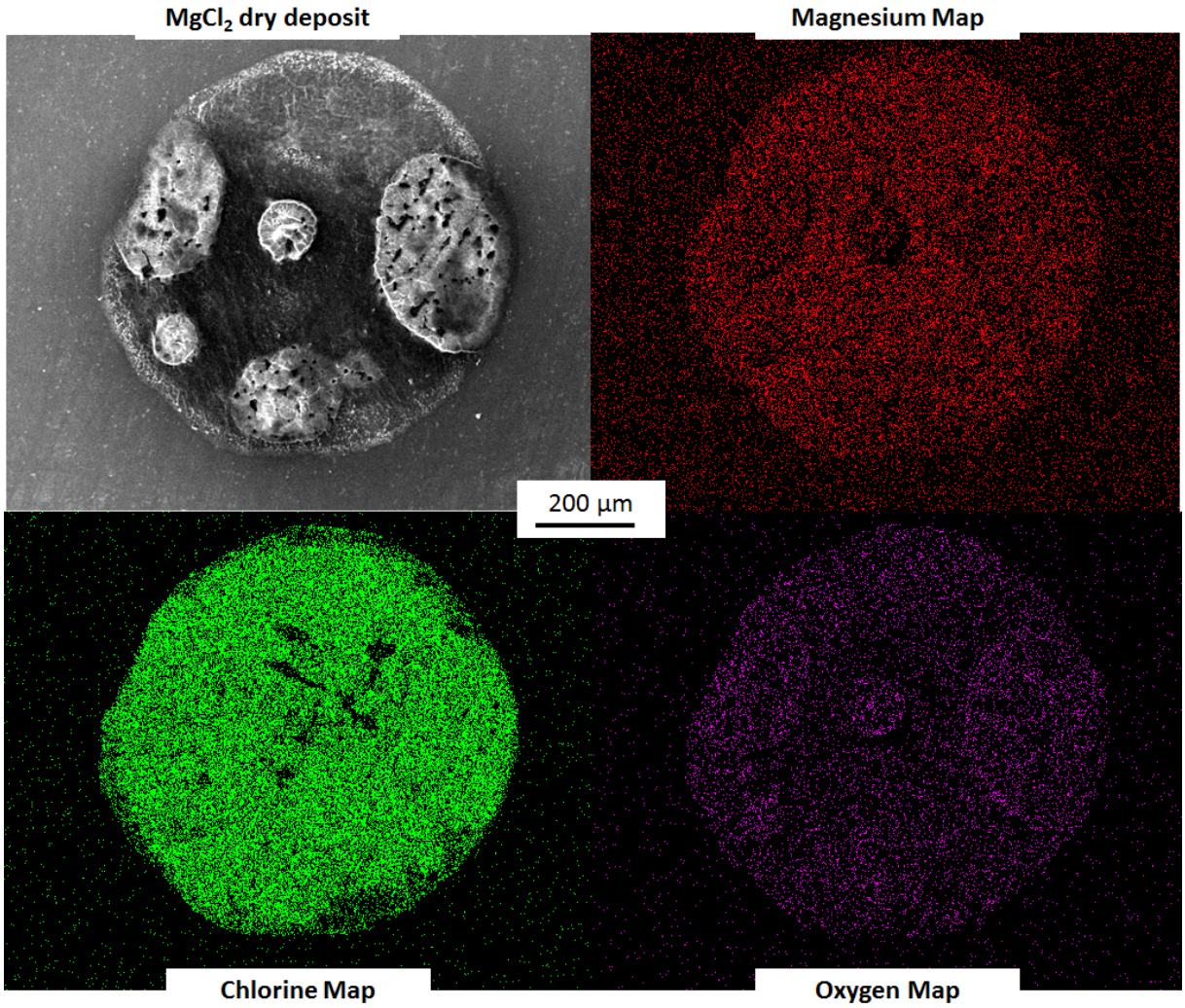


**Figure 5.5 - SEM image and EDX maps of Mg, Cl, and O of AA2024 that has corroded under a droplet of $MgCl_2$ for 24 hours at 85% RH, with an initial CDD of 500 µg/cm$^2$. and then been dried.**

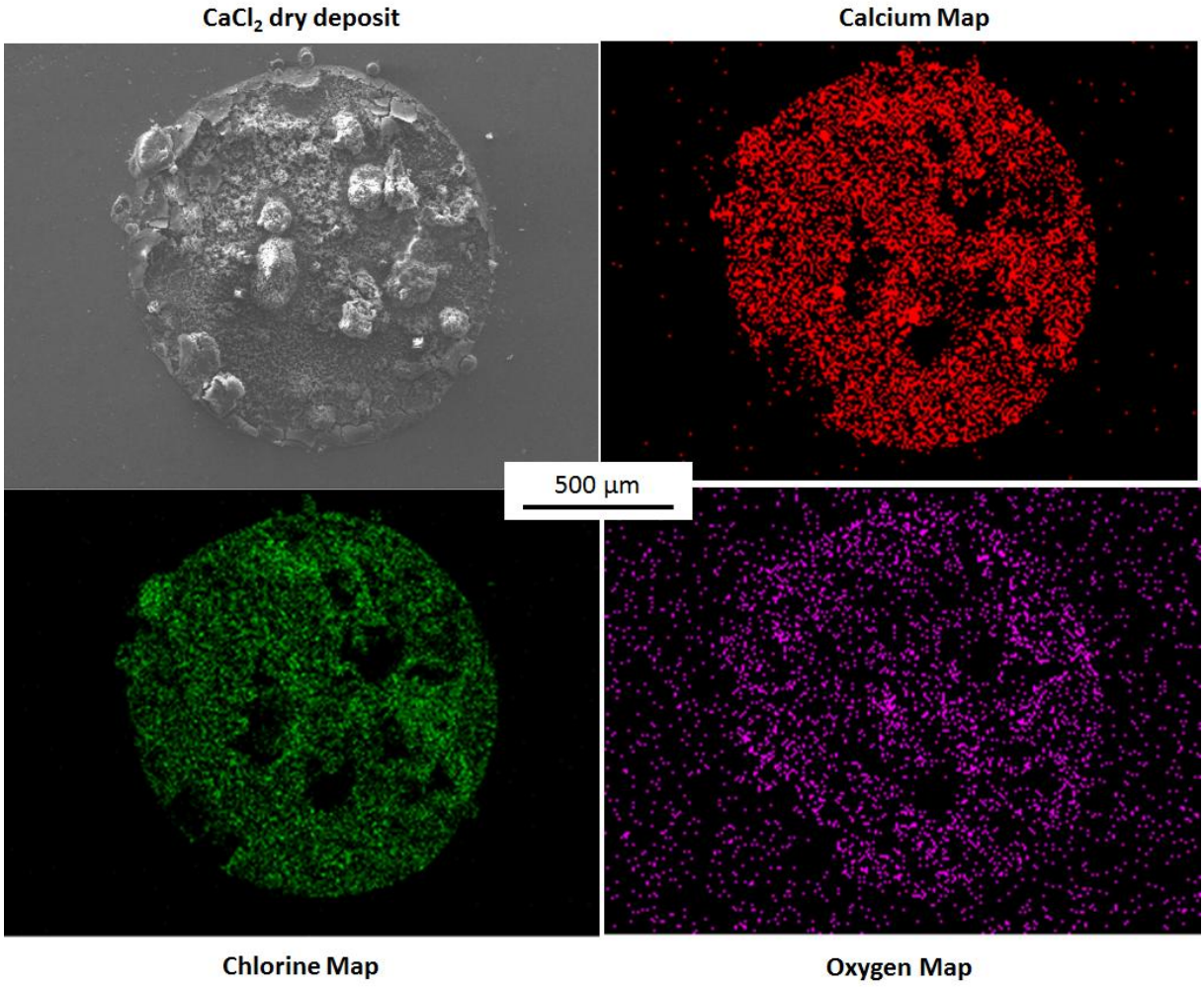


**Figure 5.6 - SEM image and EDX maps of Ca, Cl, and O of AA2024 that has corroded under a droplet of $CaCl_2$ for 24 hours at 85% RH, with an initial CDD of 500 µg/cm$^2$. and then been dried.**

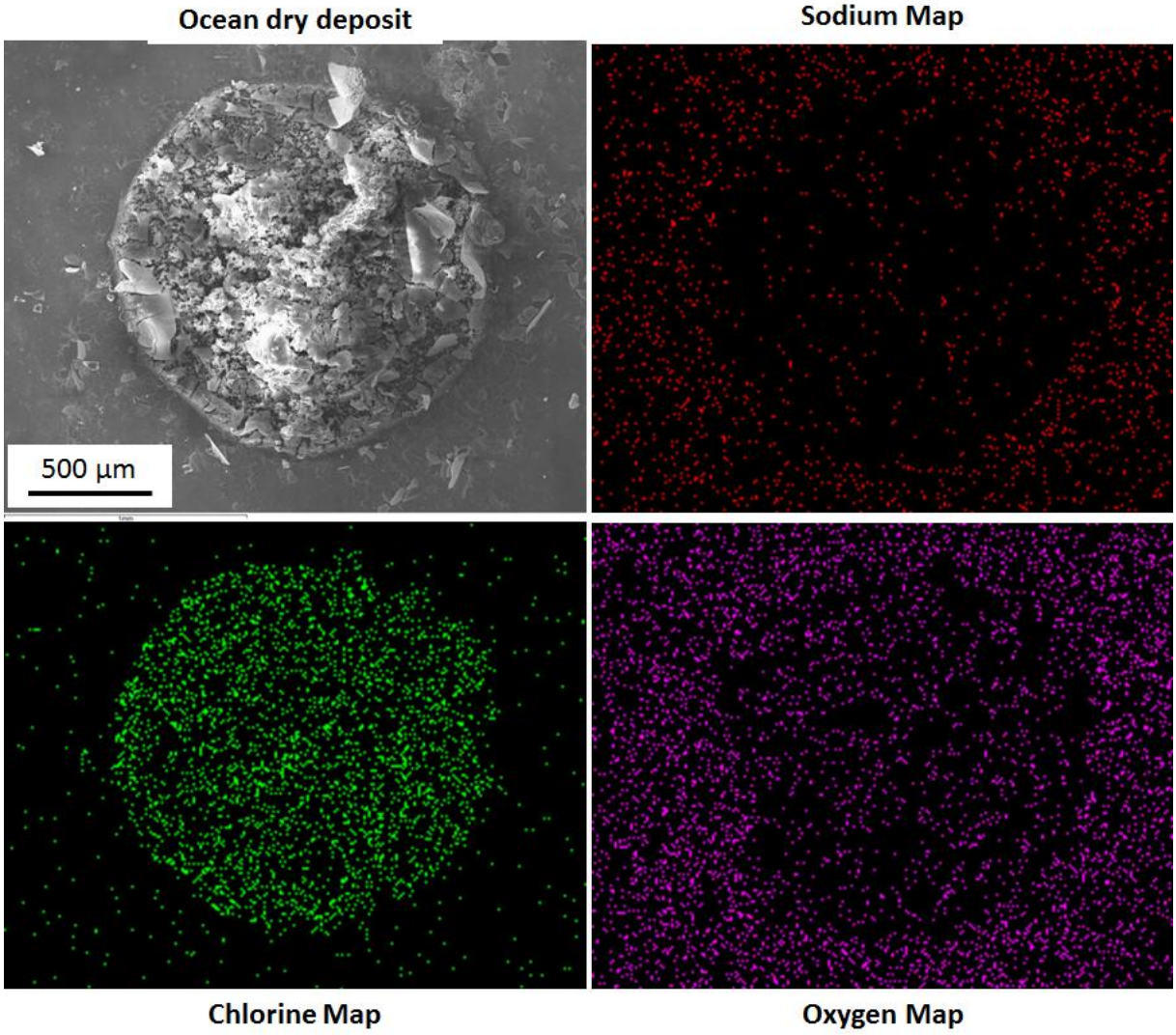


**Figure 5.7 - SEM image and EDX maps of Na, Cl, and O of AA2024 that has corroded under a droplet of simulated ocean water for 24 hours at 85% RH, with an initial CDD of 500 µg/cm$^2$. and then been dried.**

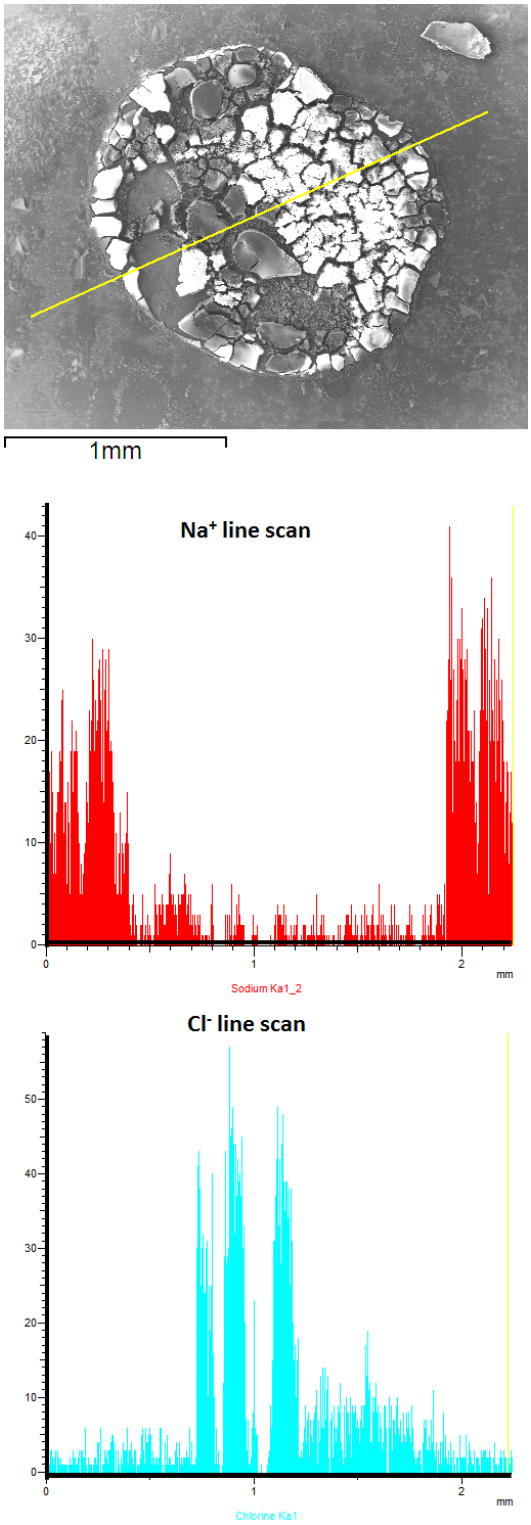


**Figure 5.8 – EDX linescan across dried NaCl salt deposit, following 24 hours at 85% RH, initial CDD 500 µg/cm$^2$. Position of linescan is indicated by yellow line, with elemental linescans for $Na^+$ and $Cl^-$ are shown below.**

Figure 5.9 shows the effect of adding $MgCl_2$ into a solution of NaCl to achieve at chloride ratio of 1:1. It can be seen that the addition of magnesium has reduced the size of the secondary spread zone which formed during a 48 hour exposure at 85% RH, when compared with the droplet of $MgCl_2$ shown in Figure 5.3.

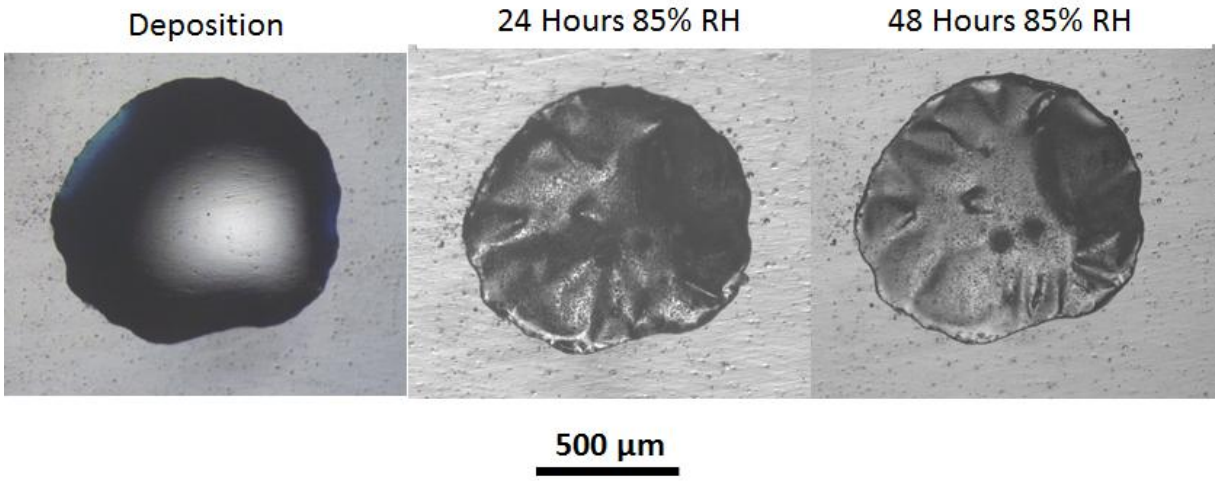


**Figure 5.9 – Mixed salt droplet of NaCl and $MgCl_2$ in chloride ratio of 1:1, with initial CDD of 500 µg/cm$^2$, droplet shown on deposition and at time points of 24 and 48 hours exposure at 85% RH**

### 5.2.3 Influence of Alloy on Spreading Behaviour

Figure 5.10 shows the behaviour of atmospheric droplets on different metallic substrates from several different aluminium alloys. It can be seen that for the AA3004 (Al-Mn-Mg) alloy the radius of secondary spreading is significantly reduced following 24 hours exposure to NaCl solution droplets when compared to that on AA2024 surfaces. There was little or no spreading around the droplets on AA5083 (Al-Mg) surfaces.

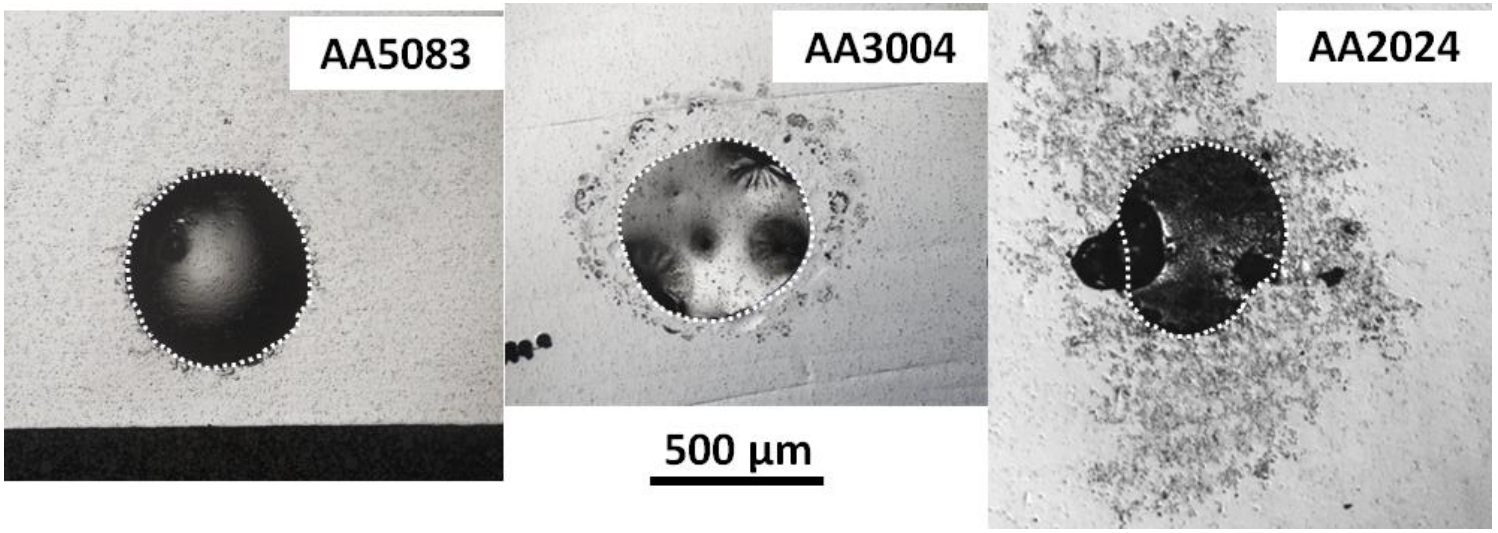
AA5083
AA3004
AA2024
500 µm

**Figure 5.10 - Influence of metallic substrate on spreading behaviour of NaCl droplets (initial CDD 500 µg/cm$^2$), exposed at 85% RH for 24 hours. Top: AA3004, middle: AA5083 and bottom: AA2024; original droplet is marked by white circle.**

The total radius of secondary spreading was determined by measuring the radius from optical images according to the method outlined in Section 3.5.2.3. The total measured radius for the different metal substrates is plotted in Figure 5.11, the radius of the spread zone on AA2024 was measured at roughly four times that on the other substrates. For AA3004 and AA5083 samples the measured radius of the secondary spread zone was seen to be more comparable through the droplets measured, with AA3004 samples showing a some spreading but none being observed for AA5083.

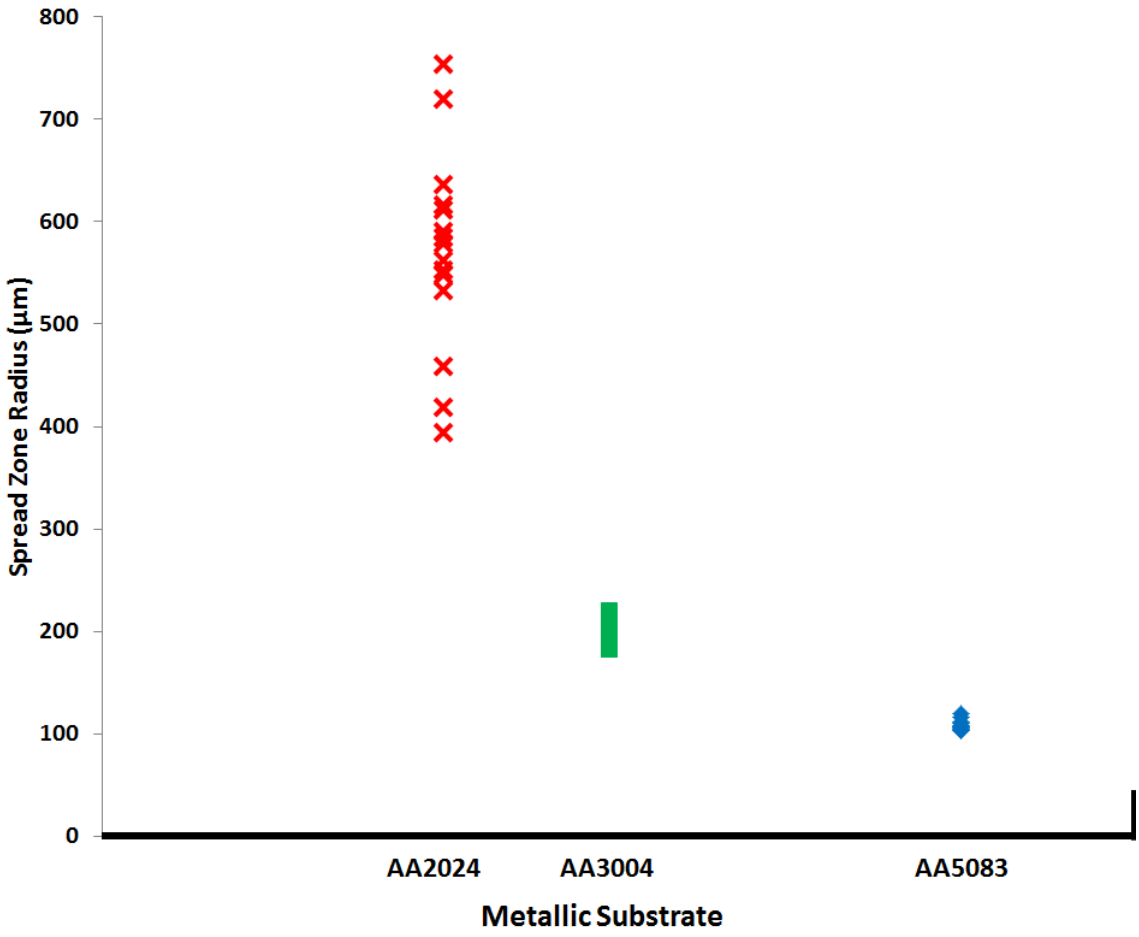


**Figure 5.11 - Measured radius of region of secondary spreading on different metallic substrates following 24 hours exposure at 85% RH, under NaCl solution droplets with initial CDD of 500 µg/cm$^2$**

### 5.2.4 Effect of Initial CDD and Exposure Relative Humidity on Secondary Spreading Behaviour on AA2024 under NaCl Solution Droplets

For 24 hour exposures no spreading was observed for $MgCl_2$ and $CaCl_2$ droplets over the CDD range 1-500 µg/cm$^2$. However, for NaCl solutions over 50 µg/cm$^2$ spreading of droplets was observed. Figure 5.12 shows spreading around NaCl droplets following 24 hours at 85% RH for initial CDD's ranging from 100-500 µg/cm$^2$. In the figure, the location of the original droplet following deposition is shown by a white circle. For CDD values ≤2000 µg/cm$^2$, the droplet spreading was in the form of discrete droplets, but at higher CDD values coalescence of micro-droplets occurred rapidly, leading to expansion of the primary droplet. The measured radius of the zone of secondary spreading or expanded droplet following 24 hours in an atmosphere of 85% RH is plotted in Figure 5.13. It can be seen that as CDD increases at levels ≤2000 µg/cm$^2$, where the continuous droplets are formed, there is very little increase in the radius of the spread zone with CDD.

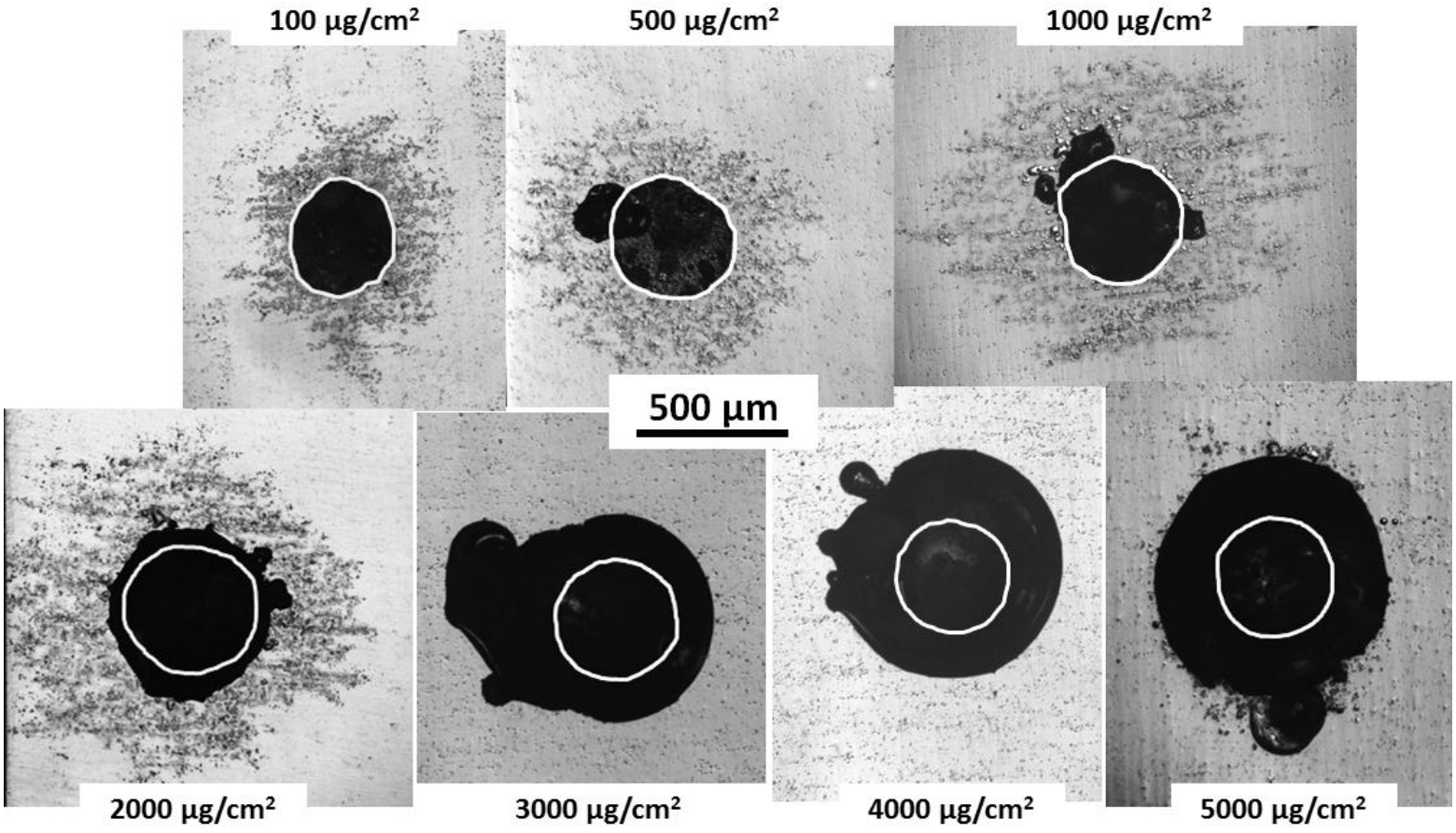
100 µg/cm²
500 µg/cm²
1000 µg/cm²
500 µm
2000 µg/cm²
3000 µg/cm²
4000 µg/cm²
5000 µg/cm²

**Figure 5.12 - Influence of CDD 100 - 5000 µg/cm$^2$ on secondary spreading behaviour on AA2024 plate under NaCl solution droplets (0.2 µl), exposed to a simulated atmosphere of ~85% RH for 24 hours. Original droplet is shown by circle.**

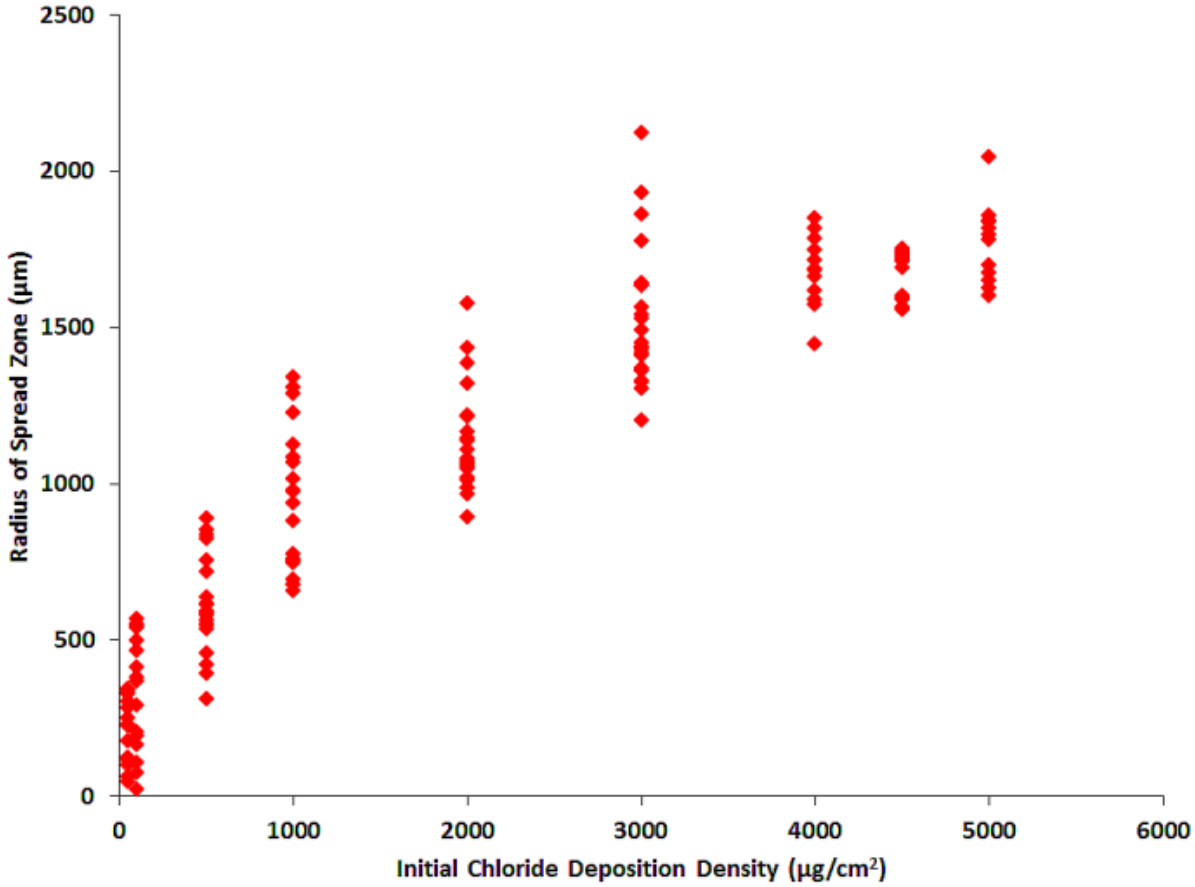


**Figure 5.13 – Plot of radius of secondary spreading region as a function of initial chloride deposition density for 0.2 µl droplets of NaCl solution exposed at 85% RH for 24 hours**

Figure 5.14 shows the effect of RH on the expansion of secondary spread zones on AA2024 under NaCl solutions of initial CDD 500 µg/cm$^2$. For RH values below 75%, the droplets dried in the early stages of exposure so no spreading took place. At 75% RH, there is little spreading after 24 hours. At 85% RH, there is extensive formation of microdroplets, and at 90% RH these undergo extensive coalescence. The average measured radius of the secondary spread zone is plotted in Figure 5.15: the increase in radius with RH is clear.

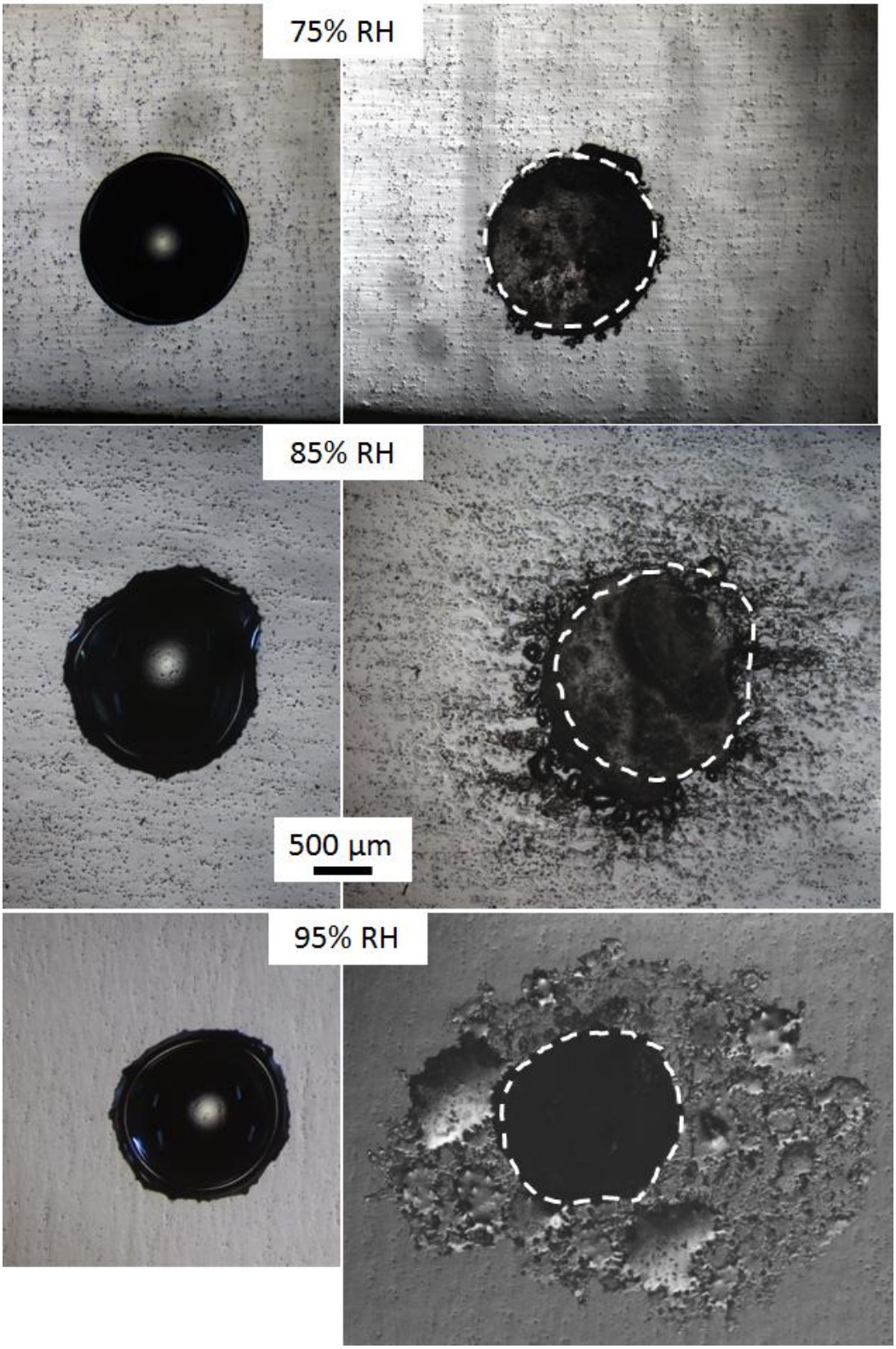


**Figure 5.14 – Secondary spread zones formed on AA2024 plate samples exposed over RH range 75-95% RH for 24 hours with initial CDD ~500 µg/cm$^2$, original droplet marked by broken white circle.**

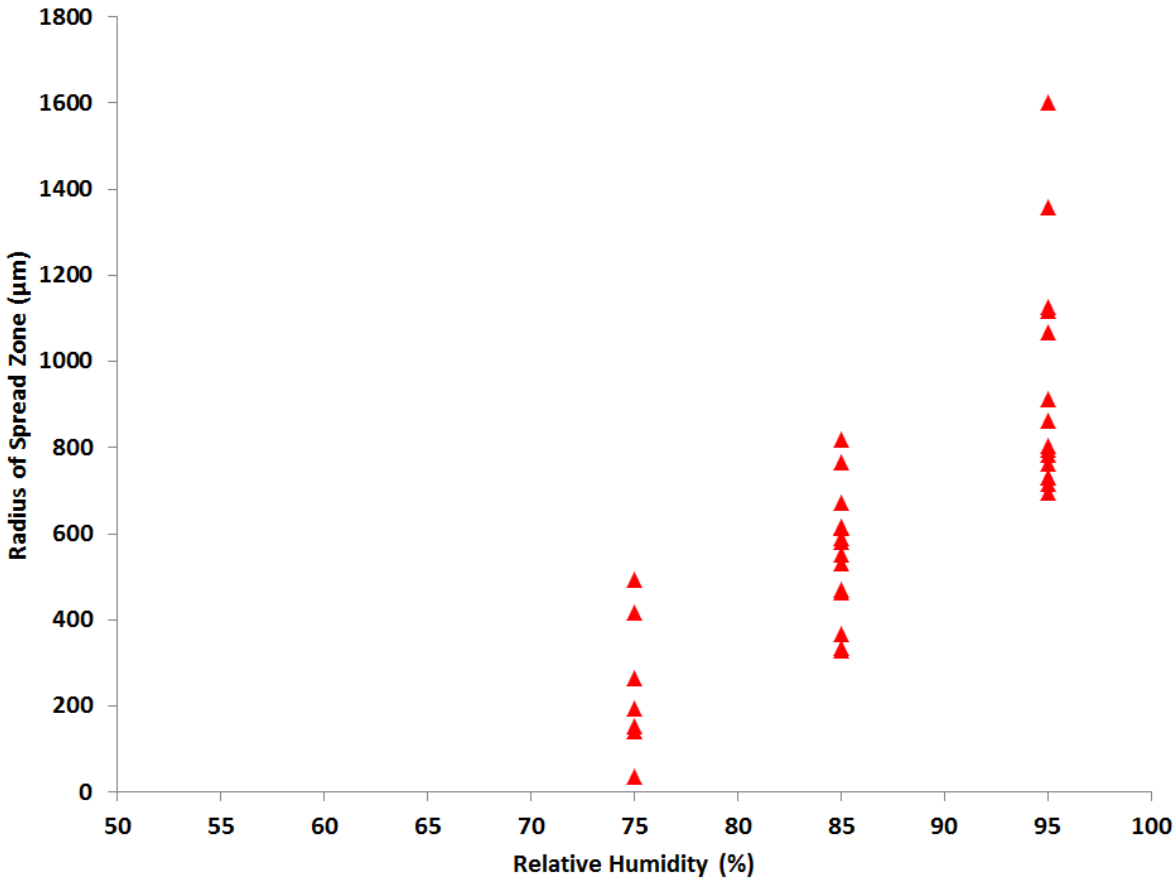


**Figure 5.15 - Measured total radius of secondary spread zone as a function of exposure RH for NaCl droplets with initial CDD of 500 µg/cm$^2$**

### 5.2.5 Influence of Exposure Time on the Secondary Spreading Behaviour on AA2024 Samples

Figure 5.16 shows the effect of TOW on secondary spreading of atmospheric droplets on AA2024 surfaces, for NaCl solutions with initial CDD 500 µg/cm$^2$ in an atmosphere of 85% RH. It can be seen that samples exposed for a greater period of time exhibited greater increases in both the size of the primary droplet and the size of the region of secondary spreading. It can be seen that the greatest growth in the

secondary spread region took place during the first week of exposure, following this the rate at which continued expansion took place was reduced.

Figure 5.17 plots the effect of exposure time on the measured radius of the zone of secondary spreading on NaCl solutions on the surface of AA2024 samples. Over time the secondary spread zone increased for a fixed CDD of 500 µg/cm$^2$ and RH of 85%. Rate at which the spread zone grows appears to remain fairly constant over time for the exposure period of 5 weeks studied herein.

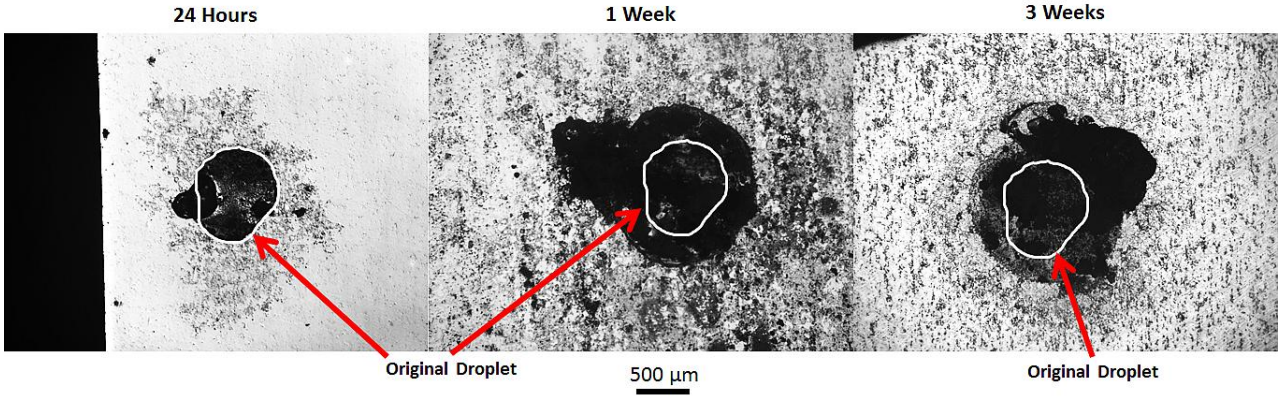


**Figure 5.16 – Spreading of atmospheric droplets on AA2024 samples as a function of TOW, under NaCl solution droplets with initial CDD of 500 µg/cm$^2$ in an atmosphere of 85% RH**

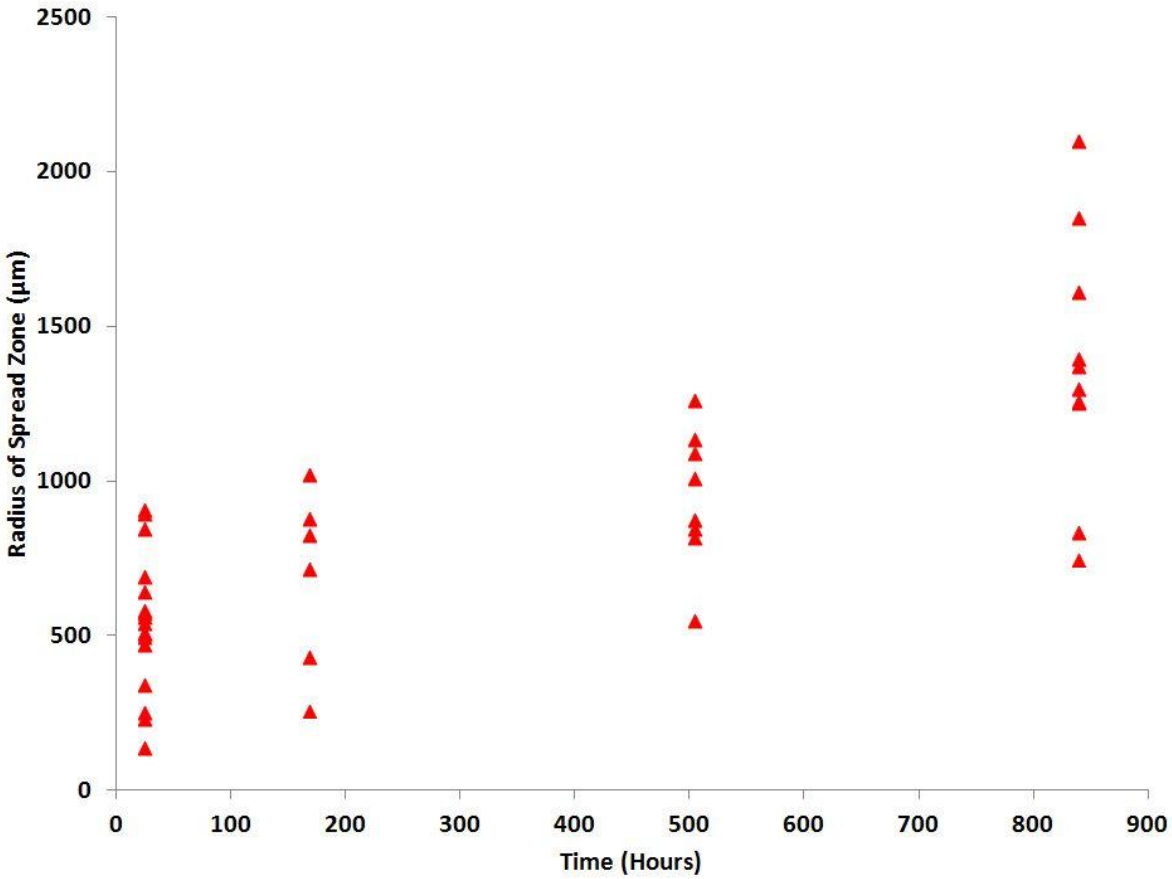


**Figure 5.17 - Measured total radius of secondary spread zone as a function of exposure time for 0.2 µl NaCl solution droplets, in an atmosphere of ~85% RH, initial CDD ~500 µg/cm$^2$**

### 5.2.6 Microstructural Observations

Following removal of salt and corrosion product form the surface of samples the presence of shiny un-attacked regions in the surrounds of localised corrosion sites, shown in Figure 5.18. Areas which have undergone localised attack show up as dark regions following removal of corrosion product from the surface of samples. This is demonstrated in Figure 5.19, where magnified image of circled corrosion site from optical image is shown (bottom). It can be seen that the dark region indicated by the

dotted white circle in the optical image (top left) is a site of localised corrosion in the magnified SEM image.

It can be seen that the region exhibiting the greatest amount of localised attack is located towards the periphery of the original droplet.

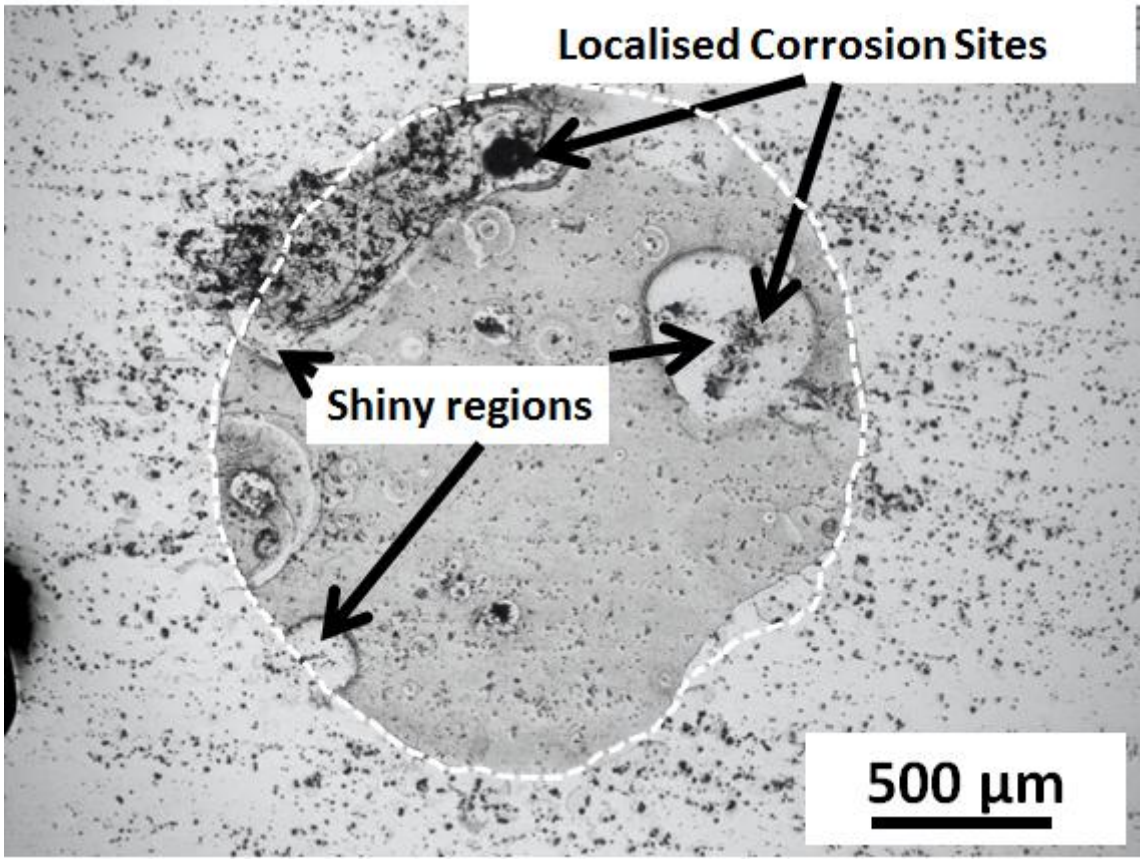


**Figure 5.18 - AA2024 plate surface following removal of corrosion product, via immersion in nitric acid and 10 second polish at 0.04 µm, shiny regions (indicated) form in the surround of localised corrosion sites (indicated), position of the primary droplet is indicated by dotted circle.**

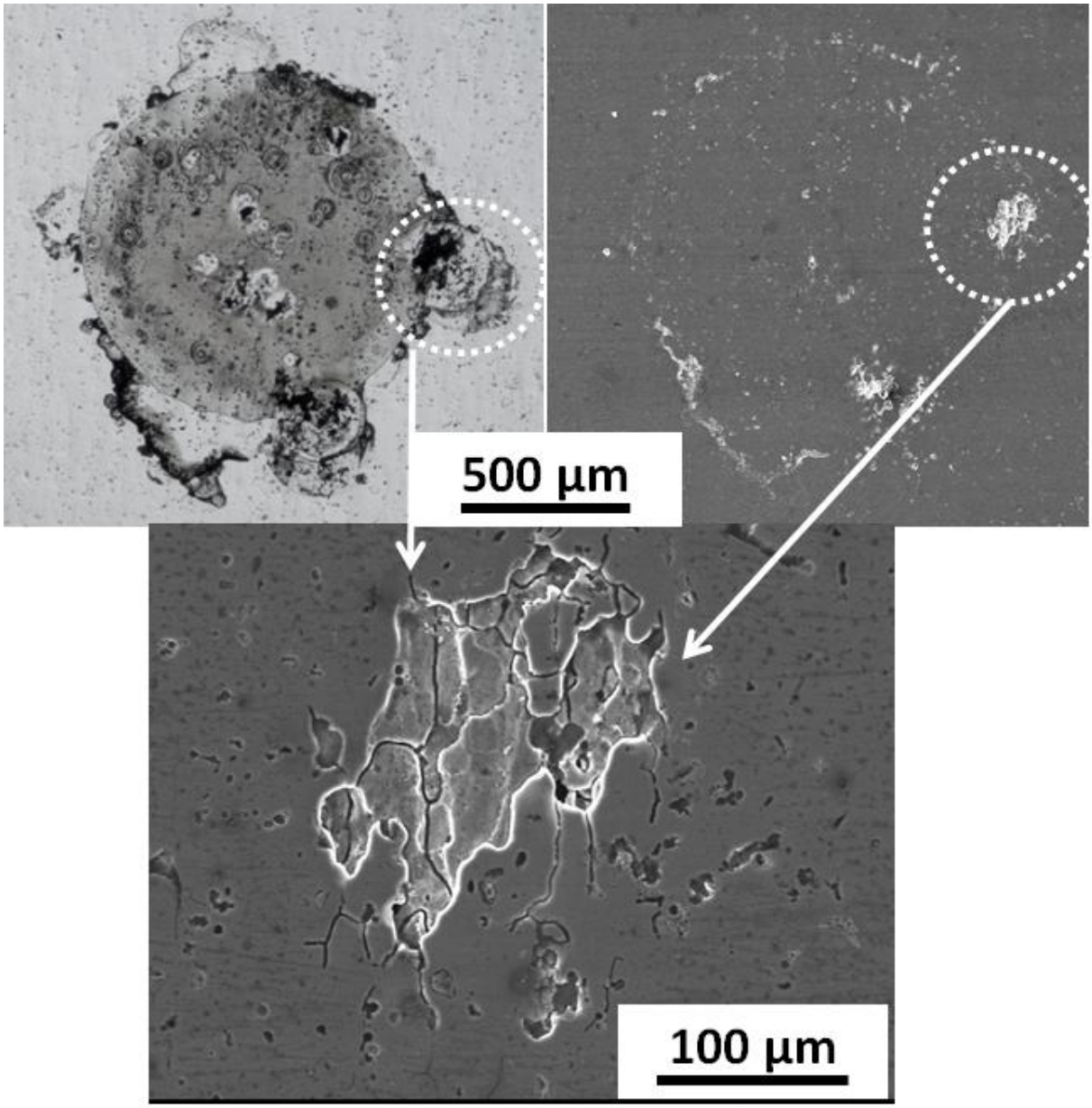


**Figure 5.19- Demonstration of "dark" regions shown in optical images of cleaned AA2024 surfaces being localised corrosion sites. Circled site in the top images both OM and SEM is shown magnified in the bottom image. Site shows shallow pit with IGC fissures formed at the base extending below the surface.**

Presence of a mildly acidic region in which the passive film on AA2024 is stable, results in the formation of a smooth region which shows up as shiny under optical imaging (Figure 5.18). This region and deposition of corrosion product in the

surrounds of this area are shown in Figure 5.20, following drying of a salt solution droplet. In addition the presence of some precipitated salt crystals were found within the pit site.

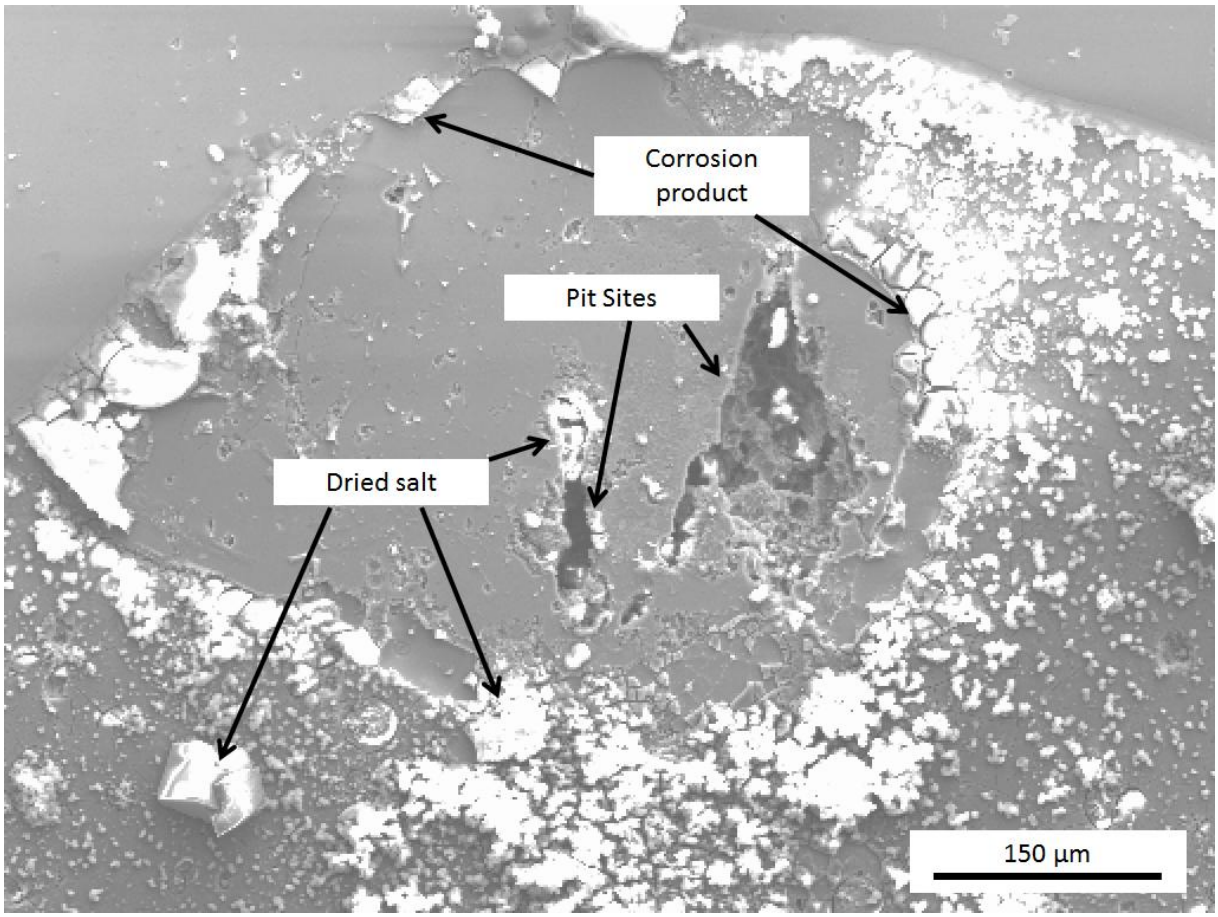


**Figure 5.20 – SEM images showing formation of smooth unattacked mildly acidic region in the surrounds of localised pit site on AA2024 surface following exposure for 24 hours at 85% RH to $MgCl_2$ solution with initial CDD 500 µg/cm$^2$ and drying in 0% RH.**

Figure 5.21 shows SEM images of precipitate intermetallic phases in the base AA2024 metal (left) and in the secondary spread zone on AA2024 (right) in un-corroded and corroded samples. In the base metal it can be seen that the intermetallic particles show no dark regions at their peripheries, whilst in the spread zone dark area were seen to surround the intermetallics. A magnified SEM image of

intermetallic particle exhibiting dark areas in its surrounds can be seen in Figure 5.22. Dark areas can be seen to be examples of trenching or grooving type behaviour which takes place on AA2024 under cathodic regimes.

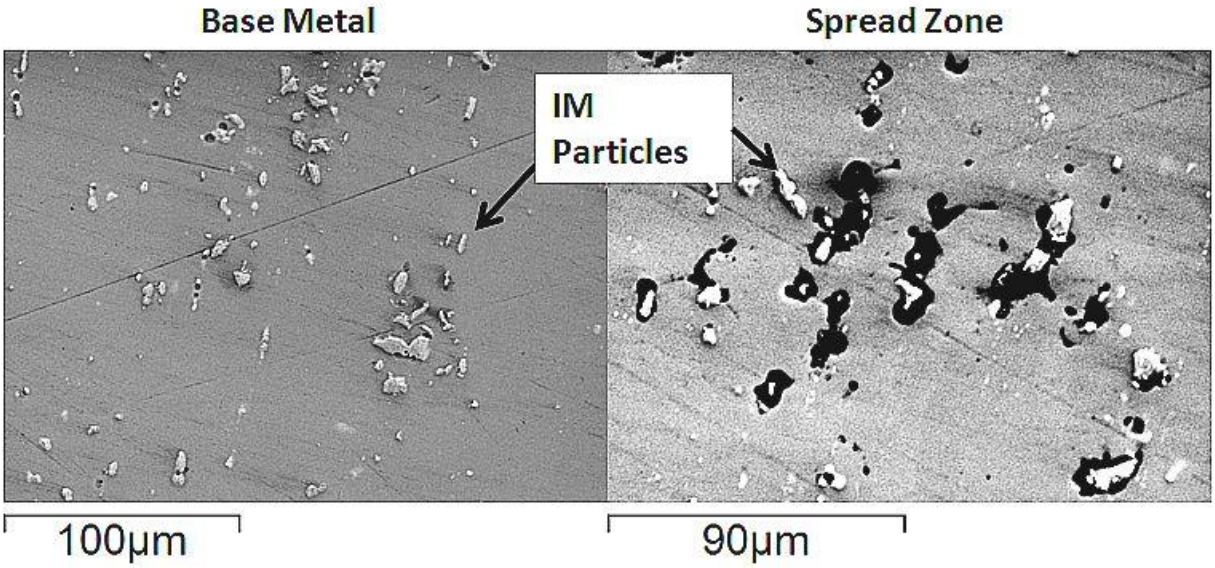


**Figure 5.21 - Attack of intermetallic precipitate phases in the region of secondary spreading following atmospheric exposure of AA2024 samples under NaCl solution droplets at 85% RH**

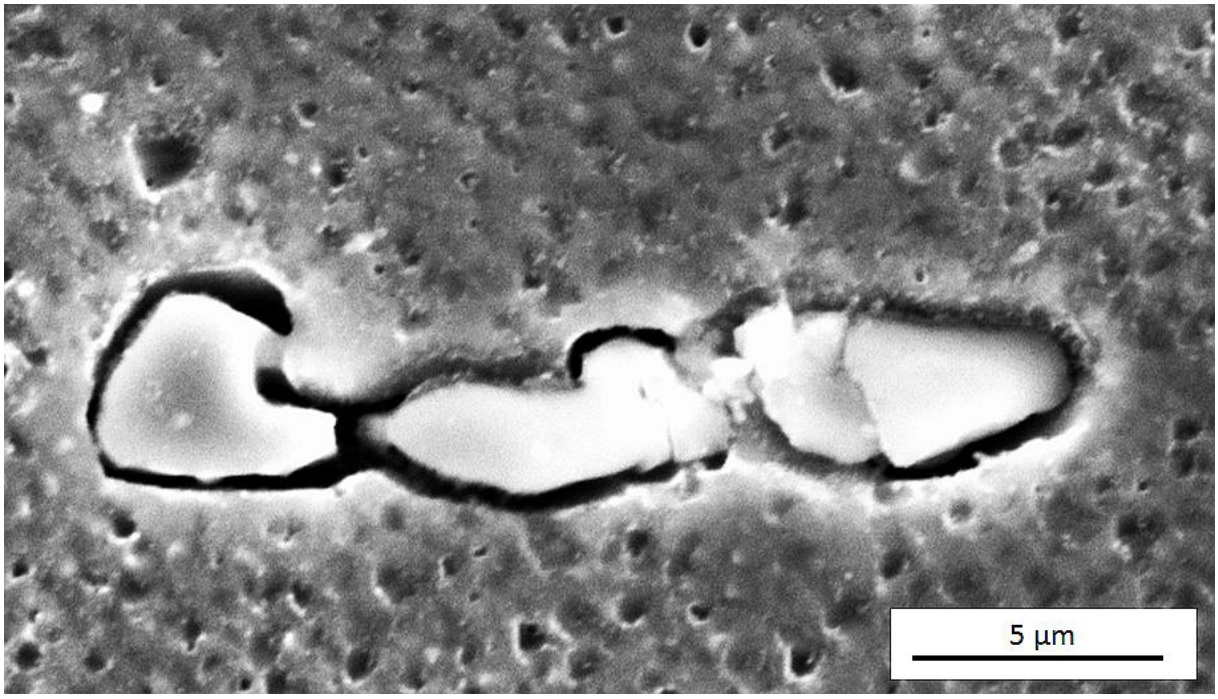


**Figure 5.22 – Trenching in the surrounds of an intermetallic precipitate phase particle in the zone of secondary spreading in AA2024 samples**

Figure 5.23 demonstrates how the surface area covered by localised corrosion sites, following removal of corrosion product, increases as a function of increasing exposure time. For 24 hour sample sites are relatively small, indicated on the far left image, whilst for 1 week and 3 week samples it is clear that the dark areas indicating localised attack have increased significantly. Location of the primary droplet is marked, it can be seen that for all exposure times the locations of the major sites is in or directly adjacent to the boundary between the primary droplet and the secondary spread zone.

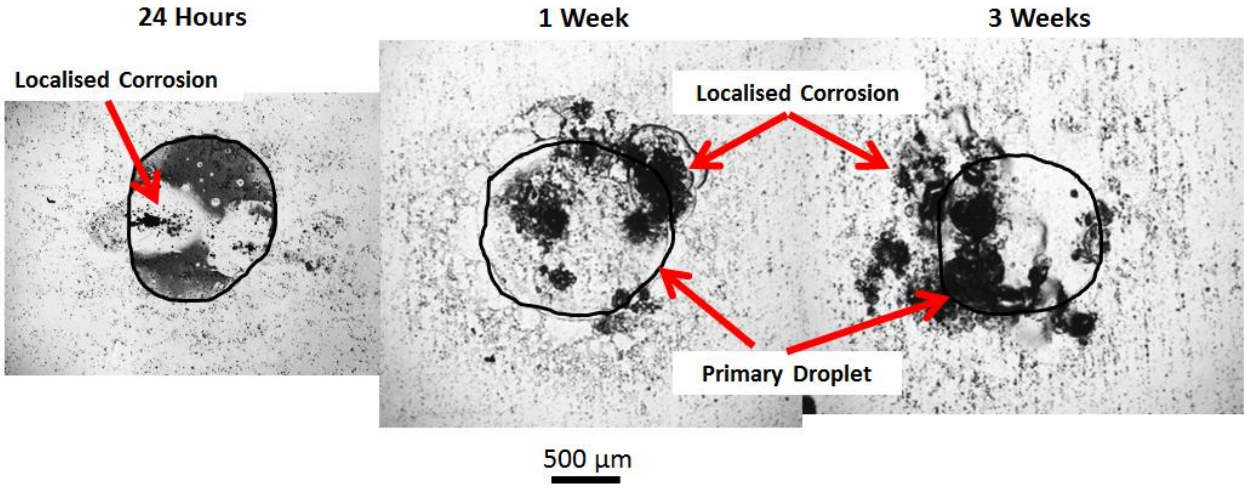


**Figure 5.23 – Influence of exposure time on the surface area coverage of localised corrosion sites following exposure to NaCl solution droplets with initial CDD of 500 µg/cm$^2$ in an atmosphere of 85% RH,**

Measured surface area coverage of localised corrosion sites is plotted as a function of the radius of the secondary spread zone in Figure 5.24. As the total measured radius of secondary spread zones increase there was a related increase in the measured surface area covered by localised corrosion. Owing to the scatter in the results it is not possible to comment further on any trends emerging.

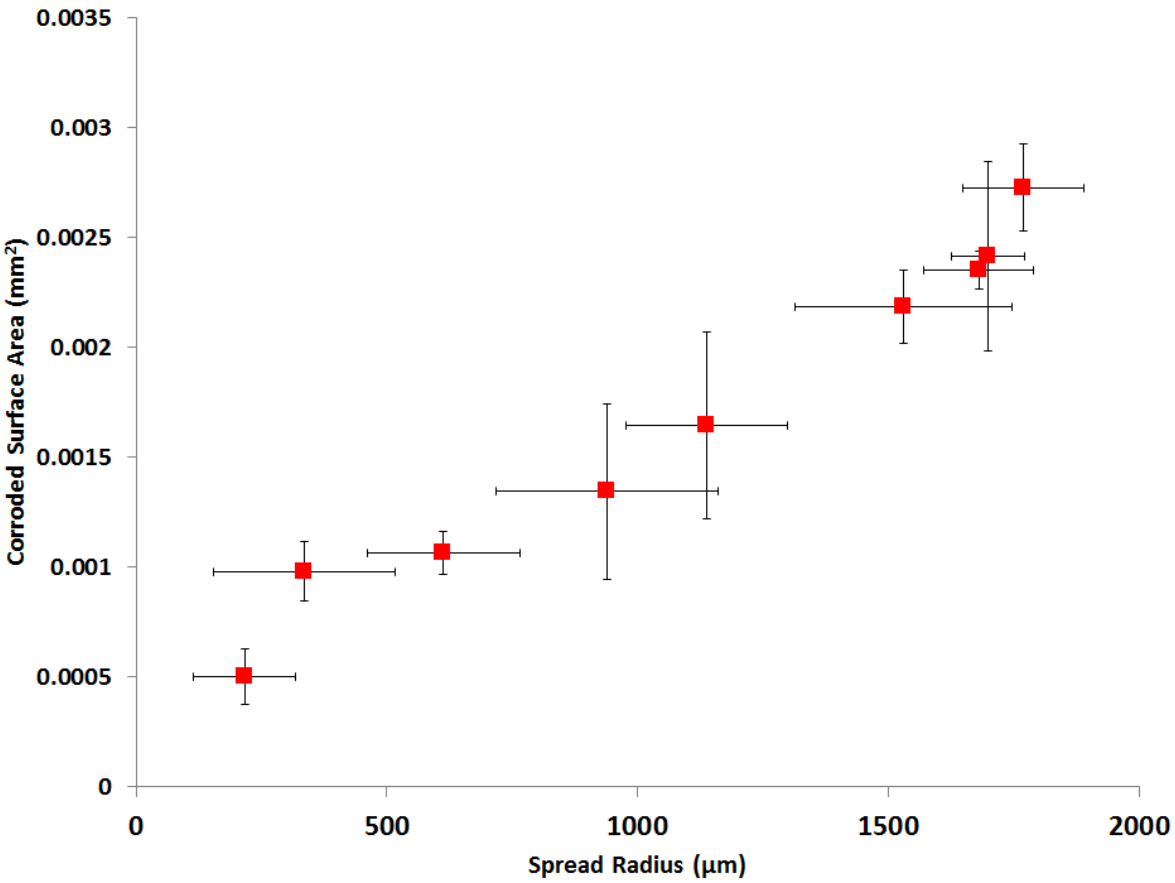


**Figure 5.24 – Measured surface area coverage of localised corrosion sites as a function of total radius of spread zone of NaCl atmospheric droplets exposed for 24 hours at 85% RH**

## 5.3 Discussion

### 5.3.1 Secondary Spreading of Droplets Containing $Na^+$

The mechanism of micro droplet and secondary spread zone formation is outlined in Section 2.4.3. Resulting from the formation of a potential gradient within the droplet leading to the formation of a cathodic region at the droplet periphery at which micro-droplets form [142-144].

Formation of micro-droplets during the early stages of atmospheric corrosion ~1 hour was observed herein on AA2024, this agrees well with previous observations during

the initial stages of atmospheric corrosion on AA7050[152] magnesium, steel and copper[145, 209, 211]. Following formation of a sufficiently large number of micro-droplets, in the near vicinity of each other, coalescence into more consolidated thin electrolyte layers. Coalescence of micro droplets takes place as growth of individual droplets results in their increasing proximity to one another leading to interaction between individual droplet boundaries. The morphology of individual micro-droplets and secondary droplets at the periphery of the primary droplet were similar to those reported to form on AA7050[152], magnesium alloys [151, 209], stainless steel [142, 145, 146, 169], copper[146, 211], zinc[150] and pure Al[145], under NaCl solution droplets.

It was determined that as with results from work on stainless steels, formation of micro-droplets occurs for NaCl droplets[142, 143, 146], but does not take place for either $MgCl_2$[146] and $CaCl_2$[143] during 24 hour exposures. However, in the case of artificial ocean water it can be seen that the occurrence of micro-droplets and zones of secondary spreading was observed, during exposure at ~85% RH for 24 hours.

EDX carried out on droplets following drying in order to determine the elemental distribution within the primary droplet and the region of secondary spreading showed that elements migrated to specific regions within the droplet. Previously elemental mapping during spreading studies has been carried out on steel[142] and zinc[149] to map NaCl deposits following occurrence of secondary spreading. The results from this work, where migration of sodium to the droplet periphery and into the zone of secondary spreading agree well with those seen on steel and zinc. Migration of $Na^+$ to this region is likely in order to maintain charge balance at the cathode following its establishment in this area.

Presence of chloride within the original droplet area and in the vicinity of the main localised sites indicates that the primary anodic regions are located within the primary droplet and towards its periphery. Further during EDX mapping and point scans it was determined that increased levels of oxygen were present in these locations, indicating that these are the primary locations in which hydroxides are precipitated. This takes place due to migration of dissociated cations towards hydroxide ions formed due to oxygen reduction at the cathode.

### 5.3.2 Influential Factors on Enhancement of Secondary Spreading

Influence of initial CDD on the spreading behaviour of NaCl solutions was observed to be quite significant, with an increase in CDD leading to an increase in the size of the secondary spread zones. This expansion can primarily be attributed to changes in droplet volume during the equilibration phase, whereby a greater amount of moisture is taken up from the environment to attain equilibrium for a greater quantity of chloride [121, 123, 139]. Greater expansion of the droplet results in a greater surface coverage under solution layer, which in turn results in an increase in the size of the available cathodic area.

Similar behaviour was observed as a function of RH, with higher RH values resulting in greater spreading, again this can be primarily attributed to droplet expansion during equilibration with the environment. The lack of micro-droplet formation for NaCl and ocean water droplets of ~60% RH and below is primarily due to this being below the DRH of NaCl which is primary component of both solution types.

Exposure time influenced the spreading behaviour of atmospheric droplets on AA2024 surfaces, to the effect that as exposure time increased the radius of the

secondary spread zone increased, for NaCl solution droplets. Over time the rate of expansion of the secondary spread zone on NaCl and Ocean samples decreased, this is likely due to a slowing in the rate of corrosion that generally takes place for an increased exposure time. As anodic rate slows the required cathodic rate and hence the size at which new cathodic areas are required to be developed is reduced accordingly.

### 5.3.3 Influence of $Mg^{2+}$ and $Ca^{2+}$ on Secondary Spreading

Magnesium hydroxide has previously been reported to precipitate towards the periphery of atmospheric droplets, and inhibit migration of ions due to its insoluble nature [146, 149]. The solubility of calcium hydroxide ($Ca(OH)_2$) and magnesium hydroxide ($Mg(OH)_2$), are both considerably lower at $0.160^{20}$ and $0.0069^{20}$ g/100g $H_2O$ respectively[129], than that of sodium hydroxide (NaOH) at $100^{25}$ g/100g $H_2O$[129]. This ring of insoluble hydroxide formed at in the cathodic region towards the droplet edge helps to prevent the migration of ions which is required for the formation of a zone of secondary spreading. As such this explains why during a 24 hour exposure spreading is observed in solutions containing $Na^+$, i.e NaCl and substitute ocean water, but not for solutions of $CaCl_2$ or $MgCl_2$. Formation of hydroxides takes place according to the following reactions:

$$Mg^{2+}(aq) + 2\,OH^-(aq) \rightarrow Mg(OH)_2\,(s)$$

$$Ca^{2+}(aq) + 2\,OH^-(aq) \rightarrow Ca(OH)_2\,(s)$$

It is possible that in addition to the formation of hydroxides the formation of carbonates may also take place. Carbonates of magnesium ($MgCO_3$) and calcium

($CaCO_3$), also show reduced solubility when compared with sodium carbonate ($Na_2CO_3$) or NaOH. Solubility's of these carbonates are $0.18^{20}$, $0.00066^{20}$ and $30.7^{25}$ g/100 g $H_2O$ respectively[129], which compare to those for hydroxides. Which indicates that if carbonates were to be precipitated in place of or in addition to hydroxides, then both would likely inhibit the migration of ions outwards to create a zone of secondary spreading.

A comparison of metallic substrate was made for several different aluminium alloys to determine changes in atmospheric droplet behaviour. The relative size of the spread zone following 24 hours exposure to NaCl solution droplets at 85% RH was to the effect that AA5083<AA3004≤AA2024. It is likely that the increased magnesium content in AA5083 inhibited the spreading processes through the formation of either magnesium hydroxides or carbonates at the droplet periphery. As has been discussed previously the reduced solubility of $Mg(OH_2)$ compared with NaOH inhibits the spreading of atmospheric droplets.

Expansion of the primary droplet was also observed, this was associated primarily with the growth of localised sites at the periphery, as sites extended beyond the bounds of the original droplet, it is likely that the surface tension of the droplet is lowered as a result. As such the droplet expands to cover the site allowing growth of the site to continue. Similar behaviour is observed under solutions of $MgCl_2$ and $CaCl_2$ where outward expansion of the primary droplet took place over an active site at the periphery of the droplet. However, little or no formation of micro-droplets was observed for $MgCl_2$ and $CaCl_2$ for exposures of up to 5 weeks.

### 5.3.4 Microstructural Phenomenology

Following removal of corrosion product form the sample surfaces, un-attacked shiny regions were observed around sites of localised corrosion on the sample surfaces. Presence of un-attacked areas have been observed previously on 5xxx series aluminium[87], during atmospheric testing at the University of Birmingham. It is likely that this shiny zone where no attack was observed presents as a region of mild acidity. As such two factors promote the protection of this region; the first is the solution pH which is in the more neutral range of 6-8 where the passive film on aluminium is stable Figure 2.4. The second is the precipitation of corrosion product which takes place at the junction between the cathode and the anode, the presence of corrosion product protects the passive film, which results in the shiny un-attacked surface observed herein. Precipitation of corrosion product around an active site of localised corrosion has also been observed during droplet studies on AA7050[152].

Trenching of intermetallic precipitate phases in AA2024 takes place primarily in alkaline regions [48, 50, 51], located towards the cathode. As such it is reasonable to surmise that the regions in which trenching was observed during this work are cathodic in nature. Trenching was primarily observed in the region of secondary spreading during atmospheric exposure to NaCl and ocean water samples, indicating that these zones are cathodic in nature. The importance of this being that as the region of secondary spreading grows the size of the potential cathodic region grows accordingly. Separated anodic and cathodic regions has previously been reported on zinc[212], and the reported presence of shiny regions in the surrounds of localised sites on 5xxx series aluminium[87] and the proposed mechanisms outlined on

AA7050[152]. This coupled with the evidence provided herein suggest that electrode separation can take place on aluminium as well.

A good correlation was observed between an increase in the radius of the spreading of atmospheric droplets and the associated amount of surface damage for NaCl droplets exposed at 85% RH. This is important as it provides support for the hypothesis that as the area of the surface covered by moisture increases the potential size of the cathodic area. As such the increase in the size of the available cathodic region allows for an increase in the corrosion rate to take place[94, 213], the result of which is a greater observed amount of localised attack, due to the enhanced anodic reaction rate associated with maintaining electrochemical neutrality.

## 5.4 Conclusions

1 Presence of $Na^+$ in atmospheric droplets on AA2024 plate surface resulted in the formation of secondary spreading zones at the periphery of primary droplets.

2 Secondary spreading effects observed for NaCl solution droplets are enhanced by increases in initial CDD, exposure time and RH. Due to increases in the solution acidity in the anodic region, an increase in cathode size is required in order generate the necessary alkalinity to maintain balance in the environment

3 Addition of Mg/Ca based salts and Mg in the alloy helps inhibit the secondary spreading process due to the formation of insoluble hydroxide and or carbonates.

4 For NaCl samples with spread zones formation of largest localised site of corrosion was observed towards the edge of the primary droplet, and growth occurred outwards from the periphery of the droplet over longer exposure periods.

5 As exposure time was increased the observed amount of localised corrosion at the surface of samples was seen to increase.

6 Presence of shiny un-attacked regions between the primary anodic and cathodic regions, were observed as a result of the passive film remaining intact in this region. Passive film was preserved in this region due to the pH being raised into the range over which the solubility of the oxide film is significantly reduced.

# 6 CYCLIC WET/DRY ATMOSPHERIC EXPOSURE OF AA2024

## 6.1 Introduction

Airframe structures are exposed to periods of wet and dry conditions. It is therefore important to understand how cycling between the wet and dry phases during atmospheric exposure influences the development of localised sites in order to develop effective PHM models. A cyclic immersion test on AA2024 revealed that greater damage accumulation occurred for this type of exposure [95], however, very little work has been carried out under more realistic wet/dry cycles on AA2024 [162]. The aim of this chapter is therefore to provide a better understanding of the processes taking place during fluctuations in relative humidity.

## 6.2 Results

### 6.2.1 Effect of Drying Phase on Atmospheric Corrosion of AA2024

Figure 6.1 provides a 3-D reconstruction of the corroded volume for an AA2024 pin sample exposed to an NaCl solution droplet of initial CDD ~4500 µg/cm$^2$. After 23 hours at ~85% RH (a,b), it can be seen that the droplet has become uneven in shape due to the presence of corrosion products at the metal surface and the presence of hydrogen bubbles in the droplet. Hydrogen bubbles can be seen to have formed at the mouth of the fissures, which grew during the wet phase of exposure.

Following 2 hours drying at ~30% RH (c,d), the droplet has dried into solid crystalline salt phases and a gel-like layer. Salt crystals are likely to be NaCl and the gel-like layer is corrosion product. During the drying phase one of the fissures has grown significantly in both depth and width, whilst the other has grown primarily in width. The fissures appear discontinuous in nature primarily due to the resolution (pixel

size) associated with the measurements, as fissures narrower than 0.75 µm were undetectable using the µCT technique used.

In (e), a reconstructed vertical section of the pin showing the point of maximum depth is shown, with solid salt phase precipitated above. The fissure on the left hand side can be seen to be much less clearly defined than that on the right, due to the pixel size of the measurements.

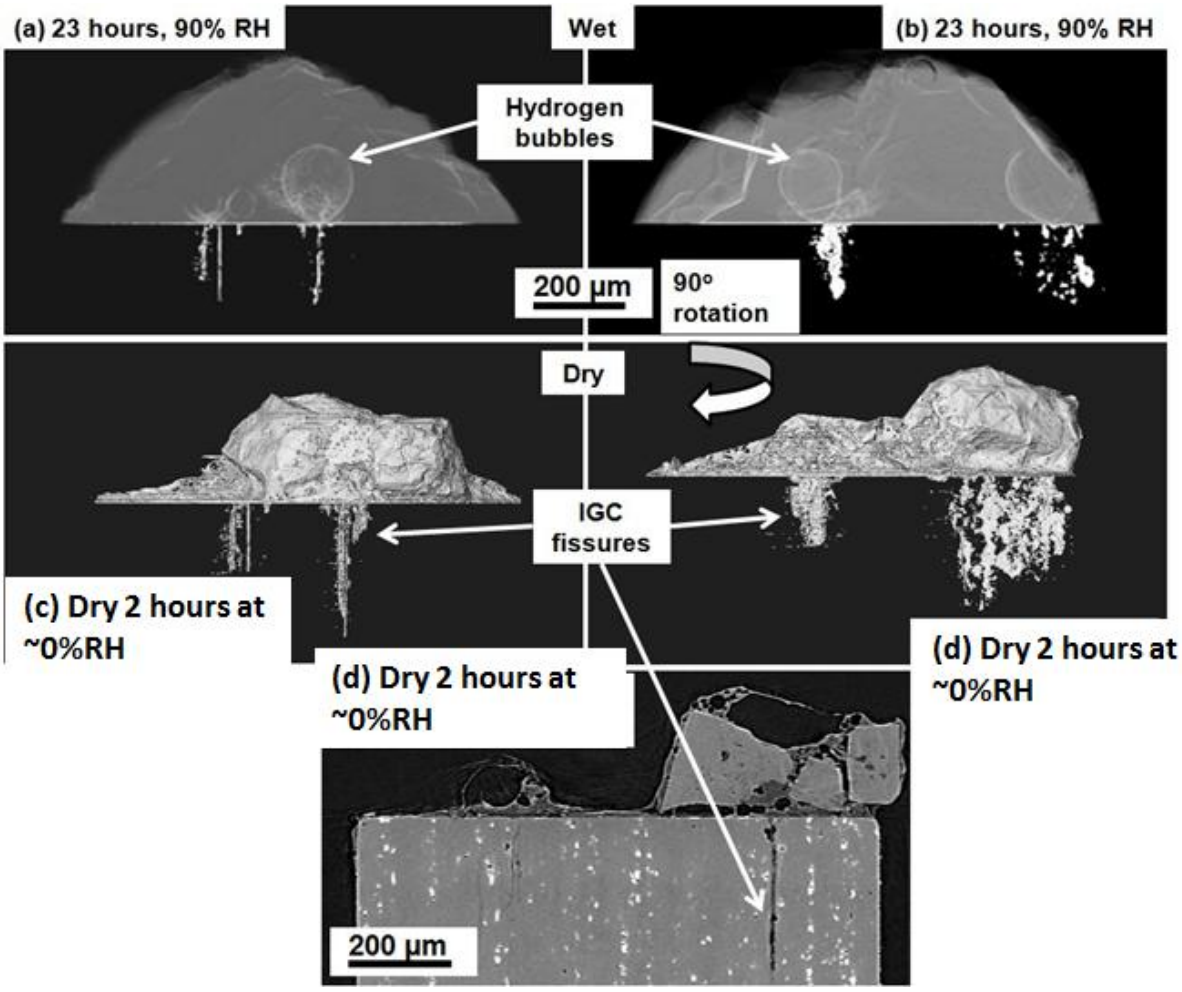


**Figure 6.1– 3-D reconstruction of IGC corrosion fissures in AA2024-T351 pin sample, NaCl droplet, CDD ~4500 µg/cm$^2$; (a) 23 hours at 85% RH, (b) rotated 90$^o$ with $H_2$ bubbles visible at surface of pin, and IGC fissures visible subsurface; (c) Following 1 hour drying at ~0% RH, (d) rotated 90$^o$ showing IGC fissure volume evolution under solid phase; (e) Vertical tomographic section of IGC under solid phase**

Figure 6.2 shows the development of fissures during drying of a droplet of simulated ocean water on an AA2024 pin sample. The top and middle image show a vertical section of the most active site, at the end of the wet phase and following drying for 1 hour at ~0% RH respectively. In the top image a large number of small hydrogen bubbles can be seen, the slightly distorted shapes of these bubbles is probably due to the presence of large numbers of bubbles which interconnect. Further the

presence of corrosion product will also influence the shape of the droplet. Following drying (middle), the salt deposits and the gelatinous layer of corrosion product can be seen to be discontinuous in the section shown. In addition a large salt crystal appears to have precipitated in the vicinity of the largest corrosion site which was the most active during the drying phase. The bottom image shows 3-D reconstructions of the fissure volumes: yellow sites are those grown during the initial 24 hour exposure and red shows the development of corrosion during the drying phase. It can be seen that most sites show little growth but two sites have grown appreciably during the drying phase.

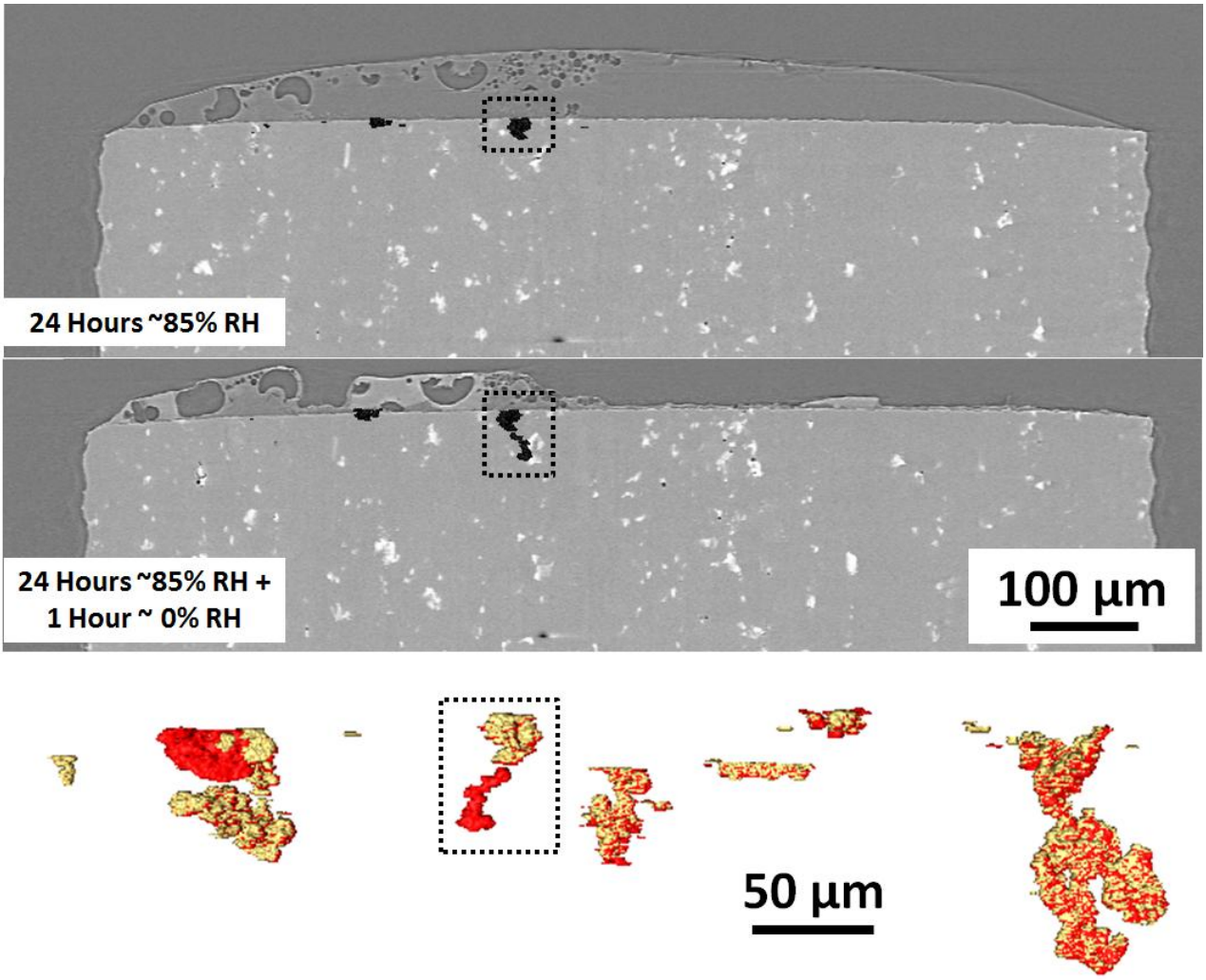


**Figure 6.2 - AA2024 pin sample under droplet of simulated ocean water (initial CDD 500 µg/cm$^2$), exposed for ~24 hours at ~85% RH and dried for 2 hours at ~0% RH, bottom row shows reconstructed volume at end of wet phase (yellow) and following drying (red), most active site during drying is highlighted**

The measured material loss in samples exposed to an initial wet phase of 85% RH and then dried either to the DRH of the salt or “0% RH” is plotted in Figure 6.3. Overall the trend which emerges is that during the drying phase either at the end of a 12 hour or a 24 hour initial exposure there was an increase in the measured rate of material loss. This relates to a rise in the rate of corrosion. For plots above the dotted

line with an initial CDD of 4500 µg/cm$^2$ the overall rate of corrosion was greater than for those below the dotted line with CDD 500 µg/cm$^2$. The rate of material loss was broadly comparable for all samples exposed at 4500 µg/cm$^2$, until the onset of a drying phase. The same was observed for samples with CDD of 500 µg/cm$^2$ where an increase in rate was observed during drying.

There is also an indication that samples dried to close to their DRH values (marked on the plot) saw a greater increase in material dissolution during the initial phase of drying compared with samples that were dried to “0% RH”.

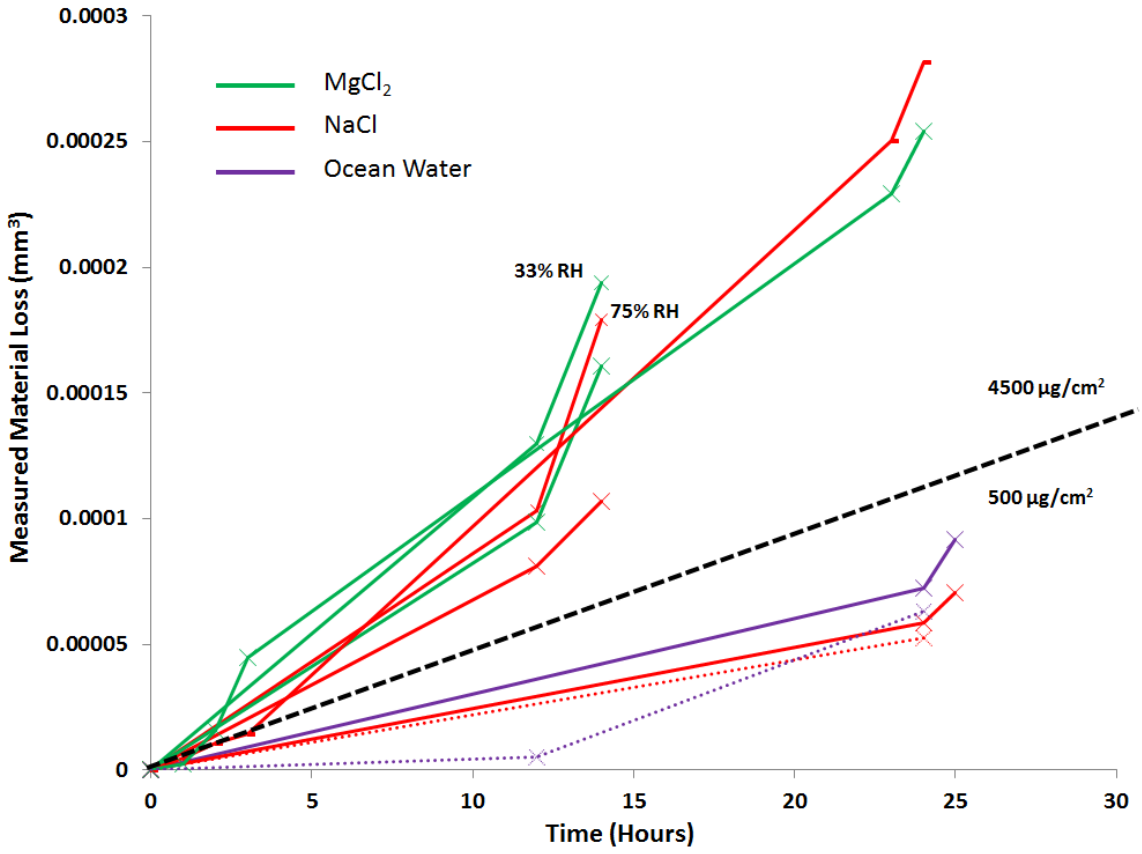


**Figure 6.3 - Measured material loss in AA2024 pin samples during µCT measurements for wet phases (85% RH) followed by drying either to "0% RH" or to their respective DRH (75% RH for NaCl and 33% RH for $MgCl_2$ and ocean water). Samples were exposed for 12 or 24 hours, at which point a tomogram was measured from which the corroded volume was measured, and the measurement was repeated following 1 hour at the changed RH. Salt types are indicated by colour, for cases where drying was not to "0% RH" the RH used is indicated. Traces above the dotted line had an initial CDD of 4500 µg/cm$^2$ and samples below had initial CDD of 500 µg/cm$^2$. Samples which remained continuously wet used as a corrosion rate comparison are shown by dotted lines.**

### 6.2.2 Influence of re-humidification of the environment on the development of localised corrosion

Following maintenance of a dry period at "0%" RH it was observed that during re-humidification of the environment to 85% RH, the formation and growth of new sites

of localised corrosion was observed (Figure 6.4). Top images show near surface sections of an AA2024 pin sample exposed to wet-dry cycling through 24 hours wet at 85% RH (left), and following 12 hours dry at “0%” RH and 20 hours re-wet at 85% RH (right) under NaCl solution of 500 µg/cm$^2$, with fissures highlighted in red. The original site grown during the initial exposure period is circled by a dotted white line, it can be seen that two new sites have formed and grown rapidly during the second wet phase. 3-D reconstructions of the fissures shown in the bottom image, highlight the original sites, it can be seen that no measurable growth has taken place, instead other IGC fissures have grown at a significantly increased rate.

Figure 6.5 plots the measured volume loss over time for the sample shown in Figure 6.4, along with a trace for a sample exposed in a constant wet state at 85% RH. It can be seen that the measured rate for both samples during the initial 24 hour exposure both rates were comparable. For the wet-dry sample it can be seen that during drying there was a small increase in rate which was followed by a drop to a phase of no localised growth during the dry phase at “0%” RH. Following re-humidifcation a further burst in the rate of corrosion was measured which was sustained through the second wet phase.

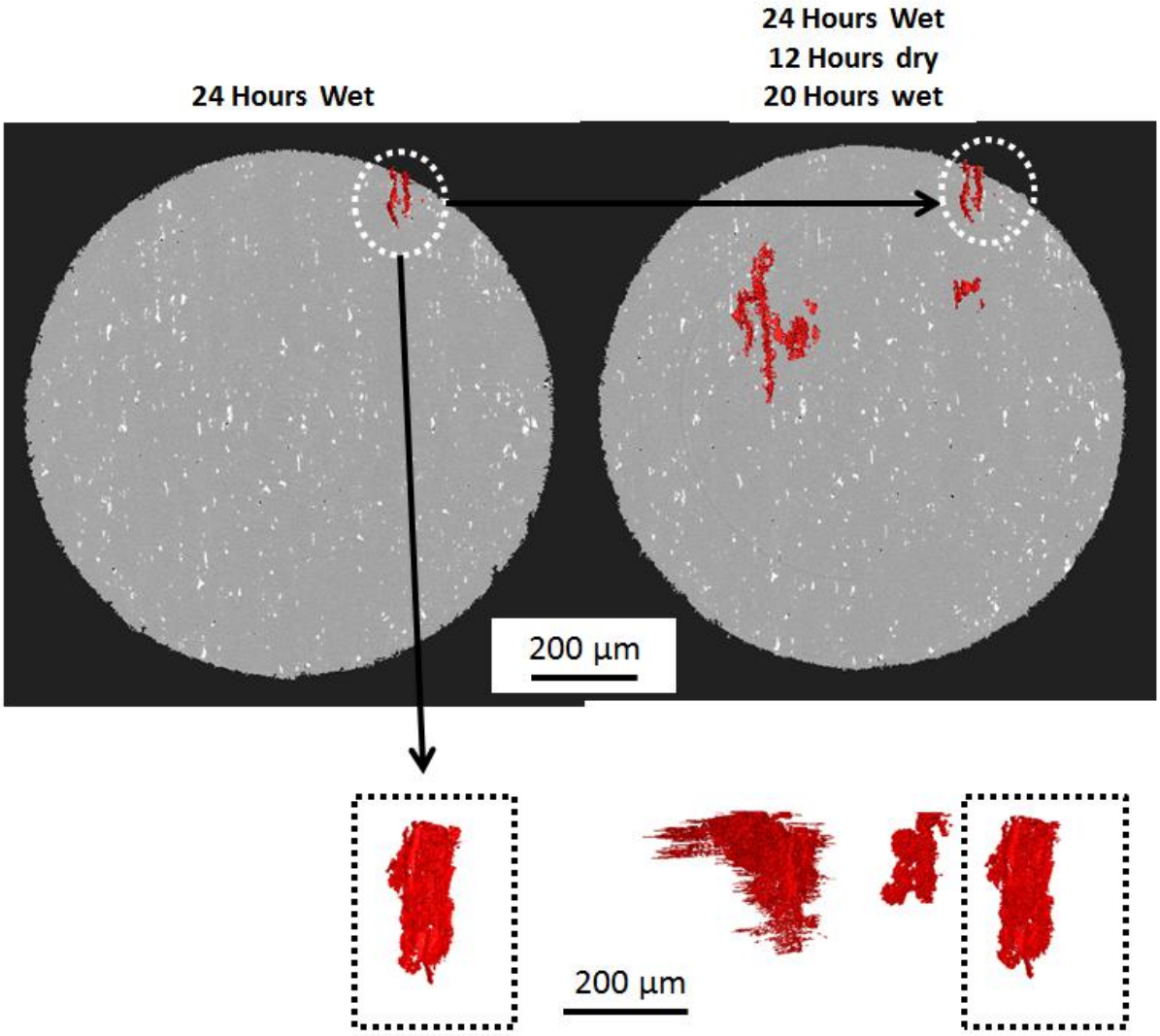


**Figure 6.4 - Development of localised corrosion in an AA2024 pin sample during a cyclic exposure to NaCl solution, initial CDD of ~500 µg/cm$^2$, left hand side shows sample following 24 hours at ~85% RH, right hand side shows sample following the drying (to "0%" RH) and re-humidification process (to 85% RH). Bottom shows 3-D reconstructions of the corroded volume, following initial wet phase (left) and following drying and re-humidification (right), the site formed during the initial wet phase is highlighted.**

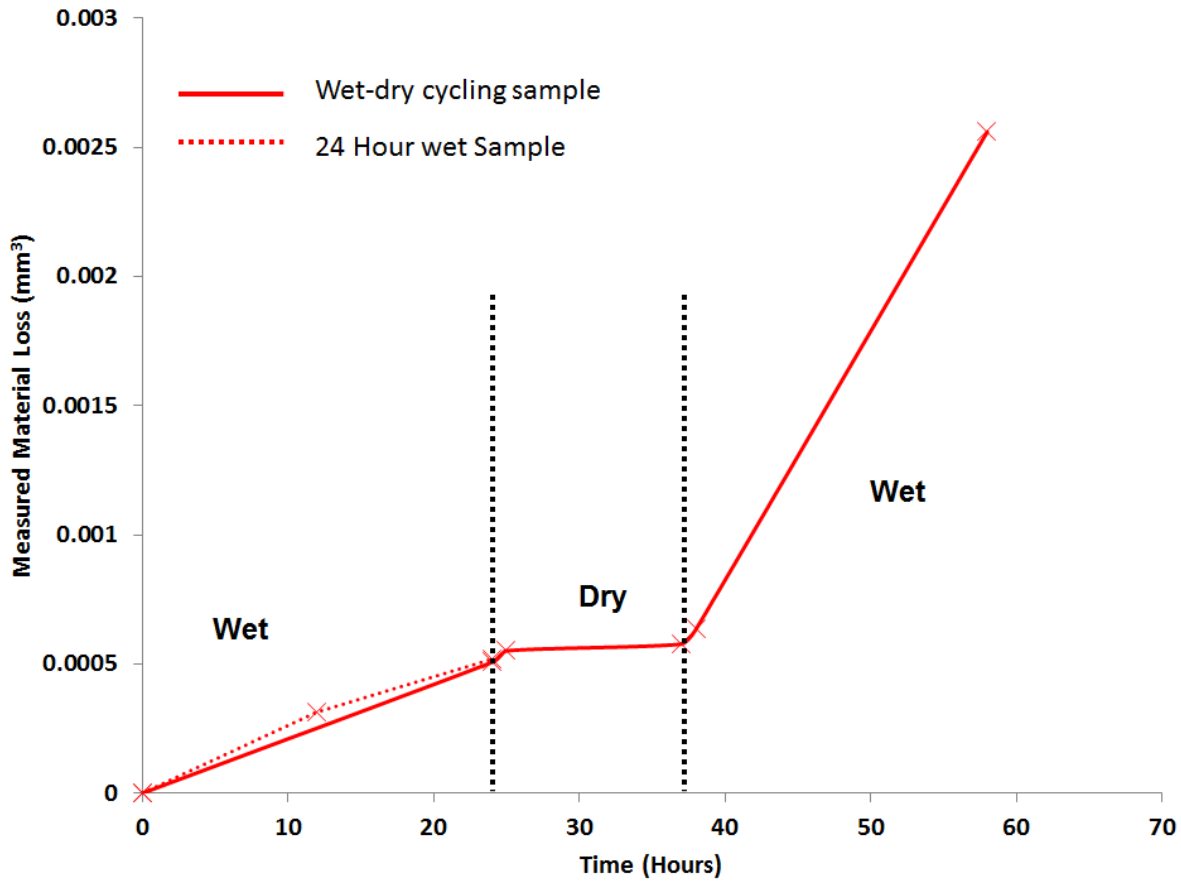


**Figure 6.5 - Measured material loss in AA2024 pin sample through a single wet/dry/wet cycle of atmospheric exposure, under a droplet of NaCl solution with initial CDD ~500 µg/cm$^2$. The sample was initially exposed to 85% RH for 24 h when the first measurement was made. The sample was immediately placed in a dry environment and measurement was made 1 hour later. A measurement was made at the end of a 12 hour dry phase, following 1 hour at 20 hours re-humidification to 85% RH. In addition plotted is the measured material loss for a sample exposed to NaCl solution with initial CDD ~500 µg/cm$^2$ for 24 hours continually as a comparison for rate of corrosion. Black dotted lines indicate time point at which RH was changed.**

Figure 6.6 plots a comparison of material loss for samples exposed to different initial CDD's of ~500 and 4500 µg/cm$^2$. Despite the different exposure times it can be seen that the behaviour with regards to trends in the corrosion rates are similar for the two conditions. With an increase during the initial phase; preceding a drop in rate to a level where growth of localised corrosion sites effectively stopped. During re-

humidification of the environment from “0%” to 85% RH a further burst in the corrosion rate was observed, the increased rate of dissolution was maintained during the second wet phase. The higher initial CDD value resulted in a greater measured loss of material at the time point for which its final measurement was made, which is to be expected from the results shown in Section 4.2.4.

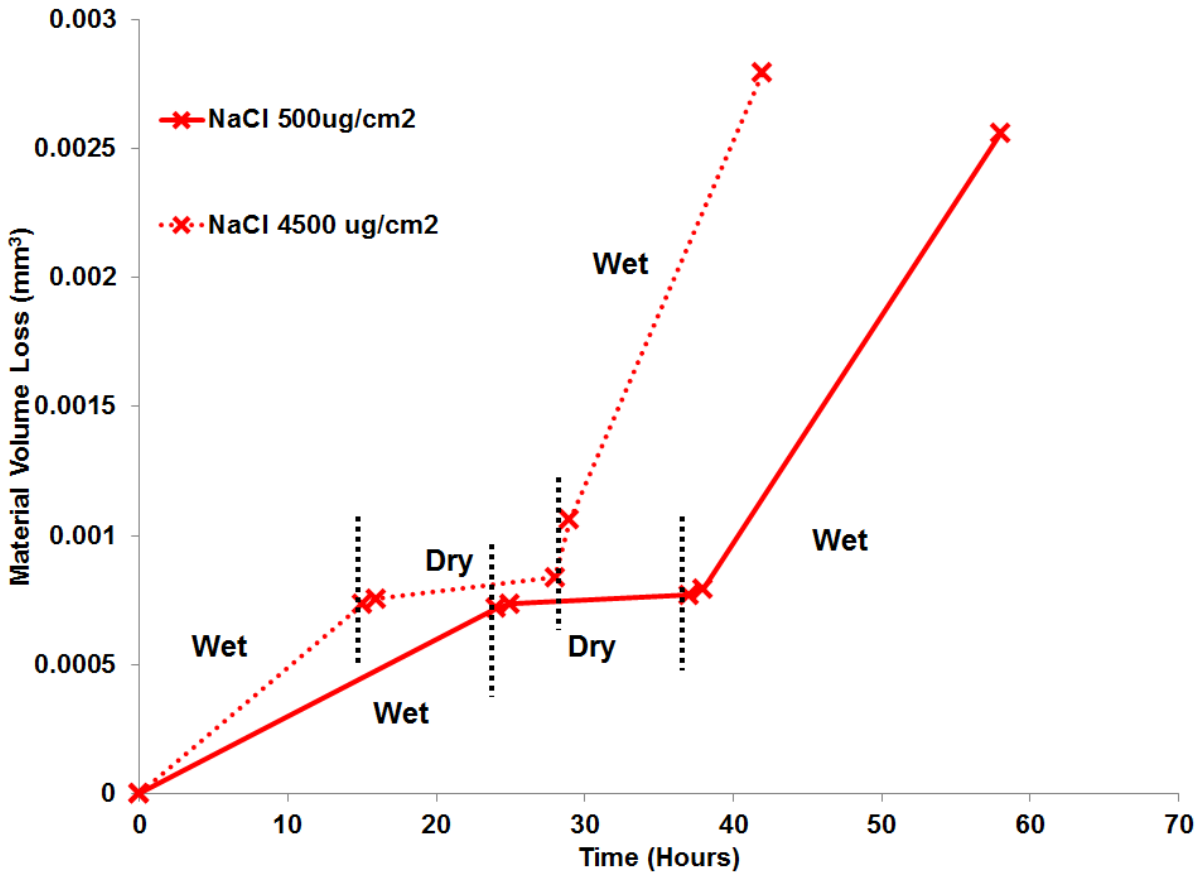


**Figure 6.6 - Measured material volume loss through single wet (85%RH)-dry (“0%” RH) - wet (85%RH), cycle for NaCl solutions, with initial CDD's of ~500 µg/cm$^2$ and of ~4500 µg/cm$^2$, black dotted lines indicate time point at which RH was changed**

### 6.2.3 Influence of Drying Regime on Development of Localised Corrosion during Wet-Dry Cycling

Figure 6.7 demonstrates how the formation of new localised corrosion sites takes place under NaCl solution droplets with fixed initial CDD of 4500 µg/cm$^2$, exposed to different wet-dry regimes. Top row shows sample exposed through cycle of 85-“0”-85% RH and bottom row through 85-75-85% RH. In both cases the initial wet phase involved 12 hours exposure at 85% RH, the sites formed during this phase are shown for both samples in the left hand column. Near surface sections are shown with fissure sites highlighted. Right hand side column shows near surface sections following wet-dry exposure, in both cases original sites are highlighted by means of dotted black squares, and new sites by dotted red circle.

It can be seen that for both regimes new sites were initiated during the second wet phase. This accounted for a significant burst in the rate of corrosion; this is shown in Figure 6.8 where measured material loss is plotted for both samples shown in Figure 6.7. It is evident that the trend observed for changes in rate with increases during the initial dry phases and the second wet phase were consistent for both samples. But following the initial dry phase it can be seen that for the sample dried to “0%” RH rate dropped to no growth, whilst for the sample dried to 75% RH some growth continued during the dry phase.

A comparison of samples measured once at the end of a single wet phase of ~60 hours, both wet-dry samples showed an increased corrosion rate at the ~40 hour time point when the final measurement was made. During the initial wet phase the rate is broadly comparable for all of the samples shown.

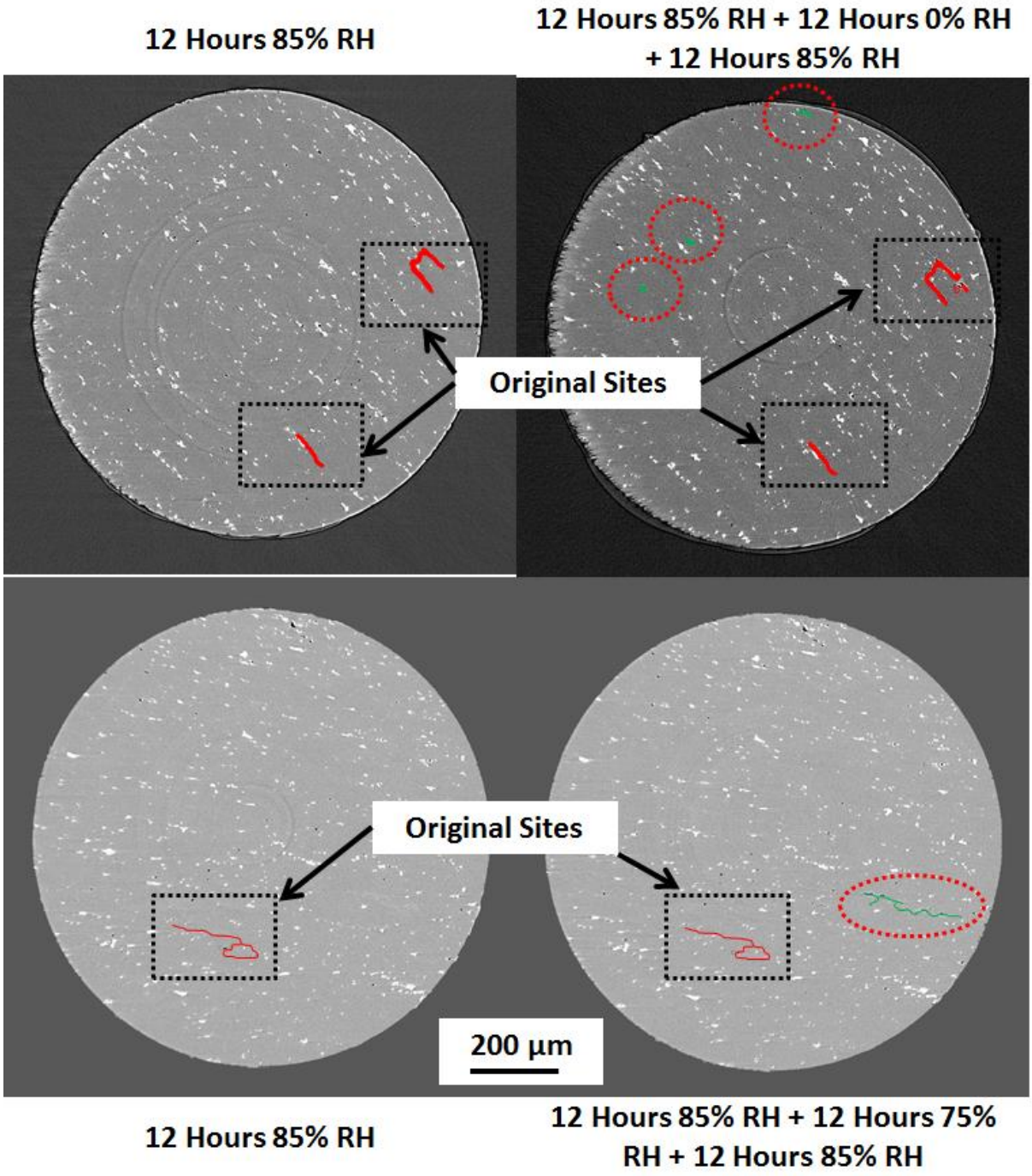


**Figure 6.7 - Development of new sites of localised corrosion in AA2024 pin samples during cyclic exposure to NaCl solution droplets with an initial CDD of ~4500 µg/cm$^2$, under different drying regimes. Top sample exposed to 85-0-85% RH, and bottom sample exposed to 85-75-85% RH, original sites black rectangles and new sites red circles**

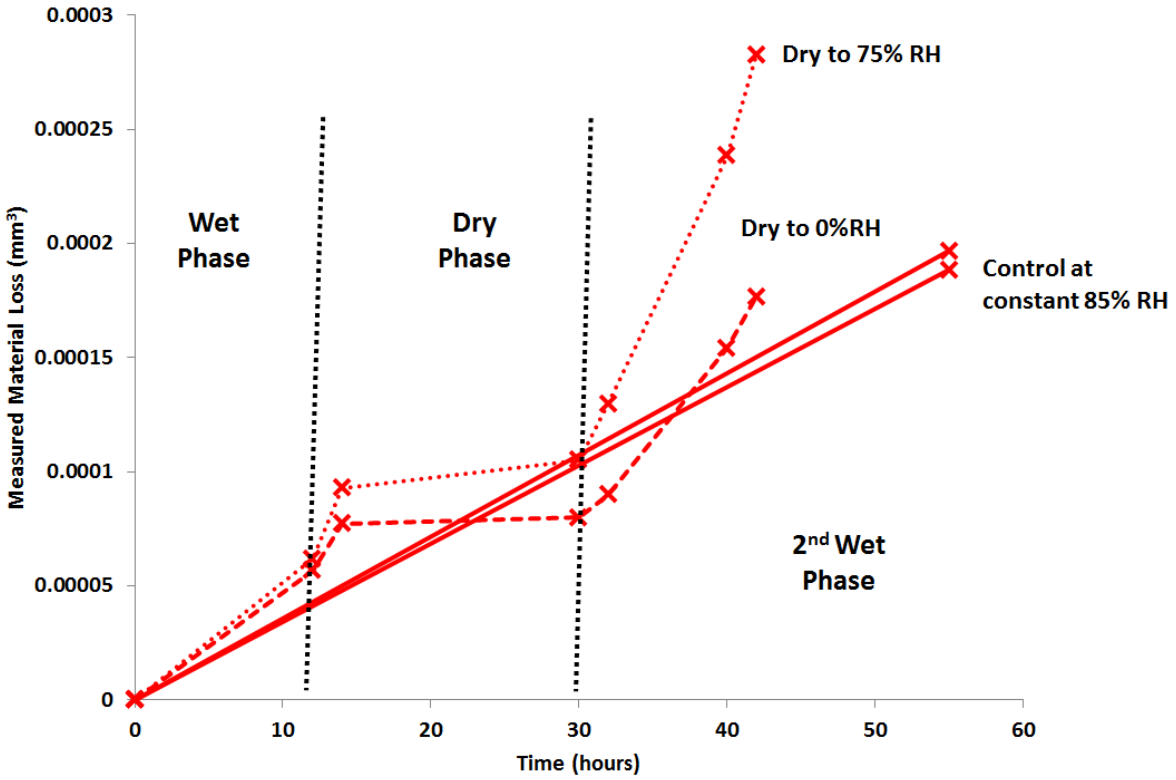


**Figure 6.8 – Measured material volume loss through a wet-dry-wet cycle under NaCl droplets of initial CDD of ~4500 µg/cm$^2$, for different drying regimes of 85-75-85% RH (dotted line) and 85-0-85% RH (dashed line), and comparison for samples left at constant RH of 85% (solid lines). Black lines indicate time points at which RH was changed, and labels indicate drying condition and if atmosphere was wet or dry.**

Localised corrosion behaviour for $MgCl_2$ samples under different wet-dry regimes is shown for a fixed CDD of 4500 µg/cm$^2$, exposed to different wet-dry regimes in Figure 6.9. Top row shows sample exposed through cycle of 85-“0”-85% RH and bottom row through 85-33-85% RH. In both cases the initial wet phase involved 12 hours exposure at 85% RH; the sites formed during this phase are shown for both samples in the left hand column. Near surface sections are shown with fissure sites highlighted. Right hand side column shows near surface sections following wet-dry exposure, in both cases original sites are highlighted by means of dotted black squares, and new sites by dotted red circle.

It can be seen that for both regimes new sites were initiated during the second wet phase. This accounted for a significant burst in the rate of corrosion; this is shown in Figure 6.10 where measured material loss is plotted for both samples shown in Figure 6.9. It is evident that the trend observed for changes in rate with increases during the initial dry phases and the second wet phase were consistent for both samples. But following the initial dry phase it can be seen that for the sample dried to "0%" RH rate dropped to no growth, whilst for the sample dried to 33% RH some growth continued during the dry phase.

A comparison of samples measured once at the end of a single wet phase of ~60 hours, both wet-dry samples showed an increased corrosion rate at the ~40 hour time point when the final measurement was made. During the initial wet phase the rate is broadly comparable for all of the samples shown.

When compared to NaCl samples, the final difference in volume for the different wet-dry regimes is reduced, this is due to the much reduced DRH value of $MgCl_2$ (33% RH). As such solution remains present at the metal surface for a prolonged period of time allowing a greater amount of dissolution to take place.

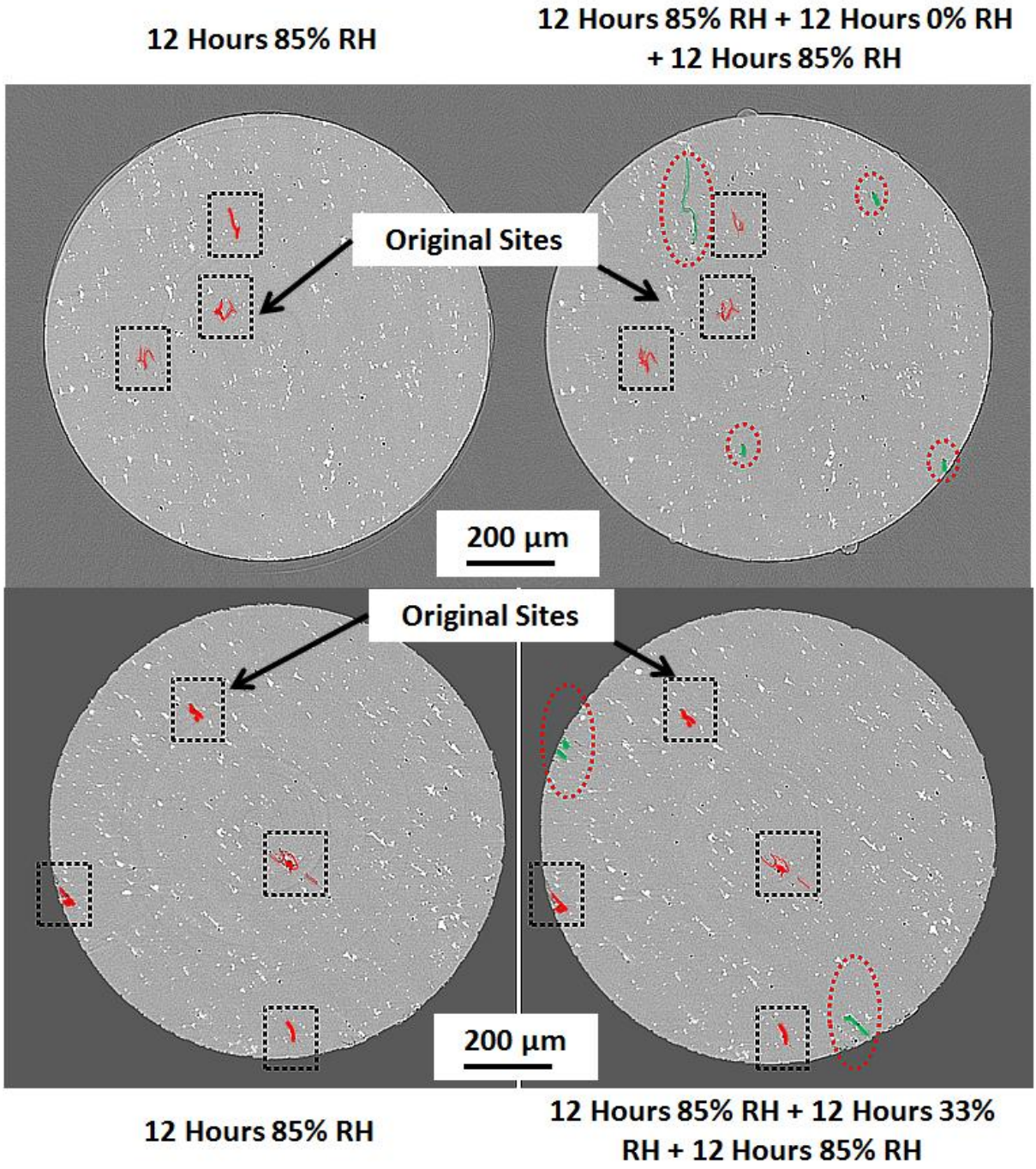


**Figure 6.9 - Development of new sites of localised corrosion in AA2024 pin samples during cyclic exposure to $MgCl_2$ solution droplets with an initial CDD of ~4500 µg/cm$^2$, under different drying regimes. Top sample exposed to 85-0-85% RH, and bottom sample exposed to 85-33-85% RH, original sites black rectangles and new sites red circles**

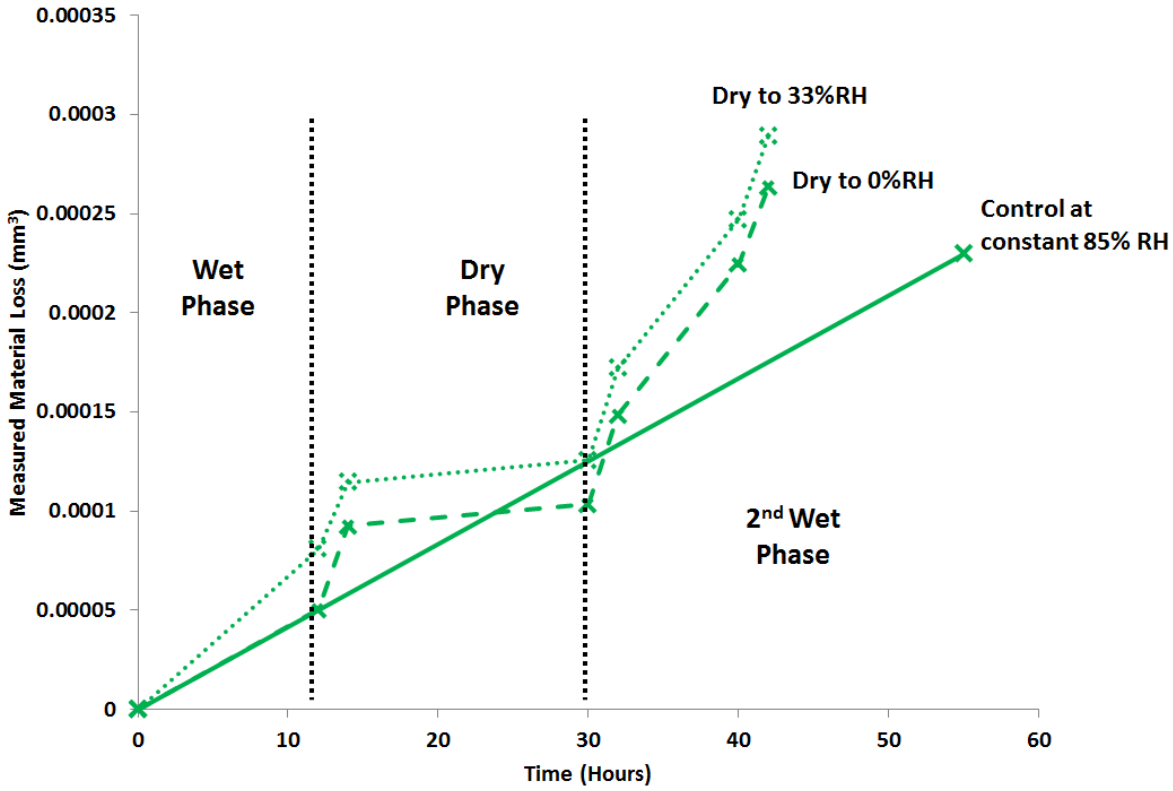


**Figure 6.10 - Measured material volume loss through a wet-dry-wet cycle under $MgCl_2$ droplets of initial CDD of ~4500 µg/cm$^2$, for different drying regimes of 85-33-85% RH (dotted line) and 85-0-85% RH (dashed line), and comparison for samples left at constant RH of 85% (solid lines). Black lines indicate time points at which RH was changed, and labels indicate drying condition and if atmosphere was wet or dry.**

Figure 6.11 shows a series of near surface sections for a sample exposed to simulated ocean water and subjected to a wet-dry cycle of 85-0-85% RH. Highlighted in each case (dotted black square) is the site formed during the original 24 hour exposure at 85% RH. It can be seen that during the initial drying phase a small new site initiated, this site formed during the initial 1 hour of drying. Following re-humidification of the environment to 85% RH it can be seen that a large number of new sites formed, these are shown in the bottom row of reconstructed sections.

3-D reconstructions of the corroded volumes are shown in Figure 6.12, the original site grown during the initial 24 hour period at 85% RH is highlighted by a black dotted square. The new sites formed during re-wetting can be seen, which have developed rapidly within the first hour of re-humidification of the environment to 85% RH. In this sample some continued growth of the pre-existing site was seen in addition to the new sites. This was the case in a small number of the samples studied during this work.

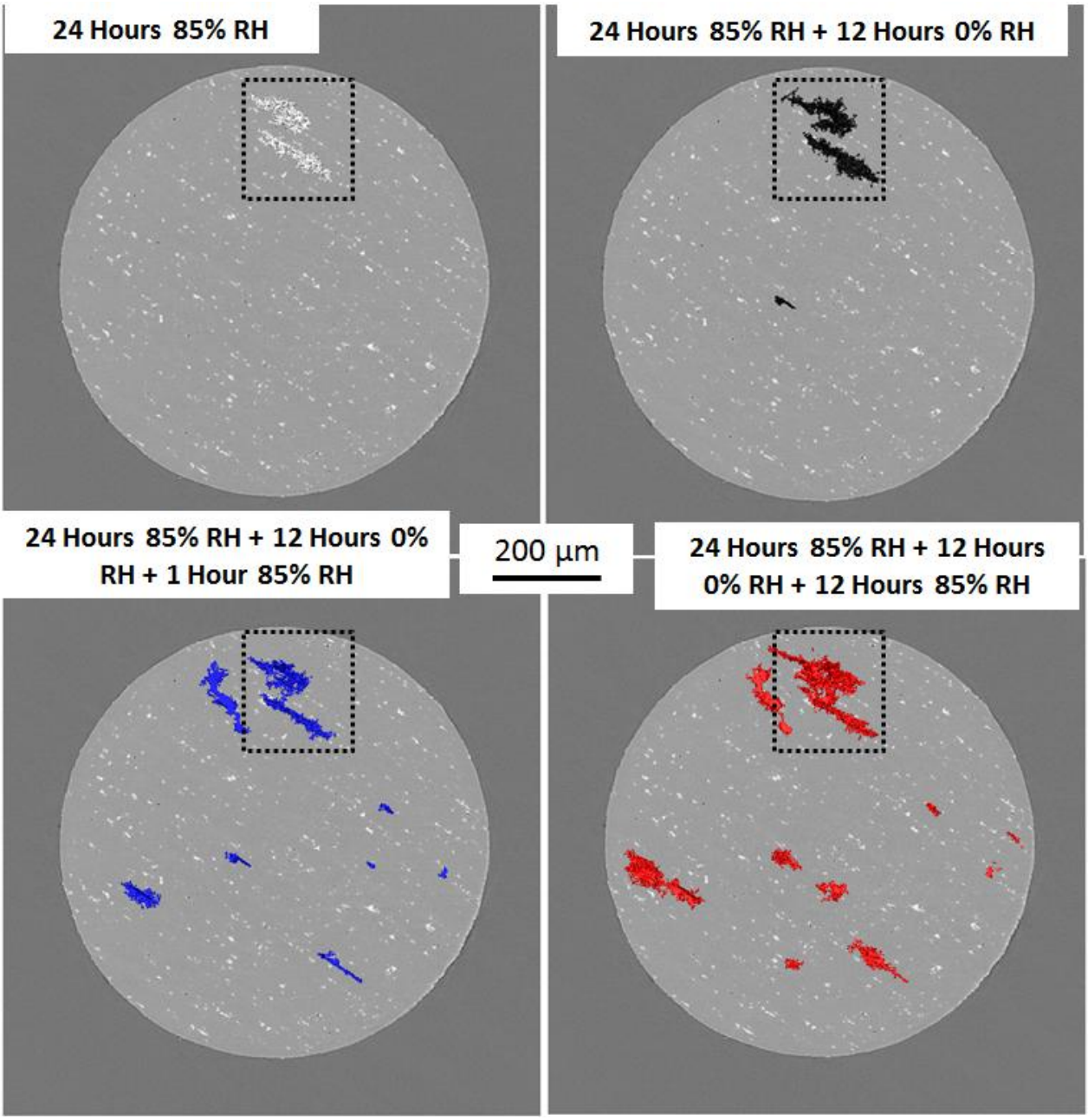


**Figure 6.11 - Near surface sections of AA2024 pin sample, µCT measurements made during wet/dry cycling, under substitute ocean water solution droplets. Under cycle of 85-0-85% RH, with initial CDD of ~500 µg/cm$^2$. Development of new localised sites of corrosion is shown, original site is highlighted by black dotted square, time points and humidities are labelled.**

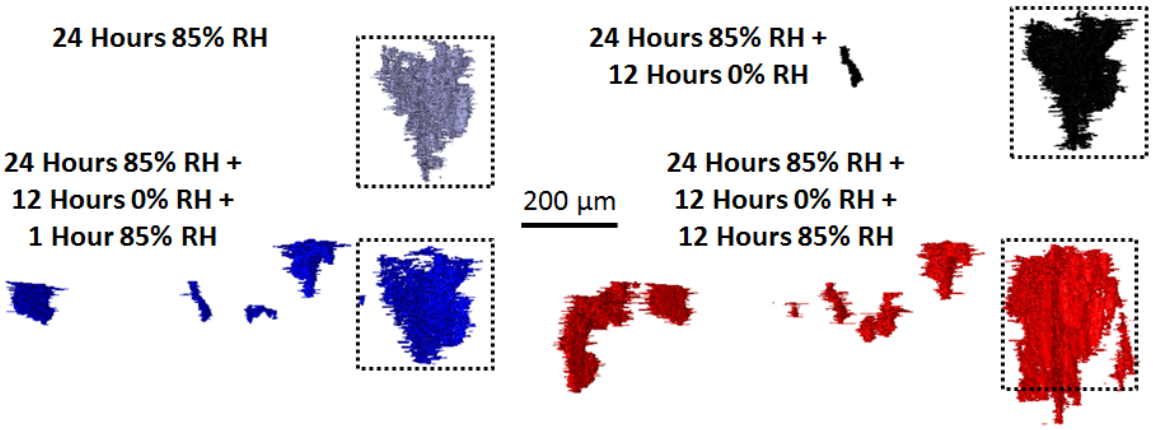


**Figure 6.12 – 3-D reconstructed corrosion fissure volumes during wet/dry cycling of AA2024 pin sample exposed to substitute ocean water droplet, under cycle of 85-0-85% RH, with initial CDD of ~500 µg/cm$^2$. Original site is highlighted by means of dotted black square, time points and humidities are labelled.**

Measured material loss is plotted for a single wet-dry cycle of 85-0-85% RH for simulated ocean water samples in Figure 6.13. It can be seen that whilst there was some scatter in the material loss for the samples, both followed the same trends with an acceleration in corrosion during the second wet phase. Plot showing the greatest volume loss corresponds to the images shown in Figure 6.11 and Figure 6.12. In addition a comparison with a sample which was left for 24 hours at 85% is shown as a comparison for the initial rate. There was a difference in the rates during the initial 12 hour period but following 24 hours the volume loss was comparable. No 12 hour measurement was made for the cycling sample so it may be that the behaviour was similar.

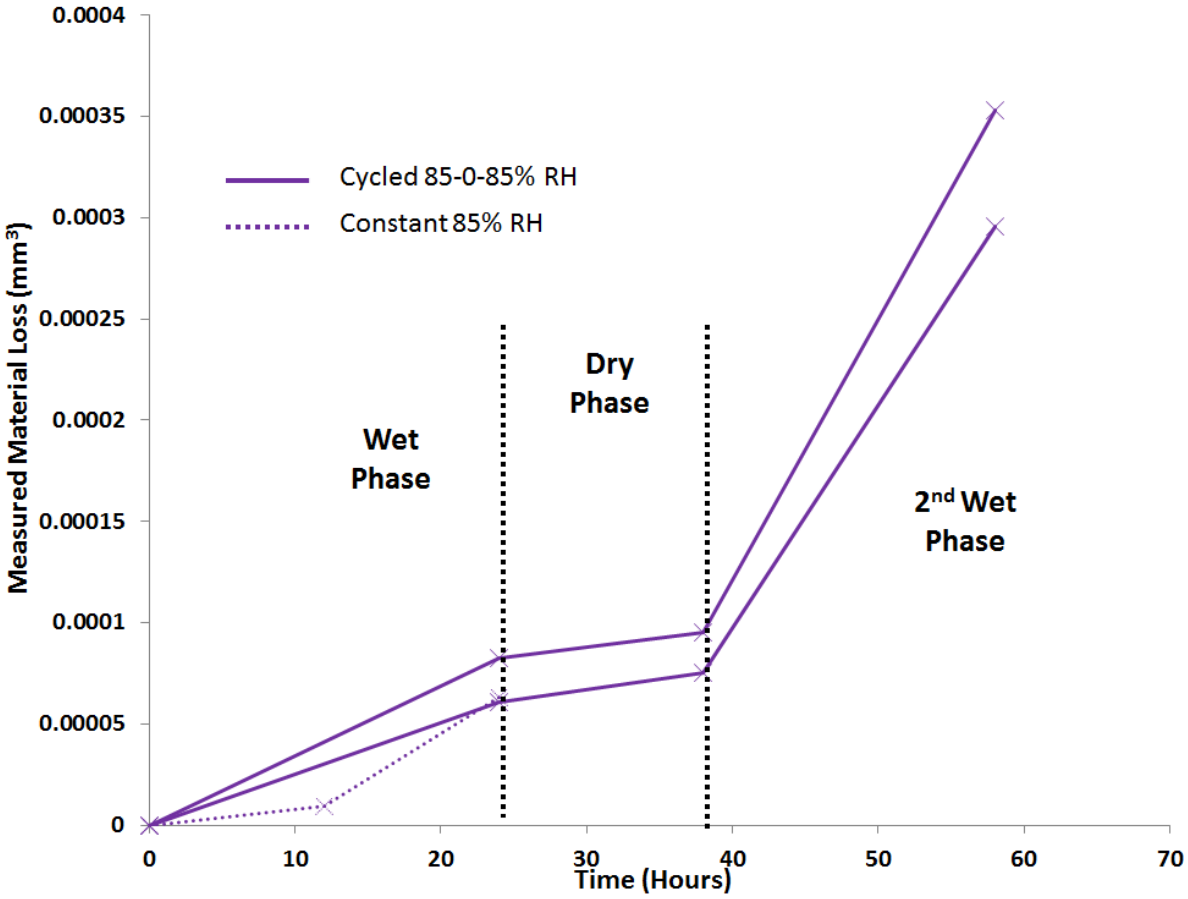


**Figure 6.13 - Measured material volume loss through a wet-dry-wet cycle under simulated ocean water droplets of initial CDD of ~500 µg/cm$^2$, for different drying regime of 85-0-85% RH (solid lines), and comparison for sample left at constant RH of 85% (dotted line). Black lines indicate time points at which RH was changed, and labels indicate if atmosphere was wet or dry.**

Development of localised corrosion fissures in an AA2024 pin sample exposed to simulated ocean water with under a wet-dry cycle of 33-85-33% RH, is shown in Figure 6.14 and Figure 6.15. Figure 6.14 shows a series of near surface sections, for time point at the end of initial 33%RH where two small sites are visible, these are also shown in the top image in Figure 6.15. Following humidification of the environment a number of new sites initiated, this is shown in the middle row in each of the figures. Following reduction of the RH to 33% these sites continued to grow,

with the addition of a number of much smaller sites which are visible on the near surface section at the bottom of Figure 6.14.

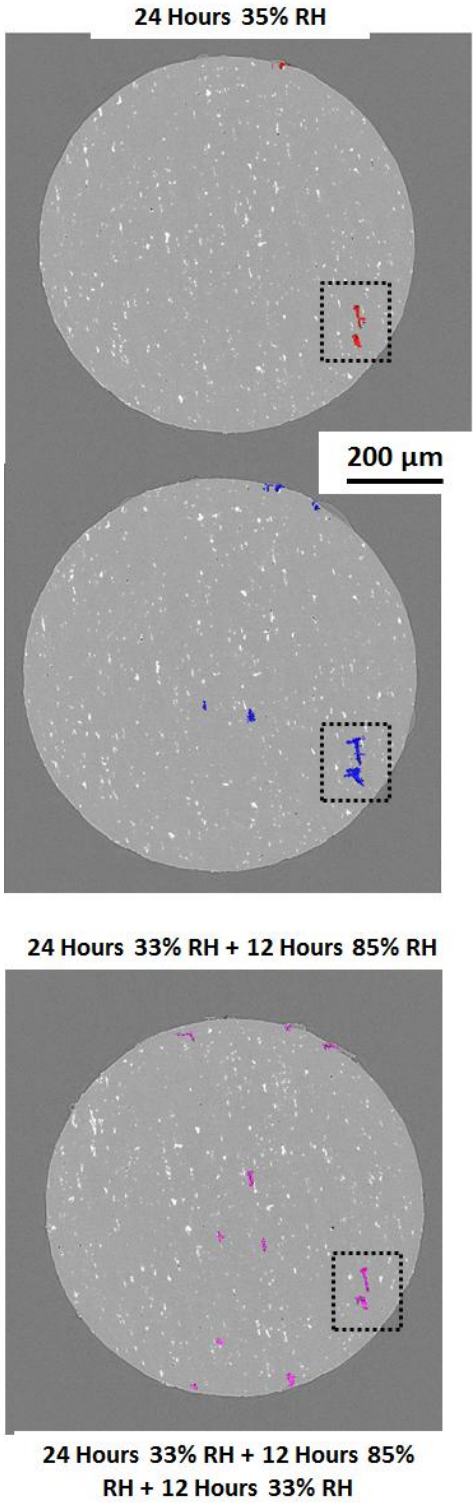


**Figure 6.14 - Surface sections of an AA2024 pin sample, µCT measurements made during the wet/dry cycling, under substitute ocean water solution droplets, under cycle of 33-85-33% RH, with initial CDD of ~500 µg/cm$^2$. Original site is highlighted by black dotted square, time points and humidities are labelled.**

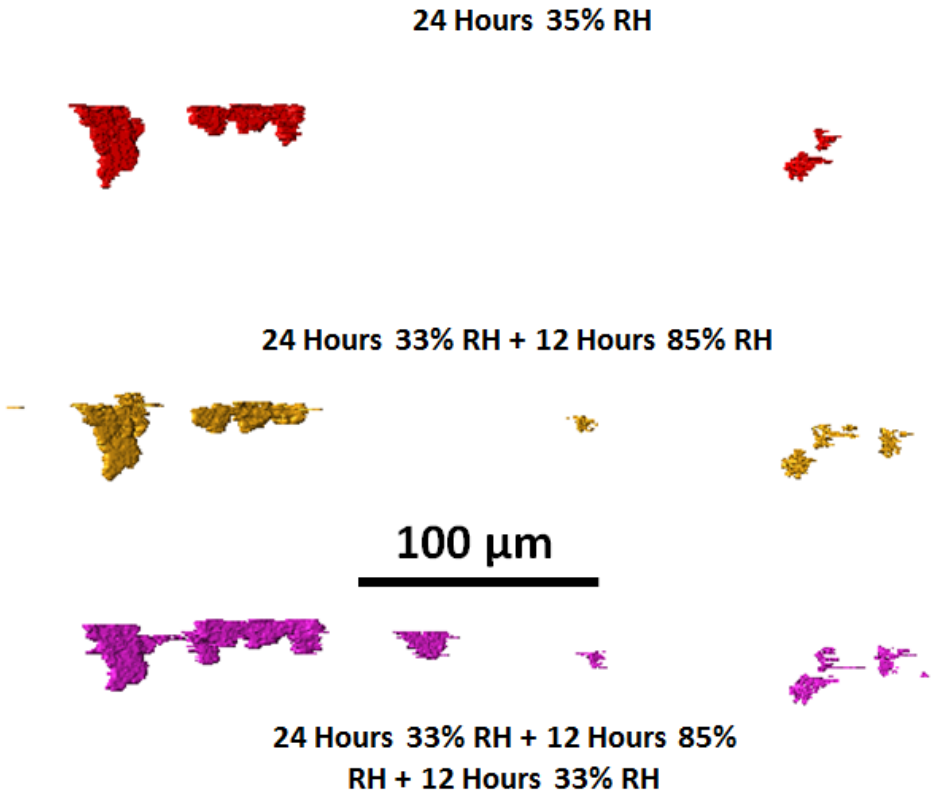


**Figure 6.15 - Reconstructed corrosion fissure volumes during the wet/dry cycling of an AA2024 pin sample exposed to substitute ocean water droplet, under cycle of 33-85-33% RH, with initial CDD of ~500 µg/cm$^2$**

The measured material loss for ocean water samples exposed to different drying regimes is plotted over time in Figure 6.16. For samples exposed to the wet-dry regime of 85-0-85, total material loss was greater than for samples exposed to 33-85-33% RH. For the latter an increase in the corrosion rate was seen following humidification of the atmosphere to 85% RH, before it slowed following drying back to 33% RH. Some scatter can be seen for each of the drying regimes, in terms of measured volume, but trends followed were the same. Also plotted are two steady state samples for a comparison of corrosion rate during the initial 24 hour period it

can be seen that they are in reasonably good agreement with the wet-dry cycling samples during this phase.

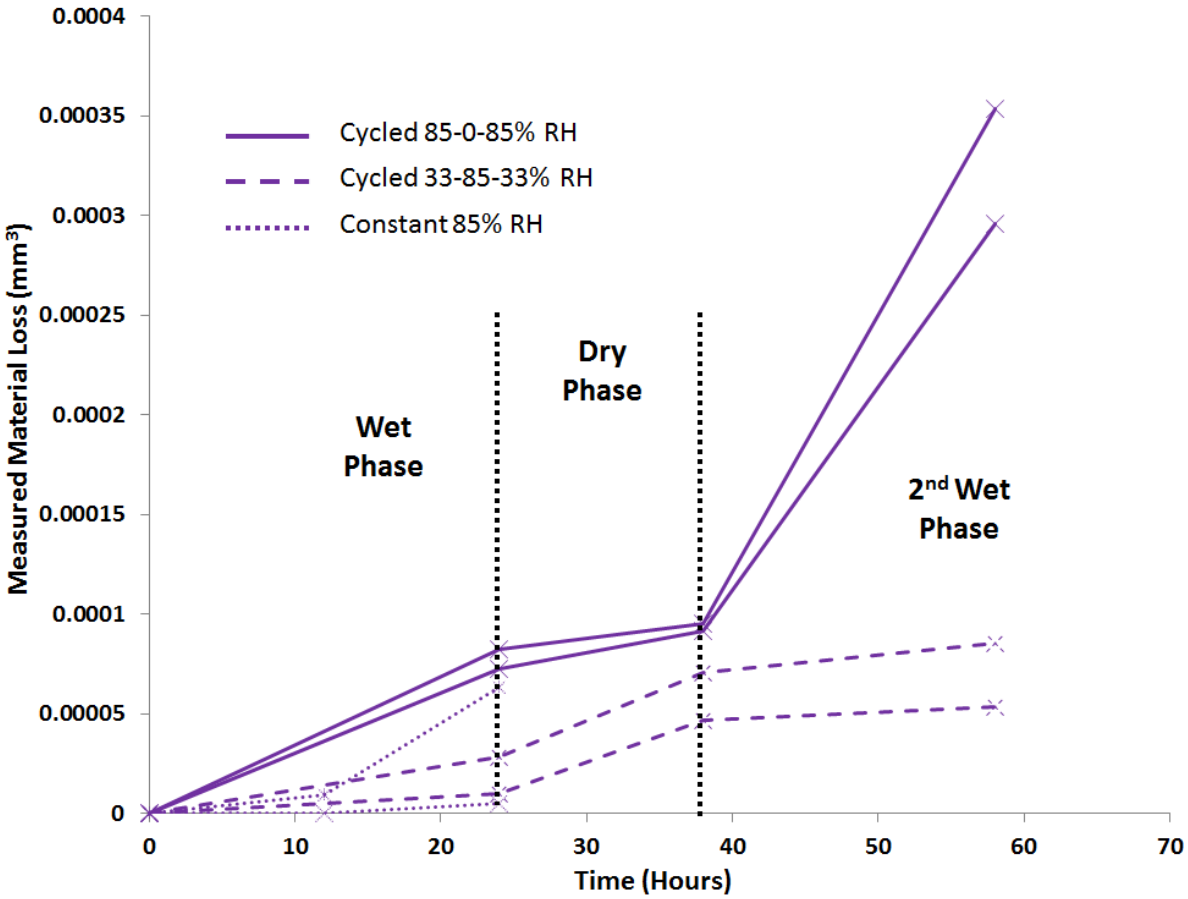


**Figure 6.16 - Measured material volume loss through different wet/dry cyclic exposures, under solution droplets of substitute ocean water, initial CDD ~500 µg/cm$^2$. Solid lines shows wet-dry regime of 85-0-85% RH, dashed lines show wet-dry regime of 33-85-33% RH, and dotted lines show samples left in "wet" state at 33% and 85% RH. Dotted black lines indicate time points at which humidity was changed, labels indicate if atmosphere was wet or dry.**

### 6.2.4 Long Term Drying Effect

Figure 6.17 demonstrates an AA2024 pin sample exposed under a droplet of $MgCl_2$ solution for 12 hours at ~85% RH, which was stored in 0% RH for 1 week before being placed back into an environment of ~85% RH. It can be seen that as with

samples which were only dried for a shortened time period (12 hours) formation of new sites took place following re-humidification of the slat present on the sample surface. This demonstrates that the phenomenon of new site imitation will take place even over longer dry periods if the salt deposit is not removed from the metal surface.

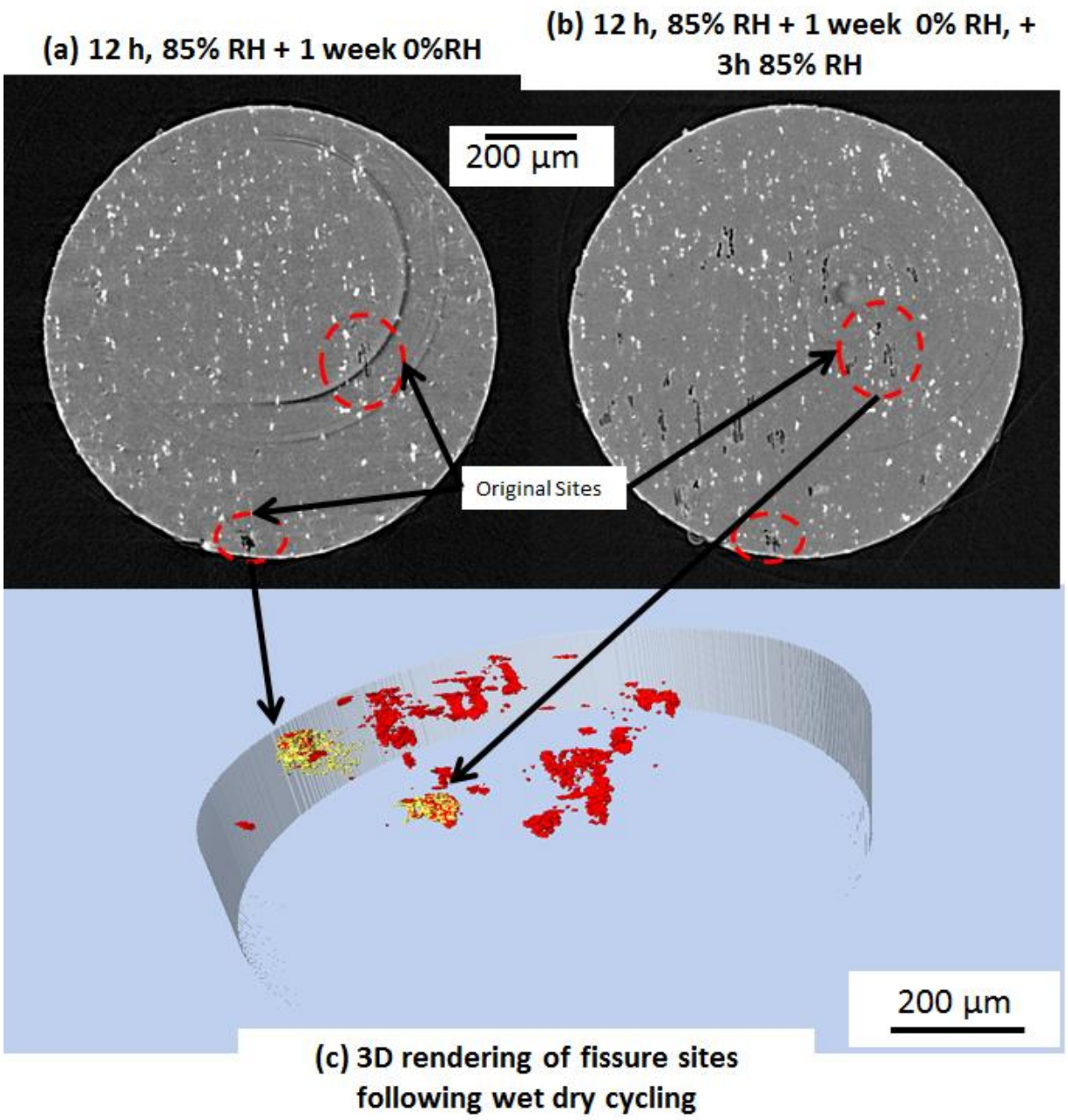


**Figure 6.17 - An AA2024-T351 pin sample exposed at 85% RH, under an $MgCl_2$ solution droplet with CDD of ~ 4500 µg/cm$^2$, (a) following the initial 12 hours in simulated atmosphere of ~85% RH, and dry for 1 week ~0% RH. (b) following 1 week dry ~0% RH and 3 hours re-humidification to 85% RH, multiple new sites are visible on the surface of the pin sample. The original corrosion sites are shown in the circles. (c) 3D rendering of the sites formed during the initial wet cycle (white), and during the second wet cycle (red)**

### 6.2.1 Precipitation of corrosion product and Salt Crystals

Figure 6.18 shows the precipitation of corrosion product at the mouth of a fissure during a wet phase of atmospheric corrosion. Precipitation of corrosion product in this area is important as it can act as a diffusion barrier to ions migrating in and out of the localised corrosion site, resulting in increasingly aggressive conditions. Presence of a hydrogen bubble can also be seen in solution, indicating that this is an active localised site.

Figure 6.19 demonstrates how during drying salt deposits can dry above a precipitated layer of corrosion product. Precipitation of the salt crystal in the presence of an active site took place in several cases for exposure under solutions containing NaCl. The indication may be that this process occurs in the vicinity of the most active site during the drying phase.

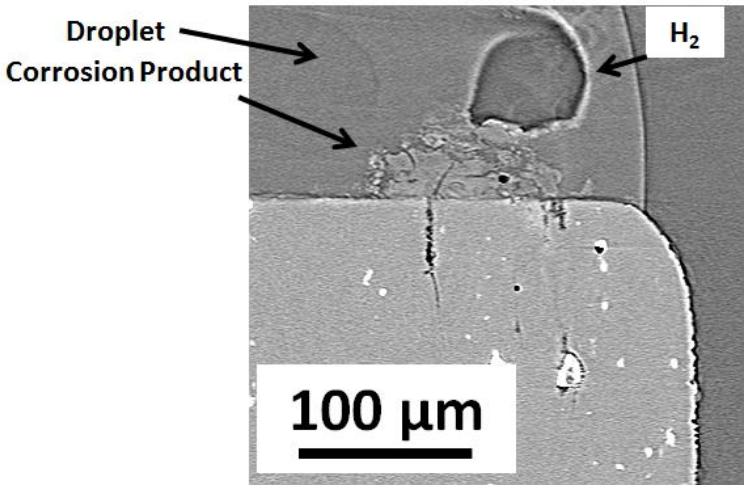


**Figure 6.18 - Precipitation of corrosion product at the mouth of active fissures during wet phase (85% RH) of atmospheric exposure to NaCl solution with initial CDD of 4500 µg/cm$^2$, with evolution of $H_2$ gas further indicating localised corrosion is proceeding**

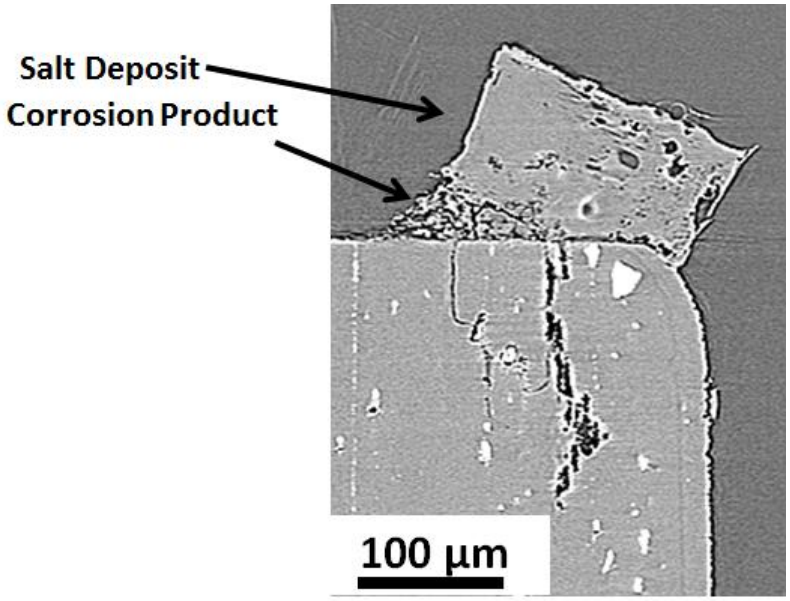


**Figure 6.19 - Dried salt deposit and precipitated layer of corrosion product at the mouth of fissure following drying (to 0% RH) after 24 hours exposed at (85% RH) of atmospheric droplet on AA2024, cubic nature of the salt deposit is typical of NaCl deposits, initial CDD 4500 µg/cm$^2$**

## 6.3 Discussion

### 6.3.1 Influence of Drying Phase on the Atmospheric Corrosion of AA2024

Following a wet phase of atmospheric exposure, drying of droplets occurs, the extent of which is dependent on the change in RH of an environment, and the salt type present on a surface. Sharp drop in RH, well below the DRH of single salts results in a very rapid drying of the droplet and salting out of solid phases. When drying to close to the deliquescent point (DRH) a slower rate of drying was observed, and moisture remained on sample surfaces below the DRH. This is consistent with the efflorescence point (ERH) being below the DRH of single salt solutions, which has been previously reported [210, 214]. This allows aqueous corrosion processes to carry on at lower RH's than the reported DRH[215].

Considering the influence of the drying phase on corrosion rate, there was an acceleration in the rate of material loss during the initial drying phase followed by a reduction in the measured rate to a point where little or no material loss continued, as the drying period was prolonged. The relative severity of the increase in rate during the initial drying phase was observed to be dependent on the quantity of salt present. In addition, sample dried to an RH close to their reported DRH, showed a greater increase in the rate of material loss than those dried to ~0% RH. Furthermore $MgCl_2$ solutions showed a greater rate of material loss than the comparable NaCl sample for the same initial CDD. This is likely due to the lower DRH of $MgCl_2$, 33%, compared with that of NaCl, 75%. As such ions remain dissolved in solution for a more prolonged period, increasing the time during which corrosion processes could proceed. A more visual representation of this acceleration in drying is shown in

Figure 6.1, where rapid growth of corrosion fissures during drying can be seen in 3-D.

This acceleration in material loss during drying has been observed on zinc and pure aluminium surfaces, as the electrolyte layer thins[160, 216]. For iron a similar acceleration in corrosion rate has been observed during the initial stage of drying of a TEL[217, 218]. Vera-Cruz observed a similar effect during drying of TEL's on steel, where the rate of corrosion increased during the initial and middle stages of drying, prior to a drop off in rate as more prolonged drying events took place[173, 219]. Morton [152] has recently shown that during evaporation of a droplet on AA7050 that a similar effect is observed.

Acceleration in the rate of corrosion during the initial phase of drying has previously been attributed to two mechanisms; (a) reduction in the oxygen diffusion distance as moisture is lost, (b) increased solution concentration as moisture is lost [152, 160, 173, 216]. Stratman [217] suggested that (a) may not hold true as he observed less of a shift in potential during a wetting phase when layer thickness is similar to that during drying, on iron surfaces. However, as is discussed later, acceleration in the rate of corrosion was observed both during re-wetting and the early stages of drying in this work.

Thus it seems reasonable to attribute the acceleration in the rate of corrosion during the drying phase measured during this work, to the same mechanisms. As during drying moisture is observed to be lost, the increased solution concentration creates a significantly more aggressive environment. This continues until solution saturation point is reached, at which time salting out occurs, but the whilst there is still moisture

present in the vicinity of these solid phases there will be highly concentrated solutions present. In addition during drying of the droplet the oxygen diffusion distance is reduced, this may increase the rate of corrosion during the drying phase as it promotes an increased oxygen diffusion rate to the cathode. However, it is likely that this will be a secondary influence, as the solution layer through which the oxygen diffusion is taking place is relatively small in the first place, and for the most part is below the 100 μm level reported as being influential during TEL studies[161].

In addition during drying, precipitation of solid crystalline salt phases was observed during the μCT measurements. It is the location at which precipitation occurs which is of interest as it appears that precipitation will occur in the vicinity of the most active fissure during the drying phase. This effect is demonstrated in Figure 6.1 and Figure 6.2 for NaCl and simulated ocean water solutions respectively, where a solid phase is clearly seen at above the fissure which has shown the greatest development during the drying phase.

To knowledge this effect has not been widely considered as it is an advantage of the particular technique employed herein. However, it seems plausible that presence of a solid phase at the mouth of the most active fissure during the drying phase of atmospheric exposure can likely be accounted for by ionic migration to maintain charge balance [40, 47, 61, 70]. To the effect that as corrosion rate increases in active sites, $Cl^-$ ions migrate to the vicinity to maintain the charge balance in the area, as solution concentration rises beyond saturation point, migration of cations is then observed in order for “salting out” of the solid phases to occur.

In addition to the precipitation of salt crystals in the presence of active sites, corrosion product forms at the surface of the metallic substrate at the mouth of active fissures. This is a well-documented process [61, 70, 72, 220], with precipitation of aluminium hydroxide corrosion shown in

Figure **6.18**. Presence of the same layer of corrosion product beneath a solid salt crystal is shown in Figure 6.19. This layer of corrosion product creates an elevated localised pH within the corrosion site, which becomes further concentrated during drying. This can further accelerate the corrosion rate suring drying. El-Mahdy[160], indicated that on pure aluminium surfaces drying events were related to an increased rate of corrosion product precipitation, which appears to be consistent with the observation on the AA2024 pin samples studied herein. The presence of this layer of corrosion product is further relevant to the processes occurring during the onset of a second wet phase, which is discussed further over the coming sections.

### 6.3.2 Influence of Re-Humidification of the Atmosphere on the Localised Corrosion of AA2024

During atmospheric exposures following a dry period a further wet cycle follows during which re-humidification of salt deposits retained on surfaces can take place. This has been shown to result in a large jump in the measured rate of material loss. This acceleration has been attributed herein to the formation of new localised corrosion sites, which develop rapidly and are separate from the original site. Formation of new sites is shown by means of near surface sections and 3-D reconstructions of corroded volumes.

Larignon[221] observed a similar effect whereby repeated immersion and drying of AA2024 plate samples resulted in an increase in the number of grain boundaries attacked when compared to samples left continually immersed. It has also been suggested that this phenomenon may take place in AA7xxx series [162], during ex-situ tomography studies. However, neither body of work has proposed mechanisms for the development of increased number of localised corrosion sites during cyclic exposure.

The following hypothesis is offered as to the preferential formation of new sites as opposed to continued growth of existing fissures. Precipitation of a layer of corrosion product at the pit mouth, during the initial wet cycle and during drying as shown in

Figure **6.18** and Figure 6.19, results in a thickened barrier layer to oxygen diffusion. As such during re-humidification of salt deposits, preferential attack takes place at locations away from the precipitated layers of corrosion product, where the diffusion barrier to the metal surface is simply the passive film. In addition the original fissure formed in the vicinity of the most active sites at the outset of exposure, as such future initiation occurs preferentially at previously un-attacked sites as they are now the locations at which there is a greater potential difference between precipitate phases and the matrix.

In addition during the dry or dryer phase of an atmospheric cycle re-passivation of the sides of the active site can take place, as the droplet dries out. At the mouth of the pit and along the fissure length re-passivation process increase the potential required for passive film breakdown[73, 222, 223]. As such the ionic diffusion length to the potential new initiation sites is much shortened in the case of surface sites, as

opposed to re-initiation occurring at the base of a pit or fissure. It is possible that over time continued growth may occur in pre-existing sites if conditions become sufficiently aggressive at the base of the localised site.

It has been observed herein that during humidification multiple new sites may initiate, but quickly one became dominant and grew whilst others began to shut down. Preferential growth of this site takes place likely due to it being in the most susceptible location with regards to the micro-structure of the alloy. As such the majority of anodic current is drawn to this location resulting in re-passivation taking place at the less susceptible sites resulting in them shutting down.

Further as with samples exposed during steady state exposure, it appears that there is a maximum limiting depth to which fissures grow, this effect has been observed in AA2024 plate samples during cycling by Larignon [221]. Limiting depth is associated as has been outlined in Section 4.2 with increased ionic migration pathway length for chloride to the fissure tip as the fissure grows, the result being that lateral growth of fissures takes place along susceptible grain boundaries along the length of the fissure.

It is interesting to note that growth of fissures during the second wet phase takes place at a greatly increased rate when compared to that seen during the initial phase. Again little has been observed with regard to this behaviour, again a hypothesis is offered as to why this is taking place.

During wetting, re-humidification of salt deposits results in time periods where extremely concentrated solutions are present on the sample surface during establishment of equilibrium with the environment. These solutions have an

increased conductivity during the wetting phase which enhances the ionic mobility promoting rapid onset and development of localised attack.

In addition during hydration of the droplet the layer thickness is very thin, which promotes a more rapid diffusion of oxygen to the surface, leading to an enhanced cathodic oxygen reduction rate. This transitionary period does not take place when a droplet is present on a surface, and as such the solution concentration is more dilute and the oxygen diffusion distance is much greater. The possible outcome of this is that there will be a reduced induction time to the onset of pit formation in the samples which are undergoing re-humidification. Once pit formation occurs growth takes place rapidly regardless of the droplet size or concentration, thus it is reasonable to suggest that it is the shortened induction time to pit formation in the smaller droplets which is responsible for the increased rate.

It is important to note that this hypothesis needs confirmation, but could be achieved by means of running samples simultaneously from a wet deposit and a dry deposit. In addition it is possible that the presence of aluminium-chloride complexes at the surface following an initial exposure period leads to a drop in the pH on dissolution of these complexes back into solution during a second wet phase which may also serve to enhance the corrosion rate seen during this time period.

Further it is likely that this initially higher rate will begin to plateau over time, assuming that the deposit remains wet. However, if subsequent cycles take place it is possible that further jumps in corrosion rate are likely. Further investigation into this is required.

This formation of new sites has been shown to be independent of salt type, with both single salt (NaCl and $MgCl_2$) and mixed salt (simulated ocean water) showing the same behaviour. Salt type was seen to influence corrosion rate during drying to a limited extent, with $MgCl_2$ and substitute ocean water samples showing a slightly greater volume loss during this period. This is primarily accounted for by the lower DRH/ERH shown by these salts, Table 2.2 when compared with NaCl, as such a solution layer will remain present at the surface for a more prolonged period of time.

The amount of salt present has also been considered, again behaviour during cyclic exposure appears to not be influenced by this with regards to formation of new sites, however, larger quantities of salt resulted in an increase in the measured corrosion rates which is consistent with the result obtained in Chapter 4.

Further there was a considerable influence observed of the drying regime on the development of localised corrosion in AA2024 pin samples during cyclic wet-dry exposures. Samples dried close to their DRH experienced a greater corrosion rate than those dried to 0% RH, this is primarily due to the fact that drying takes place more slowly and to a less complete extent. Incomplete drying is due to the fact that the reported ERH's of salts is often lower than their specific DRH values[132, 210, 215, 224], as such corrosion processes can continue when salts are dried to their reported DRH. Samples initially exposed in lower RH environments were seen to form new sites following humidification of the atmosphere to a significantly higher RH, rather than continued development of existing sites. This further supports the idea that there is a critical phase during the transition from low to high RH during which the concentration of solution and oxygen diffusion distance provide optimum conditions for rapid initiation and growth of localised fissures.

In addition it has been shown that the effect of new site formation and growth can take place following a prolonged dry period provided that the salt deposit is retained on the metallic surface. It has been demonstrated that corrosion can be limited by the removal of salt from the surface [225], however, failure to do so can lead to the development of multiple sites within a concentrated area as is demonstrated in Figure 6.17.

### 6.3.3 Limitations

During any body of scientific work there are inevitably compromises which must be reached with regards to the techniques and samples which are used. In this case as previously discussed there are several possible issues which were considered and which provided concerns. Primarily the technique of µCT involves exposure to high energy x-rays which may result in artificially induced results, especially in samples where multiple measurements were made. In order to compensate for this control samples were run ex-situ under the exact same conditions, but only scanned once at the end of the exposure period, behaviour with regards to site numbers was similar and measured volume differences were comaprable. Further there are resolution limits associated with the measurements made which were in the region of ~800 nm, the initial development of fissures can take place on a smaller length scale than this, but the resolution is sufficient to capture most information required. Sample size is a related issue with a trade-off being made between being able to achieve good resolution and having a sample with a sufficiently large cathodic area to ensure the occurrence of localised attack.

## 6.4 Conclusions

1. On drying to “0%” RH, there is an initial increase in the rate of corrosion, then rate will drop until corrosion stops, for both NaCl and $MgCl_{2.}$ However, for ocean water dried to “0%” RH corrosion may continue during the dry phase.
2. On drying to the DRH for NaCl and $MgCl_2$ there is a burst in corrosion rate during the initial drying phase, following this corrosion will continue at a reduced rate when compared with a sample left continually wet.
3. During re-wetting there is rapid increase in the rate of dissolution, which is usually associated with the formation of new sites, but on occasion growth of old sites may continue.
4. Drying to DRH followed by rewetting tends to result in an overall increase in the rate in the measured volume of corrosion compared with drying to “0%” RH.
5. Precipitation of NaCl crystals often happens above the most active site during the drying phase.

# 7 SUMMARY DISSCUSSION AND CONTEXT OF WORK

During this work, investigation has been carried out into the influence of atmospheric exposure on the localised corrosion behaviour of AA2024 with the aim of providing information which will underpin the development of health management models for ageing aircraft fleets.

It has been determined that RH, initial CDD and salt type influence the corrosion behaviour of AA2024 samples under atmospheric exposure. Some previous work has begun to establish this [63, 112, 117, 130, 136, 138, 162, 202, 203], however, detailed study of the influence of these variables on the development of localised corrosion has not been undertaken.

When considering behaviour of samples in a constantly wet condition, it has been possible to say that for NaCl and $MgCl_2$ solutions, an increase in the density of salt present on a surface results in an increase in the rate of localised corrosion. It has also been observed that increasing either the salt density or the RH results in an increase in the amount of localised corrosion for NaCl, $MgCl_2$, $CaCl_2$ and simulated ocean water solutions. This is important during the development of health management systems as it helps understand that removal of salts from contaminated surfaces is essential to prevent the build-up of further concentrated salt deposits which result in an increase in the amount of localised corrosion. Similarly for structures exposed in environments where the RH is high it is important to be aware of the fact that when salt is present on the surface the rate of corrosion will be increased.

RH influences the way in which localised corrosion develops, with a decrease in the RH leading to a decrease in the size of sites, and a shift from pit-like morphology to more sustained IGC like attack. This is important when considering the management of structural integrity, as development of sharp elongated IGC fissures results in raised localised stress concentrations which promote themselves as locations for initiation of SCC or transition to fatigue crack sites.

It is also important to be aware that on AA2024 surfaces, localised corrosion can take place with extremely low levels of salt present on a metal surface. Whilst no definite threshold has been determined small localised corrosion sites have been observed in samples exposed down to ~1 $\mu g/cm^2$ of chloride, during exposure at elevated RH.

Under service conditions, components will be exposed to conditions of cyclic wet and dry periods. This result in changes in the localised corrosion behaviour, due to exposure times when the solutions present on metal surfaces become highly concentrated. It has been shown using in-situ measurements at the start of and following a drying phase that there is a rapid increase in the measured corrosion rate during the early stages. Depending on the low point of RH during an atmospheric cycle, localised corrosion processes will either shut down completely, or proceed at a greatly reduced rate. Furthermore, localised corrosion which initiates during a dry phase will be accelerated during transition to a more prolonged wet phase, associated with higher RH.

In addition to the increase in corrosion rate seen during drying, a significant increase in the rate of corrosion, compared to that during steady exposure, was seen during the wetting phase of a wet-dry cycle. This has been attributed to the rapid formation

and growth of new localised corrosion sites, which tend to form and grow preferentially to the pre-existing sites. However, it has been observed that in some cases in addition to the formation of new sites, some growth may continue to take place in the pre-existing sites. This is important during management of structures as it means that whilst it is likely that damage will usually take place at fresh sites, and therefore does not accumulate at one corrosion site, this can take place from time to time, which means that maintenance programs should be adjusted to account for this possibility.

This work has confirmed that growth of IGC fissures will take place preferentially parallel to the direction of rolling, due to elongation of the grains in this orientation and the development of strings of intermetallic phases also aligned along the same direction. The use of in-situ μCT has shown that the sites appear to attain a maximum (or limiting) depth (parallel to the rolling direction for the experiments shown here), and following this, growth of fissures takes place laterally (parallel to the surface) along susceptible grain boundaries. The attainment of a maximum depth has been seen previously [92, 205], however, it was unclear to as to whether lateral expansion of fissures occurred simultaneously or following attainment of this depth..

In-situ measurements have enabled the precipitation of solid salt phases in droplets to be observed during atmospheric exposure and during drying. Preliminary evidence suggests that there is an association of the location at which salt crystals precipitate and the locations at which localised corrosion is occurring. This may help when considering methods of detecting localised corrosion.

Work on plate samples has shown that secondary spreading processes take place rapidly and extensively during atmospheric exposure of AA2024 under NaCl and ocean water droplets. This is of relevance to the development of prognostic models as the formation of secondary spread zones not only increases the metal surface area which is wetted, but as a result increases the size of the potential cathodic region. This has lead to an increase in the amount of damage observed in AA2024 samples, which must be considered for structure maintenance.

It has been demonstrated that the presence of sufficient $Mg^{2+}$ and $Ca^{2+}$ in atmospheric droplets inhibits the secondary spreading process. This has been attributed to the formation of insoluble hydroxides or carbonates which precipitate during the corrosion process. An exact understanding of the amounts of $Mg^{2+}$ and $Ca^{2+}$ required to be present to inhibit the spreading process has not been determined, however, an initial experiment indicated that in a 50:50 chloride ratio, $Mg^{2+}$ almost completely inhibited the spreading process.

Evidence that the primary cathodic region forms in the secondary spread region has been provided by both the migration of $Na^{+}$ ions into this region in order to maintain charge neutrality, and by the observed occurrence of grooving around intermetallic particles which is associated with an increase in pH.

The evidence of the influence of secondary spreading on the development of localised corrosion illustrates a limitation of the µCT experiments in the current project, in which the pin size was selected to maximise resolution, but did not allow droplet spreading.  Beam damage is a concern for synchrotron µCT, but in the

current work, the use of control samples that were not measured multiple times, confirmed that the extent of beam damage was not significant.

# 8 FUTURE WORK

Further bodies of work considering the atmospheric corrosion of AA2024 have many avenues open to investigation. With improvements in the capabilities of synchrotron based measurements such as those used during this work, both resolution and temporal limits are significantly improved. As such work on visualising the processes taking place during the very early stages of atmospheric exposure, especially during the transitional phase from metastable to stable pitting could be undertaken. Indication from this work is that the time to stable pitting is greatly reduced at higher RH exposures; as such a smaller number of sites are established. At lower RH values a greater number of smaller sites are established, further clarification as to whether formation is simultaneous or sequential, the latter has been hypothesised herein.

Measurements made during this work on calcium chloride indicate that acceleration in the corrosion rate appears to take place. Further investigation into the influence of $CaCl_2$ during wet/dry cycling, would provide insight into whether it follows the same behaviour as other salt types, or if owing to its lowered DRH and ERH it behaves in a different manner. In addition more statistical studies on the influence of mixed salt solutions in different ratios would provide interesting information as to corrosion behaviour under more complex solutions. Further additions of nitrates, sulphates and phosphates should be considered as they will prove influential on corrosion behaviour under atmospheric conditions.

In addition some preliminary measurements on polymer coating systems were made as part of this work as a proof of concept that in-situ measurements could be made

on coating systems during atmospheric exposure. Further investigation into different coating systems, both polymeric and paint based simulating realistic conditions for aircraft is required. This would allow for visualisation of the mechanisms involved during the failure of protective coating systems.

# 9 REFERENCES


1. Scanff, E., K.L. Feldman, S. Ghelam, P. Sandborn, M. Glade, and B. Foucher, *Life cycle cost impact of using prognostic health management (PHM) for helicopter avionics.* Microelectronics Reliability, 2007. **47**(12): p. 1857-1864.
2. Roemer, M.J., E.O. Nwadiogbu, and G. Bloor. *Development of diagnostic and prognostic technologies for aerospace health management applications*. in *Aerospace Conference, 2001, IEEE Proceedings.* 2001.
3. Hughes, A.E., A. Boag, A.M. Glenn, D. McCulloch, T.H. Muster, C. Ryan, C. Luo, X. Zhou, and G.E. Thompson, *Corrosion of AA2024-T3 Part II: Co-operative corrosion.* Corrosion Science, 2011. **53**(1): p. 27-39.
4. Guillaumin, V. and G. Mankowski, *Localized corrosion of 2024 T351 aluminium alloy in chloride media.* Corrosion Science, 1998. **41**(3): p. 421-438.
5. Zhang, W. and G.S. Frankel, *Anisotropy of Localized Corrosion in AA2024-T3.* Electrochemical and Solid-State Letters, 2000. **3**(6): p. 268-270.
6. Starke, E.A. and J.T. Staley, *Application of modern aluminum alloys to aircraft.* Progress in Aerospace Sciences, 1996. **32**(2-3): p. 131-172.
7. Harlow, D.G. and R.P. Wei, *Probabilities of occurrence and detection of damage in airframe materials.* Fatigue & Fracture of Engineering Materials & Structures, 1999. **22**(5): p. 427-436.
8. Dieulle, L., C. Bérenguer, A. Grall, and M. Roussignol, *Sequential condition-based maintenance scheduling for a deteriorating system.* European Journal of Operational Research, 2003. **150**(2): p. 451-461.
9. Williams, J.C. and E.A. Starke, *Progress in structural materials for aerospace systems.* Acta Materialia, 2003. **51**(19): p. 5775-5799.
10. Hontelez, J.A.M., H.H. Burger, and D.J.D. Wijnmalen, *Optimum condition-based maintenance policies for deteriorating systems with partial information.* Reliability Engineering & System Safety, 1996. **51**(3): p. 267-274.
11. Bai, F., H. Zuo, and S. Ren. *Average life prediction for aero-engine fleet based on performance degradation data*. in *Prognostics and Health Management Conference, 2010. PHM '10.* 2010.
12. Deyao, M., L. Chuan, S. Jianming, Z. Yingzhi, and G. Zhiqi. *Research of the military aircraft maintenance support mode based on the prognostics and health management*. in *Prognostics and Health Management Conference, 2010. PHM '10.* 2010.
13. Trueman, T., Trathen, P., Begbie, K., Davidson, L., Hinton, B.,, *The Development of a Corrosion Prognostic Health Management System for Australian Defence Force Aircraft.* Advanced Materials Research (volume 38), 2008. **Corrosion in the Military II**: p. 182-200.
14. Ofsthun, S., *Integrated vehicle health management for aerospace platforms.* Instrumentation & Measurement Magazine, IEEE, 2002. **5**(3): p. 21-24.
15. Dwight, J., *Aluminium design and construction*1999: Routledge.
16. Polmear, I.J., *Light alloys: Metallurgy of the light metals*. 3rd ed1995, New York: J. Wiley & Sons (New York). vii, 421.

17. Belov, N.A., D.G. Eskin, and A.A. Aksenov, *Chapter 3 - Alloys of the Al−Cu−Si−(Mg, Fe) System*, in *Multicomponent Phase Diagrams*2005, Elsevier: Oxford. p. 83-132.
18. Heinz, A., A. Haszler, C. Keidel, S. Moldenhauer, R. Benedictus, and W.S. Miller, *Recent development in aluminium alloys for aerospace applications.* Materials Science and Engineering A, 2000. **280**(1): p. 102-107.
19. Ahmad, Z., *Principles of Corrosion Engineering and Corrosion Control*2006: Butterworth-Heinemann. 673.
20. Bauccio, M., *ASM Metal Reference Book*. 3rd ed. Vol. 3rd Edition. 1993, Ohio: SM Internatioal. 614.
21. Buchheit, R.G., R.P. Grant, P.F. Hlava, B. McKenzie, and G.L. Zender, *Local Dissolution Phenomena Associated with S Phase (Al[sub 2]CuMg) Particles in Aluminum Alloy 2024-T3.* Journal of The Electrochemical Society, 1997. **144**(8): p. 2621-2628.
22. Chandler, H., *Heat treater's guide: practices and procedures for nonferrous alloys*1996: ASM International (OH).
23. de Freitas, E.R., E. Ferracini Jr, and M. Ferrante, *Microstructure and rheology of an AA2024 aluminium alloy in the semi-solid state, and mechanical properties of a back-extruded part.* Journal of Materials Processing Technology, 2004. **146**(2): p. 241-249.
24. Boag, A., A.E. Hughes, N.C. Wilson, A. Torpy, C.M. MacRae, A.M. Glenn, and T.H. Muster, *How complex is the microstructure of AA2024-T3?* Corrosion Science, 2009. **51**(8): p. 1565-1568.
25. Wei, R., C.-M. Liao, and M. Gao, *A transmission electron microscopy study of constituent-particle-induced corrosion in 7075-T6 and 2024-T3 aluminum alloys.* Metallurgical and Materials Transactions A, 1998. **29**(4): p. 1153-1160.
26. Vander Voort, G.F., *Metallography and microstructures*. Vol. 9. 2004: ASM International.
27. Attalah, M.M., *Microstructure-Property Development in Friction Stir Welds of Aluminium Based Alloys*, in *Metallurgy and Materials*2007, University of Birmingham: Birmingham. p. 318.
28. Luo, C., *Role of Microstructure on Corrosion Control AA2024-T3 Aluminium Alloy*, in *School of Materials Corrosion and Protection Centre*2011, University of Manchester: Manchester. p. 204.
29. Wang, S., M. Starink, and N. Gao, *Precipitation hardening in Al–Cu–Mg alloys revisited.* Scripta Materialia, 2006. **54**(2): p. 287-291.
30. Chen, C.Q. and J.F. Knott, *Effects of dispersoid particles on toughness of high-strength aluminium alloys.* Metal Science, 1981. **15**(8): p. 357-364.
31. Grard, C., H.W.L. Phillips, and C.M. Phillips, *Aluminium and Its Alloys*1922.
32. Davenport, A.J., *Corrosion of Aluminium Alloys (Undergraduate Presentation)*, 2010.
33. Sha, G., R.K.W. Marceau, X. Gao, B.C. Muddle, and S.P. Ringer, *Nanostructure of aluminium alloy 2024: Segregation, clustering and precipitation processes.* Acta Materialia, 2011. **59**(4): p. 1659-1670.
34. Shih, H.-C., N.-J. Ho, and J.C. Huang, *Precipitation behaviors in Al-Cu-Mg and 2024 aluminum alloys.* Metallurgical and Materials Transactions A, 1996. **27**(9): p. 2479-2494.

35. Huda, Z., N.I. Taib, and T. Zaharinie, *Characterization of 2024-T3: An aerospace aluminum alloy.* Materials Chemistry and Physics, 2009. **113**(2-3): p. 515-517.
36. Hutchinson, C. and S. Ringer, *Precipitation processes in Al-Cu-Mg alloys microalloyed with Si.* Metallurgical and Materials Transactions A, 2000. **31**(11): p. 2721-2733.
37. Wilson, R.N. and P.G. Partridge, *The nucleation and growth of S' precipitates in an aluminium-2.5% copper-1.2% magnesium alloy.* Acta Metallurgica, 1965. **13**(12): p. 1321-1327.
38. Adachi, H., K. Osamura, S. Ochiai, J. Kusui, and K. Yokoe, *Mechanical property of nanoscale precipitate hardening aluminum alloys.* Scripta Materialia, 2001. **44**(8–9): p. 1489-1492.
39. Bakish, R. and W.D. Robertson, *Galvanic Potentials of Grains and Grain Boundaries in Copper Alloys.* Journal of The Electrochemical Society, 1956. **103**(6): p. 320-325.
40. Davies, J.R., *Corrosion of Aluminium and Aluminium Alloys*1999: ASM International. 313.
41. Pourbaix, M., *Atlas of electrochemical equilibria in aqueous solutions.* M. Pourbaix, published 1974 by NACE, 644, 1974.
42. Jones, D.A., *Principles and Prevention of Corrosion*1991, NewYork: Macmillan Pub. Co. (New York and Toronto and New York). 568.
43. Ghali, E., *Corrosion resistance of aluminum and magnesium alloys: understanding, performance, and testing*. Vol. 12. 2010: Wiley. 640.
44. Sukiman, N.L., X. Zhou, N. Birbilis, A.E. Hughes, J.M.C. Mol, S.J. Garcia, and G.E. Thompson, *Durability and Corrosion of Aluminium and Its Alloys: Overview, Property Space, Techniques and Developments*. Aluminium Alloys - New Trends in Fabrication and Applications2012.
45. Marcus, P., *Corrosion mechanisms in theory and practice*2011: CRC PressI Llc.
46. Missert, N., J.C. Barbour, R.G. Copeland, and J.E. Mikkalson, *The localized corrosion of Al at engineered Cu islands.* JOM, 2001. **53**(7): p. 34-36.
47. Vargel, C., *Corrosion of Aluminium*. 1 ed2004: Elsevier Science. 626.
48. Svenningsen, G. *Corrosion of aluminium alloys*. in *Poster presented at The NorLight Conference*. 2003.
49. Vukmirovic, M.B., N. Vasiljevic, N. Dimitrov, and K. Sieradzki, *Diffusion-Limited Current Density of Oxygen Reduction on Copper.* Journal of The Electrochemical Society, 2003. **150**(1): p. B10-B15.
50. Schneider, O., G. Ilevbare, J. Scully, and R. Kelly, *In situ confocal laser scanning microscopy of AA 2024-T3 corrosion metrology II. Trench formation around particles.* Journal of The Electrochemical Society, 2004. **151**(8): p. B465-B472.
51. Boag, A., R.J. Taylor, T.H. Muster, N. Goodman, D. McCulloch, C. Ryan, B. Rout, D. Jamieson, and A.E. Hughes, *Stable pit formation on AA2024-T3 in a NaCl environment.* Corrosion Science. **52**(1): p. 90-103.
52. Blanc, C., B. Lavelle, and G. Mankowski, *The role of precipitates enriched with copper on the susceptibility to pitting corrosion of the 2024 aluminium alloy.* Corrosion Science, 1997. **39**(3): p. 495-510.

53. Boag, A., A.E. Hughes, A.M. Glenn, T.H. Muster, and D. McCulloch, *Corrosion of AA2024-T3 Part I: Localised corrosion of isolated IM particles.* Corrosion Science, 2011. **53**(1): p. 17-26.
54. Cabrol, S., *Modélisation de la croissance des piqûres dans l'alliage d'aluminium 2024 t351 en milieu chloruré.* Annales de Chimie Science des Matériaux, 1999. **24**(4–5): p. 307-311.
55. Campestrini, P., E.P.M. van Westing, H.W. van Rooijen, and J.H.W. de Wit, *Relation between microstructural aspects of AA2024 and its corrosion behaviour investigated using AFM scanning potential technique.* Corrosion Science, 2000. **42**(11): p. 1853-1861.
56. Chen, G.S., M. Gao, and R.P. Wei, *Microconstituent-induced pitting corrosion in aluminum alloy 2024-T3.* Journal Name: Corrosion; Journal Volume: 52; Journal Issue: 1; Other Information: PBD: Jan 1996, 1996: p. Medium: X; Size: pp. 8-15.
57. DeRose, J.A., T. Suter, A. Bałkowiec, J. Michalski, K.J. Kurzydlowski, and P. Schmutz, *Localised Corrosion Initiation and Microstructural Characterisation of an Al 2024 Alloy with a Higher Cu to Mg Ratio.* Corrosion Science, (0).
58. Lacroix, L., C. Blanc, N. Pébère, G.E. Thompson, B. Tribollet, and V. Vivier, *Simulating the galvanic coupling between S-Al2CuMg phase particles and the matrix of 2024 aerospace aluminium alloy.* Corrosion Science, 2012. **64**(0): p. 213-221.
59. Leblanc, P. and G.S. Frankel, *A Study of Corrosion and Pitting Initiation of AA2024-T3 Using Atomic Force Microscopy.* Journal of The Electrochemical Society, 2002. **149**(6): p. B239-B247.
60. Ralston, K.D., N. Birbilis, M.K. Cavanaugh, M. Weyland, B.C. Muddle, and R.K.W. Marceau, *Role of nanostructure in pitting of Al–Cu–Mg alloys.* Electrochimica Acta, 2010. **55**(27): p. 7834-7842.
61. Szklarska-Smialowska, Z., *Pitting corrosion of aluminum.* Corrosion Science, 1999. **41**(9): p. 1743-1767.
62. Zhou, X., C. Luo, T. Hashimoto, A.E. Hughes, and G.E. Thompson, *Study of localized corrosion in AA2024 aluminium alloy using electron tomography.* Corrosion Science, 2012(0).
63. Schweitzer, P.A., *Fundamentals of metallic corrosion :: atmospheric and media corrosion of metals*, 2006, Taylor & Francis.
64. Scully, J.R., T.O. Knight, R.G. Buchheit, and D.E. Peebles, *Electrochemical characteristics of the Al2Cu, Al3Ta and Al3Zr intermetallic phases and their relevancy to the localized corrosion of Al alloys.* Corrosion Science, 1993. **35**(1–4): p. 185-195.
65. Frankel, G.S., *Pitting corrosion of metals: A review of the critical factors.* Journal Name: Journal of the Electrochemical Society; Journal Volume: 145; Journal Issue: 6; Other Information: PBD: Jun 1998, 1998: p. Medium: X; Size: pp. 2186-2197.
66. Sato, N., *Anodic Breakdown of Passive Films on Metals.* Journal of The Electrochemical Society, 1982. **129**(2): p. 255-260.
67. Sato, N., *A theory for breakdown of anodic oxide films on metals.* Electrochimica Acta, 1971. **16**(10): p. 1683-1692.
68. Tomcsányi, L., K. Varga, I. Bartik, H. Horányi, and E. Maleczki, *Electrochemical study of the pitting corrosion of aluminium and its alloys—II.*

*Study of the interaction of chloride ions with a passive film on aluminium and initiation of pitting corrosion.* Electrochimica Acta, 1989. **34**(6): p. 855-859.
69. Muñoz, A.g. and J.B. Bessone, *Pitting of aluminium in non-aqueous chloride media.* Corrosion Science, 1999. **41**(7): p. 1447-1463.
70. McCafferty, E., *Sequence of steps in the pitting of aluminum by chloride ions.* Corrosion Science, 2003. **45**(7): p. 1421-1438.
71. Augustynski, J., R. Frankenthal, and J. Kruger, *Passivity of Metals.* Electrochemical Society, Princeton, NJ, 1978: p. 989.
72. Frankel, G., *Pitting corrosion.* ASM Handbook, 2003. **13**: p. 236-241.
73. Frankel, G.S., J.R. Scully, and C.V. Jahnes, *Repassivation of Pits in Aluminum Thin Films.* Journal of The Electrochemical Society, 1996. **143**(6): p. 1834-1840.
74. Tomcsányi, L., Z. Nagy, J. Somlai, and J. Borszéki, *Electrochemical study of the pitting corrosion of aluminium and its alloys—III. The role of bonded water and the kinetics of formation and reformation of a passive layer.* Electrochimica Acta, 1993. **38**(17): p. 2541-2546.
75. Foley, R.T., *Localized Corrosion of Aluminum Alloys—A Review.* Corrosion, 1986. **42**(5): p. 277-288.
76. Frankel, G., *Pitting corrosion of metals a review of the critical factors.* Journal of The Electrochemical Society, 1998. **145**(6): p. 2186-2198.
77. Trueman, A.R., *Determining the probability of stable pit initiation on aluminium alloys using potentiostatic electrochemical measurements.* Corrosion Science, 2005. **47**(9): p. 2240-2256.
78. Pride, S.T., J.R. Scully, and J.L. Hudson, *Metastable Pitting of Aluminum and Criteria for the Transition to Stable Pit Growth.* Journal of The Electrochemical Society, 1994. **141**(11): p. 3028-3040.
79. Charpentiera, D., K. Devineau, R. Mosser-Ruck, M. Cathelineau, and F. Villiéras, *Bentonite–iron interactions under alkaline condition: An experimental approach.* Applied Clay Science, 2006. **32**(1–2): p. 1-13.
80. McCafferty, E., *The electrode kinetics of pit initiation on aluminum.* Corrosion Science, 1995. **37**(3): p. 481-492.
81. Nisancioglu, K. and H. Holtan, *Measurement of the critical pitting potential of aluminium.* Corrosion Science, 1978. **18**(9): p. 835-849.
82. Böhni, H. and H.H. Uhlig, *Environmental factors affecting the critical pitting potential of aluminum.* Journal of The Electrochemical Society, 1969. **116**(7): p. 906-910.
83. Galvele, J.R., *Transport Processes and the Mechanism of Pitting of Metals.* Journal of The Electrochemical Society, 1976. **123**(4): p. 464-474.
84. Baumgärtner, M. and H. Kaesche, *Aluminum pitting in chloride solutions: morphology and pit growth kinetics.* Corrosion Science, 1990. **31**(0): p. 231-236.
85. Beck, T.R., *Salt film formation during corrosion of aluminum.* Electrochimica Acta, 1984. **29**(4): p. 485-491.
86. Brett, C., *On the electrochemical behaviour of aluminium in acidic chloride solution.* Corrosion Science, 1992. **33**(2): p. 203-210.
87. Lowden, M., *Effect of Sensitisation on Atmospheric Corrosion of AlMg*, in *Metallurgy and Materials*2012, University of Birmingham: Birmingham. p. 35.

88. Kelly, R.G.S., John R., 1958-; Shoesmith, David William; Buchheit, R. G. (Rudolph G.) *Electrochemical techniques in corrosion science and engineering* Corrosion technology (New York, N.Y.) 18 2003, New York: Marcel Dekker. 426.
89. Frankel, G.S., *The growth of 2-D pits in thin film aluminum.* Corrosion Science, 1990. **30**(12): p. 1203-1218.
90. Glenn, A.M., T.H. Muster, C. Luo, X. Zhou, G.E. Thompson, A. Boag, and A.E. Hughes, *Corrosion of AA2024-T3 Part III: Propagation.* Corrosion Science, 2011. **53**(1): p. 40-50.
91. Zhao, X., G.S. Frankel, B. Zoofan, and S.I. Rokhlin, *In situ X-ray radiographic study of intergranular corrosion in aluminum alloys.* Corrosion, 2003. **59**(11): p. 1012-1018.
92. Knight, S.P., M. Salagaras, A.M. Wythe, F. De Carlo, A.J. Davenport, and A.R. Trueman, *In situ X-ray tomography of intergranular corrosion of 2024 and 7050 aluminium alloys.* Corrosion Science, 2010. **52**(12): p. 3855-3860.
93. Augustin, C., E. Andrieu, C. Blanc, G. Mankowski, and J. Delfosse, *Intergranular Corrosion of 2024 Alloy in Chloride Solutions.* Journal of The Electrochemical Society, 2007. **154**(11): p. C637-C644.
94. Baboian, R., *Corrosion tests and standards: application and interpretation*. Vol. 20. 2005: ASTM International.
95. Larignon, C., J. Alexis, E. Andrieu, C. Blanc, G. Odemer, and J.-C. Salabura, *Corrosion damages induced by cyclic exposure of 2024 aluminum alloy in chloride-containing environments.* Journal of the Electrochemical Society, 2011. **158**(9): p. C284-C295.
96. King, P.C., I.S. Cole, P.A. Corrigan, A.E. Hughes, and T.H. Muster, *FIB/SEM study of AA2024 corrosion under a seawater drop: Part I.* Corrosion Science, 2011. **53**(3): p. 1086-1096.
97. Sehgal, A., G.S. Frankel, B. Zoofan, and S. Rokhlin, *Pit Growth Study in Al Alloys by the Foil Penetration Technique.* Journal of the Electrochemical Society, 2000. **147**(1): p. 140-148.
98. Kowal, K., J. DeLuccia, J.Y. Josefowicz, C. Laird, and G.C. Farrington, *In Situ Atomic Force Microscopy Observations of the Corrosion Behavior of Aluminum‐Copper Alloys.* Journal of The Electrochemical Society, 1996. **143**(8): p. 2471-2481.
99. Hans-Henning, S., *Fundamentals of Corrosion*, in *Corrosion Mechanisms in Theory and Practice, Third Edition*2011, CRC Press. p. 1-104.
100. Zhao, S., D.A. Wolfe, T.-S. Huang, and G.S. Frankel, *Generalized model for IGC growth in aluminum alloys.* Journal of Statistical Planning and Inference, 2007. **137**(7): p. 2405-2412.
101. Brunner, J.G., N. Birbilis, K.D. Ralston, and S. Virtanen, *Impact of ultrafine-grained microstructure on the corrosion of aluminium alloy AA2024.* Corrosion Science, 2012. **57**(0): p. 209-214.
102. Galvele, J.R. and S.M. de De Micheli, *Mechanism of intergranular corrosion of Al-Cu alloys.* Corrosion Science, 1970. **10**(11): p. 795-807.
103. Zhang, W., S. Ruan, D.A. Wolfe, and G.S. Frankel, *Statistical model for intergranular corrosion growth kinetics.* Corrosion Science, 2003. **45**(2): p. 353-370.

104. Ruan, S., D.A. Wolfe, W. Zhang, and G.S. Frankel, *Statistical modeling of minimum intergranular corrosion path length in high-strength aluminum alloy.* Technometrics, 2004. **46**(1): p. 69-75.
105. Liu, X., G.S. Frankel, B. Zoofan, and S.I. Rokhlin, *Transition from Intergranular Corrosion to Intergranular Stress Corrosion Cracking in AA2024-T3.* Journal of The Electrochemical Society, 2006. **153**(2): p. B42-B51.
106. Knight, S.P., M. Salagaras, and A.R. Trueman, *The study of intergranular corrosion in aircraft aluminium alloys using X-ray tomography.* Corrosion Science, 2011. **53**(2): p. 727-734.
107. B. J. Connolly, D.A.H., S. J. Fox, A. J. Davenport, C. Padovani,, A.T. S. Zhou, M. Preuss, N. P. Stevens, T. J. Marrow, J.-Y. Buffiere,, and A.G.a.M.S. E. Boller, *X-ray microtomography studies of localised corrosion and transitions to stress corrosion cracking.* Materials Science and Technology, 2006. **22**: p. 1076-1085.
108. Fox, S., *An In Situ X-Ray Tomography Study of the Growth and Development of Localised Corrosion in Friction Stir Welded AA2024-T351*, in *Metallurgy and Materias*2006, University of Birmingham: Birmingham (UK). p. 231.
109. King, P.C., I.S. Cole, P.A. Corrigan, A.E. Hughes, T.H. Muster, and S. Thomas, *FIB/SEM study of AA2024 corrosion under a seawater drop, part II.* Corrosion Science, 2012. **55**(0): p. 116-125.
110. Cole, I.S.G., W. D.; Paterson, D. A.; King, G. A.; Furman, S. A.; Lau, D., *Holistic model for atmospheric corrosion: Part 2 - Experimental measurement of deposition of marine salts in a number of long range studies.* Corrosion Engineering, Science and Technology, 2003. **38**: p. 259-266.
111. Sun, S., Q. Zheng, D. Li, and J. Wen, *Long-term atmospheric corrosion behaviour of aluminium alloys 2024 and 7075 in urban, coastal and industrial environments.* Corrosion Science, 2009. **51**(4): p. 719-727.
112. Cole, I.S.L., D.; Paterson, D.A., *Holistic model for atmospheric corrosion Part 6 – From wet aerosol to salt deposit.* Corrosion Engineering, Science and Technology, 2004. **39**: p. 209-218.
113. Cole, I.S. and D.A. Paterson, *Modelling aerosol deposition rates on aircraft and implications for pollutant accumulation and corrosion.* Corrosion Engineering Science and Technology, 2009. **44**(5): p. 332-339.
114. Corvo, F., J. Minotas, J. Delgado, and C. Arroyave, *Changes in atmospheric corrosion rate caused by chloride ions depending on rain regime.* Corrosion Science, 2005. **47**(4): p. 883-892.
115. Meira, G.R., C. Andrade, C. Alonso, I.J. Padaratz, and J.C. Borba, *Modelling sea-salt transport and deposition in marine atmosphere zone - A tool for corrosion studies.* Corrosion Science, 2008. **50**(9): p. 2724-2731.
116. Natesan, M., G. Venkatachari, and N. Palaniswamy, *Kinetics of atmospheric corrosion of mild steel, zinc, galvanized iron and aluminium at 10 exposure stations in India.* Corrosion Science, 2006. **48**(11): p. 3584-3608.
117. Leygraf, C., *New fundamental and environmental aspects of atmospheric corrosion.* Revista De Metalurgia, 2009. **45**(3): p. 223-227.
118. Christofer, L., *Atmospheric Corrosion*, in *Corrosion Mechanisms in Theory and Practice*2002, CRC Press. p. 529-582.
119. Tullmin, M. and P. Roberge, *Atmospheric corrosion.* Uhlig's Corrosion Handbook, 2000: p. 311-312.

120. Wörner, T. and H. Laub, *Atmospheric corrosion of metals.* Anti-Corrosion Methods and Materials, 1968. **15**(10): p. 12-13.
121. Wright, M.R., *An introduction to aqueous electrolyte solutions*2007: John Wiley & Sons.
122. Wheeler, M.J., S. Russi, M.G. Bowler, and M.W. Bowler, *Measurement of the equilibrium relative humidity for common precipitant concentrations: facilitating controlled dehydration experiments.* Acta Crystallographica Section F, 2012. **68**(1): p. 111-114.
123. Zemaitis Jr, J.F., D.M. Clark, M. Rafal, and N.C. Scrivner, *Handbook of Aqueous Electrolyte Thermodynamics: Theory & Application*2010: Wiley-AIChE.
124. Wang, P., A. Anderko, and R.D. Young, *A speciation-based model for mixed-solvent electrolyte systems.* Fluid Phase Equilibria, 2002. **203**(1–2): p. 141-176.
125. Gruszkiewicz, M., D. Palmer, R. Springer, P. Wang, and A. Anderko, *Phase Behavior of Aqueous Na–K–Mg–Ca–Cl–NO3 Mixtures: Isopiestic Measurements and Thermodynamic Modeling.* Journal of Solution Chemistry, 2007. **36**(6): p. 723-765.
126. Greenspan, L., *Humidity fixed points of binary saturated aqueous solutions.* Journal of research of the National Bureau of Standards. A, Physics and chemistry, January 1977. **81a** (1 ): p. 89-96
127. ASTM, *E104-02(2007) "Standard Practice for Maintaining Constant Relative Humidity by Means of Aqueous Solutions"*, 2007, ASTM. p. 5.
128. Winston, P.W. and D.H. Bates, *Saturated Solutions For the Control of Humidity in Biological Research.* Ecology, 1960. **41**(1): p. 232-237.
129. Lide, D.R., *CRC handbook of physics and chemistry*, 2001, CRC.
130. Racine, M., *The Effects of Temperature on the Deliquescence of Atmospheric Aerosols.* Harvard Undergraduate Research Program. Cambridge, Massachusetts: Harvard University, 2005.
131. Cole, I.S., W.D. Ganther, J.D. Sinclair, D. Lau, and D.A. Paterson, *A Study of the Wetting of Metal Surfaces in Order to Understand the Processes Controlling Atmospheric Corrosion.* Journal of The Electrochemical Society, 2004. **151**(12): p. B627-B635.
132. Gao, Y., S.B. Chen, and L.E. Yu, *Efflorescence relative humidity of airborne sodium chloride particles: A theoretical investigation.* Atmospheric Environment, 2007. **41**(9): p. 2019-2023.
133. Cole, I.S. and W. Ganther, *Experimental determination of duration of wetness on metal surfaces.* Corrosion Engineering, Science and Technology, 2008. **43**(2): p. 156-162.
134. Stokes, R.H. and R.A. Robinson, *Standard Solutions for Humidity Control at 25° C.* Industrial & Engineering Chemistry, 1949. **41**(9): p. 2013-2013.
135. Seinfeld, J.H. and S.N. Pandis, *Atmospheric chemistry and physics: from air pollution to climate change.* 2006.
136. Tsutsumi, Y., A. Nishikata, and T. Tsuru, *Pitting corrosion mechanism of Type 304 stainless steel under a droplet of chloride solutions.* Corrosion Science, 2007. **49**(3): p. 1394-1407.
137. Tomashov, N.D., *Passivity and corrosion resistance of metal systems.* Corrosion Science, 1964. **4**(1–4): p. 315-334.

138. Leygraf, C.a.G., T., *Atmospheric Corrosion*. 1st Edition ed2000: Wiley-Interscience. 368.
139. Li, J.F., B. Maier, and G.S. Frankel, *Corrosion of an Al-Mg-Si alloy under MgCl2 solution droplets.* Corrosion Science, 2011. **53**(6): p. 2142-2151.
140. Ernst, P. and R. Newman, *Explanation of the effect of high chloride concentration on the critical pitting temperature of stainless steel.* Corrosion Science, 2007. **49**(9): p. 3705-3715.
141. Jones, G. and S.K. Talley, *The Viscosity of Aqueous Solutions as a Function of the Concentration.* Journal of the American Chemical Society, 1933. **55**(2): p. 624-642.
142. Zhang, J., J. Wang, and Y. Wang, *Micro-Droplets Formation during the Deliquescence of Salt Particles in Atmosphere.* Corrosion, 2005. **61**(12): p. 1167-1172.
143. Zhang, J., J. Wang, and Y. Wang, *Electrochemical investigations of micro-droplets formed on metals during the deliquescence of salt particles in atmosphere.* Electrochemistry Communications, 2005. **7**(4): p. 443-448.
144. Li, S.X. and L.H. Hihara, *Atmospheric corrosion initiation on steel from predeposited NaCl salt particles in high humidity atmospheres.* Corrosion Engineering, Science and Technology, 2010. **45**(1): p. 49-56.
145. Bian, L., Y. Weng, and X. Li, *Observation of micro-droplets on metal surface in early atmospheric corrosion.* Electrochemistry Communications, 2005. **7**(10): p. 1033-1038.
146. Tsuru, T., K.-I. Tamiya, and A. Nishikata, *Formation and growth of micro-droplets during the initial stage of atmospheric corrosion.* Electrochimica Acta, 2004. **49**(17-18): p. 2709-2715.
147. Yan-hua, Z.J.-b.W.J.W., *Phenomenon of Micro-droplets Formation on Metals during the Deliquescence of Salt Particles in Atmosphere.* Acta Phys. Chim. Sin., 2005(21): p. 993-996.
148. Neufeld, A.K., I.S. Cole, A.M. Bond, H.S. Isaacs, and S.A. Furman, *CHARACTERIZATION OF SALT PARTICLE INDUCED CORROSION PROCESSES BY SYNCHROTRON GENERATED X-RAY FLUORESCENCE AND COMPLEMENTARY SURFACE ANALYSIS TOOLS*2001. Medium: ED; Size: 10 pages.
149. Neufeld, A.K., I.S. Cole, A.M. Bond, and S.A. Furman, *The initiation mechanism of corrosion of zinc by sodium chloride particle deposition.* Corrosion Science, 2002. **44**(3): p. 555-572.
150. Muster, T.H., A. Bradbury, A. Trinchi, I.S. Cole, T. Markley, D. Lau, S. Dligatch, A. Bendavid, and P. Martin, *The atmospheric corrosion of zinc: The effects of salt concentration, droplet size and droplet shape.* Electrochimica Acta, 2011. **56**(4): p. 1866-1873.
151. Chen, J., J. Wang, E. Han, and W. Ke, *In situ observation of formation and spreading of micro-droplets on magnesium and its alloy under cyclic wet-dry conditions.* Corrosion Science, 2007. **49**(3): p. 1625-1634.
152. Morton, S.C. and G.S. Frankel, *Atmospheric pitting corrosion of AA7075-T6 under evaporating droplets with and without inhibitors.* Materials and Corrosion, 2014. **65**(4): p. 351-361.

153. Prosek, T., D. Thierry, C. Taxén, and J. Maixner, *Effect of cations on corrosion of zinc and carbon steel covered with chloride deposits under atmospheric conditions.* Corrosion Science, 2007. **49**(6): p. 2676-2693.
154. Azmat, N.S., K.D. Ralston, T.H. Muster, B.C. Muddle, and I.S. Cole, *A High-Throughput Test Methodology for Atmospheric Corrosion Studies.* Electrochemical and Solid-State Letters, 2011. **14**(6): p. C9-C11.
155. Cole, I.S., N.S. Azmat, A. Kanta, and M. Venkatraman, *What really controls the atmospheric corrosion of zinc? Effect of marine aerosols on atmospheric corrosion of zinc.* International materials reviews, 2009. **54**(3): p. 117-133.
156. Lindstrom, R., J.-E. Svensson, and L.G. Johansson, *The Influence of Salt Deposits on the Atmospheric Corrosion of Zinc. The Important Role of the Sodium Ion.* Journal of The Electrochemical Society, 2002. **149**(2): p. B57-B64.
157. Beom, W.-J., K.-S. Yun, C.-J. Park, H.-J. Ryu, and Y.-H. Kim, *Comparison of influences of NaCl and CaCl< sub> 2</sub> on the corrosion of 11% and 17% Cr ferritic stainless steels during cyclic corrosion test.* Corrosion Science, 2010. **52**(3): p. 734-739.
158. Baes, C.F. and R.E. Mesmer, *Hydrolysis of cations*1976, New York: Wiley.
159. ASTM, *D1141-98(2008) Standard Practice for the Preparation of Substitute Ocean Water*, 2008, ASTM International: West Conshohocken.
160. El-Mahdy, G.A. and K.B. Kim, *AC impedance study on the atmospheric corrosion of aluminum under periodic wet–dry conditions.* Electrochimica Acta, 2004. **49**(12): p. 1937-1948.
161. Cheng, Y.L., Z. Zhang, F.H. Cao, J.F. Li, J.Q. Zhang, J.M. Wang, and C.N. Cao, *A study of the corrosion of aluminum alloy 2024-T3 under thin electrolyte layers.* Corrosion Science, 2004. **46**(7): p. 1649-1667.
162. Knight, S.P.W.N., A. du Plessis, D. Engleberg, A. Davenport, *Understanding the effect of wet and dry cycles on the atmospheric corrosion of aluminium alloys*, in *ACA*2011: Perth. p. 13.
163. Graedel, T.E., *Corrosion Mechanisms for Aluminum Exposed to the Atmosphere.* Journal of The Electrochemical Society, 1989. **136**(4): p. 204C-212C.
164. Dan, Z., S. Takigawa, I. Muto, and N. Hara, *Applicability of constant dew point corrosion tests for evaluating atmospheric corrosion of aluminium alloys.* Corrosion Science, 2011. **53**(5): p. 2006-2014.
165. Hastuty, S., A. Nishikata, and T. Tsuru, *Pitting corrosion of Type 430 stainless steel under chloride solution droplet.* Corrosion Science, 2010. **52**(6): p. 2035-2043.
166. Maier, B. and G.S. Frankel, *Pitting Corrosion of Bare Stainless Steel 304 under Chloride Solution Droplets.* Journal of The Electrochemical Society, 2010. **157**(10): p. C302-C312.
167. Wang, Y., W. Wang, Y. Liu, L. Zhong, and J. Wang, *Study of localized corrosion of 304 stainless steel under chloride solution droplets using the wire beam electrode.* Corrosion Science, 2011. **53**(9): p. 2963-2968.
168. Lyon, S.B., G.E. Thompson, and J.B. Johnson, *Materials Evaluation Using Wet-Dry Mixed Salt-Spray Tests*, in *New Methods for Corrosion Testing of Aluminium Alloys, ASTM STP 1134*, V.S. Agarwala and G.M. Ugiansky,

Editors. 1992, American Society for Testing and Materials, International: Philadelphia. p. 20-31.
169. Mi, N., M. Ghahari, T. Rayment, and A.J. Davenport, *Use of Inkjet Printing to Deposit Magnesium Chloride Salt Patterns for Investigation of Atmospheric Corrosion of 304 Stainless Steel.* Corrosion Science, 2011.
170. Schindelholz, E. and R.G. Kelly, *Application of Inkjet Printing for Depositing Salt Prior to Atmospheric Corrosion Testing.* Electrochemical and Solid-State Letters, 2010. **13**(10): p. C29-C31.
171. Azmat, N.S., K.D. Ralston, B.C. Muddle, and I.S. Cole, *Corrosion of Zn under fine size aerosols and droplets using inkjet printer deposition and optical profilometry quantification.* Corrosion Science, 2011. **53**(11): p. 3534-3541.
172. Mi, N., *Synchrotron X-Ray Studies of Atmospheric Pitting Corrosion of Stainless Steel*, in *Metallurgy and Materials*2013, University of Birmingham: Birmingham. p. 178.
173. Cruz, R.P.V., A. Nishikata, and T. Tsuru, *AC impedance monitoring of pitting corrosion of stainless steel under a wet-dry cyclic condition in chloride-containing environment.* Corrosion Science, 1996. **38**(8): p. 1397-1406.
174. Li, C., Y. Ma, Y. Li, and F. Wang, *EIS monitoring study of atmospheric corrosion under variable relative humidity.* Corrosion Science, 2010. **52**(11): p. 3677-3686.
175. Shi, Y.Y., Z. Zhang, J.X. Su, and J.Q. Zhang, *EIS study on 2024-T3 aluminum alloy corrosion in simulated acid rain under cyclic wet-dry conditions.* Materials and Corrosion, 2005. **56**(10): p. 701-706.
176. Yadav, A.P., A. Nishikata, and T. Tsuru, *Degradation mechanism of galvanized steel in wet–dry cyclic environment containing chloride ions.* Corrosion Science, 2004. **46**(2): p. 361-376.
177. Flannery, B.P. and W.G. Roberge, *OBSERVATIONAL STRATEGIES FOR 3-DIMENSIONAL SYNCHROTRON MICROTOMOGRAPHY.* Journal of Applied Physics, 1987. **62**(12): p. 4668-4674.
178. Cloetens, P., W. Ludwig, E. Boller, F. Peyrin, M. Chlenker, and J. Baruchel, *3D IMAGING USING COHERENT SYNCHROTRON RADIATION*. 2011. Vol. 21. 2011.
179. Grossmann, J.G., R.W. Strange, and V.P. Suller, *Synchrotron Radiation (Production and Properties). By Philip John Duke. Oxford Science Publications, 2000. Pp. 251. Price (hardback) [pound sign]70.00. ISBN 0 19 851758 0.* Journal of Synchrotron Radiation, 2001. **8**(1): p. 38.
180. Banhart, J., *Advanced Tomographic Methods in Materials Research and Engineering*2008, Berlin: Oxford University Press.
181. Willmott, P., *An introduction to synchrotron radiation: Techniques and applications*2011: John Wiley & Sons.
182. Marone, F., Stampanoni, M., *Regridding reconstruction algorithm for real time tomographic imaging.* Journal of Synchrotron Radiation, 2012 (accepted manuscript).
183. Salvo, L., P. Cloetens, E. Maire, S. Zabler, J.J. Blandin, J.Y. Buffière, W. Ludwig, E. Boller, D. Bellet, and C. Josserond, *X-ray micro-tomography an attractive characterisation technique in materials science.* Nuclear Instruments and Methods in Physics Research Section B: Beam Interactions with Materials and Atoms, 2003. **200**: p. 273-286.

184. Salvo, L., M. Suéry, A. Marmottant, N. Limodin, and D. Bernard, *3D imaging in material science: Application of X-ray tomography.* Comptes Rendus Physique. **11**(9-10): p. 641-649.
185. Baruchel, J., J.-Y. Buffiere, and E. Maire, *X-ray tomography in material science*2000.
186. Beckmann, F., R. Grupp, A. Haibel, M. Huppmann, M. Nöthe, A. Pyzalla, W. Reimers, A. Schreyer, and R. Zettler, *In-Situ Synchrotron X-Ray Microtomography Studies of Microstructure and Damage Evolution in Engineering Materials.* Advanced Engineering Materials, 2007. **9**(11): p. 939-950.
187. Hmelo, A.B., *Nondestructive evaluation of millimeter scale engineered structures using synchrotron x-ray microtomography.* Journal of X-Ray Science and Technology, 1994. **4**(4): p. 290-300.
188. Kinney, J.H. and M.C. Nichols, *X-Ray Tomographic Microscopy (XTM) Using Synchrotron Radiation.* Annual Review of Materials Science, 1992. **22**(1): p. 121-152.
189. Ghahari, S.M., A.J. Davenport, T. Rayment, T. Suter, J.-P. Tinnes, C. Padovani, J.A. Hammons, M. Stampanoni, F. Marone, and R. Mokso, *In situ synchrotron X-ray micro-tomography study of pitting corrosion in stainless steel.* Corrosion Science, 2011. **53**(9): p. 2684-2687.
190. Davenport, A.J., C. Padovani, B.J. Connolly, N.P.C. Stevens, T.A.W. Beale, A. Groso, and M. Stampanoni, *Synchrotron X-Ray Microtomography Study of the Role of Y in Corrosion of Magnesium Alloy WE43.* Electrochemical and Solid-State Letters, 2007. **10**(2): p. C5-C8.
191. Ghosh., S., *Effect of Stress Initiation and Propagation of Localised Corrosion in Aluminium Alloys*, in *Metallurgy and Materials*2007, University of Birmingham: Birmingham (UK). p. 420.
192. Institute, B.S., *Aluminium and Aluminium Alloys. Chemical Composition and form of wrought products. Numerical designation system*, in *BS EN 573-1:2004*2004, BSI Online. p. 12.
193. ASTM, *G46-94: Standard Guide for Examination and Evaluation of Pitting Corrosion*, 1994 (2005), ASTM International: West Conshohocken. p. 8.
194. Marone, F., C. Hintermüller, S. McDonald, R. Abela, G. Mikuljan, A. Isenegger, and M. Stampanoni, *X-ray Tomographic Microscopy at TOMCAT.* Journal of Physics: Conference Series, 2009. **186**(1): p. 012042.
195. Rasband, W.S., *Image J*, 1997, U.S National Institute of Health: Bethesda, Maryland, USA.
196. Liu, Z.R., J.H. Chen, S.B. Wang, D.W. Yuan, M.J. Yin, and C.L. Wu, *The structure and the properties of S-phase in AlCuMg alloys.* Acta Materialia, 2011. **59**(19): p. 7396-7405.
197. Styles, M.J., C.R. Hutchinson, Y. Chen, A. Deschamps, and T.J. Bastow, *The coexistence of two S (Al2CuMg) phases in Al–Cu–Mg alloys.* Acta Materialia, 2012. **60**(20): p. 6940-6951.
198. Wang, S.C. and M.J. Starink, *Two types of S phase precipitates in Al–Cu–Mg alloys.* Acta Materialia, 2007. **55**(3): p. 933-941.
199. Novelo-Peralta, O., I.A. Figueroa, G. Lara-Rodríguez, and G. González, *New evidence on the nature of the metastable S"-phase on Al–Cu–Mg alloys.* Materials Chemistry and Physics, 2011. **130**(1–2): p. 431-436.

200. Winkelman, G.B., K. Raviprasad, and B.C. Muddle, *Orientation relationships and lattice matching for the S phase in Al–Cu–Mg alloys.* Acta Materialia, 2007. **55**(9): p. 3213-3228.
201. Radmilovic, V., R. Kilaas, U. Dahmen, and G.J. Shiflet, *Structure and morphology of S-phase precipitates in aluminum.* Acta Materialia, 1999. **47**(15–16): p. 3987-3997.
202. Blücher, D.B., J.E. Svensson, and L.G. Johansson, *The influence of CO2, AlCl3 · 6H2O, MgCl2 · 6H2O, Na2SO4 and NaCl on the atmospheric corrosion of aluminum.* Corrosion Science, 2006. **48**(7): p. 1848-1866.
203. Dan, Z., I. Muto, and N. Hara, *Effects of Environmental Factors on Atmospheric Corrosion of Aluminium and Its Alloys under Constant Dew Point Conditions.* Corrosion Science, 2012(0).
204. Shreir, L.L., *Corrosion Metal/Environment Reactions (Third edition)*. Third ed, ed. R.A.J.a.G.T.B. L.L. Shreir. Vol. 1. 1994: Butterworth-Heinemann. 1432.
205. Ghali, E., *Aluminum and aluminum alloys*. Uhlig's Corrosion Handbook, Third Edition, ed. R.W. Revie. Vol. 51. 2011, New York: Wiley Online Library.
206. Barton, K., C. Tran Dinh, and S. Bartonova, *Influence of the Cation Composition of Chloride Solutions in Simulating the Corrosion Effects of Seashore Atmospheres.* EINFLUSS DER KATIONENZUSAMMENSETZUNG VON CHLORIDLOESUNGEN BEIM MODELLIEREN VON KORROSIONSEINFLUESSEN DER KUESTENATMOSPHAEREN., 1977. **28**(1): p. 17-19.
207. Harned, H.S. and F.M. Polestra, *The Differential Diffusion Coefficients of Magnesium and Barium Chlorides in Dilute Aqueous Solutions at 25°.* Journal of the American Chemical Society, 1954. **76**(8): p. 2064-2065.
208. Wishaw, B.F. and R.H. Stokes, *The Diffusion Coefficients and Conductances of Some Concentrated Electrolyte Solutions at 25°.* Journal of the American Chemical Society, 1954. **76**(8): p. 2065-2071.
209. Chen, J., J. Wang, E. Han, and W. Ke, *In situ observation of iniatial corrosion of MgAl9Zn1 magnesium alloy in cyclic wet-dry conditions using environmental scanning electron microscopy.* Corrosion, 2007. **63**(7): p. 661-671.
210. He, K., H. Cheng, Y. Zhu, L. Wang, and Y. Zhang, *Study on conductance of supersaturated chloride microdroplets.* Science in China, Series B: Chemistry, 2009. **52**(7): p. 879-886.
211. Chen, Z.Y., D. Persson, A. Nazarov, S. Zakipour, D. Thierry, and C. Leygraf *In Situ Studies of the Effect of CO2 on the Initial NaCl-Induced Atmospheric Corrosion of Copper.* Journal of the Electrochemical Society, 2005. **152**(9): p. B342-B351.
212. Azmat, N.S., K.D. Ralston, B.C. Muddle, and I.S. Cole, *Corrosion of Zn under acidified marine droplets.* Corrosion Science, 2011. **53**(4): p. 1604-1615.
213. McCafferty, E., *Introduction to corrosion science*2010: Springer. 302.
214. Metzger, A., B. Verheggen, J. Dommen, J. Duplissy, A.S.H. Prevot, E. Weingartner, I. Riipinen, M. Kulmala, D.V. Spracklen, K.S. Carslaw, and U. Baltensperger, *Evidence for the role of organics in aerosol particle formation under atmospheric conditions.* Proceedings of the National Academy of Sciences, 2010. **107**(15): p. 6646-6651.

215. Yang, L.T., R.T. Pabalan, and L. Browning, *Experimental determination of the deliquescence relative humidity and conductivity of multicomponent salt mixtures*, in *Scientific Basis for Nuclear Waste Management Xxv*, B.P. McGrail and G.A. Cragnolino, Editors. 2002, Materials Research Society: Warrendale. p. 135-142.
216. El-Mahdy, G.A., *Advanced Laboratory Study on the Atmospheric Corrosion of Zinc under Thin Electrolyte Layers.* Corrosion, 2003. **59**(6): p. 505-510.
217. Stratmann, M. and H. Streckel, *On the atmospheric corrosion of metals which are covered with thin electrolyte layers—II. Experimental results.* Corrosion Science, 1990. **30**(6–7): p. 697-714.
218. Stratmann, M., H. Streckel, K.T. Kim, and S. Crockett, *On the atmospheric corrosion of metals which are covered with thin electrolyte layers-iii. the measurement of polarisation curves on metal surfaces which are covered by thin electrolyte layers.* Corrosion Science, 1990. **30**(6–7): p. 715-734.
219. Cruz, R.P.V., A. Nishikata, and T. Tsuru, *Pitting corrosion mechanism of stainless steels under wet-dry exposure in chloride-containing environments.* Corrosion Science, 1998. **40**(1): p. 125-139.
220. Reboul, M., T. Warner, H. Mayer, and B. Barouk, *A Ten Step Mechanism for the Pitting Corrosion of Aluminium Alloys.* Corrosion Reviews, 2011. **15**(3-4): p. 471-496.
221. Larignon, C., J. Alexis, E. Andrieu, C. Blanc, G. Odemer, and J.C. Salabura, *Corrosion Damages Induced by Cyclic Exposure of 2024 Aluminum Alloy in Chloride-Containing Environments.* Journal of The Electrochemical Society, 2011. **158**(9): p. C284-C295.
222. Rudd, W.J. and J.C. Scully, *The function of the repassivation process in the inhibition of pitting corrosion on aluminium.* Corrosion Science, 1980. **20**(5): p. 611-631.
223. Burstein, G.T. and R.J. Cinderey, *Evolution of the corrosion potential of repassivating aluminium surfaces.* Corrosion Science, 1992. **33**(3): p. 475-492.
224. Cziczo, D.J. and J.P.D. Abbatt, *Infrared Observations of the Response of NaCl, MgCl2, NH4HSO4, and NH4NO3 Aerosols to Changes in Relative Humidity from 298 to 238 K.* The Journal of Physical Chemistry A, 2000. **104**(10): p. 2038-2047.
225. Cole, I.S.G., W. D.; Lau, D., *Field studies of surface cleaning and salt retention on openly exposed metal plates.* Corrosion Engineering, Science and Technology, 2006. **41**(4): p. 310-320.

# 10 APPENDICES

## 10.1 Appendix 1 – Data Logger Plots

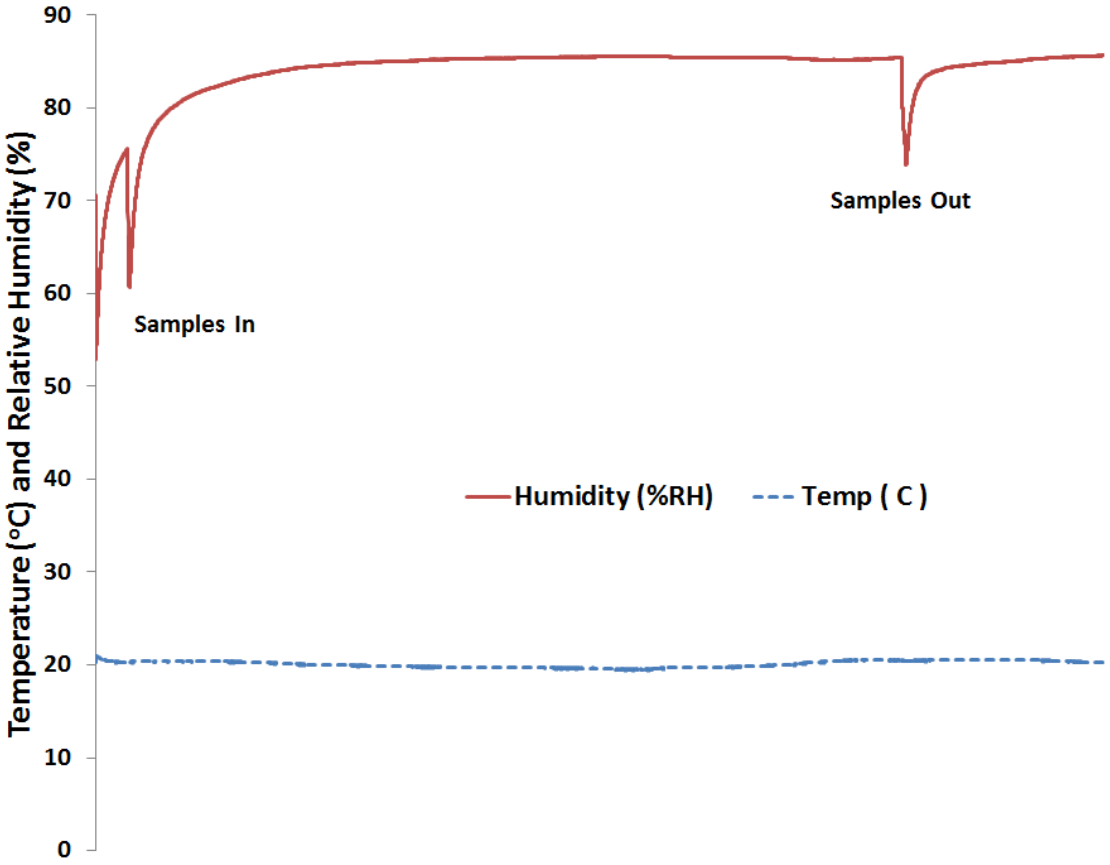


**Figure 10.1 – RH and temperature example plot from ~85% RH exposure, as measured by Omega OM-EL-USB-2-LCD data logger**

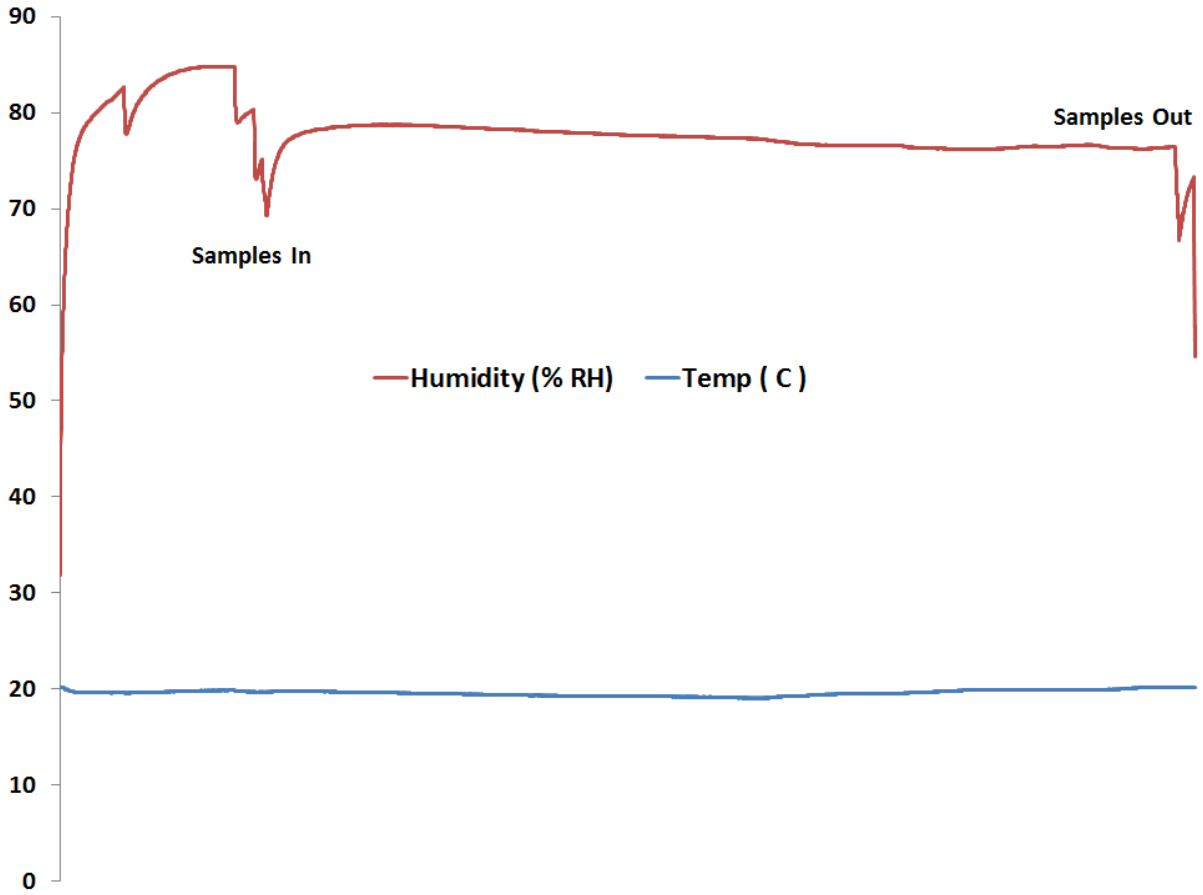


**Figure 10.2 – RH and temperature example plot from ~75% RH exposure, as measured by Omega OM-EL-USB-2-LCD data logger**

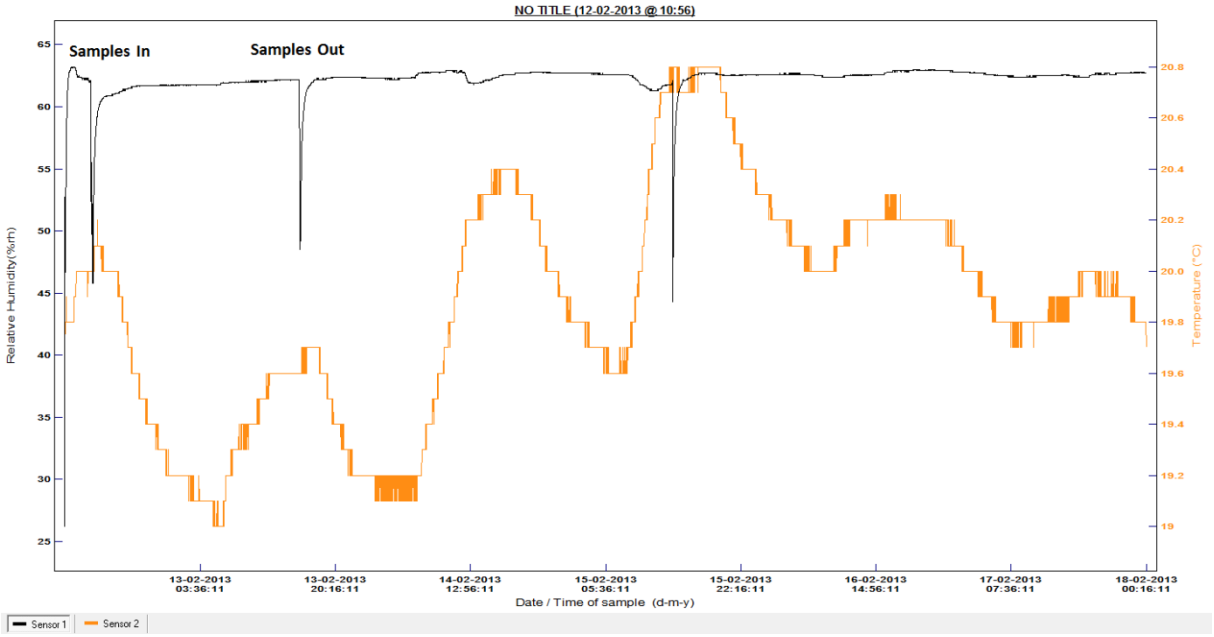


**Figure 10.3 - RH and temperature example plot from ~70% RH exposure, as measured by ThermaData Humidity-Temperature Logger**

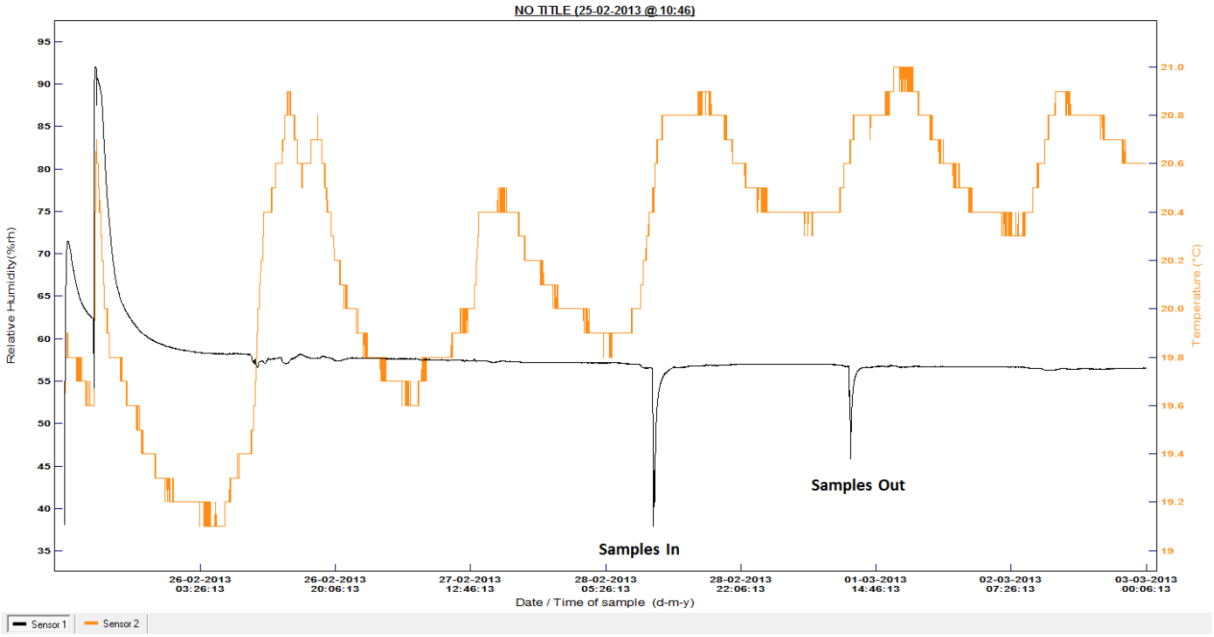


**Figure 10.4 - RH and temperature example plot from ~59% RH exposure, as measured by ThermaData Humidity-Temperature Logger**

## 10.2 Appendix 2 – Measurement of Accuracy of Droplet Volume

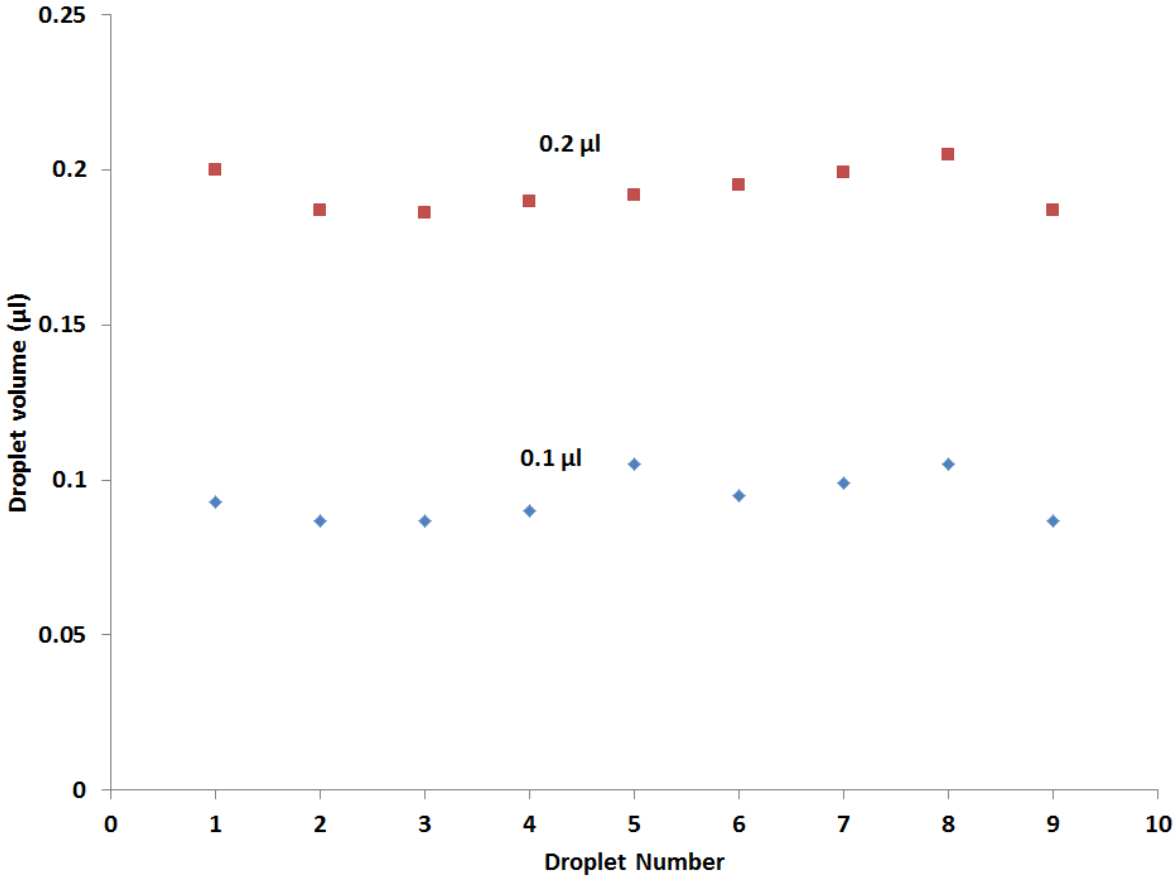


**Figure 10.5 – Measured droplet volume consistency for 0.1 µl and 0.2 µl droplets dispensed using Hamilton HPLC 7000 series micro-syringe**

## 10.3 Appendix 3 – FIJI Scripts

```
for(i=1; i<10; i++){
run("DMP Reader", "choose=E:\\disk5\\OWD4_2a\\rec_DMP\\OWD4_2a000"+i+".rec.DMP");
run("Brightness/Contrast...");
setMinAndMax(-0.0017, 0.0018);
call("ij.ImagePlus.setDefault16bitRange", 0);
run("Close");
run("8-bit");
saveAs("Tiff", "G:\\OWD4\\OWD4_2a\\rectiff\\OWD4_2a000"+i+".rec.tif");
close();
}

for(i=11; i<100; i++){
run("DMP Reader", "choose=E:\\disk5\\OWD4_2a\\rec_DMP\\OWD4_2a00"+i+".rec.DMP");
run("Brightness/Contrast...");
setMinAndMax(-0.0017, 0.0018);
call("ij.ImagePlus.setDefault16bitRange", 0);
run("Close");
run("8-bit");
saveAs("Tiff", "G:\\OWD4\\OWD4_2a\\rectiff\\OWD4_2a00"+i+".rec.tif");
close();
}


for(i=101; i<1000; i++){
run("DMP Reader", "choose=E:\\disk5\\OWD4_2a\\rec_DMP\\OWD4_2a0"+i+".rec.DMP");
run("Brightness/Contrast...");
setMinAndMax(-0.0017, 0.0018);
call("ij.ImagePlus.setDefault16bitRange", 0);
run("Close");
run("8-bit");
saveAs("Tiff", "G:\\OWD4\\OWD4_2a\\rectiff\\OWD4_2a0"+i+".rec.tif");
close();
}

for(i=1001; i<1200; i++){
run("DMP Reader", "choose=E:\\disk5\\OWD4_2a\\rec_DMP\\OWD4_2a"+i+".rec.DMP");
run("Brightness/Contrast...");
setMinAndMax(-0.0017, 0.0018);
call("ij.ImagePlus.setDefault16bitRange", 0);
run("Close");
run("8-bit");
saveAs("Tiff", "G:\\OWD4\\OWD4_2a\\rectiff\\OWD4_2a"+i+".rec.tif");
close();
}
```

**Figure 10.6 – Conversion script for .DMP image files allowing input of brightness and contrast values**

```
var sum, count;
macro "Total Areas [f9]" {
   run("Measure");
   sum += getResult('Area', nResults-1);
   count++;
   setResult('Total', nResults-1, sum);
   setResult('Average', nResults-1, sum/count);
   updateResults();
}

macro "Reset Total" {
   sum = 0;
   count = 0;
}
```

**10.7 – Area calculator script for pixel counting during surface damage assessment**